Université catholique de Louvain
Louvain School of Engineering
Institute of Mechanics, Materials and Civil Engineering

Modeling and numerical simulation of transient flows in superposed porous and pure-fluid layers

Doctoral dissertation presented by

Panagiotis Dimitrios Antoniadis

in partial fulfillment of the requirements
for the degree of Doctor in Engineering Sciences

Supervisor:

Prof. Miltiadis Papalexandris, Université catholique de Louvain

Thesis committee:

Prof. Vincenzo Armenio, Università degli Studi di Trieste
Prof. Philippe Chatelain, Université catholique de Louvain
Prof. Eric Deleersnijder, Université catholique de Louvain
Prof. Sandra Soares Frazao, Université catholique de Louvain
Prof. Grégoire Winckelmans, Université catholique de Louvain (President)

Louvain-la-Neuve, September 2015

To my parents

Acknowledgements

I would like to begin by expressing my sincere gratitude to my supervisor, Professor Miltiadis Papalexandris for his continuous support and guidance throughout my doctoral studies. Always available to discuss either the small details or the major issues, with original interest in the subject of porous media flows, his role extended beyond that of a typical supervisor, to that of a true research mentor.

I would also like to thank each one of the members of the thesis committee. Professor Grégoire Winckelmans for our beneficial discussions and his interest in the subject of shear layers at the porous medium - pure fluid interfaces. Professor Philippe Chatelain for following closely the progress of my work with a critical view from the beginning, as well as his valuable comments and suggestions for improvements. Professor Eric Deleersnijder for being a helpful referee for my FRIA application, as well as for his comments on the pertinence of the present work to environmental flows. Professor Sandra Soares Frazao for taking the time to walk me through all of her comments and suggestions for corrections of this thesis. Last but not least, Professor Vincenzo Armenio for accepting to be part of the examination committee, and for his valuable comments during my private defense.

Special thanks goes to Dr. Christos Varsakelis for the many fruitful discussions on common problems and solutions we had over the years. It also in his company that I discovered the medicinal properties of a good Belgian beer after a hard day at work.

Also I would like to thank my colleague and friend Pierre Schrooyen, for the interesting and beneficial discussions on the subject of flows at the interface between a porous medium and a pure fluid.

My years as a PhD student were also the first years living away from Greece. So, I

take this opportunity to thank Dr. Yves Marichal and Mr. Nicolas Bourgeois for their advice during the first months on how to do things the Belgian way, and also for the rest of the years we spent sharing the same office.

For any administrative task that I ever needed help with, and for all the corrections of my sloppy French writting, I want to thank Isabelle Hennau for willingly providing her time. Also, for his excellent IT support and advice I want to thank Edmond Mulemangabo.

During the last months I have also set to switch from my long academic career to a career in the private sector. My efforts on that end have been greatly strengthened with the help of Dr. Valérie Gelbgras of ANSYS Belgium, whose advice and coaching I mostly appreciate.

The financial support of the National Scientific Research Funds of Belgium (FNRS) in the form of a FRIA fellowship is gratefully acknowledged.

Completing this work would have been a lot more difficult without the support of my valued friends. First of all I thank Giannis Georgilas, Giannis Vrasidas, Giorgos Varvaras, Konstantinos Astreidis and Thomas Gkioufis for being an extended family to me for the last 21 years. My Louvain-la-Neuve experience would have not been the same without Adrienne Little, who has always offered me a different perspective of the choices I had, as well as an insight to a culture largely different to mine. Also, Marcel Medwed and Paolo Palmiery have been my first international friends and we have shared many great experiences during the first years in Belgium.

Finally, I want to express my gratitude to my parents, who have always been providing more than I could ever ask for. My studies would have never reached this far without their continuous support. I will never manage to thank them enough.

Panagiotis D. Antoniadis
Louvain-la-Neuve, October 2015.

Abstract

In this work we are concerned with the modeling and numerical simulation of transient flows in superposed porous and pure-fluid layers, with heat transfer and chemical reactions. Our study is mainly concerned with the basic underlining physical phenomena that characterize such flows. Particular attention is given to the transient characteristics of the flow evolution at the vicinity of the macroscopic interface between a porous structure and a pure-fluid region.

In the first part, we propose a single-domain approach, thermal non-equilibrium model which incorporates porosity as a field variable. As such, a single set of equations is used to describe the flow in both the porous and the pure-fluid regions, that does not require additional matching conditions at the interface. Also, the flow structures at the transition layer between the two regions are resolved, which renders this model ideal for the study of unsteady flows in the domains of interest. We further present the low-Mach number limit of the governing equations, for which the solution methodology is greatly simplified. At the end of the chapter, we also discuss the resulting equations for the non-reacting case, *i.e.* in the absence of interphasial mass exchange.

In the second part, we describe the proposed numerical algorithm for the treatment of the governing equations, which is straight-forward to implement in a computer code. It is a generalization of projection methods for the Navier-Stokes equations to multi-phase flows. A two-step advancement in time is used, for improved stability and accuracy in time. The spacial discretization is performed on a collocated grid, which requires the implementation of a flux-interpolation scheme to prevent the odd-even decoupling of the pressure field. Finally, the proposed model and algorithm are validated with two test

cases. In the first one, we perform simulations of forced flow in superposed porous and pure-fluid layers, and we compare the obtained velocity profiles, with solutions available in the literature. In the second test case, the rate of growth of an inviscid shear layer is calculated by means of a numerical simulation and, subsequently it is compared to the analytic results obtained by our linear stability analysis that is described later in this work.

In the third part, we discuss results for constant-density shear flows at the interface between a porous medium and a pure fluid. First, a linear stability analysis of inviscid shear layers is performed, which provides an insight to the main characteristics of the flows of interest. According to our results, such shear layers are unstable at all perturbation wavelengths and porosities. Next, we discuss in detail the evolution of time-developing shear layers, from our two-dimensional and three-dimensional simulations. We focus mainly on the flow structures that emerge during the transient part of the flow, as well as on the evolution of these structures at the vicinity of the macroscopic interface between the porous and the pure-fluid regions.

In the fourth part we study fluid flow with heat transfer in the domains of interest. At the beginning we are concerned with the problem of natural convection in a channel with a porous strip attached to its lower wall. Next, we focus on the effect of unstable stratification on forced flow inside a channel. Finally, we study the effect of both stable and unstable stratification on shear layers in semi-bounded domains. The discussion mainly focuses on the effect of buoyancy on the evolution of the flow structures at the interface between the porous and the pure-fluid regions. Emphasis is placed on the mechanisms that induce thermal non-equilibrium between the two phases inside the porous medium.

Finally, in the fifth part, we focus on results from our numerical simulations of reacting flows through a porous medium. The heterogeneous reaction between the two phases inside the porous material is modeled with a single-step chemical kinetics mechanism. Two problem configurations are considered. In the first one, the porous fuel is placed at the half-width of a pure-fluid channel, and reacts with hot oxidizer which enters the domain from the inflow. In the second configuration, the porous fuel is placed next to

the bottom wall of a channel, and is ignited by spark. According to our results from both cases, in highly porous media the chemical reaction rates can be significant not only at the macroscopic interface between the porous structure and the pure-fluid, but also at the interior of the porous medium.

Table of Contents

List of Figures

Nomenclature

List of symbols

c	speed of sound
c_p	specific heat of the fluid under constant pressure
c_v	specific heat of the fluid under constant volume
c_s	specific heat of the solid
d_p	diameter of a single microscopic element
e	internal energy
f	auxiliary flux
$\boldsymbol{f}$	interphasial momentum exchange rate
$\mathbf{g}$	gravity vector
h	interphasial heat transfer coefficient
h_c	convection heat transfer coefficient
k	thermal conductivity coefficient
l	length
$\hat{n}$	unit outward normal vector
p	pressure
p^0	*thermodynamic* pressure
p^1	*kinematic* pressure
p^v	bulk viscous pressure
p'	piezometric pressure, $p' = p^1 + \rho Riy$
q	heat transfer rate

r_i	distance of the cell-center from the cell-interface in the x direction
t	time
$\mathbf{u}$	velocity vector
$\tilde{\boldsymbol{u}}$	*provisional*, or *intermediate* velocity vector at the predictor step
$\breve{\boldsymbol{u}}$	*provisional*, or *intermediate* velocity vector at the corrector step
$\hat{\boldsymbol{y}}$	unit vector along the vertical direction

C_D	interfacial drag coefficient
$\mathcal{E}$	interphasial energy exchange rate
H^f	enthalpy of formation of the fluid
$\mathcal{K}$	kinetic energy of fluctuations
L_x	dimension of the domain in the stream-wise (x) direction
L_y	dimension of the domain in the normal (y) direction
L_z	dimension of the domain in the span-wise (z) direction
M_0	total fluid mass
$\mathcal{M}$	interphasial mass exchange rate
N_{s}	number density
$\boldsymbol{P}^{\mathrm{v}}$	viscous stress tensor
$\boldsymbol{P}_d^{\mathrm{v}}$	viscous shear stress tensor
$\mathcal{R}$	universal gas constant
R_{ij}	Reynolds stresses
S_Ω	the interface between the porous and the pure-fluid regions
T	temperature
$\boldsymbol{V}_d^{\mathrm{v}}$	deviatoric part of the deformation tensor

α	thermal expansion coefficient
$\boldsymbol{\beta}$	interphasial drag parameter
γ	specific heat ratio
δ_m	momentum thickness

δ_m^+	momentum thickness in the pure-fluid region
δ_m^-	momentum thickness inside the porous medium
ζ	bulk viscosity coefficient
η	entropy
κ	interphasial mass transfer coefficient
μ	dynamic viscosity coefficient
ν	kinematic viscosity coefficient
ρ	density
τ	wall stress
ϕ	volume fraction
ψ	Helmholtz free energy
Ω_{f}	pure fluid sub-domain
Ω_{p}	sub-domain covered by the porous material

Subscripts

d_p	value specified at the micro-scale
f	fluid phase
i	order of appearance of the cell along the x axis
$i+1$	value at the center of the neighbouring cell along the x direction
$i+\frac{1}{2}$	value at the cell-interface along the x direction
j	order of appearance of the cell along the y axis
k	order of appearance of the cell along the z axis
m	mixture
ref	reference value
s	solid phase
$t.w.$	top wall

xxx

Superscripts

0	term of order 0
1	term of order 1
(n)	value at the time-level n
$(*)$	predicted value

Non-dimensional numbers

$Gr = \lvert\boldsymbol{g}\rvert \, \alpha \, (T - T_{ref}) * l^3/\nu^2$	Grashof number. Measure of the ratio of buoyancy forces to viscous forces.
$Nu = h_c \, l \, / \, k$	Nusselt number. Measure of the ratio of thermal convection to pure conductive heat transfer.
$Pr = (c_p \mu)/k$	Prandtl number. Measure of the ratio of the momentum and thermal diffusivities.
$Ra = Gr \cdot Pr$	Rayleigh number. Measure of the instability of a layer of fluid, due to the differences of temperature and density along the direction of the gravity vector.
$Re = (\rho \, l \, u)/\mu$	Reynolds number. Measure of the ratio of inertia and viscous forces.
$Ri = \lvert\boldsymbol{g}\rvert \, l \, / \, u^2$	Richardson number. Measure of the ratio of gravity to the flow inertia.

Chapter 1

Introduction

1.1 Flows in domains partially occupied by porous media

Porous media are materials that consist of a solid matrix and a network of void spaces, namely the pores, Nield & Bejan (2013). Herein we address the class of porous media in which the void spaces are interconnected, so that a fluid is allowed to flow through the material. Such media are readily found in nature, for example sand, rocks, underground reservoirs, etc., but they are also manufactured for specific applications; ceramic materials, polymeric foams, bricks and others.

This work is concerned with fluid flow in domains partly occupied by a region that contains a fluid alone and partly by a porous medium which is saturated by the same fluid. Such flows occur in several scales, ranging from the microscale to the macroscale, and are encountered in both industrial processes and natural phenomena. Some representative examples are provided in the following paragraphs.

Applications in Industry

A popular technological application relevant to the flows of interest is **fuel cells**, see, for example, Promislow *et al.* (2006). These devices convert chemical energy from a fuel into electricity and have attracted the interest of the scientific community due to the unique combination of remarkably high efficiency and very low emissions. A demonstration model of a direct-methanol fuel cell is shown in Figure 1.1. Their difference

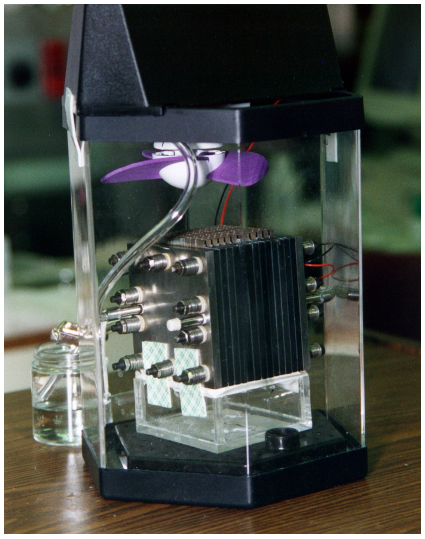

Figure 1.1: Demonstration model of a direct-methanol fuel cell. Source: NASA, JPL. `http://www2.jpl.nasa.gov/files//images/hi-res/p48600ac.tif`.

from batteries is that they operate continuously for as long as a source of fuel and an oxidizer are supplied to sustain the chemical reaction. The energy efficiency of a fuel cell is generally between $40-60\%$, or up to 85% in cogeneration if waste heat is captured for use. Furthermore, if pure hydrogen is used as a fuel, they have virtually no emissions. Fuel cells are used as power generators for buildings, in several types of vehicles, and other applications. Even though there are several different types of fuel cells, all of them share common operating principles. They consist of two electrodes, an anode and a cathode, and an electrolyte which is placed in between. Both electrodes are made of porous materials so that the fuel and the oxidizer can reach near to the surface of the electrolyte. On the side of the anode the fuel undergoes oxidation and produces ions and electrons in the presence of catalysts. The ions are drawn through the electrolyte, while the electrons travel from the anode to the cathode through an external circuit, resulting in direct current electricity. A schematic diagram of this procedure is provided in Figure 1.2. Unfortunately, even though the first fuel cells were invented in 1838, they are still very expensive for general commercial use. To render them more competitive among other well developed traditional power systems, there is a continued effort to improve their performance. One of the key elements in this respect, is the effectiveness of the

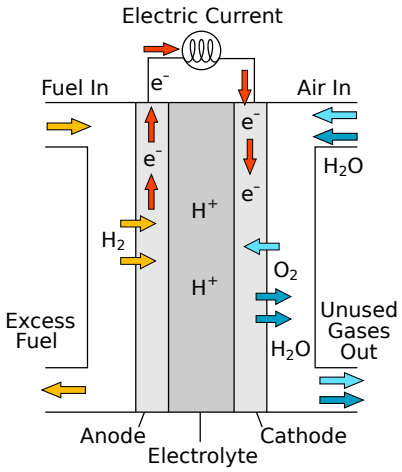

Figure 1.2: Schematic of the operation of a fuel cell. Source: Wikipedia, `https://en.wikipedia.org/wiki/File:Solid_oxide_fuel_cell.svg`.

delivery of the fuel and the oxidant on the active catalyst sites. Accordingly, the study of fluid flow through the porous electrodes, where the electrochemical reactions take place, is of great importance.

The characteristics of porous structures are also exploited in heat exchangers and **heat sinks**. Heat exchangers are devices that transfer heat between two fluids at different temperatures, that are separated by a solid wall to prevent them from mixing. Such devices are used in space heating, air-conditioning, energy production and other technological and industrial applications. On the other hand, heat sinks transfer the heat produced by an electronic or a mechanical device to a coolant fluid. This aims to improve the operating conditions of such devices, increasing their performance, efficiency and reliability. The coolant fluid may be circulating either because of natural convection (passive cooling), or due to fans that induce forced convection over the heat sink (active cooling). Figure 1.3 depicts the heat sink of the Central Processing Unit (CPU) on the motherboard of a personal computer. Due to the increased need for cooling, a fan is mounted on top of the heat sink, to increase the air flow. On the upper right corner of the same figure, another component of the motherboard is cooled by a heat sink that relies solely on natural convection. The design of heat exchangers and heat sinks is crucial to the effectiveness of their heat transfer and cooling capacities, and consequently to the

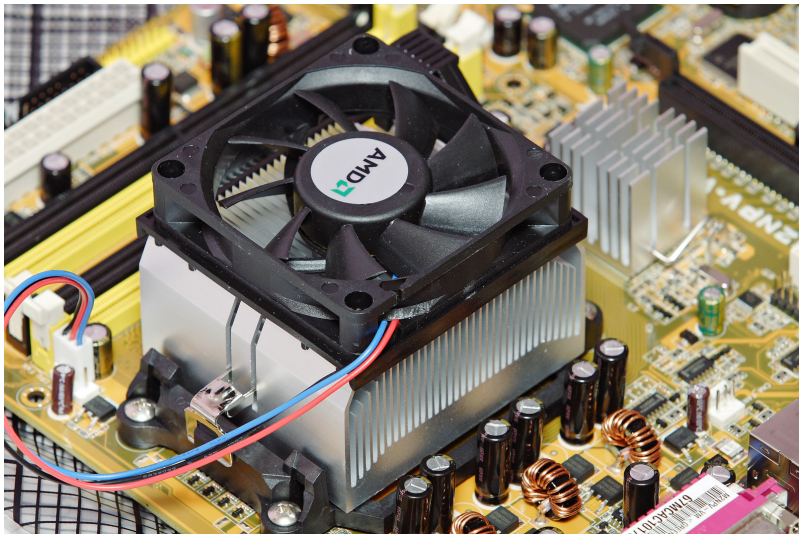

Figure 1.3: Heat sink of the Central Processing Unit (CPU) of a personal computer. Source: Wikipedia, copyright "Fir0002/Flagstaffotos", `https://upload.wikimedia.org/wikipedia/commons/2/25/AMD_heatsink_and_fan.jpg`.

performance of the systems they are embedded in. As such, the study of fluid flow under thermal stratification around such porous bodies can be greatly beneficial for relevant technological applications. In the present work, the problems of both natural and forced convection over layers of highly porous materials are discussed in Chapter 5.

On a larger scale, **underground hydrocarbon reservoirs** consist of superposed porous and pure-fluid layers. The process of extracting petroleum from such cavities is very costly, and the necessary equipment is very expensive as well. According to Harris *et al.* (2005), the cost of an off-shore production platform can be more than £1 billion, while the drilling for an individual well can cost more than £20 million. Accordingly, to minimize the risk and increase profit, the oil and gas industry is in need for predictions of the subsurface fluid flow patterns in these domains. However the numerical simulations of such flows are particularly cumbersome due to several challenges. First, the size of the physical domain necessitates the use of coarse grids in order to obtain results in rational simulation times. Further, hydrocarbon reservoirs contain multiple immiscible fluids (water, gas and/or oil), whose motion needs to be modelled. Also, the presence of faults and fractures can complicate the draining procedure even further. These challenges and others, render the study and further understanding of the fluid flow in underground

reservoirs essential for the oil and gas industry.

Environmental Applications

In nature, **submerged aquatic vegetation canopies** share common characteristics as permeable media with high porosities. The presence of such canopies has a significant impact on the surrounding aquatic systems. In particular, the hydrodynamic conditions around such bodies, owing to their porous structure, affect processes such as the transport of sediment, nutrients, contaminants, dissolved oxygen and also on fauna. For example, the growth of seagrass depends on the deposition of nutrients on the sea bed. However, the later can be hindered due to the flow structures that develop at the interface region between the canopy and the surrounding water body, see, for example, Ghisalberti & Nepf (2009).

Analogous, but at the large scale, are the characteristics of the flow above **forest canopies**, see, for example, Raupach *et al.* (1996). In these ecosystems, the flow conditions at the interior and above the canopy can have an important influence on numerous environmental variables and processes. The mass, momentum and heat transfer across the canopy top regulate the forest's microclimate, the deposition and re-entrainment of dust, seeds and other particles, water vapor etc.

Finally, we mention **dense urban areas** which can also be modeled as permeable, porous structures. Such an approach can be beneficial for the study of the consequences of modern human lifestyle on the environment of cities, such as the release of pollutants and waste heat, which eventually lead to the formation of urban heat islands. See, for example, the numerical study of Hu *et al.* (2012). In this work, the authors consider the flow around a porous medium with internal heat sources, which represent the heat flux between buildings and the ambient air, the waste heat from vehicles, etc. Further they proceed to investigate the effect of the intensity of both anthropogenic heat sources and wind on the formation of urban heat islands.

From all the above we can see that the flows of interest are central to numerous and diverse aspects of modern life, societies and nature. As such, their better understanding has been the subject of numerous research efforts over the years. However, there are

several challenges involved in the study of such flows. First of all, one is faced with not only one, but with a range of length scales that characterize the flow field, which may extend from the micro to the macro. Further, the macroscopic interfaces between the porous and pure-fluid regions introduce rich phenomenology to the flow, which needs to be resolved, as will be discussed in due course of this work. Finally, one has to take into account the coexistence and interaction between the fluid and the solid phases at the area that is occupied by the porous medium.

1.2 State of the art in modeling of flows at the interface between a pure-fluid and a porous region

Most of the theoretical and numerical studies have been based on the so-called two-domain approach. According to it, separate governing equations are prescribed on the porous medium and on the pure-fluid domain. Typically, governing equations for the porous regions are derived via volume averaging methods. This method essentially amounts to modifying the equations of fluid motion to account for the presence of the solid matrix and then averaging these equations over space. The literature on the modelling of porous media flows following the two-domain approach and on volume-averaging methods is quite extensive; see, for example, Chen (1990), Ochoa-Tapia & Whitaker (1995), Alazmi & Vafai (2001), Quintard & Whitaker (2005), Miller & Gray (2005), Chandesris & Jamet (2007), Chen *et al.* (2008), Chandesris & Jamet (2009), Jäger & Mikelić (2009), Gray & Miller (2010), Mosthaf *et al.* (2011) and references therein. A wealth of information and numerous additional references can also be found in the textbooks Whitaker (1999), Nield & Bejan (2013). This approach, however, requires the prescription of a matching condition at the material interface.

In their landmark work, Beavers & Joseph (1967) argued that shear effects are transmitted between the two subdomains via a transition layer and proposed a velocity slip condition across the interface based on experimental measurements. In their formulation, the value of the slip velocity depends on the porous microstructure. A theoretical justification for this interface condition was later provided by Saffman (1971). Subsequently, a variety of slip conditions were proposed, designed to cover specific ranges of

porosities, porous microstructures, and different types of flows. Interface conditions that can be employed in a general setting have also been proposed Ochoa-Tapia & Whitaker (1995), Valdés-Parada *et al.* (2007), Chandesris & Jamet (2009). Finally, a number of studies have been devoted to comparisons between various interface conditions Sahraoui & Kaviany (1992), Goyeau *et al.* (2003), Le Bars & Worster (2006).

Alternatively, one can opt for a single-domain approach for the study of the flows of interest; see, for example, Nield & Bejan (2013), Straughan (2005), Cowin (2008), Marle (1982), Bennon & Incropera (1987), del Rio & de Haro (1992), Drumheller (2000), de Boer (2000). This amounts to deriving a single set of governing equations that is simultaneously valid in both the porous and the pure-fluid domains, thus eliminating the need for interface conditions. According to this approach, the porosity, i.e. the volume fraction of the fluid phase, is introduced as a field variable. Then, a single set of governing equations can be derived either via volume averaging Beckermann *et al.* (1999), Le Bars & Worster (2006) or via a mixture-theoretic formalism Bennon & Incropera (1987), Séro-Guillaume & Margerit (2001).

An important difference between the two approaches is the following. In the two-domain approach, the transition layer is not resolved, which allows for discontinuities of shear stresses at the interface. A notable exception is the transition region model of Jackson *et al.* (2012), in which the interface is modelled as a transition layer instead. On the other hand, in the single-domain approach, the flow structures in the vicinity of the interface are resolved; the same also holds for the model of Jackson *et al.* (2012). For this reason, in our view, the single domain approach is better adapted for numerical simulations of unsteady flows. A quantitative comparison between the two approaches for channel flows can be found in Goyeau *et al.* (2003) and Hirata *et al.* (2007).

1.3 State of the art in the study of flows in superposed porous and pure-fluid layers

As we also mentioned above, one category of flows that occur at the macroscopic interface between a porous structure and a pure-fluid region, are flows over terrestial and vegetation canopies. Early works that were devoted to this topic, supported that the flow field

at the top of the canopy is a superposition of a boundary layer above the vegetation line, and a *roughness sublayer* below it which generates small-scale eddies produced in the plant wakes. Raupach & Thom (1981) were the first to suggest that large-scale structures dominate the flow at the transition region in such flows. Later, in the *mixing layer analogy* of Raupach *et al.* (1996), these structures were identified as the result of a *Kelvin-Helmholtz* type of instability at the interface between the canopy and the overlying pure-fluid area. Since then, numerous works were devoted to modeling and studying these flow structures, see, for example, Finnigan (2000), de Langre (2008) etc. Similar results, namely the formation of rollers resulting from the instability at the interface between a porous and a pure-fluid layer were reported in the numerical simulations of Breugem & Boersma (2005). Also, a linear stability analysis of such flows between parallel walls was later performed by Tilton & Cortelezzi (2006; 2008), which confirmed the onset of the instability on the interface, thus concuring to the previously reported results.

Also, there are applications such as heat exchangers, thermal insulation systems and others, where heat transfer is induced by buoyancy effects. One of the first works on flows with heat transfer in domains with regions of different permeability, was that of Poulikakos & Bejan (1983). According to their numerical results, the heat transfer mechanisms were greatly affected by the non-uniformity of permeability. In particular, they report that convective motions were "attracted" to the high-permeability regions. In their subsequent works, Beckermann *et al.* and Chen & Chen worked on similar problem configurations. Beckermann *et al.* (1988) conduct numerical simulations using a *non-Darcian* model inside the porous layers, that incorporates the Brinkman and Forchheimer extentions. Also, they couple the equations of the porous regions with those of the pure-fluid regions using a step function. Further they perform experiments to validate the numerical results. On the other hand Chen & Chen (1988) conduct a linear stability analysis, using the Darcy equation in the porous medium, and they also compare their results with their own experiments, published in Chen & Chen (1989).

In the more recent years there has been a wealth of works dedicated to the linear stability analysis of the flows of interest; see, for example, Hirata *et al.* (2009a), Hill & Carr (2010a) and others. In most of the cases, the authors assume that the two phases are in thermal equilibrium with each other, and therefore one energy equation is used.

However, this is not necessarily true. There are applications in which rapid heat transfer takes place in porous materials, and therefore the thermal equilibrium hypothesis may not be valid. For such applications, separate energy equations for the two phases are needed, namely, *two-temperature* models should be used. It so happens, that works based on such models are limited to steady state convection problems, see for example, Kuznetsov & Nield (2010), Nield & Kuznetsov (2011). To the best of our knowledge, results of unsteady flows in superposed porous and pure-fluid layers in the absense of thermal equilibrium have yet to appear in the literature.

The problem of flows through porous media in the presense of chemical reactions becomes particularly complex. The heterogeneous reaction between the solid and the fluid phase presents additional challenges such as the stiff reaction rates, the large heat release, the large density and specific-heat ratios between the two phases, and others. It is the combination of these challenges with the multiple heat transfer mechanisms inside the porous medium, which renders the numerical simulations of reacting flows in porous media highly demanding in computational resources. As a result, the majority of relevant works in bibliography is limited to the study of one-dimensional or steady-steady problems. On the other hand, works that focus on multi-dimensional problems have to resort to simplified models for the heterogeneous chemical reaction. A detailed survey on the modeling of porous media combustion can be found in Mujeebu *et al.* (2010).

1.4 Motivation and objectives of this PhD Thesis

In this work we focus on the flows of interest occurring at a small scale, *i.e.* flows of small to moderate Reynolds numbers. As such, the numerical results discussed in the following chapters are pertinent to fluid flow over grass, over submerged aquatic canopies, and flows occurring in technological applications such as fuel cells, or heat-sink devices of electronic components. Our study is mainly concerned with the basic underlining physical phenomena that characterize such flows. Particular attention is given to the transient characteristics of the flow evolution at the vicinity of the macroscopic interface between a porous structure and a pure-fluid region.

Despite the recent advancement in the studies of the flows of interest, there is an evident lack of numerical results of unsteady flows. Prominent exceptions are the simulations of turbulent flow in a channel with one permeable wall of Breugem & Boersma (2005) and the work of Chandesris *et al.* (2013), which extends that of Breugem & Boersma, by including heat transfer effects. This lack of numerical results can be attributed to the challenging task of resolving the fluid flow and heat transfer in the transition region between the porous and pure-fluid layers.

The present work aspires to fill this gap in the literature. To this end we propose a single-domain approach, thermal non-equilibrium model which incorporates porosity as a field variable. As such, a single set of equations is used to describe the flow in both the porous and the pure-fluid regions, that does not require additional matching conditions at the interface. Further, the flow structures at the transition layer between the two regions are resolved, which renders this model ideal for the study of unsteady flows in the domains of interest. We also propose a numerical algorithm for the treatment of the governing equations, which is straight-forward to implement in a computer code. As is discussed also in chapters 2 and 3, due to differences between the model that we propose herein and other models of the literature, we cannot use readily available software for the needs of our numerical studies. As such, the algorithm presented in Chapter 3 is implemented in our own software, in the C++ programming language. Further, we perform simulations of isothermal flows, flows with heat transfer, as well as reacting flows in the domains of interest. In all cases examined, emphasis is placed on the flow structures that emerge during the transient part of the flow, as well as on the evolution of these structures at the vicinity of the macroscopic interface between the porous and the pure-fluid regions. The content of the chapters 2 to 6 is summarized in the following paragraph.

Chapter 2 provides a detailed description of the derivation of the proposed model, which is valid for both compressible and incompressible flows. We further present the low-Mach number limit of the governing equations, for which the solution methodology is greatly simplified. At the end of the chapter, we also discuss the resulting equations for the non-reacting case, *i.e.* in the absence of interphasial mass exchange.

In Chapter 3 we describe the proposed numerical algorithm for the treatment of

the governing equations. It is a generalization of projection methods for the Navier-Stokes equations to multi-phase flows. A two-step advancement in time is used, for improved stability and accuracy in time. Finally, the spacial discretization is performed on a collocated grid, which requires the implementation of a flux-interpolation scheme to prevent the odd-even decoupling of the pressure field.

In Chapter 4 we discuss results for constant-density flows. The largest part of this chapter is dedicated to the dynamics of shear layers at the interface between a porous medium and a pure fluid. First, a linear stability analysis of inviscid shear layers is performed, which provides an insight to the main characteristics of such flows. Next, we describe in detail the evolution of time-developing shear layers, from our two-dimensional and three-dimensional simulations. Finally, we focus on the problem of forced flow in a channel, with a porous strip attached to one of its walls.

Chapter 5 is devoted to the study of fluid flow with heat transfer in the domains of interest. The chapter is divided in three parts. The first part is concerned with natural convection in a channel with a porous strip attached to its lower wall. The second part focuses on the effect of unstable stratification on forced flow inside a channel. In the third part we study the effect of both stable and unstable stratification on shear layers in semi-bounded domains. In all the problems examined, we pay particular attention to the mechanisms that induce thermal non-equilibrium between the two phases inside the porous medium.

Finally, Chapter 6 focuses on results from our numerical simulations of reacting flows through a porous medium. The heterogeneous reaction between the two phases inside the porous material is modeled with a single-step chemical kinetics mechanism. Two problem configurations are considered. In the first one, the porous fuel is placed at the half-width of a pure-fluid channel, and reacts with hot oxydizer which enters the domain from the inflow. In the second configuration, the porous fuel is placed next to the bottom wall of a channel, and is ignited by spark.

Chapter 2

A thermodynamically consistent two-phase model

2.1 Introduction

In this chapter we develop a thermo-mechanical model for the flows of interest, based on the one-domain approach. This choice is motivated by the fact that, as mentioned above, this approach is better adapted for the numerical study of unsteady flows. To this extent, we adopt a mixture-theoretic formalism, according to which both the fluid and the porous solid are treated as two separate and identifiable continua that occupy the same space and are in thermodynamic non-equilibrium with each other. As such, each continuum constituent is endowed with its own set of thermodynamic variables and is assigned its own set of balance laws. Also, the porosity (fluid volume fraction) is introduced as a field variable that measures the density of volume occupied by the fluid. Then, constitutive relations for the interaction between the two phases and for all dissipative phenomena occurring in each phase are derived via exploitation of the constraints imposed by the entropy-inequality axiom. It should be noted that the modelling of porous-media flows based on mixture-theoretic formalisms has a long history. Over the years, various models have been developed by employing different theories of non-equilibrium thermodynamics; see, for example, Marle (1982), Bennon & Incropera (1987), del Rio & de Haro (1992),

The results of this chapter have been published in: Papalexandris M.V. & Antoniadis P.D. 2015 A thermo-mechanical model for flows in superposed porous and fluid layers with interphasial heat and mass exchange. *Int. J. Heat Mass Tran.* **88**, 42–54.

Drumheller (2000), de Boer (2000), Cowin (2008), and references therein.

Our modelling, however, differentiates from earlier works in several aspects. First, we follow a particular mixture-theoretic formalism, namely the one of Papalexandris (2004), which is a generalization of the classical theory of irreversible processes to immiscible mixtures whose constituents are in thermal non-equilibrium. Second, the proposed model treats both thermal non-equilibrium between phases and heterogeneous reactions, while being valid for both compressible and incompressible fluid flows. Third, the limiting case of incompressible flows is derived via a formal asymptotic expansion, commonly known as "low-Mach number approximation", instead of assuming *a priori* that the fluid's thermodynamic pressure or density are constant.

The low-Mach number approximation is valid for flows where compressibility effects are negligible and is applicable to many practical applications and natural phenomena. An important simplification of this approximation is that the thermodynamic pressure appears only in the energy equation of the fluid phase, and not in the momentum equation. Also, the constitutive expressions for interphasial mass exchange simplify considerably. Finally, we discuss in more detail the properties of the low-Mach number approximation for the special but important case of non-reacting flows (without interphasial mass exchange), and we also elaborate on the issue of thermal condition for the porous matrix at the interface.

The chapter is organized as follows. In Section 2.2 we present the derivation of the thermo-mechanical model and in Section 2.3 we derive its low-Mach number approximation. Finally, in Section 2.4 we discuss the properties of the model for the case of non-reacting flows.

2.2 Derivation of the mathematical model

Let $\Omega \subset \mathbb{R}^3$ be an open and bounded domain that contains both porous and pure-fluid regions. The porosity distribution $\phi(\boldsymbol{x}, t)$ is introduced as a concentration parameter that measures the density of volume occupied by the fluid. According to its axiomatic definition, Goodman & Cowin (1972), Varsakelis & Papalexandris (2010), $\phi(\boldsymbol{x}, t)$ is a probability density function defined in Ω and takes values in the interval (0, 1].

Next, let $\Omega_{\rm p} \subset \Omega$ be the union of the open sub-domains that are covered by the porous material, $\Omega_{\rm p} = \{\boldsymbol{x} \in \Omega : \phi(\boldsymbol{x}) < 1\}$. In the same manner, let $\Omega_{\rm f} \subset \Omega$ be the union of the sub-domains covered by the pure fluid, $\Omega_{\rm f} = \{\boldsymbol{x} \in \Omega : \phi(\boldsymbol{x}) = 1\}$. Therefore, $\Omega = \Omega_{\rm f} \cup \Omega_{\rm p}$. Also, let S_Ω denote the boundary between $\Omega_{\rm p}$ and $\Omega_{\rm f}$. Since $\Omega_{\rm p}$ is an open subset of Ω, then along S_Ω we have that $\phi(\boldsymbol{x} \in S_\Omega, t) = 1$. In the case of a sharp interface between porous and pure-fluid regions, S_Ω coincides with the interface. In the case of a smooth interface (with finite thickness), S_Ω represents the end of the interface at the side of the pure fluid.

The assumptions upon which our model is based are the following.

i) Each phase is modelled as a continuum thermodynamic system.

ii) The two thermodynamic continua are immiscible but occupy the same space. In particular, they fill completely the space that they occupy (saturation condition).

iii) The two thermodynamic continua are open to each other and at non-equilibrium.

iv) The mass, momentum and energy exchanges between the two continua are pure, *i.e.* their sum must vanish.

v) The skeleton (or matrix) of the porous material is assumed to be a rigid solid of zero velocity and constant mass density. Also, the fluid is assumed to be simple and isotropic.

vi) The postulate of phase separation holds. In other words, irreversible phenomena associated with only one phase do not depend on the variables of the other phase.

Since the two thermodynamic systems are open and at out of equilibrium, they can interact with each other. These interactions are in the form of mass, momentum, and energy exchanges, and are denoted by $\mathcal{M}$, $\boldsymbol{f}$, and $\mathcal{E}$, respectively. In particular, mass exchange can occur due to heterogeneous reactions or phase change, while momentum exchange occurs via the action of interphasial forces.

As mentioned in the introduction, we follow the framework described in Papalexandris (2004) to immiscible mixtures whose constituents are in thermal non-equilibrium. In this context, let ρ, $\boldsymbol{u} = (u, v, w)$, p, e_t denote the density, velocity vector, pressure and total

energy of the fluid. These variables, and all variables relative to the fluid phase only, are defined in the entire domain Ω. In view of the constitutive assumptions (i)–(iv) above, the mass, momentum and energy balance laws for the fluid phase read,

$$\frac{\partial}{\partial t}(\phi\rho) + \nabla\cdot(\phi\rho\boldsymbol{u}) = \mathcal{M}\,, \tag{2.2.1}$$

$$\frac{\partial}{\partial t}(\phi\rho\boldsymbol{u}) + \nabla\cdot(\phi\rho\boldsymbol{u}\boldsymbol{u}) + \nabla(\phi p) = \nabla\cdot(\phi\boldsymbol{P}^{\mathrm{v}}) + \phi\rho\boldsymbol{g} + \boldsymbol{f}\,, \tag{2.2.2}$$

$$\frac{\partial}{\partial t}(\phi\rho e_t) + \nabla\cdot(\phi\boldsymbol{u}(\rho e_t + p)) = \nabla\cdot(\phi\boldsymbol{P}^{\mathrm{v}}\boldsymbol{u}) - \nabla\cdot(\phi\boldsymbol{q}) + \phi\rho\boldsymbol{g}\cdot\boldsymbol{u} + \mathcal{E}\,. \tag{2.2.3}$$

The total energy e_t is written as the sum of the fluid's internal and kinetic energies,

$$e_t \;=\; e + \frac{1}{2}\boldsymbol{u}\cdot\boldsymbol{u}\,. \tag{2.2.4}$$

Also, in the above equations, $\boldsymbol{q}$ is the conductive heat flux for the fluid phase and $\boldsymbol{g}$ is the vector of gravitational acceleration. Finally, $\boldsymbol{P}^{\mathrm{v}}$ stands for the viscous stress tensor of the fluid. By virtue of the isotropy of the fluid and the conservation of angular momentum, this tensor is symmetric. Then it is decomposed according to

$$\boldsymbol{P}^{\mathrm{v}} \;=\; -p^{\mathrm{v}}\boldsymbol{I} + \boldsymbol{P}^{\mathrm{v}}_d\,, \qquad p^{\mathrm{v}} \;=\; -\frac{1}{3}tr(\boldsymbol{P}^{\mathrm{v}})\,, \tag{2.2.5}$$

where p^{v} is the bulk viscous pressure and $\boldsymbol{P}^{\mathrm{v}}_d$ is the (deviatoric) viscous shear stress tensor.

By introducing equations (2.2.4)-(2.2.5) to (2.2.1)-(2.2.3), and after some rearranging, the balance laws of the fluid phase can be written as

$$\frac{\mathrm{d}(\phi\rho)}{\mathrm{d}t} + \phi\rho\nabla\cdot\boldsymbol{u} = \mathcal{M}\,, \tag{2.2.6}$$

$$\phi\rho\frac{\mathrm{d}\boldsymbol{u}}{\mathrm{d}t} + \nabla(\phi p) = \nabla\cdot(\phi\boldsymbol{P}^{\mathrm{v}}_d) - \nabla(\phi p^{\mathrm{v}}) + \boldsymbol{f} - \mathcal{M}\boldsymbol{u} + \phi\rho\boldsymbol{g}\,, \tag{2.2.7}$$

$$\begin{aligned}\phi\rho\frac{\mathrm{d}e}{\mathrm{d}t} + \phi p\nabla\cdot\boldsymbol{u} =& \phi\boldsymbol{P}^{\mathrm{v}}_d : \boldsymbol{V}^{\mathrm{v}}_d - \phi p^{\mathrm{v}}\nabla\cdot\boldsymbol{u} - \nabla\cdot(\phi\boldsymbol{q}) \\ &+ \mathcal{E} - \boldsymbol{f}\cdot\boldsymbol{u} - \mathcal{M}(e - \frac{1}{2}\boldsymbol{u}\cdot\boldsymbol{u})\,,\end{aligned} \tag{2.2.8}$$

where $\boldsymbol{V}^{\mathrm{v}}_d$ stands for the deviatoric part of the deformation tensor, and $\mathrm{d}/\mathrm{d}t(\,)$ stands for the material derivative with respect to the fluid velocity.

Similarly, let ρ_{s}, p_{s}, e_{s} denote the density, pressure (trace of the stress tensor) and internal energy of the solid matrix, respectively. These variables, and all variables relative

to the solid matrix only, are defined in the porous region Ω_{p}. By virtue of assumptions (i)–(v), the balance laws for the solid matrix read,

$$\frac{\partial}{\partial t}((1-\phi)\rho_{\mathrm{s}}) = -\mathcal{M}\,, \tag{2.2.9}$$

$$\nabla((1-\phi)p_{\mathrm{s}}) + \nabla\cdot((1-\phi)\boldsymbol{\tau}_{\mathrm{s}}) = -\boldsymbol{f} + (1-\phi)\rho_{\mathrm{s}}\boldsymbol{g}\,, \tag{2.2.10}$$

$$\frac{\partial}{\partial t}((1-\phi)\rho_{\mathrm{s}}e_{\mathrm{s}}) = -\nabla\cdot((1-\phi)\boldsymbol{q}_{\mathrm{s}}) - \mathcal{E}\,, \tag{2.2.11}$$

where $\boldsymbol{\tau}_{\mathrm{s}}$ and $\boldsymbol{q}_{\mathrm{s}}$ stands for the deviatoric part of the stress tensor and the conductive heat flux of the solid matrix, respectively.

Also, since the density of the solid phase is constant, the balance laws (2.2.9)–(2.2.11) simplify to

$$\frac{\partial\phi}{\partial t} = \frac{1}{\rho_{\mathrm{s}}}\mathcal{M}\,, \tag{2.2.12}$$

$$\nabla((1-\phi)p_{\mathrm{s}}) + \nabla\cdot((1-\phi)\boldsymbol{\tau}_{\mathrm{s}}) = -\boldsymbol{f} + (1-\phi)\rho_{\mathrm{s}}\boldsymbol{g}\,, \tag{2.2.13}$$

$$(1-\phi)\rho_{\mathrm{s}}\frac{\partial e_{\mathrm{s}}}{\partial t} = -\nabla\cdot((1-\phi)\boldsymbol{q}_{\mathrm{s}}) - \mathcal{E} + \mathcal{M}e_{\mathrm{s}}\,. \tag{2.2.14}$$

Next we introduce the balance laws of each phase to its corresponding Gibbs relation. More specifically, for the fluid phase we have that

$$T\frac{\mathrm{d}\eta}{\mathrm{d}t} \;=\; \frac{\mathrm{d}e}{\mathrm{d}t} - \frac{p}{\rho^2}\frac{\mathrm{d}\rho}{\mathrm{d}t}\,, \tag{2.2.15}$$

where T and η stand for the fluid temperature and specific entropy, respectively. Upon introduction of (2.2.6)–(2.2.8) to (2.2.15), we arrive at the following equation for the fluid's specific entropy,

$$\begin{aligned}\phi\rho T\frac{\mathrm{d}\eta}{\mathrm{d}t} =& \phi\boldsymbol{P}_d^{\mathrm{v}} : \boldsymbol{V}_d^{\mathrm{v}} - \phi p^{\mathrm{v}}\nabla\cdot\boldsymbol{u} - \nabla\cdot(\phi\boldsymbol{q}) \\ &+ \mathcal{E} - (\boldsymbol{f} - p\nabla\phi)\cdot\boldsymbol{u} - \mathcal{M}(e + \frac{p}{\rho} - \frac{1}{2}\boldsymbol{u}\cdot\boldsymbol{u} - \frac{p}{\rho_{\mathrm{s}}})\,.\end{aligned} \tag{2.2.16}$$

As regards the solid matrix, since it is assumed to be a rigid body with constant density, then its Gibbs relation simply reads

$$T_{\mathrm{s}}\frac{\partial\eta_{\mathrm{s}}}{\partial t} \;=\; \frac{\partial e_{\mathrm{s}}}{\partial t}\,, \tag{2.2.17}$$

where $T_{\rm s}$ and $\eta_{\rm s}$ are the material's temperature and specific entropy, respectively. Evidently, one could treat the solid matrix as a deformable body. In this case, the right-hand side of the above equation should include terms that describe the reversible work performed by elastic stresses. This, however, is beyond the scope of the present work. In view of (2.2.12)–(2.2.17), the specific entropy of the solid phase satisfies the following equation.

$$(1-\phi)T_{\rm s}\rho_{\rm s}\frac{\partial \eta_{\rm s}}{\partial t} \;=\; -\nabla\cdot((1-\phi)\boldsymbol{q}_{\rm s}) - \mathcal{E} + \mathcal{M}e_{\rm s}\,. \tag{2.2.18}$$

The next step is to derive a balance law for the mixture's entropy. To this end, we first introduce the mixture's density $\rho_{\rm m}$, barycentric velocity $\boldsymbol{u}_{\rm m}$ and specific entropy $\eta_{\rm m}$, respectively. In other words,

$$\rho_{\rm m} = \phi\rho + (1-\phi)\rho_{\rm s}\,, \quad \boldsymbol{u}_{\rm m} = \rho_{\rm m}^{-1}(\phi\rho\boldsymbol{u})\,, \quad \eta_{\rm m} = \rho_{\rm m}^{-1}\left(\phi\rho\eta + (1-\phi)\rho_{\rm s}\eta_{\rm s}\right)\,. \tag{2.2.19}$$

Also, let $\mathrm{d}/\mathrm{d}_{\rm m}t(\,)$ stand for the material derivative with respect to the mixture's barycentric velocity, $\mathrm{d}/\mathrm{d}_{\rm m}t(\,) = (\partial/\partial t + \boldsymbol{u}_{\rm m}\cdot\nabla)(\,)$. By combining (2.2.16), (2.2.18) and (2.2.19), we can arrive at a balance law for the mixture's entropy in the form

$$\rho_{\rm m}\frac{\mathrm{d}\eta_{\rm m}}{\mathrm{d}_{\rm m}t} \;=\; \nabla\cdot\boldsymbol{J} + \sigma\,. \tag{2.2.20}$$

The first term of the right-hand side of (2.2.20) is in divergence form, so that $\boldsymbol{J}$ is identified as the mixture's entropy flux. As such, $\nabla\cdot\boldsymbol{J}$ can be either positive or negative. The second term, σ, represents the entropy production rate and has to be non-negative in accordance with the entropy axiom,

$$\sigma \;\geq\; 0\,. \tag{2.2.21}$$

For the particular mixture in hand, in view of (2.2.16) and (2.2.18), we have that

$$\boldsymbol{J} \;=\; \frac{1}{T}\boldsymbol{q} + \frac{1}{T_{\rm s}}\boldsymbol{q}_{\rm s} + \phi\rho\eta(\boldsymbol{u}_{\rm m}-\boldsymbol{u}) + (1-\phi)\rho_{\rm s}\eta_{\rm s}\boldsymbol{u}_{\rm m}\,, \tag{2.2.22}$$

and

$$\begin{aligned}\sigma =& \frac{\phi}{T}\boldsymbol{P}_d^{\rm v} : \boldsymbol{V}_d^{\rm v} - \frac{\phi}{T}p^{\rm v}\nabla\cdot\boldsymbol{u} + \phi\boldsymbol{q}\cdot\nabla(T^{-1}) + (1-\phi)\boldsymbol{q}_{\rm s}\cdot\nabla(T_{\rm s}^{-1})\\ &+ \mathcal{M}\,\mathcal{A} - (\boldsymbol{f} - p\nabla\phi)\cdot\frac{1}{T}\boldsymbol{u} + \mathcal{E}\left(\frac{1}{T}-\frac{1}{T_{\rm s}}\right)\,,\end{aligned} \tag{2.2.23}$$

where $\mathcal{A}$ is the *affinity* of the interphasial mass exchange and is given by

$$\mathcal{A} \;=\; \left(\frac{\psi_{\mathrm{s}}}{T_{\mathrm{s}}} - \frac{\psi}{T} + \frac{p}{T}\left(\frac{1}{\rho_{\mathrm{s}}} - \frac{1}{\rho}\right) + \frac{1}{2T}\boldsymbol{u}\cdot\boldsymbol{u}\right)\,, \tag{2.2.24}$$

with $\psi = e - \eta T$ and $\psi_{\mathrm{s}} = e_{\mathrm{s}} - \eta_{\mathrm{s}} T_{\mathrm{s}}$ being the Helmholtz free energies of the fluid and solid phase, respectively.

The entropy production rate σ is thus given as a sum of products. Each product is associated to a particular irreversible phenomenon that takes place in the mixture. We identify the first terms of these products as the "thermodynamic currents" J_i, and the second ones as the "thermodynamic forces" X_i, Lebon *et al.* (2008). In other words, we have that

$$\sigma \;=\; \sum_i J_i X_i \;\geq\; 0, \tag{2.2.25}$$

with

$$J_i \;\in\; \left\{\boldsymbol{P}_d^{\mathrm{v}},\; p^{\mathrm{v}},\; \boldsymbol{q},\; \boldsymbol{q}_{\mathrm{s}},\; \mathcal{M},\; \left(\boldsymbol{f} - p\nabla\phi\right),\; \mathcal{E}\right\}\,, \tag{2.2.26}$$

and

$$X_i \in \left\{\frac{\phi}{T}\boldsymbol{V}_d^{\mathrm{v}},\; -\frac{\phi}{T}\nabla\cdot\boldsymbol{u},\; \phi\nabla\frac{1}{T},\; (1-\phi)\nabla\frac{1}{T_{\mathrm{s}}},\; \mathcal{A},\; -\frac{1}{T}\boldsymbol{u},\; \left(\frac{1}{T} - \frac{1}{T_{\mathrm{s}}}\right)\right\}. \tag{2.2.27}$$

In order to close the system of governing equations (2.2.6)–(2.2.8) and (2.2.12)–(2.2.14) constitutive relations must be provided between the above currents and forces. The simplest choice is to assume linear relations between them. This is equivalent to considering Taylor expansions around the equilibrium values $J_{i,eq} = 0$ and $X_{i,eq} = 0$ and omitting second and higher-order terms. Therefore,

$$J_i \;=\; \sum_j L_{ij} X_j\,, \tag{2.2.28}$$

where the quantities L_{ij} are the *phenomenological coefficients* of the mathematical model and are functions of the thermo-mechanical variables of the mixture. The values of the phenomenological coefficients are constrained by the requirement that the entropy production rate, σ, be non-negative.

The values of these coefficients can further be constrained by invoking certain postulates. For example, it is customary to invoke the postulate of phase separation, according

to which thermodynamic currents associated with one phase depend only on variables of the same phase. Accordingly, these currents cannot couple with thermodynamic forces associated with interphasial phenomena. Further, since the fluid is an isotropic medium, the coefficients between fluid-related currents and forces of different tensorial character are zero, by virtue of the representation theorem of isotropic tensors. (This statement is often referred to as the Curie principle). The values of the phenomenological coefficients can be constrained even further by invoking the Onsager-Casimir reciprocal relations.

Herein, we make an even stronger, albeit commonly used, assumption and consider that the couplings between non-conjugate currents and forces are altogether negligible. This amounts to assuming that the matrix of phenomenological coefficients is diagonal, ie $L_{ij} = 0$ for $i \neq j$. Under this assumption, we arrive at the following linear constitutive relations for the viscous stresses,

$$\boldsymbol{P}_d^{\mathrm{v}} = L_{11}\frac{\phi}{T}\boldsymbol{V}_d^{\mathrm{v}}, \qquad p^{\mathrm{v}} = -L_{22}\frac{\phi}{T}\nabla\cdot\boldsymbol{u}\,, \tag{2.2.29}$$

the conductive heat fluxes,

$$\boldsymbol{q} = L_{33}\phi\nabla(T^{-1}), \qquad \boldsymbol{q}_{\mathrm{s}} = \underset{\sim}{\boldsymbol{L}}_{44}(1-\phi)\nabla(T_{\mathrm{s}}^{-1})\,, \tag{2.2.30}$$

and the interphasial relaxation phenomena,

$$\mathcal{M} = L_{55}\mathcal{A}\,, \qquad \boldsymbol{f} - p\nabla\phi = -\underset{\sim}{\boldsymbol{L}}_{66}\frac{1}{T}\boldsymbol{u}\,, \qquad \mathcal{E} = L_{77}\left(\frac{1}{T_{\mathrm{s}}} - \frac{1}{T}\right)\,. \tag{2.2.31}$$

In these equations all phenomenological coefficients are scalar, except for $\underset{\sim}{\boldsymbol{L}}_{44}$ and $\underset{\sim}{\boldsymbol{L}}_{66}$ which, in the general case, are 2nd-order tensors due to the anisotropy of the solid matrix. The first four phenomenological coefficients are related to the well-known transport coefficients (fluid shear and bulk viscosities μ and ζ, and fluid and solid conductivities k and $\underset{\sim}{\boldsymbol{k}}_{\mathrm{s}}$) via the following equations,

$$L_{11} = \frac{T}{2\,\phi}\mu\,, \qquad L_{22} = \frac{T}{\phi}\zeta\,, \qquad L_{33} = \frac{T^2}{\phi}k\,, \qquad \underset{\sim}{\boldsymbol{L}}_{44} = \frac{T_{\mathrm{s}}^2}{(1-\phi)}\underset{\sim}{\boldsymbol{k}}_{\mathrm{s}}\,, \tag{2.2.32}$$

so that the constitutive relations in (2.2.29), (2.2.30) can be written in the familiar forms of Newton's law of viscosity

$$\boldsymbol{P}_d^{\mathrm{v}} = \mu\boldsymbol{V}_d^{\mathrm{v}}, \qquad p^{\mathrm{v}} = -\zeta\nabla\cdot\boldsymbol{u}\,, \tag{2.2.33}$$

and Fourier law of heat conduction,

$$\boldsymbol{q} = -k\nabla T, \qquad \boldsymbol{q}_{\mathrm{s}} = -\underset{\sim}{\boldsymbol{k}}_{\mathrm{s}}\nabla T_{\mathrm{s}}\,, \tag{2.2.34}$$

Finally, we can define the interphasial mass and heat transfer coefficients and drag-parameter tensor

$$\kappa = L_{55}, \qquad h = -\frac{L_{77}}{T\,T_{\mathrm{s}}}, \qquad \underset{\sim}{\boldsymbol{\beta}} = \frac{\underset{\sim}{\boldsymbol{L}}_{66}}{T}, \tag{2.2.35}$$

respectively. With these definitions the constitutive relations (2.2.31) read,

$$\mathcal{M} = \kappa\mathcal{A}\,, \qquad \boldsymbol{f} = p\nabla\phi - \underset{\sim}{\boldsymbol{\beta}}\boldsymbol{u}\,, \qquad \mathcal{E} = h(T_{\mathrm{s}} - T)\,. \tag{2.2.36}$$

The functional form of κ, h and $\underset{\sim}{\boldsymbol{\beta}}$ should be such that they are all equal to zero at the pure-fluid regions Ω_{f}, *i.e.* when $\phi(\boldsymbol{x}, t) = 1$.

At this point it is worth reiterating that the solid conductivity $\underset{\sim}{\boldsymbol{k}}_{\mathrm{s}}$ and the interphasial drag parameter $\underset{\sim}{\boldsymbol{\beta}}$ are in general second-order tensors because of the anisotropy of the solid matrix. It should also be noted that the interphasial mass exchange can involve heterogeneous reactions that are considerably fast, depending on the participating species and flow conditions. In this case, the validity of the linear constitutive law $\mathcal{M} = \kappa\mathcal{A}$ is limited and an Arrhenius-type law would be more appropriate for the reaction rate. Then, the linear law would be an approximation of the Arrhenius law near the equilibrium points of the chemical reaction.

The balance laws (2.2.6)–(2.2.8) and (2.2.12)–(2.2.14), together with the constitutive relations (2.2.33)–(2.2.36) and a state equation for the fluid, constitute a closed system of governing equations for the flows of interest. These governing equations are valid for both smooth and sharp interfaces between the porous and pure-fluid layers. Mathematically speaking, when the interface is smooth, the solutions to the governing equations can be defined in the *strong* sense, *i.e.* the solutions can be sufficiently smooth. However, when the interface is sharp, the solutions to the governing equations must be understood in the *weak sense*, *i.e.* they solve the variational formulation of the equations. As such, the solutions are not necessarily smooth across the interface.

Finally, it is worth mentioning that all thermodynamic and kinematic variables that appear in the model derived above, including the porosity distribution $\phi(\boldsymbol{x}, t)$, are well

defined in their respective domains of definition. Consequently, the model is *formally* valid at any length-scale. However, its validity is limited by the continuum hypothesis regarding the porosity distribution, which breaks down at the scale of the porous micro-structure. Also, most often, the parameterizations of the interphasial drag and heat transfer are performed via an averaging or homogenization procedure; see, for example, the derivation of $\underset{\sim}{\boldsymbol{\beta}}$ and h in the numerical examples below. For this reason, even if the above model is formally valid at any length-scale, in reality it cannot resolve flow scales inside the porous medium whose size is comparable to the length-scale of the porous micro-structure.

2.3 Low-Mach number approximation

The flow model developed in the previous section, (2.2.6)–(2.2.8), (2.2.12)–(2.2.14) and (2.2.33)–(2.2.36), is valid for both compressible and incompressible fluids. In many flows of interest, however, the fluid velocity is very small with respect to the speed of sound and, consequently, compressibility effects are negligible. Then, one can use the square of the Mach number as a perturbation parameter and perturb the governing system of equations with respect to this parameter. The result of this procedure is a perturbed system of equations, referred to as the *low-Mach number approximation*, that is simpler than the unperturbed one in several important ways. In this section, we present the derivation of the low-Mach number approximation for the flow model developed in the previous section. Since the procedure is standard, we describe only the basic steps of the derivation. For a more detailed description on the derivation of the low-Mach number approximation for two-phase flow models, the reader is referred to Varsakelis & Papalexandris (2011).

Step 1. We introduce an equation of state for the fluid. For the sake of simplicity, we consider the ideal-gas law,

$$p = \mathcal{R}\rho T \tag{2.3.1}$$

with $\mathcal{R}$ being the gas constant. Then, the fluid's internal energy can be written as

$$e \;=\; H^f + c_v(T - T_{\mathrm{ref}})\,, \tag{2.3.2}$$

where H^f is the fluid's enthalpy of formation at temperature T_{ref} and c_v is the fluid's specific heat under constant volume. We could have considered any other state equation

but this would not affect the final result. Also, since $\rho_{\rm s}$ is assumed to be constant, the internal energy of the solid material can be written as

$$e_{\rm s} \;=\; H_s^f + c_{\rm s}(T_{\rm s} - T_{\rm ref})\,, \tag{2.3.3}$$

where H_s^f is the solid's enthalpy of formation at temperature $T_{\rm ref}$ and $c_{\rm s}$ is the solid's specific heat.

Step 2. We consider a set of reference variables, $l_{\rm ref}$, $u_{\rm ref}$, $\rho_{\rm ref}$, $T_{\rm ref}$ and $p_{\rm ref} = \mathcal{R}\rho_{\rm ref}T_{\rm ref}$. Also, we consider reference values for the specific heats, the shear viscosity and conductivity, $c_{p,ref}$, $c_{v,ref}$, $\mu_{\rm ref}$, and $k_{\rm ref}$, respectively.

Step 3. The reference speed of sound is $c = \sqrt{\gamma p_{\rm ref}/\rho_{\rm ref}}$ with γ being the fluid's Poisson ratio, $\gamma = c_{p,\rm ref}/c_{v,ref}$. Then, the square of the reference Mach number, scaled with γ, is $\epsilon = \gamma(u_{\rm ref}/c)^2$ and serves as the perturbation parameter.

Step 4. All variables, transport coefficients, and derivatives appearing in the mathematical model are non-dimensionalized with respect to these reference values. For example, the pressure p is non-dimensionalized with respect to $p_{\rm ref}$, energies are non-dimensionalized by $c_{p,\rm ref}T_{\rm ref}$ and so on, so forth.

Henceforth, in order to avoid the introduction of additional symbols, every variable is understood to be non-dimensionalized.

Step 5. All variables are expanded in perturbation series of powers of ϵ. For example,

$$p \;=\; p^0 + \epsilon\, p^1 + O(\epsilon^2)\,, \quad \boldsymbol{u} \;=\; \boldsymbol{u}^0 + \epsilon\, \boldsymbol{u}^1 + O(\epsilon^2)\,, \quad etc. \tag{2.3.4}$$

Step 6. We insert the perturbation expansions of all variables to the governing system of equations and collect terms of the same order.
Then, at order $O(1/\epsilon)$, the fluid's momentum equation (2.2.7) yields

$$\phi^0 \nabla p^0 \;=\; 0\,, \tag{2.3.5}$$

In other words, p^0 is a function of time only. (p^0 is usually referred to as the "thermodynamic pressure"). By combining (2.3.5) and (2.2.36), the momentum equation for the solid phase (2.2.13) reads, at order $O(1/\epsilon)$,

$$\nabla\left(\phi^0(p_{\rm s}^0 - p^0)\right) \;=\; 0\,. \tag{2.3.6}$$

For the derivation of this equation we considered that the shear stresses τ_{ij} acting on the porous material, *cf.* (2.2.13), are induced by the fluid flow only. As such, they scale with $\rho_{ref} u_{ref}^2$ and they are of order $O(1)$, whereas the pressure gradients are of order $O(1/\epsilon)$. Further, we note that equation (2.3.6) is valid for any porosity distribution ϕ^0. This implies that the two thermodynamic pressures have to be equal,

$$p_{\mathrm{s}}^0 \;=\; p^0\,. \tag{2.3.7}$$

Further, we note that in low-Mach number flows, the fluid's kinetic energy is of order $O(\epsilon)$ with respect to its enthalpy. Due to this fact and by virtue of (2.2.24) the expression (2.3.6) for $\mathcal{A}^0$ simplifies to

$$\mathcal{A}^0 \;=\; \left(\frac{\psi_{\mathrm{s}}}{T_{\mathrm{s}}} - \frac{\psi}{T} + \frac{p^0}{T}\left(\frac{1}{\rho_{\mathrm{s}}} - \frac{1}{\rho}\right)\right)\,. \tag{2.3.8}$$

When the two phases are in thermal equilibrium, the above relation reduces to the difference of the chemical potentials divided by the (common) temperature.

At order $O(1)$, the balance laws of the fluid phase (2.2.6)–(2.2.8), combined with the constitutive relations (2.2.33)–(2.2.36) and the fluid's equation of state (2.3.2), yield

$$\frac{\mathrm{d}(\phi^0\rho^0)}{\mathrm{d}t} + \phi^0\rho^0\nabla\cdot\boldsymbol{u}^0 \;=\; \kappa\mathcal{A}^0\,, \tag{2.3.9}$$

$$\begin{aligned}\phi^0\rho^0\frac{\mathrm{d}\boldsymbol{u}^0}{\mathrm{d}t} + \phi^0\nabla p^1 = {}& \frac{1}{Re}\nabla\cdot(\phi^0\mu\boldsymbol{V}_d^{\mathrm{v}0}) + \frac{1}{Re}\nabla(\phi^0\zeta\nabla\cdot\boldsymbol{u}^0)\\ & - \underset{\sim}{\boldsymbol{\beta}}\boldsymbol{u}^0 - Ri\,\phi^0\rho^0\hat{\boldsymbol{y}} - \kappa\mathcal{A}^0\boldsymbol{u}^0\,,\end{aligned} \tag{2.3.10}$$

$$\begin{aligned}\phi^0\rho^0 c_p\frac{\mathrm{d}T^0}{\mathrm{d}t} - \phi^0\frac{\gamma-1}{\gamma}\frac{\partial p^0}{\partial t} = {}& \frac{1}{RePr}\nabla\cdot(\phi^0 k\nabla T^0) + h(T_{\mathrm{s}}^0 - T^0)\\ & - \kappa\mathcal{A}^0\left(e + \frac{\gamma-1}{\gamma}\left(\frac{p^0}{\rho^0} - \frac{p^0}{\rho_{\mathrm{s}}^0}\right)\right)\,,\end{aligned} \tag{2.3.11}$$

where $\mathcal{A}^0$ is given by (2.3.8). As usual, Re and Pr stand for the Reynolds and Prandtl numbers with respect to the reference variables. Also, $Ri = |\boldsymbol{g}|\, l_{ref}/u_{ref}^2$ stands for the Richardson number and $\hat{\boldsymbol{y}}$ is the unit vector in the direction opposite to the gravitational force.

Similarly, the balance laws for the solid phase (2.2.12)–(2.2.14), combined with the constitutive relations (2.2.33)–(2.2.36) and the solid's equation of state (2.3.3) yield,

$$\frac{\partial \phi^0}{\partial t} = \frac{1}{\rho_{\rm s}^0} \kappa \mathcal{A}^0 \,, \tag{2.3.12}$$

$$\begin{aligned}(1-\phi^0)\rho_{\rm s}^0 c_{\rm s} \frac{\partial T_{\rm s}^0}{\partial t} =& \frac{1}{RePr} \nabla \cdot \left((1-\phi^0) \underset{\sim}{\boldsymbol{k}}_{\rm s} \nabla T_{\rm s}^0 \right) \\ & - h \left(T_{\rm s}^0 - T^0 \right) + \kappa \mathcal{A}^0 e_{\rm s} \,. \end{aligned} \tag{2.3.13}$$

We note that since the solid matrix is assumed to be a rigid body, its equation of balance of forces (2.2.13) at order $O(1)$ becomes inconsequential for the flows of interest and, therefore, it is omitted. An important advantage resulting from the low-Mach number approximation is that the thermodynamic pressure appears only in the fluid's energy equation and not in the momentum equation. This greatly simplifies the numerical algorithm that we propose for the treatment of the governing equations, and is presented in the following chapter. All of the work that is presented in this thesis from this point onward, is based on the governing equations (2.3.9) to (2.3.13). It should be emphasized that these equations do not describe phenomena associated with abrupt changes of pressure, such as acoustic waves, pressure waves, and others. Finally, as mentioned earlier, the constitutive relation for the interphasial mass exchange in the low-Mach number regime is simplified according to (2.3.8).

2.4 The non-reacting case

In this section, we shift our focus to non-reacting flows and we discuss certain implications resulting from the structure of the flow model. We also discuss the issue of implementation of boundary conditions at S_Ω.

In the non-reacting case, the porosity distribution $\phi(\boldsymbol{x})$ is constant with time and both sides of the mass balance equation for the solid phase (2.3.12) become identically zero. Also, all terms relative to interphasial mass exchange vanish. Further, we make the assumption that the bulk viscous pressure of the fluid is zero (Stokes' hypothesis). Then the low-Mach number equations (2.3.9) - (2.3.13) reduce to

$$\phi\frac{\partial\rho^0}{\partial t}+\nabla\cdot(\phi\rho^0\boldsymbol{u}^0)=0\,, \tag{2.4.1}$$

$$\phi\rho^0\frac{\mathrm{d}\boldsymbol{u}^0}{\mathrm{d}t}+\phi\nabla p^1=\frac{1}{Re}\nabla\cdot(\phi\mu\boldsymbol{V}_d^{\mathrm{v}\,0})-\underset{\sim}{\boldsymbol{\beta}}\boldsymbol{u}^0-Ri\,\phi\rho^0\hat{\boldsymbol{y}}\,, \tag{2.4.2}$$

$$\phi\rho^0c_p\frac{\mathrm{d}T^0}{\mathrm{d}t}-\phi\frac{\gamma-1}{\gamma}\frac{\partial p^0}{\partial t}=\frac{1}{RePr}\nabla\cdot(\phi k\nabla T^0)+h(T_{\mathrm{s}}^0-T^0)\,, \tag{2.4.3}$$

$$(1-\phi)\rho_{\mathrm{s}}^0c_{\mathrm{s}}\frac{\partial T_{\mathrm{s}}^0}{\partial t}=\frac{1}{RePr}\nabla\cdot\left((1-\phi)\underset{\sim}{\boldsymbol{k}}_{\mathrm{s}}\nabla T_{\mathrm{s}}^0\right)-h(T_{\mathrm{s}}^0-T^0)\,. \tag{2.4.4}$$

The above system is closed with the equation of state for the fluid phase.

This model can be viewed as a generalization of the well-known *Darcy - Brinkman* equations to flows with heat transfer in absence of thermal equilibrium. The two phasial energy equations (2.4.3) - (2.4.4) are quite similar to the ones that have been commonly used in thermal convection problems, Nield & Bejan (2013). The most crucial difference is the location of the porosity with respect to the gradients in the divergence terms. In our model, $\phi(\boldsymbol{x})$ is "inside" these terms, *i.e.* it is a multiplier of the conductive heat fluxes themselves. This is the result of taking the integral form of the energy conservation equations over a control volume that is occupied partially by the fluid and partially by the solid phase. By contrast, in the commonly used energy equations, the porosity $\phi(\boldsymbol{x})$ is a multiplier of the divergence terms for the conductive heat fluxes. The numerical treatment of such terms is more simple and less computationally expensive as compared to the treatment required for the terms appearing in equations (2.4.3) - (2.4.4), however, they are simply approximations of the later. The same also applies of the viscous stress tensor that enters the right-hand side of the momentum equation. Moreover, the differences discussed above can have a significant effect on the flow, in regions of spatially varying porosity and, most notably, at interfaces between porous and pure-fluid layers.

It should also be mentioned that such discrepancies between our governing equations and other models in the literature, prevent us from using readily available commercial software packages to conduct our numerical studies. Instead, for the needs of the present work we have developed our own software from scratch, which implements the numerical method described in the following chapter.

An important characteristic of the model in hand is that the balance equations for the fluid (2.4.1) - (2.4.3) are defined in the entire domain Ω. As such, there is no need for matching conditions for the fluid variables at S_Ω. On the other hand, the energy equation for the solid phase (2.4.4) is defined only in the porous regions, Ω_p. This necessitates the introduction of a boundary condition for (2.4.4) at S_Ω.

The prescription of thermal boundary conditions at porous medium - pure fluid interfaces has been a topic of considerable discussion. Thus far, various relations have been put forward; see, for example, Ochoa-Tapia & Whitaker (1997), Alazmi & Vafai (2001), Yang & Vafai (2010), Nield & Kuznetsov (2011), Nield (2012), as well as the literature survey in Nield & Bejan (2013). The large number of available options is to be expected, because boundary conditions are generally problem-dependent. Further, the prescription of boundary conditions unavoidably relies on physical arguments and assumptions. For this reason, it is unlikely to derive a boundary condition for T_s that is unambiguously valid in all cases.

Herein, and for smooth interfaces, we propose to take advantage of the fact that $\phi = 1$ at S_Ω. Due to this fact, the conductive heat flux for the solid material at S_Ω is exactly zero,

$$(1-\phi)(\underset{\sim}{\boldsymbol{k}}_\mathrm{s}\nabla T_\mathrm{s}^0)\cdot\boldsymbol{n} \;=\; 0 \;\; \text{at } S_\Omega\,, \tag{2.4.5}$$

where $\boldsymbol{n}$ is the unit vector normal to the interface. This relation constitutes an intrinsic boundary condition for (2.4.4). The introduction of (2.4.5) tacitly assumes that the interphasial heat exchange across S_Ω is zero. This assumption is compatible with the mixture-theoretic formalism employed herein, according to which interphasial heat exchange is modelled as a purely volumetric effect, *cf* (2.2.3) and (2.2.11). Further, by considering the balance of energy flux across S_Ω, it can be shown that (2.4.5) holds exactly in the case of smooth interfaces.

However, in the case of a sharp interface, there is a heat flux from one phase to the other due to the jump in the porosity across the interface. For this interphasial heat flux additional information is needed. In other words, we need another thermal condition for the solid matrix at sharp interfaces. For a methodology to incorporate interphasial heat flux across porous medium - pure fluid interfaces, the reader is referred to Ochoa-Tapia & Whitaker (1997). One can still try to employ (2.4.5) but this amounts to assuming

that the interphasial heat flux across the interface is zero. Therefore, for sharp interfaces, condition (2.4.5) is only an approximation. Such approximation is deemed reasonable for highly porous layers, *i.e.* when the jump of ϕ across the interface is small. Evidently, the minimum porosity for which condition (2.4.5) can still be employed across sharp interfaces depends on the properties of the fluid and solid materials.

2.5 Conclusions

In this chapter, we presented a thermo-mechanical model for flows in superposed porous and fluid layers with interphasial heat and mass exchange. This model is based on a mixture-theoretic formalism, according to which, the fluid and the solid phases are treated as two coexisting but open thermodynamic continua that interact with each other. As such, each phase is endowed with its own set of thermodynamic variables and conservation laws. In particular, each phase is endowed with its own temperature field, thereby allowing for thermal non-equilibrium between the two phases. Constitutive equations for all dissipative and relaxation phenomena occurring in both phases are derived by exploiting the constraints imposed by the entropy axiom when applied to the entire mixture.

This formalism is inline with the so-called one-domain approach for porous media. Its advantage of is that it does not require additional conditions at porous medium - pure fluid interfaces, which renders it convenient for the numerical simulation of unsteady, temporally-evolving flows. Further, according to our model, the conductive heat flux for the solid matrix is zero at interfaces. This provides an intrinsic boundary condition for the temperature of the solid matrix at these interfaces. Such a condition holds exactly in the case of smooth interfaces but it is certainly an approximation in the case of sharp interfaces, especially in the case of dense porous media.

It is also worth mentioning that the proposed mathematical model is valid for both compressible and incompressible flows. In this chapter, we have also presented the derivation of its low-Mach number approximation, which is substantially simpler than the full model and, therefore, more convenient for flows where compressibility effects are negligible. Finally, we have provided the equations for the non-reacting case.

Chapter 3

Numerical Algorithm

3.1 Introduction

In this chapter, we provide a description of the numerical algorithm employed throughout this work for the treatment of the governing equations (2.3.9) - (2.3.13). It constitutes a generalization to multi-phase flows of the projection method proposed for the variable-density low-Mach number Navier-Stokes equations in Lessani & Papalexandris (2006). A two-step advancement in time is used and the spatial discretization is performed on a collocated rectilinear grid. Another multi-phase extension has been previously adapted to flows of fluid-saturated granular materials in the work of Varsakelis & Papalexandris (2014), where complications different to the ones presented in this work have to be addressed, such as that of the moving granular material and the resolution of the moving interface between the two phases. For the purposes of the Introduction, it is deemed useful to elaborate on the critical issues presented in using a projection method to obtain a numerical solution for the governing equations and for the flows of interest. More particular, the challenges are attributed to i)the presence of two phases that are in thermodynamic non-equilibrium with each other, ii)the presence of macroscopic interfaces in the flow domain, iii)steep temperature gradients as well as iv)chemical reactions.

The first critical issue that we discuss is the presence of macroscopic interfaces in the flow domain, which translates into steep gradients of the fluid volume fraction (porosity) ϕ. For the method that is employed herein, the presence of interfaces presents us with a variable-coefficient elliptic equation for the pressure, which can be challenging to

solve. Having to deal with an elliptic equation is a common bottleneck for all projection methods, which stems from applying the divergence operator on the momentum equation. For the model studied herein, the pressure term of the momentum equation then becomes $\nabla\cdot(\phi\nabla p)$ as can be seen from equation (2.3.10). Additionally, in the case of flows with chemical reactions, ϕ is a function of time as well. For such flows the stencil of the resulting linear system of equations, has to be reconstructed at every time-iteration. This is a computationally intensive task that increases the simulation time. These are challenges that one does not encounter in the constant density Navier-Stokes equations, since taking the divergence of the momentum equation results in a Poisson equation, see Chorin (1967) and Temam (1968).

The second critical issue is that for variable density flows, the fluid velocity is not divergence-free. This is worth elaborating on, because a kinematic constraint for the velocity field is required at the projection step of the method, as we explain in the detailed description that follows. Indeed, taking the divergence of the momentum equation, gives rise to the term $\nabla\cdot(\rho\phi\boldsymbol{u})$, which cannot be readily calculated. Instead, it needs to be substituted and in our case, an appropriate expression is provided by the continuity equation of the fluid phase, (2.3.9). Making this substitution however, gives rise to the temporal derivative of the fluid density on the right-hand side of the elliptic equation, which is subsequently divided by the time step. This term is stiff and potentially a source of instability for flows with high temperature gradients and hence high density variations.

Some works in order to avoid dealing with this term, obtain a different expression for $\nabla\cdot(\rho\phi\boldsymbol{u})$ by substituting the continuity equation in the energy equation. Such a choice, however, does not enforce conservation of mass on the projection step. In the present work we consider this feature a fundamental component of the algorithm and we pursue the formerly mentioned methodology, *i.e.*, we obtain the expression for $\nabla\cdot(\rho\phi\boldsymbol{u})$ from the continuity equation of the fluid. Furthermore, in order to cope with instability issues that can potentially arise from this term, we take caution in discretizing it and we also perform an additional re-integration of the energy equations of both phases at the end of each time-step. In the subsequent chapters that describe numerical results obtained using this method, it is shown that these measures are sufficient in dealing with any stability issues that may arise in the flows of interest.

Another key point is that we choose to perform the spatial discretization on a collocated grid instead of a staggered one. Staggered grids are most often used for computations in Cartesian coordinates because they are fully conservative with respect to the kinetic energy. On the other hand, collocated grids offer the advantage of simplicity in their implementation, as well as straightforward extension to curvilinear coordinate systems. See, for example, Kooshkbaghi & Lessani (2013). On the other hand, schemes based on such grids will always contain kinetic energy conservation errors. This drawback however, can be considerably aleviated with the use of appropriate interpolation methodologies, as is discussed in Felten & Lund (2001).

Furthermore, collocated grids are prone to numerical instability: they develop spurious oscillations of the pressure field when used for calculations of incompressible flows. To address this problem, which is referred to in the bibliography as *odd-even decoupling*, we employ herein a flux-interpolation technique. This technique was first introduced by Rhie & Chow (1983) for steady-state constant-density incompressible flows. Since then, it has been extended by various researchers to other types of flows. For example, its extension to transient variable-density flows has been presented by Lessani & Papalexandris (2006).

At this point, it is appropriate to reiterate that, discrepancies between our governing equations and other models in the literature, prevent us from using readily available commercial software packages to conduct our numerical studies. Instead, for the needs of the present work we have developed our own software from scratch, which implements the numerical method presented in the following sections.

In the section that follows, we provide a detailed description of the two-step time discretization of the governing equations. Next, the spatial discretization of the governing equations on a collocated grid is presented and analyzed.

3.2 Time Discretization

This section provides the sequential order in which the field variables are evaluated in one complete time iteration of the algorithm, so that it can be directly incorporated in a computer code. As mentioned above, the method that we employ uses a two-step advancement in time for improved accuracy in time and stability. As such, a preliminary

evaluation of the field variables is first performed at the "predictor" step. Subsequently the variables are updated once again in the "corrector" step before the completion of the cycle.

In what follows, we make use of the following notation convention. First, we drop the superscript $()^0$, used in the previous chapter to indicate variables of zeroth order in the description of the low-Mach number approximation. We only keep the superscript of the *thermodynamic* pressure p^0 so that it can be distinguished from the *kinematic* pressure p^1. Further we introduce the superscripts $(n-1)$, (n) and $(n+1)$ to denote values at the corresponding time levels and the superscript $(^*)$ to denote predicted values. The time-step is Δt, so that $t^{(n+1)} = t^{(n)} + \Delta t$. It should be noted that the thermodynamic variables c_s, ρ_s, c_p and γ are assumed to be constant and therefore in the discretized equations they appear without superscripts. Further, for our computations the fluid is assumed to behave like a perfect gas, while the solid is considered to be a rigid body.

3.2.1 Predictor step

i) At the beginning of each time-step, we first upgrade the volume fraction from ϕ^n to ϕ^* from the mass-balance law of the solid phase (2.3.12), which is discretized as follows:

$$\frac{\phi^{(*)} - \phi^{(n)}}{\Delta t} = \frac{1}{\rho_\mathrm{s}} \cdot \mathcal{M}^{(n)}. \tag{3.2.1}$$

ii) Subsequently, we proceed to evaluate the predicted temperatures of the two phases, $T^{(*)}$ and $T_\mathrm{s}^{(*)}$. First, we elaborate on the treatment of the diffusive terms that appear on the energy equations of the two phases. In the flows considered in this work, there are steep temperature gradients which render the terms with second-order derivatives stiff. A way to obtain a stable solution without lowering the time-step to prohibitively low values, is to treat such terms implicitly. However, choosing to employ implicit schemes for terms with derivatives along all of the three directions is prohibitively complex. It would require solving linear systems with sparse but complicated stencils. Such stencils are tedious to construct and the linear systems require iterative solvers with high demands in both computational time and resources.

At this point we should also mention that in the rich literature of numerical methods for the Navier-Stokes equations, there are alternative semi-implicit schemes which aim to reduce the need for computational resources. A popular example is the *approximate factorization* method, which essentially splits the multi-dimensional problem in a series of one-dimensional ones, see, for example, Kim & Moin (1985). As such, it requires the solution of several linear systems with tri-diagonal matrices, one for each direction, instead of a single linear system with a large and complicated matrix. However, the implementation of such methods for our system of governing equations is not straightforward, due to the spatial variation of the volume fraction ϕ, and lies beyond the scope of the present work.

Alternatively, one can opt to treat implicitly the terms with derivatives along a single direction. This would result in linear systems with tri-diagonal stencils, that are easy to solve and require less computational resources. Herein we follow the later scheme, which offers a compromise between a low, albeit acceptable Δt and manageable computational complexity. In particular, we treat implicitly the terms with gradients along the y direction while the terms with gradients along the x and z are treated explicitly. This choice is justified by the fact that the gravity vector is aligned in the $y-$direction, and hence the direction of preference for buoyancy effects. Furthermore, for the majority of the variable-density flows studied in this work, the initial conditions involve steep $T-$gradients on the $y-$direction.

Proceeding with the calculation of $T_{\mathrm{s}}^{(*)}$, the explicitly-treated diffusive terms, as well as the interphasial heat and mass transfer terms are grouped in the quantity $Res_{T_{\mathrm{s}}}$:

$$Res_{T_{\mathrm{s}}} = \frac{1}{RePr}\left(\frac{\partial}{\partial x}\left((1-\phi)k_{\mathrm{s}_{11}}\frac{\partial T_{\mathrm{s}}}{\partial x}\right)+\frac{\partial}{\partial z}\left((1-\phi)k_{\mathrm{s}_{33}}\frac{\partial T_{\mathrm{s}}}{\partial z}\right)\right) \\ -h(T_{\mathrm{s}}-T)+\mathcal{M}\,c_{\mathrm{s}}(T_{\mathrm{s}}-1). \tag{3.2.2}$$

For the discretization of the energy equation of the solid phase, the terms included in $Res_{T_{\mathrm{s}}}$ are treated via an Adams-Bashforth method, while the Crank-Nicolson

method is used for the implicitly treated diffusive term:

$$c_{\mathrm{s}}(1-\phi^{(n)})\rho_{\mathrm{s}}\frac{T_{\mathrm{s}}^{(*)}-T_{\mathrm{s}}^{(n)}}{\Delta t} = \frac{3}{2}Res_{T_{\mathrm{s}}}^{(n)} - \frac{1}{2}Res_{T_{\mathrm{s}}}^{(n-1)} + \frac{1}{RePr}\frac{\partial}{\partial y}\left((1-\phi^{(n)})k_{\mathrm{s}_{22}}^{(n)}\left(\frac{1}{2}\frac{\partial T_{\mathrm{s}}}{\partial y}^{(*)} + \frac{1}{2}\frac{\partial T_{\mathrm{s}}}{\partial y}^{(n)}\right)\right). \tag{3.2.3}$$

iii) The time-discretization for the fluid phase energy equation is performed in an analogous manner and follows the same guidelines. More specifically, the quantity Res_T is given by the following expression:

$$Res_T = -c_p\phi\rho\boldsymbol{u}\cdot\nabla T + \frac{1}{RePr}\left(\frac{\partial}{\partial x}\left(\phi k\frac{\partial T}{\partial x}\right) + \frac{\partial}{\partial z}\left(\phi k\frac{\partial T}{\partial z}\right)\right) + h(T_{\mathrm{s}}-T) - \mathcal{M}\left(\mathcal{H}^f + (T-1) - \frac{\gamma-1}{\gamma}\frac{p^0}{\rho_{\mathrm{s}}}\right). \tag{3.2.4}$$

The terms included in Res_T are treated via an Adams-Bashforth method, while the implicitly treated diffusive term is discretized with the Crank-Nicolson method. For the remaining terms, we use values of the time-frame (n), so that :

$$c_p\phi^{(n)}\rho^{(n)}\frac{T^{(*)}-T^{(n)}}{\Delta t} = \frac{\gamma-1}{\gamma}\phi^{(n)}\frac{p^{0(n)}-p^{0(n-1)}}{\Delta t} + \frac{3}{2}Res_T^{(n)} - \frac{1}{2}Res_T^{(n-1)} + \frac{1}{RePr}\frac{\partial}{\partial y}\left(\phi^{(n)}k^{(n)}\left(\frac{1}{2}\frac{\partial T}{\partial y}^{(*)} + \frac{1}{2}\frac{\partial T}{\partial y}^{(n)}\right)\right). \tag{3.2.5}$$

iv) After the evaluation of $T^{(*)}$, the predicted value of the fluid density $\rho^{(*)}$ is obtained by the equation of state (2.3.1). If the flow domain is closed, p^0 changes with time, and as such, $p^{0(*)}$ needs to be calculated in advance. Moreover, it is given by the integral of the equation of state over the flow domain:

$$p^{0(*)} = \frac{M_0}{\int\frac{1}{T^{(*)}}\boldsymbol{d}V_f}\ , \tag{3.2.6}$$

where M_0 is the total fluid mass.

v) Once we have evaluated $\phi^{(*)}$, $T_{\mathrm{s}}^{(*)}$, $T^{(*)}$ and $\rho^{(*)}$, we continue with the calculation of the fluid dynamic pressure p^1 and the fluid velocity field $\boldsymbol{u}$. First, the momentum

equation is written in conservative form, which serves better the purposes of our flux interpolation scheme that is analyzed in the following section. To this end, the material derivative of u in (2.3.10) is expanded and $\nabla\cdot(\rho\phi\boldsymbol{u})$ is substituted from the continuity equation (2.3.9), so that we arrive at:

$$\frac{\partial(\rho\phi\boldsymbol{u})}{\partial t}+\nabla\cdot(\rho\phi\boldsymbol{u}\,\boldsymbol{u})+\phi\nabla p^1=\frac{1}{Re}\nabla\cdot(\phi\mu\boldsymbol{V}_d^{\mathrm{v}})-\underset{\sim}{\boldsymbol{\beta}}\boldsymbol{u}-Ri\,\phi\rho\,\hat{\boldsymbol{y}}. \tag{3.2.7}$$

Furthermore, the presence of interfaces encountered in the problems studied herein, in combination with steep temperature gradients can render the body force abruptly variable in both space and time. In such cases it is useful to write the momentum equation in terms of the piezometric pressure, $p'=p^1+\rho Riy$, see for example Hong & Walker (2000). This is done by substituting

$$\rho Ri=\frac{\partial(\rho Riy)}{\partial y}-y\,\frac{\partial(\rho Ri)}{\partial y}, \tag{3.2.8}$$

in equation (3.2.7) to finally obtain,

$$\frac{\partial(\rho\phi\boldsymbol{u})}{\partial t}+\nabla\cdot(\rho\phi\boldsymbol{u}\,\boldsymbol{u})+\phi\nabla p'=\frac{1}{Re}\nabla\cdot(\phi\mu\boldsymbol{V}_d^{\mathrm{v}})-\underset{\sim}{\boldsymbol{\beta}}\boldsymbol{u}+\phi Riy\,\nabla\rho, \tag{3.2.9}$$

where y is the coordinate along the direction opposite to that of the gravity vector.

A first step toward the computation of the variables $\boldsymbol{u}$ and p', is to calculate the quantity $\tilde{\boldsymbol{u}}$, known in the bibliography of projection methods as the *provisional*, or *intermediate* velocity. This vector, has velocity dimensions and in our algorithm is defined as the solution to the momentum equation without the pressure term and the body force:

$$\frac{\partial(\rho\phi\boldsymbol{u})}{\partial t}+\nabla\cdot(\rho\phi\boldsymbol{u}\;\boldsymbol{u})=\frac{1}{Re}\nabla\cdot(\phi\mu\boldsymbol{V}_d^{\mathrm{v}})-\underset{\sim}{\boldsymbol{\beta}}\boldsymbol{u}. \tag{3.2.10}$$

For the time-discretization of (3.2.10), the interphasial drag terms are treated implicitly with the Crank-Nicolson method. The same applies for the diffusive terms which include second-order derivatives of the provisional velocity $\tilde{\boldsymbol{u}}$ in the $y-$direction. The remaining diffusive terms, as well as the convective terms are grouped in the vector $Res_{\boldsymbol{u}}=(Res_u,Res_v,Res_w)^T$ and they are treated explicitly

via the Adams-Bashforth method. To clarify things, here we provide the expressions for all components of $Res_{\boldsymbol{u}}$:

$$\begin{aligned} Res_u = &- \nabla\cdot(\rho\phi\boldsymbol{u}\,u) + \frac{1}{Re}\left[\frac{\partial}{\partial x}\left(\mu\phi\left(2\frac{\partial u}{\partial x} - \frac{2}{3}\nabla\cdot\boldsymbol{u}\right)\right)\right. \\ &\left. + \frac{\partial}{\partial y}\left(\mu\phi\frac{\partial v}{\partial x}\right) + \frac{\partial}{\partial z}\left(\mu\phi\left(\frac{\partial u}{\partial z} + \frac{\partial w}{\partial x}\right)\right)\right], \end{aligned} \tag{3.2.11a}$$

$$\begin{aligned} Res_v = &- \nabla\cdot(\rho\phi\boldsymbol{u}\,v) + \frac{1}{Re}\left[\frac{\partial}{\partial x}\left(\mu\phi\left(\frac{\partial u}{\partial y} + \frac{\partial v}{\partial x}\right)\right)\right. \\ &\left. - \frac{2}{3}\frac{\partial}{\partial y}\left(\mu\phi\left(\frac{\partial u}{\partial x} + \frac{\partial w}{\partial z}\right)\right) + \frac{\partial}{\partial z}\left(\mu\phi\left(\frac{\partial v}{\partial z} + \frac{\partial w}{\partial y}\right)\right)\right] \quad \text{and} \end{aligned} \tag{3.2.11b}$$

$$\begin{aligned} Res_w = &- \nabla\cdot(\rho\phi\boldsymbol{u}\,w) + \frac{1}{Re}\left[\frac{\partial}{\partial x}\left(\mu\phi\left(\frac{\partial u}{\partial z} + \frac{\partial w}{\partial x}\right)\right)\right. \\ &\left. + \frac{\partial}{\partial y}\left(\mu\phi\frac{\partial v}{\partial z}\right) + \frac{\partial}{\partial z}\left(\mu\phi\left(2\frac{\partial w}{\partial z} - \frac{2}{3}\nabla\cdot\boldsymbol{u}\right)\right)\right]. \end{aligned} \tag{3.2.11c}$$

Further, to facilitate the presentation of the discretized momentum equation (3.2.10) we group the coefficients of the stress-tensor terms that are treated implicitly, in the auxiliary diagonal tensor $\underset{\sim}{\boldsymbol{c}}$. In particular, this tensor, contains the coefficients of the terms $\frac{\partial}{\partial y}\left(\phi\mu\frac{\partial \boldsymbol{u}}{\partial y}\right)$ in equation (3.2.10), minus the coefficients of the same terms in $Res_{\boldsymbol{u}}$, in expressions (3.2.11). This yields, $\underset{\sim}{\boldsymbol{c}} = \mathrm{d}iag(1, \frac{4}{3}, 1)$. Then, the discretized equation (3.2.10) can be written as follows.

$$\begin{aligned} \frac{\rho^{(*)}\phi^{(*)}\tilde{\boldsymbol{u}} - \rho^{(n)}\phi^{(n)}\boldsymbol{u}^{(n)}}{\Delta t} = &\frac{3}{2}Res_{\boldsymbol{u}}^{(n)} - \frac{1}{2}Res_{\boldsymbol{u}}^{(n-1)} \\ &+\frac{1}{2}\underset{\sim}{\boldsymbol{c}}\frac{1}{Re}\frac{\partial}{\partial y}\left(\phi^{(*)}\mu^{(*)}\frac{\partial\tilde{\boldsymbol{u}}}{\partial y}\right) + \frac{1}{2}\underset{\sim}{\boldsymbol{c}}\frac{1}{Re}\frac{\partial}{\partial y}\left(\phi^{(n)}\mu^{(n)}\frac{\partial\boldsymbol{u}^{(n)}}{\partial y}\right) \\ &-\underset{\sim}{\boldsymbol{\beta}}^{(n)}\left(\frac{1}{2}\tilde{\boldsymbol{u}} + \frac{1}{2}\boldsymbol{u}^{(n)}\right). \end{aligned} \tag{3.2.12}$$

Having calculated $\tilde{\boldsymbol{u}}$, we proceed with the discretization of the momentum equation, (3.2.9). This is done in an analogous manner to the discretization of (3.2.10) and using values of the time-frame $(*)$ for the pressure and body-force terms. Then, we arrive at,

$$\frac{\rho^{(*)}\phi^{(*)}\boldsymbol{u}^{(*)}}{\Delta t} = \frac{\rho^{(*)}\phi^{(*)}\tilde{\boldsymbol{u}}}{\Delta t} - \phi^{(*)}\nabla p'^{(*)} + \phi^{(*)}Ri\nabla\rho^{(*)}y. \tag{3.2.13}$$

At this point we perform the projection step. In particular, we take the divergence of (3.2.13) and we substitute the expression for $\nabla\cdot(\rho^{(*)}\phi^{(*)}\boldsymbol{u}^{(*)})$ as provided by (2.3.9). In this manner we arrive to an elliptic equation in which p' is the only unknown:

$$\begin{aligned}\nabla\cdot(\phi^{(*)}\nabla p'^{(*)}) =&\frac{1}{\Delta t}\nabla\cdot(\rho^{(*)}\phi^{(*)}\tilde{\boldsymbol{u}}) - \frac{1}{\Delta t}\mathcal{M}^{(*)}\frac{\rho_{\mathrm{s}}-\rho^{(*)}}{\rho_{\mathrm{s}}}\\ &+\frac{3\rho^{(*)}-4\rho^{(n)}+\rho^{(n-1)}}{2\Delta t^2}\phi^{(*)} + Ri\nabla\cdot(\phi^{(*)}\nabla\rho^{(*)}y). \qquad (3.2.14)\end{aligned}$$

The spatial discretization of the above equation results in a linear system of algebraic equations. In the problems that we are concerned with, both the right-hand side terms and the coefficients on the left hand-side of this system can be highly irregular. Nonetheless, in order to obtain the solution we employ the stabilized bi-conjugate gradient method (Bi-CGSTAB), van der Vorst (1992), which turns out to be sufficiently stable to handle such irregularities.

Once $p'^{(*)}$ is calculated, the predicted values of the velocity field $\boldsymbol{u}^{(*)}$ are directly calculated from (3.2.13).

3.2.2 Corrector step

In the corrector step, the field variables are updated to time $t=(n+1)\Delta t$, following the same sequence of steps that was described in detail for the predictor step.

i) First, the fluid volume fraction is updated from equation (2.3.12):

$$\frac{\phi^{(n+1)}-\phi^{(n)}}{\Delta t} = \frac{1}{\rho_{\mathrm{s}}}\cdot\mathcal{M}^{(*)}. \qquad (3.2.15)$$

ii) For the evaluation of $T_{\mathrm{s}}^{(n+1)}$, the solid energy equation is discretized as in (3.2.3), the only difference being that the explicitly treated terms, are discretized with a trapezoidal rule, using the values of $Res_{T_{\mathrm{s}}}$ at the time-frames $(*)$ and (n):

$$\begin{aligned}c_{\mathrm{s}}(1-\phi^{(*)})\rho_{\mathrm{s}}\frac{T_{\mathrm{s}}^{(n+1)}-T_{\mathrm{s}}^{(n)}}{\Delta t} =&\ \frac{1}{2}Res_{T_{\mathrm{s}}}^{(*)}+\frac{1}{2}Res_{T_{\mathrm{s}}}^{(n)}\\ &+\frac{1}{RePr}\frac{\partial}{\partial y}\left((1-\phi^{(*)})k_{\mathrm{s}22}^{(*)}\left(\frac{1}{2}\frac{\partial T_{\mathrm{s}}}{\partial y}^{(n+1)}+\frac{1}{2}\frac{\partial T_{\mathrm{s}}}{\partial y}^{(n)}\right)\right). \qquad (3.2.16)\end{aligned}$$

Once the values of T_{s} are updated, the thermal conductivity of the solid phase $\underset{\sim}{\boldsymbol{k}}_{\mathrm{s}}$ is updated as well, *i.e* we compute $\underset{\sim}{\boldsymbol{k}}_{\mathrm{s}}^{(n+1)} = \underset{\sim}{\boldsymbol{k}}_{\mathrm{s}}(T_{\mathrm{s}}^{(n+1)})$

iii) Accordingly, for the calculation of $T^{(n+1)}$, the fluid energy equation is discretized as follows:

$$\begin{aligned} c_p\phi^{(*)}\rho^{(*)}\frac{T^{(n+1)}-T^{(n)}}{\Delta t} &= \frac{\gamma-1}{\gamma}\phi^{(n)}\frac{p^{0(n)}-p^{0(n-1)}}{\Delta t}+\frac{1}{2}Res_T^{(*)}+\frac{1}{2}Res_T^{(n)} \\ &+\frac{1}{RePr}\frac{\partial}{\partial y}\left(\phi^{(*)}k^{(*)}\left(\frac{1}{2}\frac{\partial T^{(n+1)}}{\partial y}+\frac{1}{2}\frac{\partial T^{(n)}}{\partial y}\right)\right). \end{aligned} \tag{3.2.17}$$

iv) Subsequently, $\rho^{(n+1)}$ is calculated from the state equation, as in the predictor step. In the case of a closed domain, $p^{0(n+1)}$ needs to be updated from the expression,

$$p^{0(n+1)} = \frac{M_0}{\int \frac{1}{T^{(n+1)}}\boldsymbol{d}V_f}. \tag{3.2.18}$$

v) For the calculation of the provisional velocity for the corrector step, $\breve{\boldsymbol{u}}$, the fluid momentum equation excluding the pressure and body-force terms is discretized as follows:

$$\begin{aligned} \frac{(\rho\phi)^{(n+1)}\breve{\boldsymbol{u}}-(\rho\phi)^{(n)}\boldsymbol{u}^{(n)}}{\Delta t} &= \frac{1}{2}Res_{\boldsymbol{u}}^{(*)}+\frac{1}{2}Res_{\boldsymbol{u}}^{(n)} \\ &+\frac{1}{2}\underset{\sim}{\boldsymbol{c}}\frac{1}{Re}\frac{\partial}{\partial y}\left((\phi\mu)^{(n+1)}\frac{\partial\breve{\boldsymbol{u}}}{\partial y}\right)+\frac{1}{2}\underset{\sim}{\boldsymbol{c}}\frac{1}{Re}\frac{\partial}{\partial y}\left((\phi\mu)^{(n)}\frac{\partial\boldsymbol{u}^{(n)}}{\partial y}\right) \\ &-\underset{\sim}{\boldsymbol{\beta}}^{(*)}\left(\frac{1}{2}\breve{\boldsymbol{u}}+\frac{1}{2}\boldsymbol{u}^{(n)}\right). \end{aligned} \tag{3.2.19}$$

Next, we consider the fluid momentum equation written in terms of $\breve{\boldsymbol{u}}$:

$$\begin{aligned} \frac{\rho^{(n+1)}\phi^{(n+1)}\boldsymbol{u}^{(n+1)}}{\Delta t} &= \frac{\rho^{(n+1)}\phi^{(n+1)}\breve{\boldsymbol{u}}}{\Delta t}-\phi^{(n+1)}\nabla p'^{(n+1)} \\ &+\phi^{(n+1)}Ri\nabla\rho^{(n+1)}y. \end{aligned} \tag{3.2.20}$$

Subsequently, we apply the projection step by taking the divergence of (3.2.20) and evaluate $\nabla\cdot(\rho^{(n+1)}\phi^{(n+1)}\boldsymbol{u}^{(n+1)})$ using the continuity equation (2.3.9). This procedure leads to,

$$\begin{aligned} \nabla\cdot(\phi^{(n+1)}\nabla p'^{(n+1)}) &= \frac{1}{\Delta t}\nabla\cdot(\rho^{(n+1)}\phi^{(n+1)}\breve{\boldsymbol{u}})-\frac{\mathcal{M}}{\Delta t}\frac{\rho_{\mathrm{s}}-\rho^{(n+1)}}{\rho_{\mathrm{s}}} \\ &+\frac{3\rho^{(n+1)}-4\rho^{(n)}+\rho^{(n-1)}}{2\Delta t^2}\phi^{(n+1)}+Ri\nabla\cdot(\phi^{(n+1)}\nabla\rho^{(n+1)}y). \end{aligned} \tag{3.2.21}$$

The above equation is solved for $p'^{(n+1)}$, which is subsequently introduced in (3.2.20) to obtain $\boldsymbol{u}^{(n+1)}$.

vi) At the end of the corrector step, the temperatures of both phases are re-integrated from $t^{(n)}$ to $t^{(n+1)}$, taking into account $\phi^{(n+1)}$,$\rho^{(n+1)}$ and $\boldsymbol{u}^{(n+1)}$:

$$c_p\phi^{(n+1)}\rho^{(n+1)}\frac{T^{(n+1)}-T^{(n)}}{\Delta t} = \frac{\gamma-1}{\gamma}\phi^{(n)}\frac{p^{0(n)}-p^{0(n-1)}}{\Delta t}+\frac{1}{2}Res_T^{(n+1)}+\frac{1}{2}Res_T^{(n)} + \frac{1}{RePr}\frac{\partial}{\partial y}\left(\phi^{(n+1)}k^{(n+1)}\left(\frac{1}{2}\frac{\partial T}{\partial y}^{(n+1)}+\frac{1}{2}\frac{\partial T}{\partial y}^{(n)}\right)\right), \tag{3.2.22}$$

$$c_{\mathrm{s}}(1-\phi^{(n+1)})\rho_{\mathrm{s}}\frac{T_{\mathrm{s}}^{(n+1)}-T_{\mathrm{s}}^{(n)}}{\Delta t} = \frac{1}{2}Res_{T_{\mathrm{s}}}^{(n+1)}+\frac{1}{2}Res_{T_{\mathrm{s}}}^{(n)} + \frac{1}{RePr}\frac{\partial}{\partial y}\left((1-\phi^{(n+1)})k_{\mathrm{s}_{22}}^{(n+1)}\left(\frac{1}{2}\frac{\partial T_{\mathrm{s}}}{\partial y}^{(n+1)}+\frac{1}{2}\frac{\partial T_{\mathrm{s}}}{\partial y}^{(n)}\right)\right). \tag{3.2.23}$$

A similar re-integration of the energy equation at the end of time-step is performed in Lessani & Papalexandris (2006). According to numerical experiments performed by the authors therein, this additional calculation reduces substantially energy conservation errors that may arise in flows subjected to strong thermal gradients.

3.3 Spatial Discretization

The spatial discretization of the governing equations is performed on a collocated grid system. For the description that follows, the grid cells are uniquely identified by the indices (i, j, k), corresponding to the cell's order of appearance along the x, y and z axis respectively. The dimensions of each cell are $(2r_i, 2r_j, 2r_k)$ i.e. r_i, r_j and r_k are the distances of the cell interfaces in the 3 directions from the center of the cell. Further, subscripts with integer coefficients preceding the aforementioned indices, stand for quantities at the center of the cell or the center of the neighboring cells. When half-integer coefficients are used, the quantities correspond to the cell-interfaces along the direction

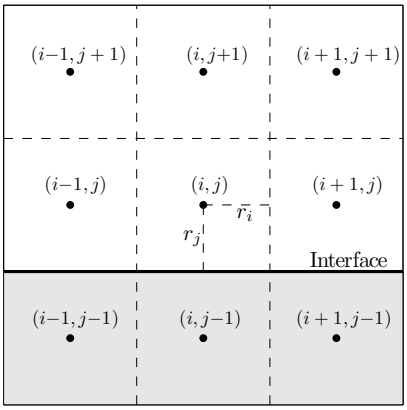

Figure 3.1: Representation of grid cells at the vicinity of the porous medium – pure fluid interface. The shaded area indicates the part of the domain that is occupied by the porous medium.

that the index represents. A schematic of grid cells at the vicinity of the porous medium - pure fluid interface, along the notation convention that we use in this section, is provided in Figure 3.1. As is shown in this figure, the macroscopic interface between the porous medium and the pure-fluid domain is aligned with the interfaces of the cells.

For the manipulation of the discrete operators, as well as for the implementation of the discretization in the computer code, we assumed a *rectilinear* grid, *i.e.* a grid in which the size of the cells in each of the three directions varies only along the respective direction ($r_i = r_i(i)$, $r_j = r_j(j)$ and $r_k = r_k(k)$). However, it should be clarified that for all the numerical simulations performed for this work, the grid spacing was uniform, so that $r_i = r_j = r_k$.

The discrete operations performed in the description that follows, are described based on two elementary operators. The interpolation operator, which is denoted with the overbar, and its effect along the $x-$axis on a discrete function $\mathrm{f}(i, j, k)$ is given by the following expression:

$$\overline{\mathrm{f}}^{x}_{i\pm\frac{1}{2}} = \frac{\mathrm{f}_{i\pm1} r_i + \mathrm{f}_i r_{i\pm1}}{r_i + r_{i\pm1}}. \tag{3.3.1}$$

Further, we introduce the finite-difference operator which is annotated by $\frac{\delta}{\delta x}$, $\frac{\delta}{\delta y}$ and $\frac{\delta}{\delta z}$

along the three directions. Its effect along the $x-$axis and at the interfaces of a cell is given as follows:

$$\left.\frac{\delta \mathrm{f}}{\delta x}\right|_{i\pm\frac{1}{2}} = \pm\,\frac{\mathrm{f}_{i\pm1} - \mathrm{f}_i}{r_{i\pm1} + r_i}, \tag{3.3.2}$$

while at the center of the cell is given by,

$$\left.\frac{\delta \mathrm{f}}{\delta x}\right|_{i} = \frac{\overline{\mathrm{f}_{i+\frac{1}{2}}}^{x} - \overline{\mathrm{f}_{i-\frac{1}{2}}}^{x}}{2\,r_i}. \tag{3.3.3}$$

Analogous expressions apply for both operators along the other two directions.

A key point of the method followed herein is the flux interpolation technique which prevents the afore-mentioned oscillations of the pressure field. According to this scheme the velocities are interpolated on the interfaces of the cells to yield the values that are used in the calculations of the convective terms, instead of the cell centered values. Herein, we employ the generalized version of the flux interpolation method proposed by Lessani & Papalexandris (2006). This amounts to calculating the quantity $(\rho\phi\boldsymbol{u})$, which appears in the convective terms of the governing equations, on the interfaces of the cells, using equations (3.2.13) and (3.2.20). Furthermore, we introduce the auxiliary fluxes f_u, f_v and f_w, so that:

$$f_u|_{i+\frac{1}{2}} = \rho\phi u|_{i+\frac{1}{2}} = \overline{(\rho\phi\tilde{u})_{i+\frac{1}{2}}}^{x} - \overline{\phi_{i+\frac{1}{2}}}^{x}\left.\frac{\delta p'}{\delta x}\right|_{i+\frac{1}{2}}\Delta t + Ri\;\overline{\phi_{i+\frac{1}{2}}}^{x}\left.\frac{\delta \rho}{\delta x}\right|_{i+\frac{1}{2}} y\,\Delta t\,, \tag{3.3.4a}$$

$$f_v|_{j+\frac{1}{2}} = \rho\phi v|_{j+\frac{1}{2}} = \overline{(\rho\phi\tilde{v})_{j+\frac{1}{2}}}^{y} - \overline{\phi_{j+\frac{1}{2}}}^{y}\left.\frac{\delta p'}{\delta y}\right|_{j+\frac{1}{2}}\Delta t + Ri\;\overline{\phi_{j+\frac{1}{2}}}^{y}\left.\frac{\delta \rho}{\delta y}\right|_{j+\frac{1}{2}}\overline{y_{j+\frac{1}{2}}}^{y}\,\Delta t\,, \tag{3.3.4b}$$

$$f_w|_{k+\frac{1}{2}} = \rho\phi w|_{k+\frac{1}{2}} = \overline{(\rho\phi\tilde{w})_{k+\frac{1}{2}}}^{z} - \overline{\phi_{k+\frac{1}{2}}}^{z}\left.\frac{\delta p'}{\delta z}\right|_{k+\frac{1}{2}}\Delta t + Ri\;\overline{\phi_{k+\frac{1}{2}}}^{z}\left.\frac{\delta \rho}{\delta z}\right|_{k+\frac{1}{2}} y\,\Delta t\,. \tag{3.3.4c}$$

These expressions are valid for the predictor step. For the corrector step, the *provisional* velocities $\tilde{\boldsymbol{u}}$ have to be replaced by $\breve{\boldsymbol{u}}$, according to equation (3.2.20). Note that for the initialization of the algorithm at $t = 0$, the auxiliary fluxes used in the calculation of $Res_{\boldsymbol{u}}$ and Res_T are given only as a function of the velocity, density and volume fraction

profiles at the initial condition:

$$f_u|^{(0)}_{i+\frac{1}{2}} = \overline{(\rho\phi u)^{(0)}_{i+\frac{1}{2}}}^{x}, \quad f_v|^{(0)}_{j+\frac{1}{2}} = \overline{(\rho\phi v)^{(0)}_{j+\frac{1}{2}}}^{y}, \quad f_w|^{(0)}_{k+\frac{1}{2}} = \overline{(\rho\phi w)^{(0)}_{k+\frac{1}{2}}}^{z}. \tag{3.3.5}$$

Having established the basic operations for interpolation and differentiation of the discrete functions, we proceed with the description of the spatial discretization of terms of interest, following their order of appearance in the previous section. The first terms we examine are the explicitly-treated diffusive terms, in the expression of Res_{T_s}; see, equation (3.2.2). For these terms, as well as for all the terms that appear in a divergence operator, we do not use the product rule; instead, we apply the divergence theorem on the cell where the quantity is calculated. As an example, we consider the first term of (3.2.2) which is discretized as follows:

$$\frac{\partial}{\partial x}\left((1-\phi)k_{\mathrm{s}_{11}}\frac{\partial T_\mathrm{s}}{\partial x}\right) = \frac{\overline{[k_{\mathrm{s}_{11}}(1-\phi)]_{i+\frac{1}{2}}}^{x}\ \frac{\delta T_\mathrm{s}}{\delta x}\big|_{i+\frac{1}{2}} - \overline{[k_{\mathrm{s}_{11}}(1-\phi)]_{i-\frac{1}{2}}}^{x}\ \frac{\delta T_\mathrm{s}}{\delta x}\big|_{i-\frac{1}{2}}}{2\,r_i} \tag{3.3.6}$$

Next, we examine the convective part of the fluid energy equation, as it appears in the expression for Res_T, (3.2.4). As was mentioned above, $(\rho\phi\boldsymbol{u})$ is interpolated on the cell-interfaces with the aid of equations (3.3.4a) to (3.3.4c) for use in the convective terms of the fluid momentum and energy equations. As such, we choose to discretize $\phi\rho\boldsymbol{u}\cdot\nabla T$ taking advantage of this calculation:

$$\begin{aligned}\phi\rho\boldsymbol{u}\cdot\nabla T =& \frac{f_u|_{i+\frac{1}{2}}\ \frac{\delta T}{\delta x}\big|_{i+\frac{1}{2}} + f_u|_{i-\frac{1}{2}}\ \frac{\delta T}{\delta x}\big|_{i-\frac{1}{2}}}{2} + \frac{f_v|_{j+\frac{1}{2}}\ \frac{\delta T}{\delta y}\Big|_{j+\frac{1}{2}} + f_v|_{j-\frac{1}{2}}\ \frac{\delta T}{\delta y}\Big|_{j-\frac{1}{2}}}{2} \\ &+ \frac{f_w|_{k+\frac{1}{2}}\ \frac{\delta T}{\delta z}\big|_{k+\frac{1}{2}} + f_w|_{k-\frac{1}{2}}\ \frac{\delta T}{\delta z}\big|_{k-\frac{1}{2}}}{2}\end{aligned} \tag{3.3.7}$$

In contrast to the convective term of the fluid energy equation, that of the momentum equation appears in a divergence in equation (3.2.7), since we chose to solve the equation in its conservative form. As such, the discretization is performed after we apply the divergence theorem on the cell where the term is calculated, the same way we did for (3.3.6):

$$\begin{aligned}\nabla\cdot(\rho\phi\boldsymbol{u}\,\boldsymbol{u}) =& \frac{f_u|_{i+\frac{1}{2}}\,\overline{\boldsymbol{u}_{i+\frac{1}{2}}}^{x} - f_u|_{i-\frac{1}{2}}\,\overline{\boldsymbol{u}_{i-\frac{1}{2}}}^{x}}{2\,r_i} + \frac{f_v|_{j+\frac{1}{2}}\,\overline{\boldsymbol{u}_{j+\frac{1}{2}}}^{y} - f_v|_{j-\frac{1}{2}}\,\overline{\boldsymbol{u}_{j-\frac{1}{2}}}^{y}}{2\,r_j} \\ &+ \frac{f_w|_{k+\frac{1}{2}}\,\overline{\boldsymbol{u}_{k+\frac{1}{2}}}^{z} - f_w|_{k-\frac{1}{2}}\,\overline{\boldsymbol{u}_{k-\frac{1}{2}}}^{z}}{2\,r_k}.\end{aligned} \tag{3.3.8}$$

Finally, for completion purposes, we provide the discretization of terms that originate from the fluid's stress tensor. The challenge involved in the manipulation of these terms, is the discretization of the cross derivatives. For example, for the second diffusive term in the expression (3.2.11a) we employ the same methodology that we followed so far for all terms that arise from the expansion of the divergence of diffusive fluxes. As such, we need to evaluate the derivative of v along the x on the interfaces of the cell along the y direction, *i*.e $\frac{\partial v}{\partial x}\big|_{j\pm\frac{1}{2}}$. In such terms, the derivative is first calculated at the center of the cells on both sides of the interface and then interpolated on the interface following the expression (3.3.1):

$$\left.\frac{\partial v}{\partial x}\right|_{j\pm\frac{1}{2}} = \overline{\frac{\delta v}{\delta x}_{j\pm\frac{1}{2}}}^{y} . \tag{3.3.9}$$

According to this rule, the discretization of the second term of expression (3.2.11a) in its entirety is discretized as follows:

$$\frac{\partial}{\partial y}\left(\mu\phi\frac{\partial v}{\partial x}\right)_j = \frac{\overline{(\mu\phi)_{j+\frac{1}{2}}}^{y}\ \overline{\frac{\delta v}{\delta x}_{j+\frac{1}{2}}}^{y} - \overline{(\mu\phi)_{j-\frac{1}{2}}}^{y}\ \overline{\frac{\delta v}{\delta x}_{j-\frac{1}{2}}}^{y}}{2\,r_j} \tag{3.3.10}$$

The rest of the components of the stress tensor are treated in the same manner.

3.4 Intermediate velocity boundary conditions

The method presented in the last two sections is second-order accurate in time for $\boldsymbol{u}$. However, in Brown *et al.* (2001), it is argued that in order to achieve second-order accuracy up to the boundary for p' as well, then the boundary condition for the *intermediate* velocities $\tilde{\boldsymbol{u}}$, $\breve{\boldsymbol{u}}$ must be compatible with those applied for p' via equations (3.2.13) and (3.2.20) respectively. The description that follows is based on the boundary condition of $\tilde{\boldsymbol{u}}$, however the same applies for $\breve{\boldsymbol{u}}$ in the corrector step.

The afore-mentioned limitation does not pose a problem for the boundary condition of the *provisional* velocity component that is normal to the boundary, $\tilde{\boldsymbol{u}}\cdot\hat{n}$. In this case, we apply the same boundary condition that we use for $\boldsymbol{u}\cdot\hat{n}$. The information that we introduce in the domain by applying the boundary condition, is taken into account for the solution of $p'^{(*)}$. This is achieved via the calculation of the term $\nabla\cdot(\rho\phi\tilde{\boldsymbol{u}})$ in the right-hand side of the elliptic equation (3.2.14). Therefore the profiles of the solution of

$p'^{(*)}$ at the vicinity of the boundary are inherently compatible with the applied boundary condition.

On the other hand, the boundary conditions of the two other components of the *provisional* velocity are not taken into account in the calculation of $p'^{(*)}$ in equation (3.2.14). In order to ensure the compatibility with the boundary conditions of p' as expressed by Brown *et al.* (2001), they have to be taken in accordance with (3.2.13). For example, in a 2-D problem that we enforce no-slip conditions at the top boundary, the boundary condition applied to $\tilde{u}$ would have to be,

$$\tilde{u} = u + \frac{\Delta t}{\rho^{(*)}} \left(\frac{\partial p'^{(*)}}{\partial x} - Ri \frac{\partial \rho^{(*)}}{\partial x} y \right) . \tag{3.4.1}$$

In the 3-D analogue of this case, appropriate boundary conditions would need to be applied to both components of $\tilde{\boldsymbol{u}}$ tangential to the boundary, *i.e.* both $\tilde{u}$ and $\tilde{w}$.

It should be noted, that at the point of the algorithm when we need to apply the $\tilde{u}$ boundary condition, $p'^{(*)}$ is not readily available. It suffices however, to approximate its spatial derivative on the boundary with that of $p'^{(n)}$.

3.5 Test cases

In this section we are concerned with the validation of the proposed model, as well as the testing of the algorithm and software that were developed for the needs of this thesis. For the purposes of software testing, we performed a series of simulations for problems in pure-fluid domains, with analytic solutions, and others with readily-available numerical results. In particular, we reproduced the laminar boundary layer of pure-fluid flow over a flat plate, and measured its growth over a fixed distance for various grid resolutions. The same was also done for laminar flow between parallel plates, where the 1-dimensional analytical solution was confirmed along all three directions, *i.e.* configuring different problem cases, in which the streamwise direction was along the x, y and z axis. Finally, we performed three-dimensional simulations of turbulent flow in a pure-fluid channel, and we successfully obtained the logarithmic law of the wall.

However, the following subsections cover results from tests cases with fluid flow in super-posed porous and pure fluid layers. First, the proposed model is validated by

reproducing numerically the stream-wise velocity profiles obtained in Le Bars & Worster (2006) for poiseuille flow in a channel with a permeable wall. Next, the conservation properties of the proposed algorithm are tested via a numerical simulation of the growth of an inviscid shear layer at the interface of a porous structure. The results of this simulation are then compared to the analytic results of our linear stability analysis presented in Chapter 4, Section 4.2. At this point it should be mentioned that the algorithm and software were further tested by means of comparison of results from our simulations with readily available experimental data. However, this was done for the problem of natural convection in superposed porous and pure-fluid layers, and as such, this description makes up a part of Chapter 5, which is dedicated to our study of heat transfer phenomena in the domains of interest.

3.5.1 Poiseuille flow in a fluid overlying a porous layer

The discussion that follows concerns the comparison of numerical results produced with our model and software, with those reported in Le Bars & Worster (2006) for the problem of poiseuille flow in a channel with a permeable wall. Such flows are of interest due to their pertinence to the problem of solidification in the mushy layer between two alloys.

As is the case in the present work, Le Bars & Worster are also based on the single domain approach, however they use a different variation of the Darcy-Brinkman equation. As such, the essential difference between the momentum equation used therein, and equation (2.4.2) that is used in this thesis, is in the position of the volume fraction within each term. In particular, the equation of Le Bars & Worster results from averaging the Navier-Stokes equation over a mesoscopic volume, and accounting for the presence of the solid matrix. The size of this elementary volume, namely the averaging length δ_a, is typically a few pore lengths, so that

$$\delta_a = a\sqrt{K(\phi_0)}\,, \tag{3.5.1}$$

where $a = O(1)$, and K the permeability of a medium with porosity ϕ_0. By changing δ_a, the sharpness of the macroscopic interface between the porous medium and the pure-fluid region changes as well. More specifically, they assume that the profile of the volume fraction is linear inside a transition region of size $2\delta_a$, which extends symmetrically on

both sides of the interface. In turn, the thickness of this interface region affects the profiles of the streamwise velocity component in the pure-fluid domain, as well as in the vicinity of the macroscopic interface. For reasons of consistency in the comparison that follows, the expression that we employ for the interphasial drag parameter $\underset{\sim}{\boldsymbol{\beta}}$, is the Darcy law in the form that is given in Le Bars & Worster (2006), so that

$$\underset{\sim}{\beta}_{11} = \frac{\mu\phi}{K(\phi)}\,. \tag{3.5.2}$$

First, we provide the description of the problem setup. The pure-fluid and the porous layers are assumed to be parallel to the x direction, which is periodic, and the macroscopic interface between them is located at $y = 0$. The porous medium is located below the pure-fluid layer, so that according to the description of the transition region provided above, the distribution of the fluid volume fraction is given by,

$$\phi(y) = \begin{cases} \phi_0\,, & y < -\delta_a, \\ (1-\phi_0)y/\,2\,\delta_a + (1+\phi_0)/2\,, & -\delta_a \leq y \leq \delta_a, \\ 1\,, & y > \delta_a\,. \end{cases} \tag{3.5.3}$$

Along the normal direction the pure-fluid domain is bounded by a rigid wall at a distance $h = 1m$ above the interface, while for negative y, the porous medium extends far below it.

The solution we seak within the context of this test is one-dimensional. As such, and for reasons of computational savings, the extent of the domain along the streamwise direction is considerably smaller than its extent in the cross-stream direction. Accordingly, the size of the domain is $0.1h \times 2h$ and it is discretized over a uniform grid with a resolution of 100 cells per unit-length.

At the beginning of the simulation, the streamwise velocity profile in the pure-fluid domain is parabolic, while inside the porous medium the velocity is zero. One could also opt to set the fluid at rest throughout the domain as initial condition. However, the distribution of our choice has been selected instead, for purposes of computational savings. The cross-stream component of the velocity is set equal to zero. Finally, a pressure gradient that drives the flow is applied along the streamwise direction. Its value

is such that $\mu^{-1}\partial p/\partial x = -1/(m\,s)$. In a pure-fluid channel with impermeable walls and width h, this value would maintain the initially prescribed parabolic profile.

For the results presented below, the porosity of the medium is set to $\phi_0 = 0.9$, and the porous skeleton is assumed to consist of an ensemble of uniformly distributed spheres of diameter $d_p = 0.049h$. Accordingly, the permeability function in equation (3.5.2) is given by the Kozeny - Carman expression for an ensemble of spheres of diameter d_p and porosity ϕ,

$$K(\phi) = \frac{d_p^2\,\phi^3}{175\,(1-\phi)^2}\,, \tag{3.5.4}$$

see, for example, Beckermann *et al.* (1988).

In the following, we change the thickness of the transition region between between the porous and pure-fluid layers, and we compute the corresponding streamwise velocity profiles along the cross-stream direction, $u(y)$. This is repeated for the three values of δ_a that are considered in Le Bars & Worster (2006), by setting $a = 1$, $a = 10$ and $a = 0$ (sharp interface) in the expression (3.5.1). Of particular interest are the velocity profiles at the vicinity of the interface, which have been a subject of long discussions among authors, and the main point of differentiation between the models of the literature. Figure 3.2a shows the profiles computed in our simulation alongside the ones provided in Le Bars & Worster (2006). Despite the differences between the two models, the resulting velocity profiles, for the flow considered in this comparison, collapse. Further, we can infer that, the velocity at the centerline for $a=10$ is considerably lower than in the case of a sharp interface ($a = 0$), even though the fluid volume fraction in the transition region assumes high values. Accordingly, the velocity gradients at $y = 0$ are more smooth than the other two cases examined, as is evidenced by the detail of the plots at the vicinity of the interface region, provided in Figure 3.2b.

3.5.2 Growth rate of an inviscid shear layer

The second test that we discuss in this section, is based on the problem of inviscid shear layers at the interface between a porous medium and a pure fluid. The flow is considered to be inviscid in the sense that the viscous fluxes of the momentum equation (2.3.10) are neglected. However, the interphasial drag, which arises from friction between the fluid

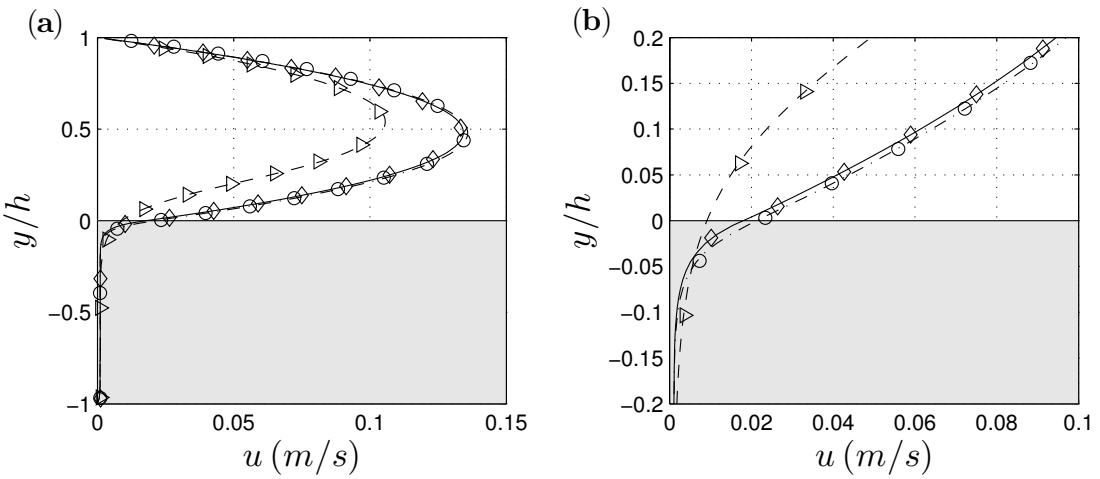

Figure 3.2: Comparison with the work of Le Bars & Worster (2006): Poiseuille flow profiles for three different sizes of the transition region between the porous medium and the pure-fluid. (a) Profiles throughout the computational domain. (b) Detail of the plots at the vicinity of the interface. The symbols correspond to the profiles in Le Bars & Worster (2006) and the lines to the results from our simulations. ($\diamond$ and — : $a = 0$; $\circ$ and -·- : $a = 1$; $\triangleright$ and - - - : $a = 10$).

and the solid matrix, is taken into account. According to our linear stability analysis that is presented in the next chapter, such flows are unconditionally unstable regardless of the porosity of the medium and for all perturbation wavelengths. In the following, we compare the growth rate of such layers as predicted by our simulations, with the analytical results of the linear stability analysis.

For the setup of the problem, we consider a porous medium of constant porosity $\phi < 1$, that occupies the lower half-plane, $y \leq 0$, of an unbounded domain. The upper half-plane, $y > 0$, is covered by a pure fluid ($\phi = 1$). The basic flow is assumed to be an unbounded shear layer consisting of a piecewise linear profile, and zero pressure gradient,

$$\boldsymbol{u}_0 = (u_0(y), 0), \quad \text{with} \quad u_0 = \begin{cases} 0, & y \leq 0\,, \\ U_0 \dfrac{y}{l}\,, & 0 < y \leq l\,, \\ U_0, & l < y\,, \end{cases} \tag{3.5.5}$$

and

$$p_0 \;=\; 0\,. \tag{3.5.6}$$

In the above expressions U_0 is constant and the constant pressure field, without loss of generality, is set equal to zero. Further, we consider small perturbations $\boldsymbol{u}_1 = (u_1,\, v_1)$ and p_1 of the basic flow so that

$$\boldsymbol{u} = \boldsymbol{u}_0 + \epsilon\, \boldsymbol{u}_1\,, \tag{3.5.7}$$

$$p = p_0 + \epsilon\, p_1\,, \tag{3.5.8}$$

with $\epsilon << 1$. In particular, $\boldsymbol{u}_1$ and p_1 are simple waves traveling along the x-direction:

$$u_1 \;= \frac{1}{\phi}\,\hat{u}\, e^{i\alpha(x-ct)}\,, \tag{3.5.9a}$$

$$v_1 \;= \frac{1}{\phi}\,\hat{v}\, e^{i\alpha(x-ct)}\,, \tag{3.5.9b}$$

$$p_1 \;= \hat{p}\, e^{i\alpha(x-ct)}\,, \tag{3.5.9c}$$

where the wavenumber α is a positive real number, and the phase velocity c is a complex number, $c = c_R + ic_I$. For further details regarding the setup of the inviscid shear layer, the reader is referred to Section 4.2 of the next chapter.

In the following, we provide the description of the simulation that we performed in order to calculate numerically the growth rate $c_I\alpha$ of an inviscid shear layer, for a fixed wavenumber α. For the non-dimensionalization of the problem, we employ the initial thickness l of the shear layer as the reference length, and the free-stream velocity in the pure-fluid domain U_0 as the reference velocity. Based on these values, the Reynolds number is set to $Re = 50$.

As regards the porous material, it is assumed to be an isotropic medium that consists of uniformly distributed spherical particles. Accordingly, the interphasial drag parameter $\underset{\sim}{\boldsymbol{\beta}}$ in equation (2.3.10) is given by the following expression:

$$\underset{\sim}{\beta}_{ij} \;= \begin{cases} (1-\phi)\,18/(Re\, d_p^2)\,, & i = j\,, \\ \\ 0\,, & i \neq j\,. \end{cases} \tag{3.5.10}$$

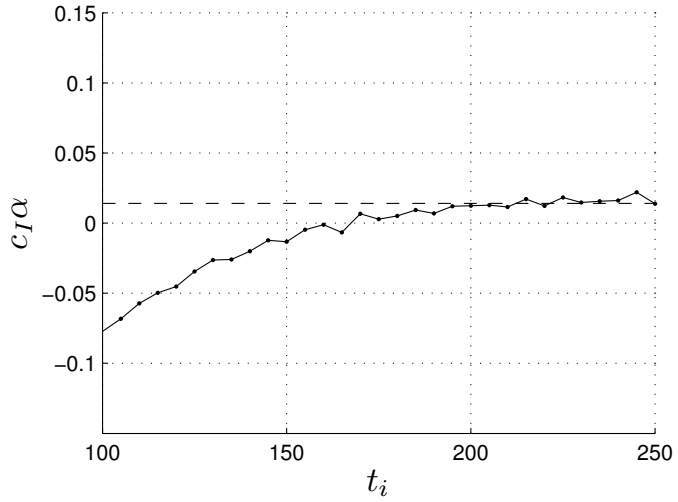

Figure 3.3: Non-dimensional growth rates of the disturbances, $c_I\alpha$, as a function of the number of iterations of the algorithm in time, t_i. The horizontal dashed line at $c_I\,\alpha = 0.01412$ indicates the analytic result that is calculated from the linear stability analysis.

A detailed description of the derivation of the above expression is provided in Appendix B. For the results presented below, the porosity of the material is set to $\phi = 0.9$, and the diameter of the sperical particles to $d_p = 1/10$.

The size of the computational domain is 5×5 non-dimensional units, and it is discretized over a uniform grid with a resolution of 50 cells per unit-length. The boundary conditions along the streamwise (x) direction are periodic, while outflow conditions are applied on both boundaries along the cross-stream (y) direction. The interface between the porous and the pure-fluid regions is placed 2 non-dimensional units above the bottom boundary.

The initial perturbation that we apply on the two components of the velocity and on the pressure field, consists of the real part of the expressions (3.5.9). The amplitude of the prescribed waves is constant throughout the domain, and in particular, $\hat{u} = \hat{v} = \hat{p} = 10^{-3}$. As regards the wavenumber, it is set to $\alpha = 1.257$, so that period of the perturbations equals the length of the domain. The simulation is executed for 300 iterations, and for a constant time-step $\Delta t = 0.01$.

The history of the growth rate as predicted by our simulation is shown in Figure 3.3. For the calculation of $c_I\,\alpha$ in this plot, we have taken the ratios of the perturbation

amplitudes in intervals of 5 steps. The horizontal line at $c_I\,\alpha = 0.01412$ indicates the analytic result that is calculated from the linear stability analysis, for the wavenumber α of the initial condition. As can be inferred from this plot, at early time steps the numerical predictions show decay of the instabilities instead of growth. This can be attributed to the initialization of the algorithm as is implemented in the computer code. In particular, according to equations (3.2.11) and (3.2.12), the velocity values at the time $^{(n-1)}$ are needed for the calculation of $\tilde{\boldsymbol{u}}$ at the predictor step. However these values are not available for the first iteration of the algorithm, and as such we set $\boldsymbol{u}^{(n-1)} = \boldsymbol{u}^{(n)}$. This choice is expected to have an impact on the performance of the algorithm during the first iterations. In later times this effect fades, and as is shown in Figure 3.3, after the step 200 the predicted growth rate fluctuates around the analytic solution.

At this point it should be stressed that the algorithm presented in this chapter is not designed for inviscid flows. Therefore, we cannot expect that simulations such as the one described above, confirm accurately analytic results relevant to such flows. Nevertheless this test shows that the predicted growth rates are in reasonable agreement with the ones that come from our linear stability analysis.

3.6 Conclusions

In this chapter we have provided a detailed description of the proposed numerical algorithm for the treatment of the governing equations (2.3.9) to (2.3.13). It is an extension to multi-phase flows of projection methods used for variable-density Navier-Stokes equations. This method uses two-step advancement in time for improved accuracy in time and stability. Namely, the field variables are first evaluated at the 'predictor' step and they are updated once again in the 'corrector' step before the completion of one cycle of the algorithm.

An important choise in our method, is the special treatment of the diffusive terms with second-order derivatives along the y direction, in the momentum equation of the fluid and the energy equations of both phases. These terms may become stiff due to the steep temperature and density gradients present in the flows of interest. For this reason they are integrated implicitly in time, via the Crank-Nicolson method. The rest of the

diffusive terms and the convective terms are integrated via the Adams-Bashforth method in the predictor step, while in the corrector step they are discretized with the trapezoidal rule.

As in all projection methods, the most crucial step in our algorithm, is the projection step. This involves taking the divergence of the momentum equation, and exploiting the kinematic constrain to obtain an expression for $\nabla \cdot (\rho\phi\boldsymbol{u})$. The resulting elliptic equation has the pressure as the only unknown and it can be challenging to solve due to the highly irregular terms on both the left- and the right-hand sides. In this work we use the stabilized bi-conjugate gradient method (Bi-CGSTAB) to obtain the solution. As is shown in the following chapters, this method is sufficiently stable to handle any irregularities that may arise.

Finally, a key point is that the spatial discretization is performed on a collocated grid system. This choice offers simplicity in the implementation of the method, as well as straightforward extension to curvilinear coordinate systems. Furthermore, a flux interpolation scheme is used, to prevent the odd-even decoupling of the pressure field which is known to occur in calculations of incompressible flows.

Chapter 4

Shear flows at porous medium - pure fluid interfaces

4.1 Introduction

In this chapter we are concerned with the dynamics of temporally evolving, open shear layers as well as the dynamics of forced flow at the interface of a highly porous medium and a pure fluid. First, we reduce the mathematical model presented in the previous chapter, to its constant-density derivative. The resulting set of equations is the *unsteady Darcy-Brinkman* model. Even though the general form of this model is well known, several variations of it can be found in the literature. As pointed out in Le Bars & Worster (2006), the essential difference between variants is the location of the porosity within each term.

Based on these equations, we perform a linear stability analysis of inviscid shear layers at the interfaces of interest, in unbounded domains. Further, we perform detailed numerical simulations of the flows of interest in both two and three dimensions and for various porosities. To the best of our knowledge, such numerical study has not appeared in the literature yet.

Our work focuses on highly porous materials because it is motivated by the problem of flow over small-scale vegetation canopies, such as grass or aquatic vegetation canopies;

Selected results from this chapter have been published in: Antoniadis P.D. & Papalexandris M.V. 2015 Dynamics of shear layers at the interface of a higly porous medium and a pure fluid. *Phys. Fluids* **27**, 014104.

such structures are typically represented as a permeable medium with high porosity. Initially it was proposed that this type of flow resembles a boundary layer and that the canopy essentially plays the role of a rough wall. However, in later studies, it has been argued that flow over vegetation canopies resembles a turbulent mixing layer and not a boundary layer, see Raupach *et al.* (1996), Ghisalberti & Nepf (2002; 2009), Finnigan *et al.* (2009), de Langre (2008), Belcher *et al.* (2012). Indeed, as it will be shown below, our simulations predict the development of an unstable shear layer that transitions to turbulence, thus corroborating the mixing-layer analogy.

This chapter is organized as follows. In Section 4.2 we perform the linear stability analysis of shear layers at porous medium - pure fluid interfaces in unbounded domains. In Section 4.3 we describe in detail the set-up for the numerical simulations. In Section 4.4 we present and discuss the results of two-dimensional simulations of semi-bounded shear layers in the domains of interest. Finally, in Section 4.5 we extend our study of semi-bounded shear layers based on the results of our three-dimensional simulation.

4.2 Linear stability analysis of shear layers over porous media in unbounded domains

The stability of flows over porous layers has received considerable attention and the relevant literature is quite rich. A wealth of results are available for flows in bounded domains such as Poisseuille flows over porous layers (see, for example, Goyeau *et al.* (2003), Chang *et al.* (2006), Hill & Straughan (2008), Liu *et al.* (2008)), flows of films on porous inclined planes (Pascal (1999; 2006), Sadiq & Usha (2008), Liu & Liu (2010)), convection through porous layers (Thiele *et al.* (2009), Hill & Straughan (2009), Sadiq *et al.* (2010), Hill & Carr (2010*a*)), Couette flows (Chang (2005), Kumar *et al.* (2013)), and others.

However, in this chapter we examine the stability of a different type of flow, namely, shear layers at the interface of a highly porous medium and a pure fluid, in unbounded domains. Our analysis aims at providing a first and straightforward step to gain insight on the roles of porosity and interphasial drag on the instability of this type of flow. Also, it allows for comparisons between the shear layers of interest and shear layers in pure

fluids.

First, we provide the governing equations for isothermal flows. In that case, both phasial temperatures T and $T_{\rm s}$, are constant and the equations (2.4.3) and (2.4.4) are trivially satisfied. Further, the density of the fluid ρ is constant and equal to the reference density. For the type of flows studied herein, the Richardson number is very small and therefore we neglect the contribution of the gravity term. Then, the governing equations eqs. (2.4.1) to (2.4.4) reduce to,

$$\nabla \cdot (\phi \boldsymbol{u}) \ = 0 \,, \tag{4.2.1a}$$

$$\phi \left(\frac{\partial \boldsymbol{u}}{\partial t} + \boldsymbol{u} \cdot \nabla \boldsymbol{u} \right) + \phi \nabla p \ = \frac{1}{Re} \nabla \cdot (\phi \boldsymbol{V}^v) - \underset{\sim}{\boldsymbol{\beta}} \boldsymbol{u} \,. \tag{4.2.1b}$$

In these expressions, we have dropped the superscipts of the original equations for reasons of clarity. As before, $\boldsymbol{u} = (u, v, w)$ and p stand for the velocity vector and the *kinematic* pressure of the fluid phase respectively. Also, Re stands for the Reynolds number of the problem with respect to the macroscopic length-scale of the problem. Further, $\underset{\sim}{\boldsymbol{\beta}}$ is the interphasial drag parameter. In the general case of an anisotropic granular material, $\underset{\sim}{\boldsymbol{\beta}}$ is a two-tensor, $\underset{\sim}{\boldsymbol{\beta}} = \{\underset{\sim}{\beta}_{ij}\}$. The values of its components depend on both the porosity $\phi(x)$ and the characteristics of the microstructure of the porous medium.

Equation (4.2.1b) is a variation of the well-known unsteady Darcy-Brinkman equation. For pure-fluid domains, i.e. when $\phi = 1$, all components of the drag-parameter tensor $\underset{\sim}{\boldsymbol{\beta}}$ go to zero so that the above system (4.2.1a)-(4.2.1b) reduces to the Navier-Stokes equations. It is also interesting to mention that this system can be applied for porous media of spatially varying porosity, since $\phi(\boldsymbol{x})$ is allowed to vary in space.

Herein we are concerned with inviscid flows in the sense that the viscous fluxes of the momentum equation (4.2.1b) are neglected. However, interphasial drag, which also arises from friction between the fluid particles and the solid matrix, is taken into account. This is equivalent to assuming that viscous effects are confined on the surface of the solid matrix, resulting to interphasial drag. The procedure we follow is standard; see, for example Drazin & Reid (1982). For this reason, only the main steps of the analysis are presented. Our results are based on a two-dimensional flow but their extension to three-dimensional flows is straightforward.

In order to fix ideas, let us consider an isotropic porous medium of constant porosity covering the lower half-plane $y \leq 0$ and a pure fluid covering the upper one $y > 0$. In other words, $\phi < 1$ for $y \leq 0$, whereas $\phi = 1$ for $y > 0$. Since the porous medium is isotropic, for the drag parameter we have that

$$\underset{\sim}{\beta}_{ij} \;=\; \begin{cases} (1-\phi)\beta\,, & i = j\,, \\ \\ 0\,, & i \neq j\,. \end{cases} \tag{4.2.2}$$

The basic flow is assumed to be an unbounded shear layer consisting of a piecewise linear velocity profile and zero pressure gradient,

$$\boldsymbol{u}_0 = (u_0(y), 0), \quad \text{with} \quad u_0 \;=\; \begin{cases} 0, & y \leq 0\,, \\ U_0 \dfrac{y}{l}\,, & 0 < y \leq l\,, \\ U_0, & l < y\,, \end{cases} \tag{4.2.3}$$

and

$$p_0 \;=\; 0\,. \tag{4.2.4}$$

In the above relations U_0 is constant and, without loss of generality, the constant pressure field is set equal to zero. It is straightforward to verify that the shear layer described by (4.2.3) – (4.2.4) satisfies the governing equations (4.2.1a) – (4.2.1b).

Next, we consider small perturbations $\boldsymbol{u}_1 = (u_1,\, v_1)$ and p_1 of the basic flow so that

$$\boldsymbol{u} = \boldsymbol{u}_0 + \epsilon\, \boldsymbol{u}_1\,, \tag{4.2.5}$$

$$p = p_0 + \epsilon\, p_1\,, \tag{4.2.6}$$

with $\epsilon << 1$. By introducing (4.2.3) – (4.2.6) to (4.2.1a) and (4.2.1b), and by omitting terms of order ϵ^2, we arrive at the following linear equations for $\boldsymbol{u}_1$ and p_1,

$$\frac{\partial \phi u_1}{\partial x} + \frac{\partial \phi v_1}{\partial y} \;= 0\,, \tag{4.2.7a}$$

$$\frac{\partial u_1}{\partial t} + u_0 \frac{\partial u_1}{\partial x} + \frac{\partial p_1}{\partial x} + v_1 \frac{\mathrm{d}u_0}{\mathrm{d}y} \;=\; -\,\beta\, \frac{1-\phi}{\phi} u_1\,, \tag{4.2.7b}$$

$$\frac{\partial v_1}{\partial t} + u_0 \frac{\partial v_1}{\partial x} + \frac{\partial p_1}{\partial y} \;=\; -\,\beta\, \frac{1-\phi}{\phi} v_1\,. \tag{4.2.7c}$$

Further, the drag parameter β is assumed to be constant, which is a valid assumption for small amplitude of the perturbation velocity, i.e., for $\epsilon << 1$. As such, the value of β is determined by ϕ and by the characteristics of the microstructure of the porous medium.

At this point, it is worth elaborating on our choice of the basic flow-profile (4.2.3) – (4.2.4). Since viscous effects outside the pore surfaces are assumed to be zero, a flow outside the porous medium can be maintained without pressure gradient in the x-direction. However, without pressure gradient, the velocity inside the porous medium will eventually vanish due to interphasial drag. In other words, a non-zero velocity inside the porous medium requires a pressure gradient in the x-direction. But in this case we would end up with a pressure jump across the material interface which, in turn, would cause acceleration of the fluid in the y direction. This means that the resulting basic flow-profile would not be a steady-state solution of the governing system. For this reason, the velocity of the basic flow-profile, u_0, inside the porous medium is set equal to zero.

One could then try to impose a constant velocity at the pure-fluid domain, which would imply a jump in u_0 across the interface. This corresponds to an unbounded vortex sheet located right on the interface. But the integrability condition for equations (4.2.7a) – (4.2.7c) is such that only trivial solutions for $\boldsymbol{u}_1$ are admissible for this case. In other words, the vortex sheet cannot coincide with the interface. Therefore, we are led to consider the shear layer of the form (4.2.3)-(4.2.4) as the simplest basic flow that is appropriate for stability analysis.

Next, we assume that the perturbation velocity $\boldsymbol{u}_1$ and pressure p_1 consist of simple waves travelling along the x-direction. In other words, we seek solutions of the form,

$$u_1 = \frac{1}{\phi}\,\hat{u}(y)\,e^{i\alpha(x-ct)}\,, \tag{4.2.8a}$$

$$v_1 = \frac{1}{\phi}\,\hat{v}(y)\,e^{i\alpha(x-ct)}\,, \tag{4.2.8b}$$

$$p_1 = \hat{p}(y)\,e^{i\alpha(x-ct)}\,, \tag{4.2.8c}$$

with the wavenumber α being a positive real number and the phase velocity c being a complex number, $c = c_R + ic_I$.

With the above ansatz, equations (4.2.7a) – (4.2.7c) reduce to the following system

of ordinary differential equations,

$$i\alpha\hat{u} + \frac{\mathrm{d}\hat{v}}{\mathrm{d}y} = 0\,, \tag{4.2.9a}$$

$$i\alpha(u_0 - c)\hat{u} + \hat{v}\frac{\mathrm{d}u_0}{\mathrm{d}y} + i\alpha\hat{p} = -\beta\frac{1-\phi}{\phi}\hat{u}\,, \tag{4.2.9b}$$

$$i\alpha(u_0 - c)\hat{v} + \frac{\mathrm{d}\hat{p}}{\mathrm{d}y} = -\beta\frac{1-\phi}{\phi}\hat{v}\,. \tag{4.2.9c}$$

Upon substitution of (4.2.9a) to (4.2.9b) and (4.2.9c), we finally arrive at

$$\left(-(u_0 - c) + i\frac{\beta}{\alpha}\frac{1-\phi}{\phi}\right)\frac{\mathrm{d}\hat{v}}{\mathrm{d}y} + \hat{v}\frac{\mathrm{d}u_0}{\mathrm{d}y} + i\alpha\hat{p} = 0\,, \tag{4.2.10a}$$

$$\left(-(u_0 - c) + i\frac{\beta}{\alpha}\frac{1-\phi}{\phi}\right)\hat{v} + i\frac{1}{\alpha}\frac{\mathrm{d}\hat{p}}{\mathrm{d}y} = 0\,. \tag{4.2.10b}$$

By requiring boundedness of the solution at $\pm\infty$, integration of the above system yields,

$$\hat{u} = \begin{cases} \alpha\, e^{\alpha y}\,, & y \le 0\,, \\ \alpha\left(C_1 e^{\alpha y} - C_2 e^{-\alpha y}\right)\,, & 0 < y \le l\,, \\ -\alpha\, C_3\, e^{-\alpha y}\,, & y > l\,, \end{cases} \tag{4.2.11}$$

$$\hat{v} = \begin{cases} -i\,\alpha\, e^{\alpha y}\,, & y \le 0\,, \\ -i\alpha\left(C_1 e^{\alpha y} + C_2 e^{-\alpha y}\right)\,, & 0 < y \le l\,, \\ -i\alpha\, C_3\, e^{-\alpha y}\,, & y > l\,, \end{cases} \tag{4.2.12}$$

and

$$\hat{p} = \begin{cases} \left(\alpha c + i\beta\dfrac{1-\phi}{\phi}\right)\dfrac{1}{\phi}\, e^{\alpha y}\,, & y \le 0\,, \\ C_1\left(\dfrac{U_0}{l} + \left(c - \dfrac{U_0}{l}y\right)\alpha\right)e^{\alpha y} + C_2\left(\dfrac{U_0}{l} - \left(c - \dfrac{U_0}{l}y\right)\alpha\right)e^{-\alpha y}\,, & 0 < y \le l\,, \\ \alpha(U_0 - c)\, C_3\, e^{-\alpha y}\,, & y > l\,. \end{cases} \tag{4.2.13}$$

The three integration constants C_1, C_2, and C_3 and the eigenvalue relation $c = c(\alpha)$ are determined via appropriate jump conditions at the material interface $y = 0$ and via matching conditions at $y = l$. More specifically, the jump conditions are derived by integrating (4.2.10a) and (4.2.10b) from $y = -\epsilon'$ to $y = \epsilon'$ and then taking the limit as $\epsilon' \to 0$. We observe that, due to the discontinuity of ϕ at $y = 0$, the integral of (4.2.10a) exists only if $\hat{v}$ is continuous at $y = 0$. Then, by performing the integration and taking the limit as $\epsilon' \to 0$, equations (4.2.10a) and (4.2.10b) yield

$$\hat{p}|_{y=0^-} = \hat{p}|_{y=0^+}\,, \quad \text{with} \quad \hat{v}|_{y=0^-} = \hat{v}|_{y=0^+}\,, \tag{4.2.14}$$

respectively. The second condition is just a re-statement of the conservation of fluid mass across the interface: $(\phi\, v_1)_{y=0^-} = (\phi\, v_1)_{y=0^+}$. The matching conditions at $y = l$ can be derived by the same procedure, which yields

$$\hat{p}|_{y=l^-} = \hat{p}|_{y=l^+}\,, \quad \text{and} \quad \hat{v}|_{y=l^-} = \hat{v}|_{y=l^+}\,. \tag{4.2.15}$$

Upon introduction of (4.2.14) and (4.2.15) to the solutions (4.2.12) and (4.2.13), and after some algebraic manipulations, we finally arrive at the following eigenvalue relation,

$$(4 + 2A)\, c^2\alpha^2 + (A\Gamma - 4\alpha U_0 - i2B)\, c\alpha - \Gamma\frac{U_0}{l} - iB\Gamma \;=\; 0\,, \tag{4.2.16}$$

with

$$A \;\triangleq\; \frac{1-\phi}{\phi}\,, \quad B \;\triangleq\; \beta\frac{1-\phi}{\phi^2}\,, \quad \Gamma \;\triangleq\; \frac{U_0}{l}\left(1 - 2\alpha l - e^{-2\alpha l}\right)\,. \tag{4.2.17}$$

Relation (4.2.16) can be solved to determine $c(\alpha)$. In particular, the condition for neutral stability, $c_I = 0$, reads

$$1 - 2\alpha l - e^{-2\alpha l} \;=\; 0\,, \tag{4.2.18}$$

which does not admit any real positive roots α for any value of l. Further, from (4.2.17) it can be shown that, for any choice of wavenumber $\alpha > 0$, porosity $0 < \phi < 1$ and drag coefficient β, the eigenvalue relation (4.2.16) admits at least one solution $c(\alpha)$ with positive imaginary part.

This means that a shear layer over an isotropic porous medium in an unbounded domain is *unconditionally unstable*, regardless of the medium's porosity and regardless

of the characteristics of its microstructure which the drag parameter β depends upon. By contrast, in the absence of a porous medium, a shear layer between two streams of an inviscid fluid is unstable only for wavenumbers below a limit value α_s, i.e. for $0 < \alpha < \alpha_s$. Clearly, the unconditional instability of shear layers in porous media is due to the interphasial drag, which enters the expression for the coefficient B in (4.2.17). In other words, the interphasial drag has a *destabilizing* effect to the flows of interest, despite being a dissipative, entropy-producing mechanism.

We further remark that, even though a shear layer over a porous medium is unconditionally unstable, the growth rate and the phase velocity of the disturbances depend on both ϕ and β, as relations (4.2.16) – (4.2.17) imply. This can be illustrated with the following example. We consider an isotropic porous medium whose structure is given by an ensemble of uniformly distributed identical spherical particles, and a shear layer of the form (4.2.3) – (4.2.4). The non-dimensionalization of the variables is performed by employing the free-stream velocity above the vortex layer as the reference velocity, and the initial thickness of the shear layer as the reference length-scale. In other words, we set $U_0 = 1$ and $l = 1$. Further, the diameter of the spherical particles is assumed to be one tenth unit lengths, *i.e.* $d_p = 1/10$.

This particular porous microstructure (uniformly distributed spheres) has been chosen because it yields simple expressions for the drag parameter β so that the eigenvalue relation (4.2.16) can be solved directly to calculate the instability growth rates. In other words, our choice of porous microstructure has been made for purposes of convenience and simplicity in the computations. However, we emphasize again that the eigenvalue relation (4.2.16) is valid for any microstructure of an isotropic porous medium.

Indeed, the number density N_s of the spherical particles is related to the volume fraction of the fluid via $N_s = 6(1-\phi)/(\pi d_p^3)$. By combining this relation with Stoke's law of drag for a sphere and (4.2.2), we readily arrive in the following expression for the drag parameter β,

$$\beta \;=\; \frac{18}{Re_0 d_p^2}\,. \tag{4.2.19}$$

A detailed description of the derivation of this expression, as well as its non - dimensionalization can be found in Appendix B. In the above expression, Re_0 is based on the

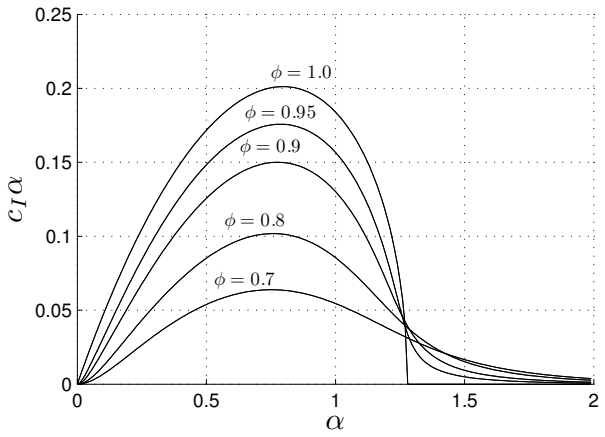

Figure 4.1: Non-dimensional growth rates of the disturbances, $c_I\alpha$, as a function of the (non-dimensional) wavenumber α, for various porosities. The growth rates are positive for all $0 < \phi < 1$. In other words, inviscid shear layers over a porous media are unconditionally unstable. In this example, $Re_0 = 1000$ and $d_p = 1/10$.

reference length and velocity, as well as on the fluid viscocity ν. Re_0 should not be confused with the particle Reynolds number, which by virtue of (4.2.3) and (4.2.5) is defined as $Re_p = \epsilon|\boldsymbol{u}_1|d_p\, Re_0$. In particular, the value of ϵ can be adjusted so that Re_p is always sufficiently small for Stoke's law of drag to hold, regardless of the value of Re_0.

In Figure 4.1 we present plots of the non-dimensional growth rates of the disturbances, $c_I\alpha$, as a function of the (non-dimensional) wavenumber α for various values of ϕ. The growth $c_I\alpha$ is made non-dimensional with respect to the ratio of the reference length divided by the reference velocity. Further, the wavenumber is made non-dimensional with respect to the inverse of the reference length. As mentioned above, the reference length is the initial thickness of the shear layer, and the reference velocity is the initial free-stream velocity above the vortex layer. For this example we have taken $Re_0 = 1000$ and $d_p = 1/10$. It can be verified that in the absence of porous medium, in which case $\phi = 1$ everywhere, we recover the result reported in Drazin & Reid (1982) for an unbounded shear layer of a pure fluid. In particular, in this case, the shear layer is unstable for $0 < \alpha < \alpha_s$, with $\alpha_s \simeq 1.28$, and neutrally stable for $\alpha > \alpha_s$. On the other hand, for $0 < \phi < 1$, the shear layer is unconditionally unstable.

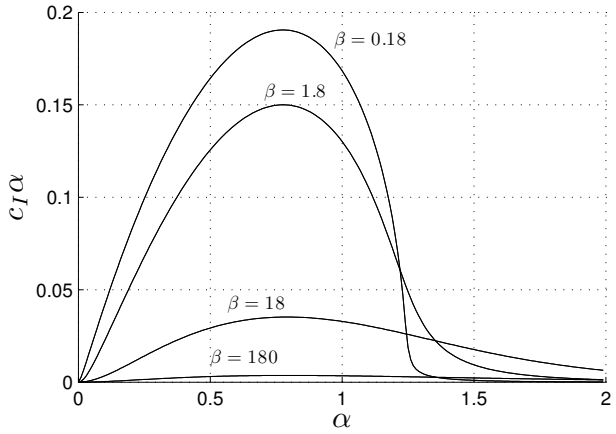

Figure 4.2: Non-dimensional growth rates of the disturbances $c_I\alpha$ as a function of the (non-dimensional) wavenumber α, for various values of the drag parameter β. In this example, $\phi = 0.9$ and $d_p = 1/10$.

In the same figure we also observe that the maximum growth rate increases monotonically with the porosity ϕ. Moreover, the wavenumber corresponding to the maximum growth rate increases only slightly with ϕ. For example, for $\phi = 0.7$ the maximum growth rate is attained at $\alpha \simeq 0.76$, whereas for $\phi = 1.0$ it is attained at $\alpha \simeq 0.80$. Beyond this maximum value, the growth rate drops monotonically with α and converges asymptotically to zero as $\alpha \to \infty$. As a matter of fact, the higher ϕ is, the faster $c_I\alpha$ drops.

Finally, in Figure 4.2 we present results for the growth rates of the disturbances at different Re_0. In this example, the porosity of the medium is $\phi = 0.9$ and the characteristic length of the porous microstructure is $d_p = 1/10$. We observe that the maximum growth rate increases with Re_0. Also, the wavenumber that maximizes the growth rate is approximately the same for all Re_0.

Further, since the drag parameter β is inversely proportional to Re_0, according to (4.2.19), the growth rates converge rapidly to those when Re_0 goes to infinity. In this example, the growth-rate profiles differ very little for $\beta < 0.18$. By virtue of (4.2.19), we can see that the limit $Re_0 \to \infty$ is equivalent to $\beta \to 0$. However, attention should be paid to the fact that this limit, $Re_0 \to \infty$, does not correspond to the case of a shear layer of a pure fluid ($\phi = 1$ everywhere), even though the right-hand sides of (4.2.7b) and

(4.2.7c) vanish in both occasions. The reason for this difference is the presence of ϕ in the continuity equation (4.2.7a).

4.3 Computational set up

In this section we present the configuration of the computational domain and provide the values of the various physical and computational parameters that are employed in the simulations.

The porous medium is assumed to occupy the bottom part of the computational domain $-h \leq y \leq 0$, i.e., it starts at the bottom boundary and its height equals h. Also, it spans over the entire computational domain in both streamwise and spanwise directions. As regards its microstructure, we consider a *generic*, highly porous orthotropic medium whose drag parametrization with respect to porosity is inspired by that of a dilute conglomerate of identical and uniformly distributed cylinders. Further, it is assumed that the cylinders are parallel to each other and aligned vertically to the bottom boundary of the domain.

The interphasial drag parameters in the horizontal (streamwise and spanwise) directions, $\underset{\sim}{\beta}_{11}$ and $\underset{\sim}{\beta}_{33}$ respectively, can be approximated as follows. We consider the expression for the drag per unit length induced by a 2D flow around a cylinder and we multiply it by the height of the cylinder, h, and the number density of cylinders $N_s = 4(1-\phi)/(\pi d_p^2 h)$. This results in the following expressions for $\underset{\sim}{\beta}_{11}$ and $\underset{\sim}{\beta}_{33}$ in non-dimensional form,

$$\underset{\sim}{\beta}_{11} \;=\; \underset{\sim}{\beta}_{33} \;=\; \frac{2}{\pi}\, C_D\, \rho\, \frac{(1-\phi)}{d_p}\, \sqrt{u^2+w^2}\,. \tag{4.3.1}$$

Relations for the drag coefficient for a cylinder, C_D, can be found in standard textbooks.

Given that the porous medium is orthotropic, the value for the interphasial drag parameter in the cross-stream direction, $\underset{\sim}{\beta}_{22}$, is generally different from the value of $\underset{\sim}{\beta}_{11}$. To derive an expression for $\underset{\sim}{\beta}_{22}$, we consider the skin-friction drag for flow over a flat plate over a distance h and we multiply it by the perimeter of the cylinder and the number density of cylinders. The final expression, in non-dimensional form, reads

$$\underset{\sim}{\beta}_{22} \;=\; \frac{2.656}{\sqrt{Re}}\, \frac{(1-\phi)}{d_p} \sqrt{\frac{\mu\rho|v|}{h}}\,. \tag{4.3.2}$$

In the above relation, the Reynolds number Re is calculated with respect to the macroscopic reference length and fluid velocity. Finally, due to the orthotropicity of the porous layer, the off-diagonal elements of $\underset{\sim}{\boldsymbol{\beta}}$ are equal to zero. Also, we have to point out that all variables appearing in (4.3.1) and (4.3.2) have been non-dimensionalized with respect to the reference values. Therefore in constant-density flows, as is the case for the problems examined in this chapter, $\rho = 1$ and $\mu = 1$.

It should be acknowledged that the above drag parametrization is only an approximation of the drag experienced by an ensemble of cylinders. In particular, even though the Reynolds number with respect to the cylinder's diameter is quite low (below 40 for the simulations presented herein), the length of the wake of an individual cylinder can still be large enough, Sen *et al.* (2009), so as to have a shadow effect between adjacent cylinders. Despite this limitation, the above drag parametrization is deemed adequate for the purposes of our study because herein we are concerned with a generic orthotropic porous medium.

As regards boundary conditions, the flow is assumed to be periodic in the streamwise and spanwise directions. In the cross-stream direction, the no-slip condition is prescribed at the bottom boundary whereas the free-slip condition is prescribed at the top boundary. Initial conditions for the simulations are generated via a preliminary simulation of forced (pressure-driven) flow. This preliminary simulation starts from a fluid at rest that is accelerated by a constant pressure gradient. The fluid velocity above the material interface increases due to the applied pressure gradient, whereas inside the porous medium it reaches a steady state due to interphasial drag. Let U_1 denote the free-stream velocity above the interface and U_2 denote the free-stream velocity inside the porous medium. In other words, U_2 is defined as the velocity at the points lying outside the bottom boundary layer and the shear layer at the interface. The preliminary simulation is terminated when a prescribed difference $\Delta U = U_1 - U_2$ has been attained. Such a velocity profile is shown in Figure 4.3. In this figure we can observe a thin boundary layer next to the bottom wall and a thin shear layer across the interface of the porous medium and the pure-fluid domain. The transition region between the porous layer and the pure-fluid is shown in detail in Figure 4.4. As expected, the spread of the shear layer is not symmetric

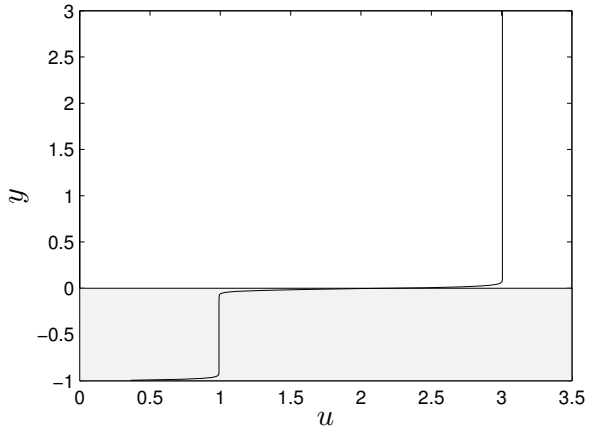

Figure 4.3: Initial profile of the streamwise velocity component, computed by a preliminary pressure-driven simulation. The velocity inside the porous medium has reached steady state.

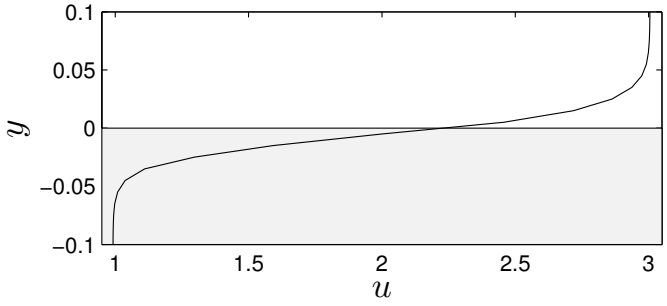

Figure 4.4: Detail of the initial profile of the streamwise velocity component, at the vicinity of the interface.

with respect to the interface due to the interphasial drag inside the porous layer. In particular, the streamwise velocity gradients are steeper inside the porous layer than they are in the pure-fluid domain. However, it should be stressed that this velocity profile is not a stready-state profile for the preliminary run of forced flow. As was also mentioned above, the velocity in the pure-fluid domain continues to increase, due to the applied pressure gradient, and in fact, this shear layer eventually becomes unstable (further discussion about the forced shear layer in semi-bounded domains goes out of the scope of the present work). The velocity profile shown in Figures 4.3 and 4.4, corresponds to an early time of the preliminary simulation, when ΔU has reached an appropriate value to be used as initial condition for our simulation of unforced temporally-evolving shear layers at porous medium - pure fluid interfaces.

At this point it should also be emphasized that in the absense of forcing in our "principal" simulation, the free-stream velocity inside the porous medium U_2 drops fast to zero at the early stages of flow evolution. This leaves only one velocity scale in the flow, well before the development of the instabilities, and as such, allows us to observe the self-similar characteristics that are discussed in the following sections.

The physical problem that we consider herein is the flow of air at a speed of $0.11m/s$, through a layer of grass that is $0.16m$ high. For non-dimensionalization purposes, the height of the porous layer is used as the reference length of the problem, whereas the initial free-stream velocity inside the porous medium is used as the reference velocity. In other words we set $h = 1$ and $U_2(t = 0) = 1$. Based on these values, the Reynolds number in our simulations is set to $Re = 1110$. Unless otherwise noticed, the porosity of the medium is $\phi = 0.9$ and the characteristic length of the porous microstructure is $d_p = 0.032$.

In the discussion of the numerical results, we make use of the following notation. The brackets $\langle\, .\,\rangle$ denote plane averaging, i.e. averaging on the $x - z$ plane. The velocity components u, v, w are decomposed into their mean (plane-averaged) values and their fluctuations, i.e. $(u, v, w) = (U + u', V + v', W + w')$, where $U = \langle u\rangle$, $V = \langle v\rangle$, $W = \langle w\rangle$ and the prime superscript denotes the fluctuating components. Accordingly, the kinetic energy of the fluctuations is given by

$$\mathcal{K} \;=\; \frac{1}{2}\,\phi\,(\,\langle u'u'\rangle + \langle v'v'\rangle + \langle w'w'\rangle\,)\,, \tag{4.3.3}$$

and the Reynolds stresses are defined as follows.

$$\mathbf{R} = \{R_{ij}\} = \phi \begin{bmatrix} \langle u'u' \rangle & \langle u'v' \rangle & \langle u'w' \rangle \\ \langle u'v' \rangle & \langle v'v' \rangle & \langle v'w' \rangle \\ \langle u'w' \rangle & \langle v'w' \rangle & \langle w'w' \rangle \end{bmatrix} . \tag{4.3.4}$$

Finally, the momentum thickness of the shear layer is given by the following expression,

$$\delta_m \;=\; \frac{1}{(U_1 - U_2)^2} \int_F^T \phi(U - U_2)\,(U_1 - U)\,\mathrm{d}y\,. \tag{4.3.5}$$

The upper limit in the above integration is the coordinate of the top boundary of the computational domain. The lower limit is taken at a point on the free-stream region inside the porous medium. Its cross-stream coordinate is denoted by F, $-1 < F < 0$. Accordingly, the streamwise velocity component at this point equals to U_2. It should be pointed out that U_2 in expression (4.3.5) is not constant. Instead, it is updated to its respective value at the time for which δ_m is calculated. Nonetheless it should be mentioned that, as will be shown next, in the problems examined herein, U_2 drops to zero quite fast and during the early stages of growth of the hydrodynamic instabilities. Further, we decompose the momentum thickness δ_m in two parts, δ_m^- and δ_m^+, that represent the extent of the shear layer inside the porous medium and in the pure-fluid domain, respectively. In other words, $\delta_m = \delta_m^- + \delta_m^+ \triangleq \int_F^0 + \int_0^T$.

4.4 Numerical simulations of two-dimensional shear layers

In this section we present results from simulations of two-dimensional shear layers at the interface of a highly porous medium and a pure fluid. As mentioned above, we examine the case of temporally evolving shear layers. Emphasis is placed on the structures that emerge during the growth of the layer and on the interaction of these structures with the porous medium. This study is motivated by the fact that important features of two-dimensional layers are also encountered in their three-dimensional counterparts.

At this point it should be mentioned that, exceptionnally for the case of 2D simulations presented in this section and in view of the available computational resources for

the problem in hand, we opted for an explicit integration of all diffusive terms. In particular, these terms are integrated via the Adams-Bashforth method for the predictor step and the trapezoidal rule for the corrector step. However, as mentioned in the previous chapter, the "standard" implementation of the algorithm employs implicit integration of the diffusive terms in the cross-stream direction; this standard implementation has been used subsequently for all the other simulations of the thesis.

We consider a computational domain with dimensions 10×4. In other words, the height of the porous medium is one unit-length, whereas the height of the pure-fluid domain is three unit-lengths. The spacial discretization is performed on a uniform grid with a resolution of 100 cells per unit-length. Also, the time-step Δt is chosen so that both of the following expressions apply:

$$\frac{|u|_{max}\,\Delta t}{\Delta x^2} \leq 4 \quad \text{and} \quad \frac{|v|_{max}\,\Delta t}{\Delta y^2} \leq 4\,, \tag{4.4.1}$$

where $|u|_{max}$ and $|v|_{max}$ are the maximum absolute values of the streamwise and cross-stream components of the velocity throughout the domain. The above restriction arises from the viscous terms of the governing equations. These terms may become stiff due to the flow structures that develop in the course of the simulations, combined with the steep gradients of the volume fraction at the vicinity of the interface. The initial profile is shown in Figure 4.3 and $\Delta U|_{t=0} = 2$. No perturbation is added to these initial profiles. Instead, we let the round-off errors produce the perturbations on the initial flow profiles.

The growth history of the momentum thickness δ_m of the shear layer is shown in Figure 4.5. Based on this plot, the evolution of the layer can be divided in three phases. The first one is characterized by the onset and growth of the Kelvin-Helmholtz instability and terminates at, approximately, $t \simeq 10.5$. The second phase is characterized by vortex formation and pairing, Figure 4.6, that lead to rapid growth of δ_m. This phase terminates at, approximately, $t \simeq 19.0$. The third phase is characterized by moderate, linear growth of δ_m and further increase of the size of the rollers, until it becomes comparable to the height of the pure-fluid domain. The simulation is terminated at $t = 25.0$, well before the shear layer interacts with the top boundary of the domain, so that our confidence in the statistics of the flow is not compromised.

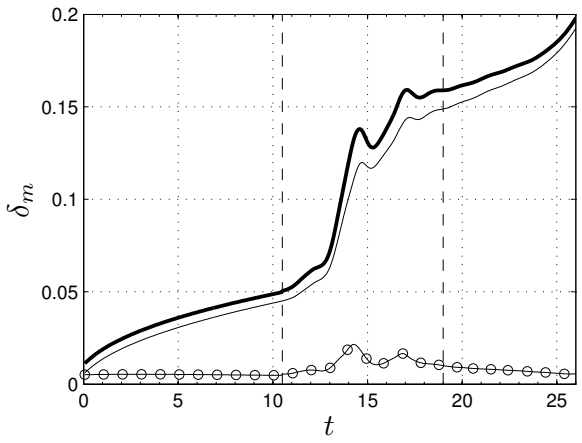

Figure 4.5: Growth history of the momentum thickness δ_m of a two-dimensional shear layer at the interface of a porous medium and pure fluid. The porosity is set at $\phi = 0.9$. The properties of the porous medium are given in Subsection 4.3. (— : δ_m ; — : δ_m^+ ; ∘: δ_m^- ; - - - : the vertical dashed lines indicate the approximate time of termination of one phase and the beginning of the next one).

During the **first phase**, the velocity of the fluid inside the porous strip drops monotonically with time due to interphasial drag. We note that as early as $t = 0.98$, the free-stream velocity U_2 is reduced to less than 14% of its initial value. This corresponds to a Reynolds number with respect to d_p of approximately 5. At $t = 2.5$, U_2 is reduced to less than 3% of its initial value. After this time, U_2 continues to drop until it becomes zero, albeit at a slower rate. Further, the thickness of the shear layer grows and the vorticity distribution spreads out. In particular, during this phase of evolution, the flow is diffusion dominated. For this reason δ_m^+, which measures the momentum thickness of the shear layer in the pure-fluid domain, grows as a function of $\sqrt{t}$. On the other hand, δ_m^-, remains constant during this phase. Therefore, the overall growth of δ_m during this phase also scales with $\sqrt{t}$.

Also, the shear layer grows in a self-similar manner during this phase. This can be confirmed by the collapse of the instantaneous, streamwise-averaged velocity profiles U under self-similar scaling, shown in Figure 4.7. In particular, U is scaled by the instantaneous free-stream velocity difference $\Delta U = U_1 - U_2$ whereas the cross-stream

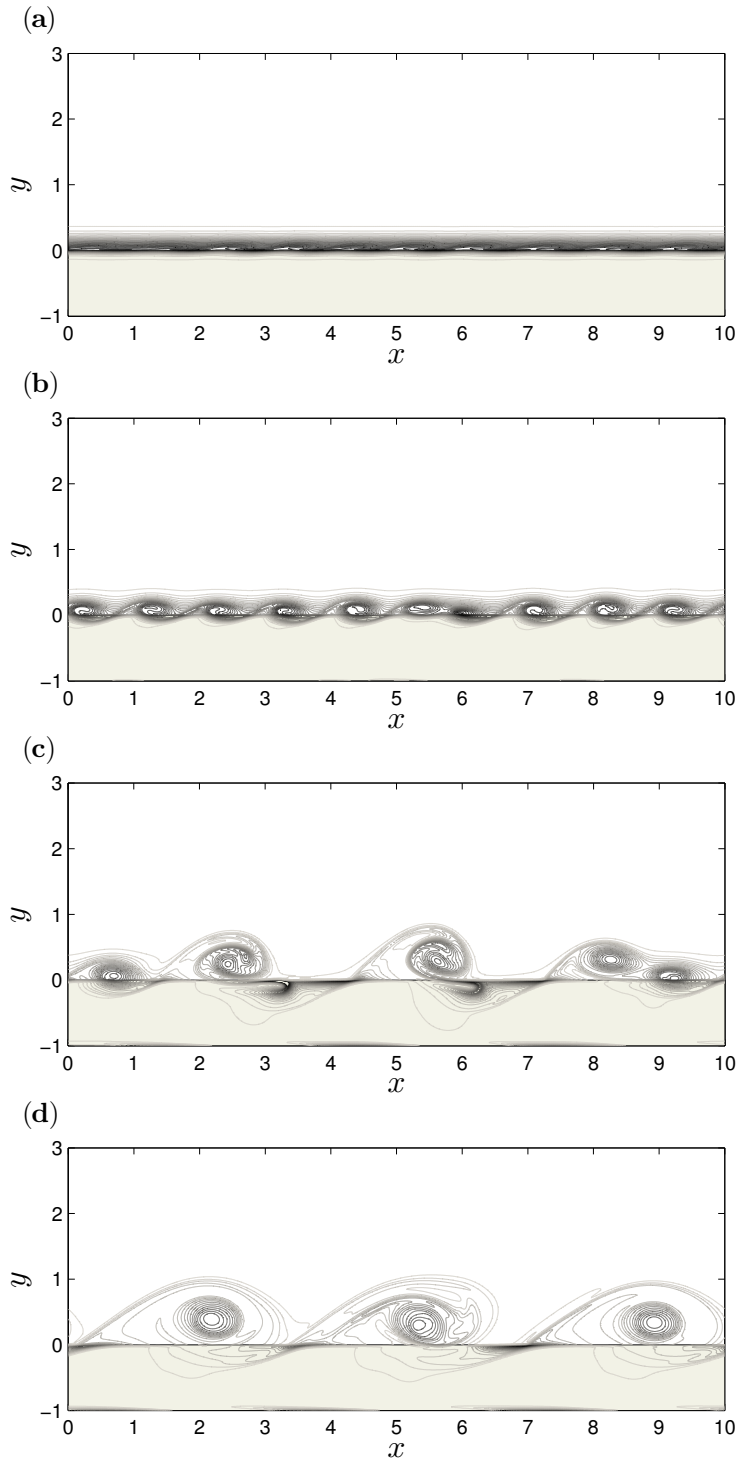

Figure 4.6: Vorticity field at selected instances during the growth of the shear layer. (a) $t = 10.11$; (b) $t = 11.50$; (c) $t = 14.0$; (d) $t = 18.05$. The shaded area indicates the location of the porous medium.

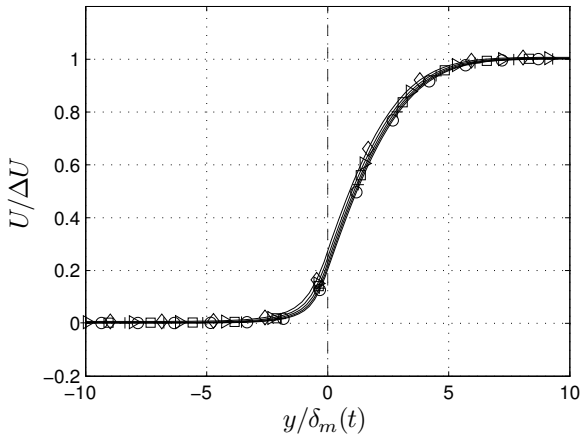

Figure 4.7: Mean streamwise velocity profiles at early times. The collapse of the profiles suggests self-similar growth of the shear layer in the first phase of its evolution. $\diamond$: $t = 4.06$; $\triangleright$: $t = 5.26$; $\square$: $t = 6.52$; $+$: $t = 7.79$; $\circ$: $t = 9.05$. The interface location is at $y/\delta_m = 0$ and is denoted by the dashed line.

coordinate y is scaled by δ_m. As is well known, a more sensitive indicator for self-similarity in shear flows is the collapse of the profiles of Reynolds stresses, Rogers & Moser (1994). Nonetheless, during this phase of evolution, the Reynolds stresses remain very close to zero.

At, approximately, $t = 10.5$, the Kelvin-Helmholtz instabilities have grown enough to lead to the formation of spanwise vortex structures (rollers). This marks the beginning of the **second phase** of evolution of the shear layer. As shown Figures 4.6 and 4.8, the rollers cross the interface and extend into the porous medium, thus producing significant fluid recirculation in it. However, due to reduced fluid volume ($\phi < 1$) and interphasial drag inside the porous medium, most of the area of the rollers lies above the interface. In other words, the rollers tend to shift towards the pure-fluid domain. By contrast, in the case of plane mixing layers the rollers do not shift towards any stream, i.e. those layers are symmetric, Pope (2000).

Another point of interest is that the forward arm of a roller is misaligned with respect to the backward arm of the roller ahead. The misaligned arms start to interact with each other in the braid regions, i.e., the regions between two successive rollers. This leads to

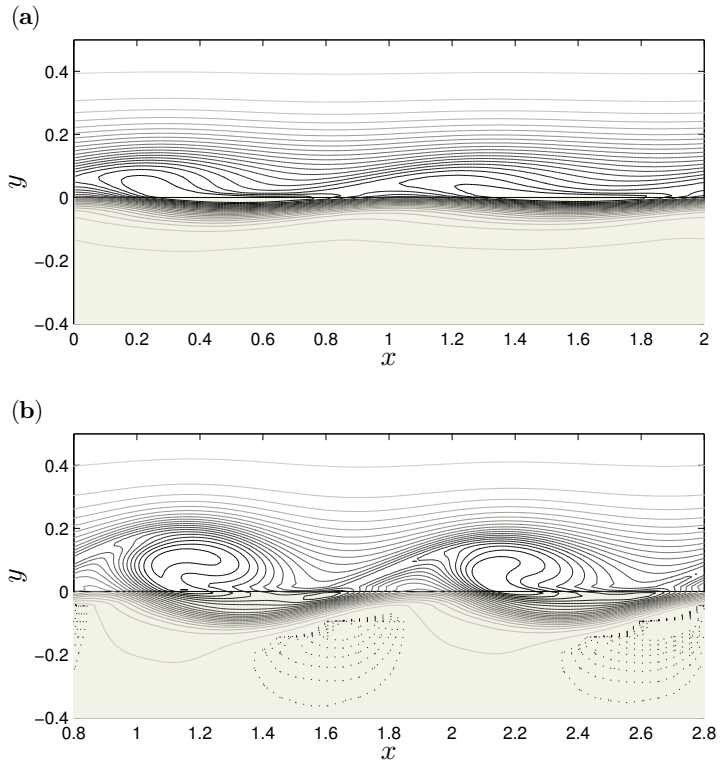

Figure 4.8: Vorticity plots at (a) $t = 10.78$ and (b) $t = 11.44$. A vortical structure is formed in the braid region, right below the interface, due to misalignment of the arms of the upstream and downstream rollers. Also, a secondary structure of positive vorticity is formed inside the porous medium. The solid contours show negative vorticity at increments of 0.8 units, while the dotted contours show positive vorticity at increments of 0.05 units.

the formation of an additional structure of negative vorticity located in the braid region and right below the interface, as shown in Figure 4.8b. Also, at these locations, fluid that follows the motion of one roller decelerates as it enters the porous medium, and subsequently gets entrained in the downstream roller. This creates a counter-clockwise rotation of the velocity field locally, namely a secondary structure of weak positive vorticity, below the rollers' arms inside the porous medium. Its vorticity amplitude is at the order of 5 to 10 % of the vorticity amplitude of the upstream roller. Such structures have not been reported in temporally-evolving plane mixing layers.

Soon after their formation, the rollers begin to pair. The first vortex pairing is

completed at, approximately, $t \simeq 12$. This event is marked by the first bump in the momentum-thickness plot in Figure 4.5. From this point on, the shear layer grows due to both fluid entrainment through the braid regions and vortex pairing. When two rollers merge, the upstream roller first absorbs the afore-mentioned negative vorticity structure of the braid region just ahead. Subsequently, it climbs on top of the roller ahead and pushes it towards the porous medium; see Figure 4.9a. Next, the two rollers spiral towards each other until they form a single larger roller, as depicted in Figure 4.9b. During a pairing, the vortical structures in the surviving braid regions are somewhat attenuated but do not vanish. By contrast, in plane mixing layers, the surviving braid regions are deprived of vorticity; see Moser & Rogers (1993). Once the pairing is completed, the new roller transfers vorticity in the surviving braid region ahead of it via its arms, thus strengthening the pre-existing negative-vorticity structure located right below the interface. This redistribution of vorticity in the braid region takes about 0.5 time units.

During this second phase of growth, which is characterized by vortex formation and pairings, the shear layer is no longer self-similar. More specifically, the mean velocity profiles U still collapse but the Reynolds-stress profiles do not; see Figure 4.10. Actually, it can be inferred from this figure that the (scaled) Reynolds stresses increase substantially. This is a typical feature of shear layers during the initial vortex pairing. The kinetic energy of fluctuations also increases substantially during this period, as shown in Figure 4.11.

From Figures 4.10 and 4.11 it can be inferred that, as expected, the profiles of R_{ij} and $\mathcal{K}$ are all asymmetrical and skewed towards the pure-fluid domain. This is attributed to the interphasial drag inside the porous medium that acts as a momentum sink and tends to damp velocity fluctuations. Further, we observe that R_{11} and $-R_{12}$ drop significantly across the interface, but R_{22} does not. This can be explained by the fact that the gradient of u' across the interface is much steeper than that of v' due to the different values of the interphasial parameters parameters in the x and y directions. This difference in the gradients of the velocity fluctuations across the interface is also responsible for the change of the phase difference between u' and v'. This, in turn, results in a sign change of R_{12} inside the porous medium, as depicted in Figure 4.10. Finally, in this figure, we observe that all Reynolds-stress components decay rapidly to zero away from the interface. This

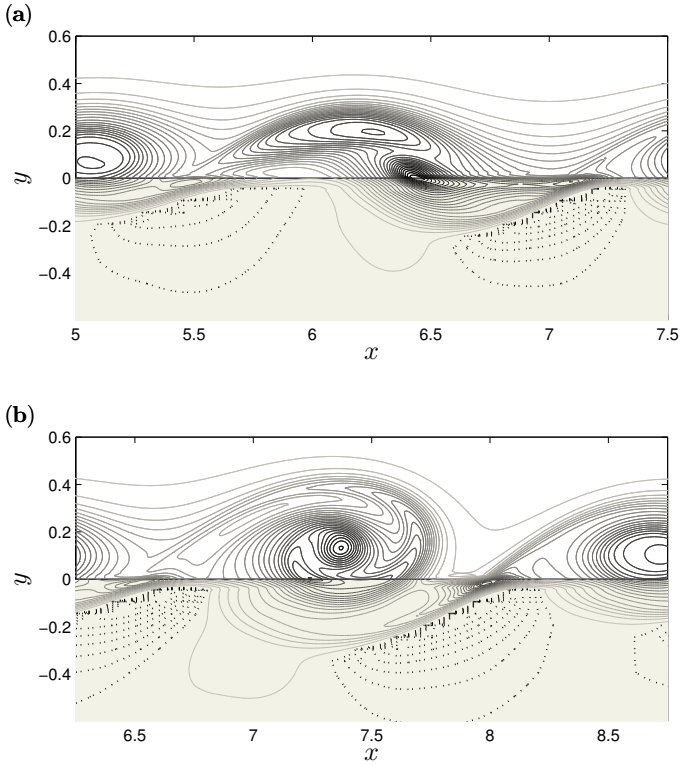

Figure 4.9: Vorticity plots during and after roller pairing, (a) $t = 11.96$ and (b) $t = 12.62$, respectively. After the pairing, the tail of the newly formed spiral will transfer vorticity in the braid region. The solid contours show negative vorticity at increments of 0.8 units, while the dotted contours show positive vorticity at increments of 0.2 units.

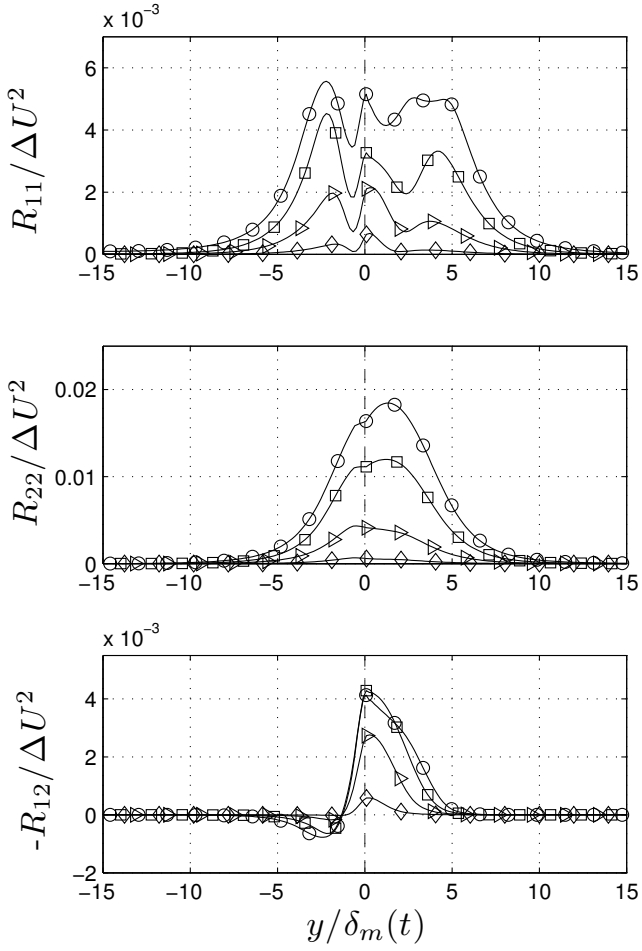

Figure 4.10: Reynolds stresses during the first pairing process. The curves are skewed towards the pure-fluid domain, indicating an asymmetric growth with respect to the material interface. ($\diamond : t = 10.51$; $\triangleright : t = 11.05$; $\square : t = 11.51$; $\circ : t = 12.03$).

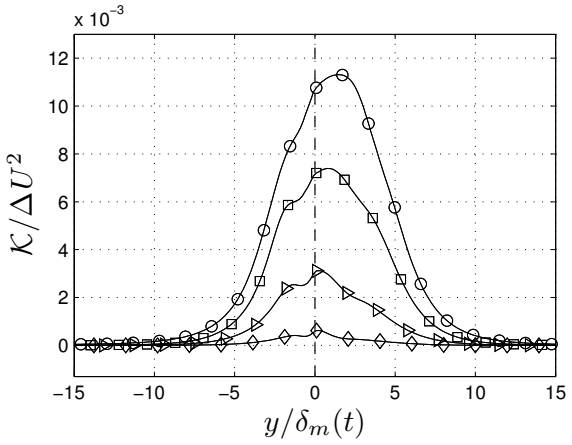

Figure 4.11: Kinetic energy of fluctuations during the first pairing process. (Symbols as in Figure 4.10).

implies that, up to the time that the first pairing is completed at $t \simeq 12.6$, there is no interaction at all between the shear layer and the top and bottom boundaries.

From the completion of the first pairing, $t \simeq 12.6$, and until the end of the second phase at $t \simeq 19.0$, the other rollers also start to pair and merge. According to our numerical predictions, occasionally two different pairings may occur at the same time, which makes the shear layer grow at a much faster rate. For example, during this period, the momentum thickness δ_m has increased by a factor of 2.5. Moreover, as deduced from Figure 4.5, the momentum thickness inside the porous medium, δ_m^-, no longer remains constant but, instead, starts to increase. In fact, at $t = 14.6$ and inside the porous medium, the shear layer has grown enough to interact with the bottom wall. This is evidenced by the non-zero values of the Reynolds stress R_{11} right next to the wall, as shown in Figure 4.12.

The growth of the shear layer inside the porous medium can be attributed to the fact that multiple rollers enter the porous medium simultaneously during this period. The peak value of δ_m^- is approximately 0.02, i.e. four times larger than the (constant) value of δ_m^- during the first phase of the layer's growth. This peak value occurs at $t = 14.6$ and coincides with a local maximum of δ_m^+. Therefore, δ_m peaks at this time also. As in the case of plane mixing layers, Moser & Rogers (1993), a local maximum of δ_m marks the completion of a pairing process. Beyond this time, δ_m^+ increases due to subsequent

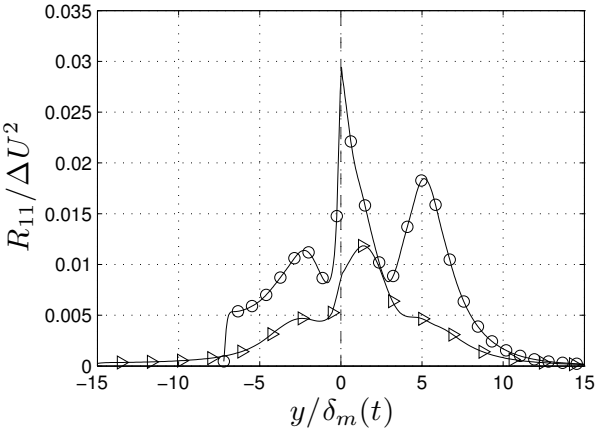

Figure 4.12: Plots of the R_{11} Reynold stress at the beginning of the second phase. $\triangleright$: $t = 12.62$; $\circ$: $t = 14.61$. The non-zero values next to the bottom wall at $t = 14.61$ indicate interaction of the shear layer with the boundary. By contrast, at the end of the first pairing, at $t \simeq 12.6$, R_{11} decays smoothly to zero.

pairings, and so does δ_m. On the other hand δ_m^- begins to decrease, albeit in a non-monotone manner. Finally, during this period, $12.6 < t < 19.0$, the Reynolds stresses continue to grow but also in a non-monotone fashion.

The **third phase** starts at the end of the pairing process, $t \simeq 19.0$. At this time, the computational domain is occupied by three large rollers, which spread throughout its streamwise direction. Due to their size, these rollers do not merge by climbing on top of each other as we described above for the second phase of evolution. Instead, their growth is attributed to entrainment of fluid from the adjacent rollers, as well as to further entrainment of irrotational fluid from the pure-fluid and porous regions. As such, during this phase the shear layer continues to grow, albeit at lower rates. More specifically, in Figure 4.5, we observe a moderate, linear growth of δ_m. In the case of plane mixing layers, this is suggestive of self-similarity; see, for example, Rogers & Moser (1994). It turns out that the shear layers under study are also self-similar for such growth. This can be evidenced by the collapse of the Reynolds stresses shown in Figure 4.13, as well as the collapse of the streamwise-averaged velocity profiles shown in Figure 4.14.

On the other hand, the momentum thickness inside the porous medium δ_m^- decreases slowly and converges to its initial value. However, the shear layer is still large enough

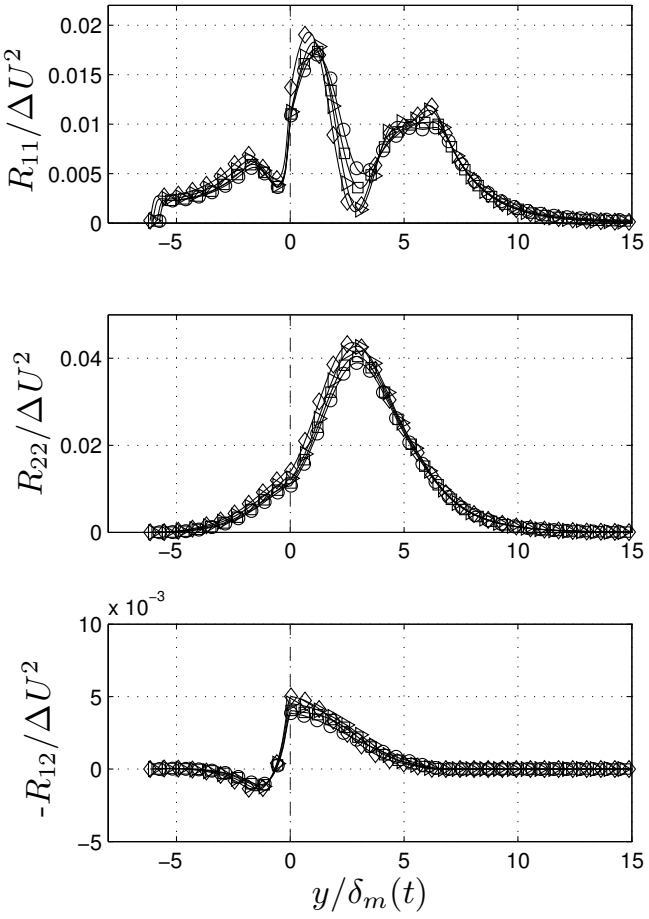

Figure 4.13: Collapse of the (scaled) Reynolds stresses as evidence of self-similarity during the third phase of evolution. ($\diamond$: $t = 20.01$; $\triangleright$: $t = 21.0$; $\square$: $t = 22.42$; $\circ$: $t = 23.17$).

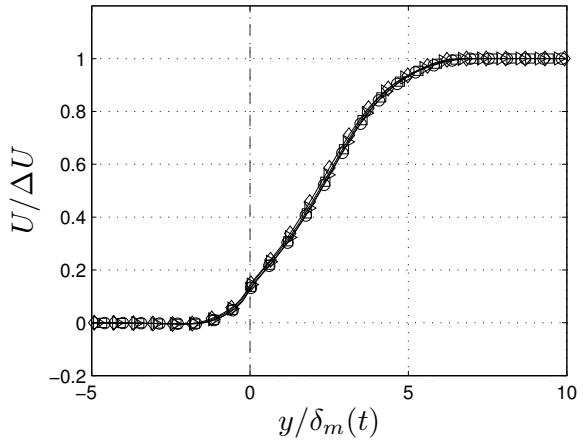

Figure 4.14: Mean streamwise velocity profiles during the third phase of evolution. The collapse of the profiles along with the collapse of the Reynolds stresses profiles, Figure 4.13, suggests that self-similarily is re-established during this phase. (Symbols as in Figure 4.13).

to cover the entire porous medium. This is deduced from the non-zero values of R_{11} right next to the bottom boundary; see Figure 4.13. At $t = 23.3$, the growth rate of the momentum thickness increases once again. This signals the initiation of yet another series of vortex pairings and the break-down of self-similarity. After a few time-units, the size of the rollers becomes comparable to the height of the pure-fluid domain. The simulation is terminated at $t = 25$, before the shear layer interacts with the top boundary of the domain.

4.4.1 Parametric study with respect to porosity

As mentioned in Section 4.2, our linear stability analysis asserts that shear layers at interfaces of a porous medium and a pure fluid are unconditionally unstable. However, the growth rates of the instabilities decrease substantially as the porosity ϕ decreases. In this sub-section, we investigate further the role of ϕ in the temporal evolution of the shear layers of interest, via a parametric study. The simulation parameters and set-up are exactly the same as before and the only parameter that varies is the porosity ϕ via modification of the number density of solid elements. Below we compare the numerical predictions for three different porosities, namely, $\phi = 0.70,\ 0.90,\ 0.95$.

The growth histories of δ_m for these cases are shown in Figure 4.15. From these plots

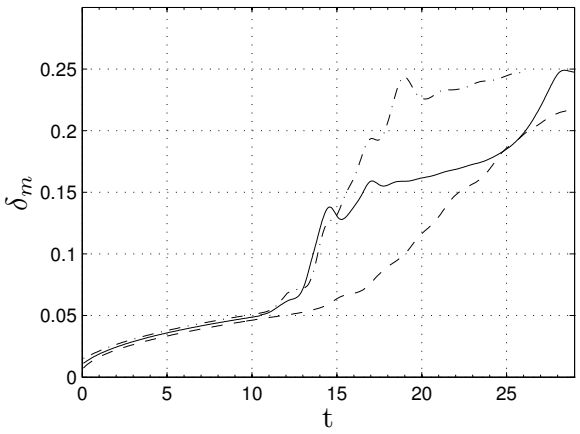

Figure 4.15: Parametric study with respect to porosity: growth history of the momentum thickness for different values of ϕ. (-·-: $\phi = 0.95$; — : $\phi = 0.9$; - - - : $\phi = 0.7$).

we can identify the same three phases of evolution as before: *i*) self-similar evolution and growth of δ_m according to the $\sqrt{t}$ -law, *ii*) vortex formation and pairing accompanied by rapid growth of δ_m, and *iii*) self-similar evolution and moderate, linear growth of δ_m. Moreover, the evolution of δ_m at early times is identical for all cases.

On the other hand, the growth rate of the shear layers decreases as ϕ becomes smaller. Interestingly, this trend is also predicted by the linear stability analysis of inviscid shear layers that was described earlier. Because of the slower growth rates, the durations of the three phases of evolution become longer. In particular, the required time for roller formation and pairing also increases as the porosity becomes smaller. For example, for $\phi = 0.7$, the first pairing occurs at $t \simeq 16$ and the slope of $\delta_m(t)$ changes only slightly during this process. By contrast, for $\phi = 0.95$ the first pairing occurs at $t \simeq 11.5$ and is accompanied by a sharp increase of $\delta_m(t)$.

Further, the extent of the shear layer inside the porous medium decreases substantially as ϕ becomes smaller, as expected. This is clearly illustrated in the mean velocity profiles shown in Figure 4.16. At the same time, due to increased interphasial drag, the Reynolds stresses drop significantly as the porosity decreases; see Figure 4.17. In this figure, we also observe that the drop of R_{11} across the interface is much sharper than the one of R_{22}. This can be attributed to the non-isotropic behavior of the porous medium, which implies different values for the interphasial drag parameters along the x and y directions.

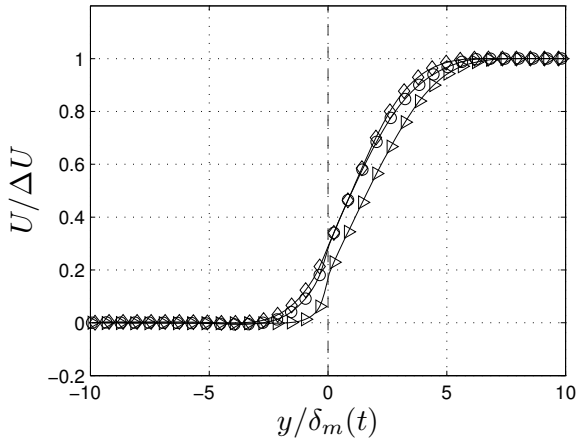

Figure 4.16: Parametric study with respect to porosity: mean velocity profiles when $\delta_m = 0.1$. The profiles show the decrease of the extent of the shear layer inside the porous medium as ϕ decreases. ($\diamond$: $\phi = 0.95$ and $t = 13.89$; $\circ$: $\phi = 0.9$ and $t = 13.61$; $\triangleright$: $\phi = 0.7$ and $t = 19.01$).

Finally, it is worth mentioning that the simulations predicted that the size of the rollers gets larger as ϕ decreases. Also, the vortical structures in the braid regions and right below the interface intensify. The later is due to the sharp drop of u across the interface which confines vorticity and prevents the spread of the shear layer inside the porous medium.

4.5 Numerical simulation of three-dimensional shear layers

In this section we present results from three-dimensional simulations of temporally-evolving shear layers at the interface of a highly porous medium and a pure fluid. Emphasis is placed on the study of the three-dimensionality of the vorticity field and on the characteristics of the flow during transition to turbulence.

As before, the height of the porous medium is defined to be the unit length. The dimensions of computational domain in the x, y and z directions are assumed to be L_x, L_y and L_z respectively. Further, their non-dimensional values are set to $L_x = 10.24$, $L_y = 4$ and $L_z = 2.56$. Periodic boundary conditions are applied in the streamwise (x) and spanwise (z) directions. Also, on the bottom and top boundaries we apply zero-slip

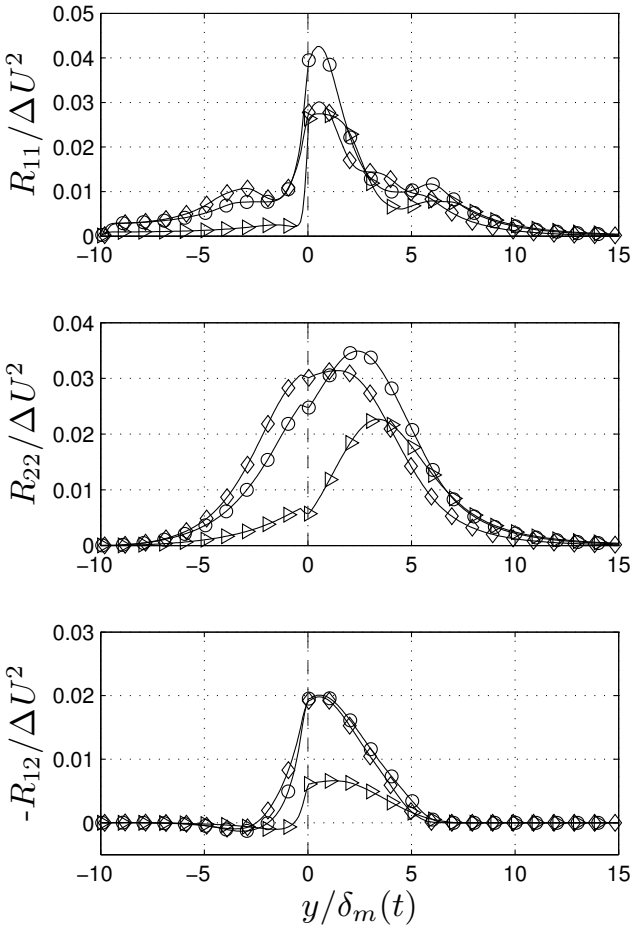

Figure 4.17: Parametric study with respect to porosity: Reynolds stresses when $\delta_m = 0.1$. The symbols are the same as in Figure 4.16.

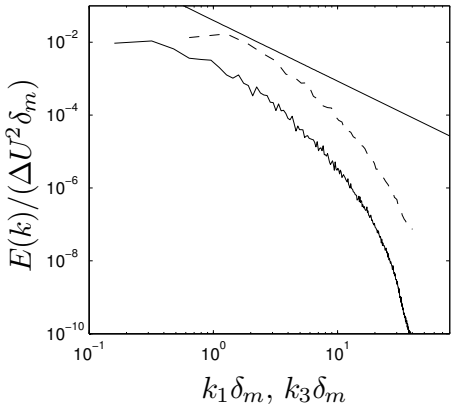

Figure 4.18: One-dimensional energy spectra at the interface between the porous medium and the clear fluid, at time $t = 13.47$. (— : $E_{11}(k_1)$; - - - : $E_{11}(k_3)$) . The solid straight line has a slope of $-5/3$. The fact that $E_{11}(k_1)$ maintains that slope for over half a decade, indicates that the Reynolds number achieved in the simulation is sufficiently high to produce turbulent flow.

and free-slip conditions, respectively.

The properties of the porous medium and the initial condition are the same as in the two-dimensional simulations. In this case, however, a perturbation is superimposed on all components of the velocity field so as to accelerate the growth of the instabilities. Herein we choose to apply the same perturbation in all directions:

$$u' = v' = w' = \sum_{N_{pert}=1,2} A_{pert}\, cos(\frac{2\pi}{L_x} x\, N_{pert})\, cos(\frac{2\pi}{L_z} z\, N_{pert})\,, \tag{4.5.1}$$

where $A_{pert} = 5{\times}10^{-4}\, e^{-20\, y^2}$. As the above expression suggests, the perturbation consists of two sinusoidal disturbances in the x and z directions. The period of the first disturbance equals unity in both the streamwise and the spanwise directions, while the second disturbance is the subharmonic of the first one. Further, the disturbances assume their maximum amplitude at $y = 0$, and they follow a Gaussian profile in the y direction.

The computational domain is discretized on a uniform grid of $512 \times 200 \times 128$ computational cells. The one-dimensional energy spectra at the end of the simulation are shown in Figure 4.18. In this figure we can see that there is at least a two-decade falloff in the dissipation range of both spectra. This implies that the selected grid resolution is sufficient to resolve the important length scales of the flow.

Figure 4.19 shows the growth history of the momentum thickness of the three-dimensional

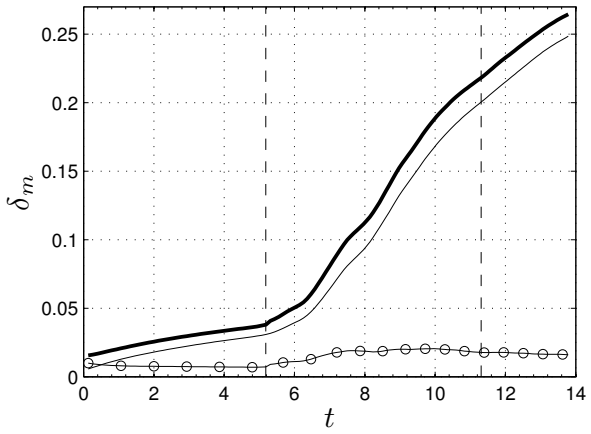

Figure 4.19: Growth history of the momentum thickness of the three-dimensional shear layer. (— : δ_m; — : δ_m^+ ; ∘ : δ_m^- ; - - - : the vertical dashed lines indicate the approximate time of termination of one phase and the beginning of the next one).

shear layer. As in the two-dimensional case, we can distinguish three separate phases of evolution with the same characteristics as their two-dimensional counterparts. The first phase is characterized by self-similar behavior and growth of δ_m according to the $\sqrt{t}$ -law. In fact, during this phase, the growth of the spanwise instabilities remains very slow. Consequently, the flow remains predominantly two-dimensional.

At the beginning of the second phase, self-similarity is lost and patches of streamwise vorticity begin to form; see Figure 4.20. These structures stretch in the area between two adjacent (spanwise) rollers. They start from below the upstream roller, cross the interface at the braid region and terminate on the top of the roller ahead. This shape resembles that of the well-known "rib" vortices of plane mixing layers. But in this case, the large majority of the structures have a large extent in the spanwise direction and tend to stretch around the rollers. However, localy and in the vicinity of distorted spanwise rollers, we could also identify streamwise vortical structures of thin, cylindrical shape which is very similar to the usual rib shape as reported, for example in Moser & Rogers (1991). These structures appear in pairs of opposite vorticity sign, as shown in Figure 4.21. From the same figure it can be evidenced that these rib vortices are linked via vortex lines. As mentioned in Finnigan *et al.* (2009), such structures can be interpreted as head-up or head-down hairpins.

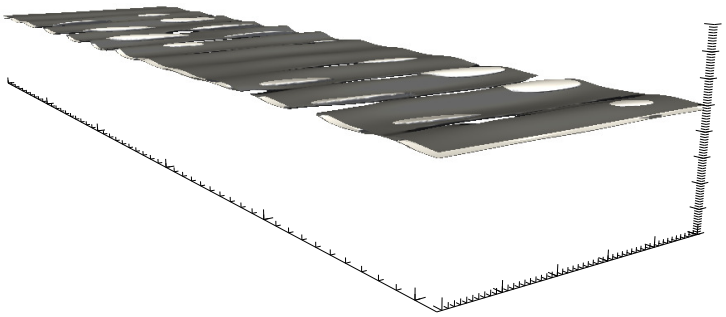

(a)

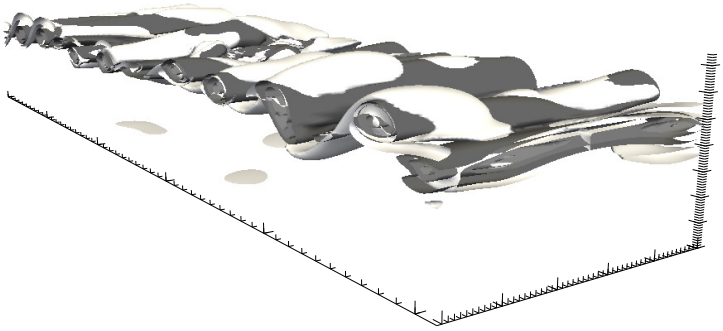

(b)

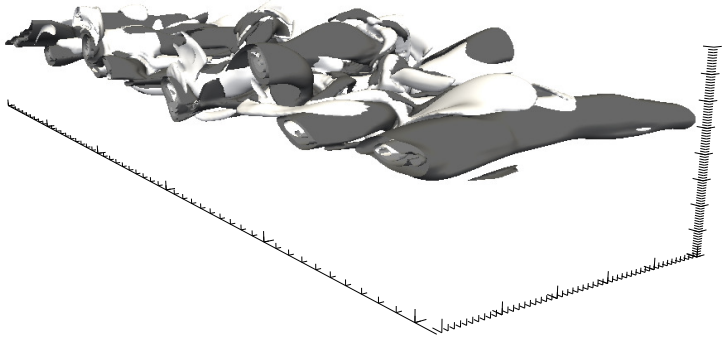

(c)

Figure 4.20: The vorticity field of the three-dimensional simulation at three different times. The dark surfaces show spanwise vorticity, while the white surfaces show streamwise vorticity.

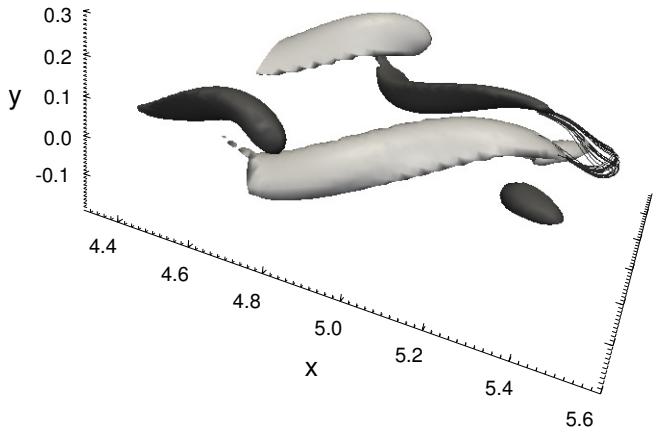

Figure 4.21: Detail of the vorticity field showing thin, cylindrical streamwise vorticity structures (ribs) at $t = 6.1$. The light-gray isosurfaces show areas of positive vorticity with amplitude 20 and the dark surfaces show areas of negative vorticity and same amplitude. Two ribs of opposite are "linked" via vortex lines. The material interface is located at $y = 0$.

Another important characteristic of this phase of growth is vortex pairing. The occurrence of the first pairing can be identified with the change of slope of the history of δ_m, at $t \simeq 5.3$, shown in Figure 4.19. Subsequently, multiple pairings occur almost concurrently throughout the streamwise direction. The occurrence of multiple pairings causes an additional increase of the growth rate of δ_m. Visualization of vortex pairings are provided in Figures 4.20(b) and 4.20(c).

Further, we observe that up to the completion of the first pairing at approximately $t \simeq 6.9$, the Reynolds stresses R_{ij} increase monotonically. However, during the sequence of multiple pairings, the amplitude of the Reynolds stresses fluctuates. At the same time, the coherent structures described above start to break down into many small-scale vortical structures of either positive or negative sign. Eventually, the regularity of the vorticity field is lost. This regularity breakdown can be observed in Figures 4.22 and 4.23, which show plots of the same spanwise vortical structures at two different times, and on the $x - y$ and $x - z$ planes respectively. By contrast, in the two-dimensional simulation, the vortical structures maintain their coherence while they grow. Despite

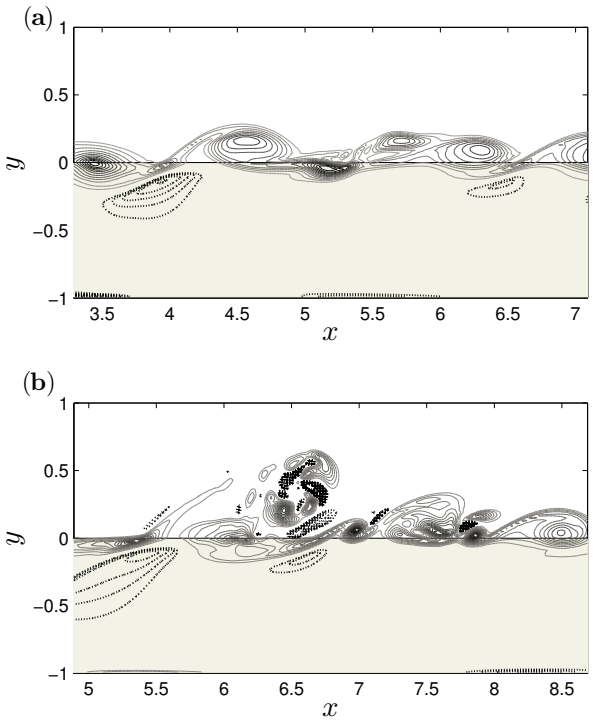

Figure 4.22: Contour plots of the spanwise vorticity field on the $z = 2$ plane, (a) $t = 6.57$ and (b) $t = 7.49$, respectively. The solid contours show negative vorticity at increments of 2 units, while the dotted contours show positive vorticity at increments of 0.3 units.

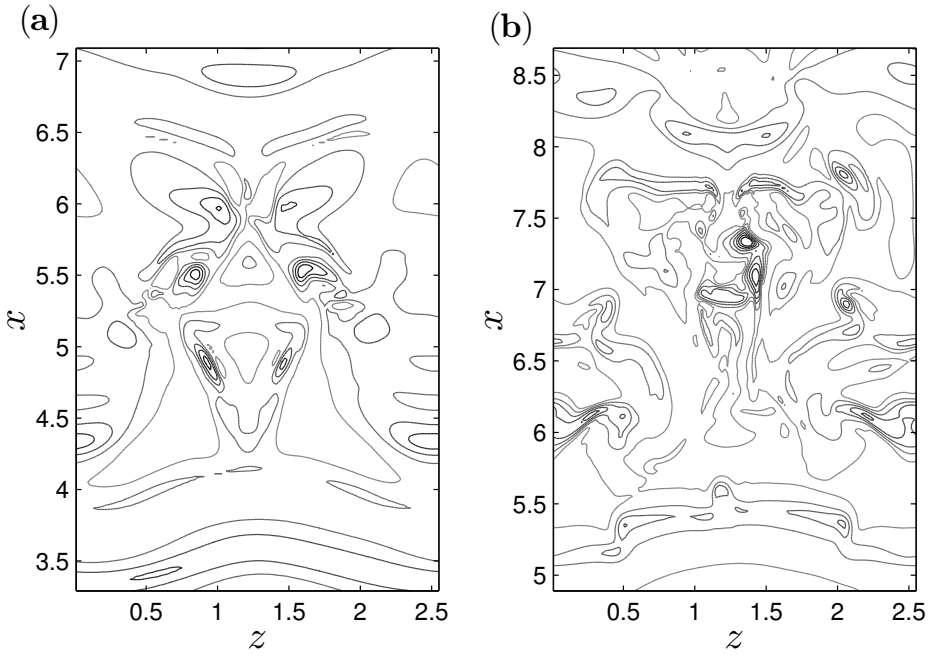

Figure 4.23: Contour plots of spanwise vorticity at the interface, at the same times as in Figure 4.22. The contours show negative vorticity at increments of 8 units.

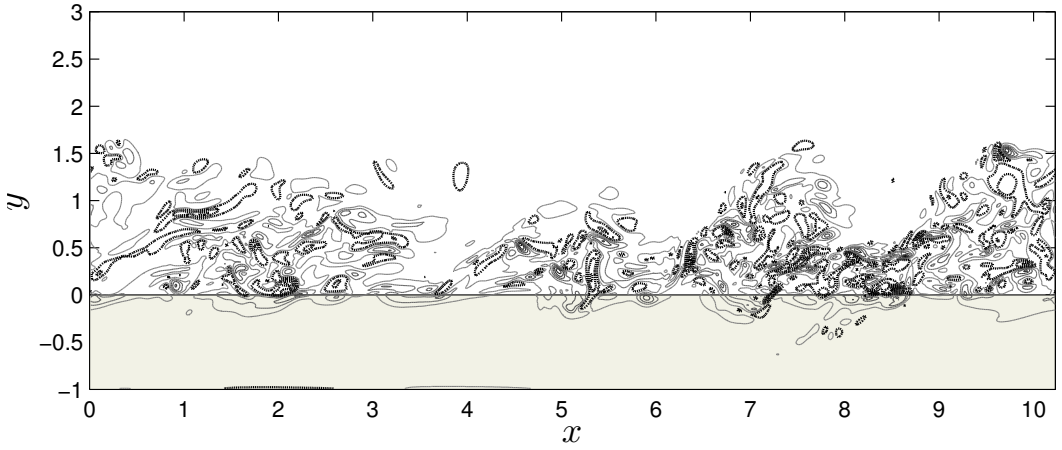

Figure 4.24: Spanwise vorticity field at $z = 1.28$ plane and $t = 13.47$. At this time the flow has completed transition to turbulence.

the large differences in the vorticity, the Reynolds stresses have only small discrepancies between the two-dimensional and three-dimensional simulations.

The decrease of the growth rate of δ_m at $t \simeq 11.31$ marks the beginning of the third phase. In particular, δ_m grows linearly, with a dimensionless growth rate equal to $(\Delta U)^{-1}(\mathrm{d}\delta_m/\mathrm{d}t) = 0.0068$. Also, during this phase, the self-similarity of the shear layer is re-established.

As time evolves, the vorticity field becomes more and more fragmented and irregular. This can be evidenced upon comparison of the spanwise vorticity at times $t = 7.49$ and $t = 13.47$ in Figures 4.22 and 4.24, respectively. The breakdown of the regularity of the vorticity field and the linear growth of δ_m are characteristics of post-transitional shear layers. Further, the plots of one-dimensional energy spectra at $t = 13.47$, Figure 4.18, show that $E_{11}(k_1)$ has approximately a slope of $-5/3$ for over half a decade of wavenumbers k_1. As mentioned in Rogers & Moser (1994), this is an indication that the Reynolds number achieved in the simulation is sufficiently high to produce turbulent flow. We therefore infer that, by the end of the simulation, the shear layer of our study has completed transition to turbulence.

Finally, we note that even at the late stages of the simulation, the small-scale structures of the vorticity field cannot advance deep inside the porous medium; see Figure

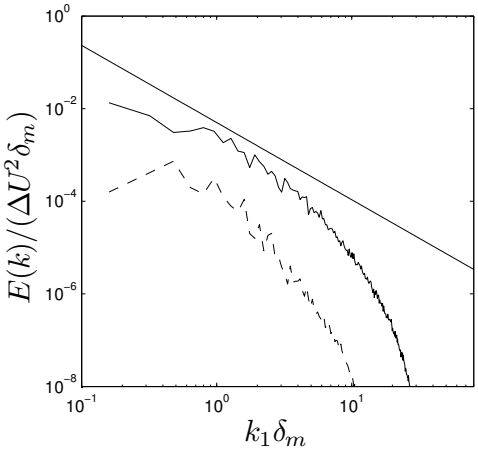

Figure 4.25: One-dimensional energy spectra at two different locations in the cross-stream direction, $t = 13.47$. (— : $E_{11}(k_1)$ at y = 0.3 ; - - - : $E_{11}(k_1)$ at y = -0.3) .

4.24. This is due to interphasial drag that causes dissipation of these small-scale structures below the interface. This is also supported by the comparison of the energy spectra inside and outside the porous medium, Figure 4.25. According to this figure, the spectra inside the porous medium is at least one decade lower than that in the pure-fluid domain. As a consequence of the limited advancement of the vortical structures in the porous medium, the shear layer is not large enough to interact with the bottom wall.

4.6 Conclusions

In this chapter, the dynamics of unsteady shear flows at the interface of a highly porous medium and a pure fluid has been investigated theoretically and numerically. Our study is based on a variation of the unsteady Darcy-Brinkman model. It was confirmed, via linear stability analysis and numerical simulations, that the flows at the interfaces of interest are in fact shear layers that produce significant recirculation inside the porous medium, and not boundary layers.

In particular, our linear stability analysis of the inviscid case showed that such shear layers are unstable at all perturbation wavelengths and porosities. Interestingly, at high wave-numbers, the growth rates of instabilities decrease with porosity. Nonetheless, the maxima of the growth rates occur at low wave-numbers and increase with porosity, as

expected.

The evolution of the instabilities was further investigated via numerical simulation of temporally-evolving shear layers at the interfaces of interest. Both two-dimensional and three-dimensional flows have been studied numerically. In both cases, it was found that at early times the shear layer is self-similar and its momentum thickness grows as a function of $\sqrt{t}$. The flow instabilities lead to the formation of spanwise vortices that grow and merge. In turn, this results in a rapid growth of the shear layer both outside and inside the porous medium. Also, secondary vortical structures are developed right below the interface, resulting from the misalignment of the arms of adjacent rollers and from the tendency of these rollers to shift toward the pure fluid. Such secondary structures have not been observed in plane mixing layers. Further, in the three-dimensional case, our simulations predict the formation of streamwise vortex structures that resemble the rib vortices of plane mixing layers.

Once the process of vortex-pairing is completed, the shear layers assume a moderate and linear growth rate. Further, self-similarity is re-established. However, in three-dimensional flows, the regularity of the vorticity field eventually breaks down and the large vortices get fragmented. This leads to the formation of multiple small-scale structures, and the flow eventually becomes turbulent.

In the simulations presented herein, we considered a generic orthotropic porous medium whose drag parametrisation is inspired by that of a dilute conglomerate of identical and uniformly distributed cylinders. Additional simulations with different porous microstructures that were conducted in the context of the present study, predicted similar shear-layer dynamics and flow characteristics as the ones described above.

Chapter 5

Transient flows in coupled porous and pure-fluid layers with heat transfer

5.1 Introduction

The study of fluid flow with heat transfer in porous media dates back to the 1940s. Horton & Rogers (1945) and Lapwood (1948) independently from each other were the first ones who were concerned with the equivalent of the Rayleigh-Bénard problem inside a permeable structure. In this problem, the porous medium is subjected to unstable thermal stratification, which can result into convective fluid motion at its interior. In the decades that followed, many studies focused on the stability, fluid flow and heat transfer characteristics of this problem. Examples include the linear stability analysis of Nield (1968), the experiments of Katto & Masuoka (1967), the computational work of Gupta & Joseph (1973) and others. In all these cases, however, the flow domain considered is entirely occupied by a porous material.

The interest for stratified flows and heat transfer in domain. An early study devoted to such domains include the one of Poulikakos & Bejan (1983). Subsequently, the relevant

The results of Section 5.4 have been published in: Papalexandris M.V. & Antoniadis P.D. 2015 A thermo-mechanical model for flows in superposed porous and fluid layers with interphasial heat and mass exchange. *Int. J. Heat Mass Tran.* **88**, 42–54.

The results of Sections 5.5 and 5.6 have been included in: Antoniadis P.D. & Papalexandris M.V. 2015 Numerical study of unsteady, thermally-stratified shear flows in superposed porous and pure-fluid domains. *Submitted for publication.*

literature grew considerably, especially as regards the stability of thermal convection in superposed fluid and porous layers; see, for example, Beckermann *et al.* (1987; 1988), Chen & Chen (1988; 1992), Chang (2005), Hirata *et al.* (2007), Thiele *et al.* (2009), Hirata *et al.* (2009*b*;*a*), Hill & Straughan (2009), Sadiq *et al.* (2010), Hill & Carr (2010*a*;*b*) and references therein. More recently, the authors of Chandesris *et al.* (2013) presented Reynolds-averaged simulations for statistically stationary turbulent heat transfer in such domains. In all the above studies it has been assumed that the fluid and the solid matrix are in thermal equilibrium, so a single equation describing the energy balance of the mixture is used.

However, there are applications, such as devices for rapid heat transfer etc, where the thermal-equilibrium hypothesis might no longer be valid. In this case, two energy equations are needed: one for the fluid phase and a separate one for the solid matrix. This increases significantly the complexity of the corresponding mathematical models. Nonetheless, due to their growing importance in technological applications, the study of convection in absence of thermal equilibrium has attracted considerable interest in recent years.

An influential contribution to this field is that of Ochoa-Tapia & Whitaker (1997); therein the authors provided a set of governing equations, based on the two-domain approach, and thermal boundary conditions at the interface. Subsequently, steady-state convection problems in domains partially covered by porous media have been studied numerically in Min & Kim (2005), Rees & Pop (2005), Kuznetsov & Nield (2010), Nield & Kuznetsov (2011). By contrast, the study of unsteady stratified flows under thermal non-equilibrium conditions between has been limited to domains that are completely occupied by the porous medium; see, for example,Banu & Rees (2002), Straughan (2006) and Malashetty *et al.* (2005). To the best of our knowledge, numerical results of transient flows in absence of thermal equilibrium in superposed pure-fluid and porous layers have yet to appear in the literature.

In this chapter we employ the model discussed in Chapter 2 to study non-Bousinesque fluid flow with heat transfer in domains of superposed porous and pure-fluid layers. We perform simulations of natural and forced convection as well as simulations of shear flows in thermally-stratified domains. The different cases that are considered for each type

	T_b/T_t	Re	Ri	Pr	ϕ	Subsection
Comparison with Experiments	1.0341*	35.608	1	12671	0.38	5.2.1
Natural Convection	1.05	375	1	0.71	0.9	5.4.1
	2.0	375	1	0.71	0.9	5.4.2
Forced Convection	1.5	5000	3.5493	0.71	0.9	5.5.1
	2.0	5000	3.5493	0.71	0.9	5.5.2
Stratified Shear Layers	1.5	1110	20	0.71	0.9	5.6.1
	0.666	1110	10	0.71	0.9	5.6.2

Table 5.1: Overview of the problems with heat transfer discussed in this chapter.

of problem, along with the respective non-dimensional parameters are provided in Table 5.1. It should be noted that for the description of the problem setup in each case, we provide the ratios of the boundary temperatures rather than temperature differences, as is typical for incompressible flows with heat transfer. As will be shown in the discussion that follows, for all the problems that we examine, the intensity of the temperature differences between the two phases inside the porous medium depends on the fluid structures that develop at the interface.

This chapter is organized as follows. In Section 5.2, the numerical algorithm proposed in Chapter 3 is tested by comparing results from a numerical simulation of natural convection, with experimental data readily available in the literature. In Section 5.3, we present the parametrization of the interphasial heat transfer between the porous skeleton and the fluid phase. In Section 5.4 we discuss our results of natural convection in unstably-stratified channels horizontal with wall-temperature ratios of $T_b/T_t = 1.5$ and $T_b/T_t = 2.0$. In Section 5.5 we discuss the effect of unstable stratification on forced flow between parallel walls. The wall-temperature ratios are the same as those in Section 5.4. Finally, in Section 5.6 we discuss the effect of both stable and unstable stratification on the development of a temporally-evolving shear layer on the interface of a porous strip.

*For the setup of the problem that is compared to experimental data, the side walls are kept in different temperatures, so that $T_L/T_R = 1.0341$.

5.2 Comparison with experiments

In this section we test the proposed algorithm by conducting a simulation of fluid flow with heat transfer, and comparing the results with readily available experimental data of the literature. In particular, we reproduce numerically an experiment of natural convection in superposed porous and pure-fluid layers that has been conducted in Beckermann *et al.* (1988). In this paper, the authors consider a rectangular enclosure, with the two layers aligned parallel to two of the vertical walls, which are kept at different temperatures. The remaining walls are covered with insulating material creating adiabatic conditions.

First, we provide a detailed description of the experimental setup. The test cell is of square cross-section. The length of each side of the square is equal to $11.43\,cm$, while the depth of the enclosure sizes $3.97\,cm$. The porous medium consists of randomly-packed, spherical glass beads of diameter $6\,mm$, which are held in place by a fibreglass grid. This configuration results in a permeable structure of porosity $\phi = 0.38$. The screen is placed vertically at the half-distance between the two vertical sides of the square cross-section, and it is, in turn, supported by small-diameter glass rods. A representative illustration of the square cross-section of the flow domain is provided in Figure 5.1.

Once the porous layer is constructed, the entire domain is filled with glycerine. Then, the temperature of the vertical wall from the side of the pure-fluid layer is raised to $T_h = 303.15K$, while the temperature of the wall on the side of the porous layer is maintained at $T_c = 293.15K$. To make sure that the system has reached steady state, the authors have allowed for a time-window of 12 hours before taking measurements. Herein, we compare our results with temperature measurements taken at the vertical centerplane of the test cell and at 3 locations along the y axis. These locations are marked with the dashed lines in Figure 5.1.

Next, we focus on the realization of the simulation, and in particular on the parametrization of the transport coefficients. As regards the intephasial drag coefficient, we employ the Darcy's law with the Forchheimer's extension. This choise is well-suited for low-porosity media, such as the packed bed of spheres of the experiment described above, and it is also used in the models of Beckermann *et al.* (1987; 1988). In the general case, the interphasial drag coefficient in equation (2.4.2) is a second order tensor. Due to

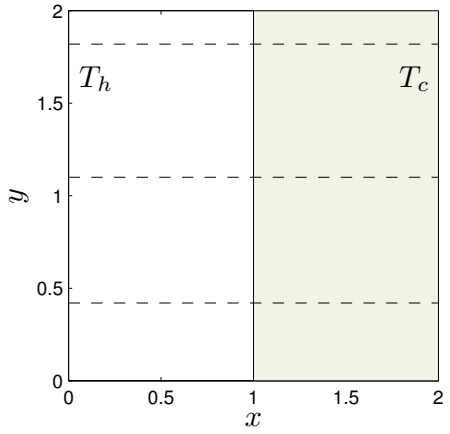

Figure 5.1: Comparison with the experiment of natural convection in a cavity of Beckermann *et al.* (1988). Representative illustration of the square cross-section of the domain. The shaded area indicates the porous region, while the dashed lines indicate the stations along the y, at which our predicted temperature profiles are compared with the experimental data.

the isotropicity of the porous material in the problem examined herein, the off-diagonal components of $\boldsymbol{\beta}$ are zero, and the diagonal components are equal. Finally, according to the extended Darcy's law,

$$\beta_{ij} = \begin{cases} \frac{\mu}{K} + \frac{\rho C}{\sqrt{K}} |\boldsymbol{u}| \,, & i = j, \\ 0 \,, & i \neq j. \end{cases} \tag{5.2.1}$$

In this expression, K is the permeability of the medium, determined by the Kozeny-Carman equation for a packed bed of beads of diameter d_p (see, for example, Beckermann *et al.* (1988)),

$$K = \frac{d_p^2 \, \phi^3}{175 \, (1-\phi)^2}. \tag{5.2.2}$$

Further, C is the inertia coefficient, which according to Ergun can be calculated by the following empirical formula:

$$C = \frac{1.75 \, (1-\phi)}{\phi^3 d_p} \sqrt{K}. \tag{5.2.3}$$

As regards the aproximation of the interphasial heat transfer parameter, we consider the expression for the rate of steady-state heat transfer across the surface of a single

spherical bead (see, Incropera *et al.* (2007)) and we multiply it with the number density of spheres $N_{\rm s}$. This yields the following expression in non-dimensional form,

$$h = \frac{6\,(1-\phi)}{d_p^2}\,\frac{\overline{Nu}_{d_p}}{PrRe}\,k\,. \tag{5.2.4}$$

In this relation, the Reynolds and Prandtl numbers are based on the macroscopic reference values, whereas Nu_{d_p} is the Nusselt number at the micro-scale, averaged over the surface of a single element. Herein we employ the widely used empirical correlation for Nu_{d_p} for high Prandtl numbers,

$$\overline{Nu_{d_p}} = 0.595\,Ra_{d_p}^{1/4}\,. \tag{5.2.5}$$

In the above expression, Ra_{d_p} is the Rayleigh number at the micro-scale, which based on our reference values, can be calculated by,

$$Ra_{d_p} = Ri_{d_p}\,Pr\,Re_{d_p}^2\,(\frac{T_h}{T_c} - 1). \tag{5.2.6}$$

For the non-dimensionalization of the problem variables, the distance of the fibreglass screen from the hot and cold walls is taken as the reference length. As regards the material properties, these are non-dimensionalized with the values of the properties of glycerine at the reference temperature, which is that of the cold wall, T_c. Based on these variables the Reynolds number is equal to $Re = 35.61$, the Richardson number is equal to $Ri = 1$ and the Prandtl number is $Pr = 12671$.

Initially, the fluid is assumed to be at rest, while the phasial temperatures are equal (thermal equilibrium). Throughout the pure-fluid region, T is set equal to the temperature of the hot wall. Inside the porous medium, we prescribe a linear temperature profile. According to this profile, the phasial temperatures equal to T_c at the right wall and equal to T_h at the interface between the two sub-regions. As regards the boundary conditions of the walls along the vertical direction, they are assumed to be adiabatic. Accordingly, we prescribe zero normal gradients for both T and $T_{\rm s}$ on the boundaries.

At the interface, we need to take into account the presence of the fibreglass grid that keeps the beads in place. This is expected to obstract the fluid flow from the pure-fluid to the porous region, thus increasing the residence times of fluid at the interface region. We opt to model this effect, by considering thermal equilibrium between the two phases at the interface between the porous and the pure-fluid regions.

5.2.1 Discussion of the numerical results

In this subsection, the results obtained from our simulation are compared with the experimental results reported in Beckermann *et al.* (1988). To conform with the experimental procedure, we allow the simulation to run for 570×10^3 non-dimensional time units, so that the velocity and the temperature fields reach steady state. This duration corresponds to the dimensional time of 12 hours required for the experiment. To compensate for the long simulation times, we restrict the domain resolution to 25 cells per unit length.

At this point it should be noted that the authors in Beckermann *et al.* (1988) report on a single temperature field throughout the domain. However, it is not specified if during the measurements inside the porous medium the thermocouples were floating in glycerine, or if they were in contact with the glass beads. Furthermore, in the same work, the measured values are compared with results from numerical simulations, which were based on a single temperature model. Accordingly, in the comparison discussed herein, the experimental results are juxtaposed with the temperature of the mixture, T_m, from our simulation, which is calculated as follows:

$$T_m = \frac{\rho\phi\, T + \rho_{\mathrm{s}}(1-\phi)\, T_{\mathrm{s}}}{\rho\phi + \rho_{\mathrm{s}}(1-\phi)}\,. \tag{5.2.7}$$

This comparison in provided in Figure 5.2.

In this figure, the temperatures are plotted along the x direction from the hot to the cold wall, and at 3 stations along the normal direction. The lowest station is at $y = 0.42$, the second highest station is at $y = 1.1$, while the highest is at $y = 1.82$. According to the figure, the plot that corresponds to the highest station is in very good agreement with the experimental results, throughout the entire length of the domain. Inside the porous medium, the convective heat transfer is negligible, so both the predicted and the experimental profiles are linear from the interface at $\frac{x}{2} = 0.5$, to the cold wall. The small difference in the slopes can be attributed to the non-uniformities in the porosity of the material at the vicinity of the wall, which is caused by the stacking of the beads. According to Beckermann *et al.*, such non-uniformities are expected to result in channeling of the flow along the wall, a behaviour that is not modelled in the numerical simulation. Furthermore, the insulating material that is used at the top and bottom walls to create adiabatic conditions, has physical limitations. At the large times required for

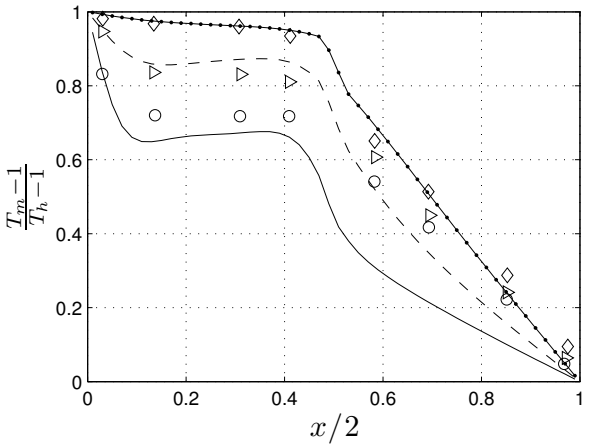

Figure 5.2: Comparison with the experiment of natural convection in a cavity of Beckermann *et al.* (1988). The symbols correspond to the experimental data and the lines to predicted temperature profiles, taken at 3 stations along the y: ($\circ$) and (—) at $y = 0.42$; ($\triangleright$) and (- - -) at $y = 1.1$; ($\diamond$) and (-·-) at $y = 1.82$.

the experimental set-up to reach steady state, the effectiveness of the material to create such conditions is questionable. This is another parameter which adds uncertainty to the measured temperature values.

At the two lower stations of the domain and inside the porous medium, the numerical predictions show that T_m assumes a non-linear profile, which is not present in the experimental results. This is attributed to the convective heat transfer effects, which appear overestimated in comparison with the experiment of Beckermann *et al.*. It should be noted, however, that the fibreglass screen that keeps the glass beads in place, is expected to cause an additional blocking of the fluid flow from the pure-fluid domain to the porous region. Such blocking, in turn results in further inhibition of the convective motions inside the porous medium, which is not taken into account in our drag parametrization. Accordingly, the predicted values of the temperature of the mixture at the interface, affect the profiles in the pure fluid domain. These show small discrepancies from the experimental values (the maximum difference is approximately 8% for the values of lowest station).

Overall, our numerical predictions come in reasonable agreement with the experimental measurements, despite the uncertainties introduced by the domain set-up of Beckermann *et al.*, which are also emphasized in their article.

5.3 Parametrization of the transport coefficients

In the simulations described in this chapter, we consider a *generic*, highly porous orthotropic medium whose physical properties are those of birch wood. The drag and interphasial heat transfer parameterizations of the porous skeleton with respect to porosity, are inspired by that of a dilute conglomerate of identical and uniformly distributed cylinders. Further, it is assumed that the cylinders are parallel to each other and aligned vertically to the bottom boundary of the domain. As such, the interphasial drag parameters for the streamwise (β_{11}) and cross-stream (β_{22}) directions are the ones provided by the expressions (4.3.1) and (4.3.2), derived in the previous chapter.

In the following, we describe our approximation for the interphasial heat transfer parameter h that appears in the energy equations of the two phases (2.3.11) and (2.3.13). The reasoning behind the approximation is the same as that employed for derivation of the interphasial drag coefficients β_{11} and β_{22}. In the description that follows, the symbols under a hat ($\hat{}$) designate dimensional quantities, while plane symbols stand for un-dimensional ones.

First, we consider statistically steady-state fluid flow normal to the axis of a single element with diameter $\hat{d}_p$ and height $\hat{l}$. The averaged Nusselt number over the surface of a cylinder is defined as $\overline{Nu_{d_p}} = \frac{\overline{\hat{h}_{d_p}}\hat{d}_p}{\hat{k}}$, where $\overline{\hat{h}_{d_p}}$ is the average convection coefficient for the entire surface of the cylinder and $\hat{k}$ is the conduction coefficient of the surrounding fluid. Empirical or semi-empirical expressions for Nu_{d_p} as a function of the cylinder's geometry and the Reynolds and Pradtl numbers can be found in standard textbooks. Herein we opt for the empirical expression found in Incropera *et al.* (2007) for flow around a circular cylinder and for $Pr \leq 0.7$:

$$\overline{Nu_{d_p}} = C\, Re_{d_p}^{m} Pr^{1/3}\,, \tag{5.3.1}$$

where Re_{d_p} is the Reynolds number with respect to the cylinder's diameter. The parameters C and m depend on Re_{d_p} and their values can be obtained from look-up tables.

The heat transfer rate between the cylinder and the surrounding fluid will then be:

$$\hat{q}_{cyl} = \overline{Nu_{d_p}}\hat{k}\,\hat{l}\pi(\hat{T}_{cyl} - \hat{T}) \tag{5.3.2}$$

where $\hat{T}_{cyl}$ is the temperature of the cylinder and $\hat{T}$ is the temperature of the fluid outside the thermal boundary layer that surrounds the cylinder.

In order to obtain an expression for h in the energy equations (2.3.11) and (2.3.13), we assume that the heat transfer rate between the two phases inside the porous medium amounts to the cumulative effect of each of the cylinders at the microscale. To this extent, we first multiply equation (5.3.2) with the number density of cylinders, namely, $N_s = 4(1-\phi)/(\pi\hat{d}_p^2\,\hat{l})$. Then we substitute the resulting product in equations (2.3.11) and (2.3.13), page 24. Upon non-dimensionalization, we arrive at:

$$h = \frac{4(1-\phi)}{d_p^2}\frac{\overline{Nu}_{d_p}}{PrRe}\,k \tag{5.3.3}$$

where the Reynolds and the Prandtl numbers are based on the macroscopic reference values.

It should be emphasized once more that the above parameterization is only an approximation of the interphasial heat-transfer on an ensemble of cylinders. For example, it does not take into account a number of factors, such as the unsteady nature of the flow, the finite height of the individual cylinders, and others. However, it is deemed adequate for the purposes of our study because herein we are concerned with a generic orthotropic porous medium.

As regards the conductivity of the solid matrix, we use the empirical expressions given in Yu *et al.* (2011) for birch wood. According to this work, the component of $\underset{\sim}{\boldsymbol{k}}_{\mathrm{s}}$ in the lateral direction, $k_{\mathrm{s}11}$ changes linearly with temperature according to the following relation,

$$k_{\mathrm{s}11} \;=\; 0.4253 + 4.1591\,T\,. \tag{5.3.4}$$

Also, the expression for the component of $\underset{\sim}{\boldsymbol{k}}_{\mathrm{s}}$ in the wall-normal direction reads,

$$k_{\mathrm{s}22} \;=\; 1.8k_{\mathrm{s}11}\;. \tag{5.3.5}$$

Finally, the (non-dimensional) thermal conductivity and viscosity of the fluid phase are approximated via a simplified Sutherland law:

$$\mu = k = T^{0.7}\,. \tag{5.3.6}$$

5.4 Natural convection between parallel walls

In the simulations presented in this section, the porous medium is assumed to occupy the bottom part of the computational domain $-l \leq y \leq 0$, *i.e.* it starts at the bottom boundary and its height equals l. Also, it spans the entire computational domain in the streamwise direction.

In the problem that we consider herein, the height of the porous medium is $0.015m$, while the top cold wall is kept at is room temperature (approximately $300K$). This setup corresponds to natural convection of air in a passive cooling device for electronic components. For non-dimensionalization purposes, the height $\hat{l}$ of the porous layer is used as the reference length, whereas the characteristic velocity is set equal to $\sqrt{\hat{g}\hat{l}}$. The reference values of the various transport properties are those of the fluid phase at the reference temperature, which is assumed to be the temperature of the top cold wall, $\hat{T}_t$. Based on these values, the Reynolds number in our simulations is set to $Re = 375$, the Richardson number is $Ri = 1$ and the Prandtl number is $Pr = 0.71$. The porosity of the medium is $\phi = 0.9$ and the characteristic length of the porous microstructure is $d_p = 0.032$. Examples of porous materials with such high porosities are: carbon nano-tube forests, carbon-fiber substrates, and others.

The dimensions of computational domain in the x and y directions are assumed to be L_x and L_y respectively. Further, their non-dimensional values are set to $L_x = 10$ and $L_y = 4$. In other words, the height of the porous medium is one unit-length, l, whereas the height of the pure-fluid domain is equal to $3l$. A schematic of the domain configuration is provided in Figure 5.3. As for all simulations described in this chapter, the computational domain is discretized on a uniform grid with a resolution of 100 cells per unit-length. Also, the Courant number is set equal to 0.04.

As regards boundary conditions, the domain is assumed to be periodic along the (streamwise) $x-$direction. For the top and bottom channel walls, no-slip conditions are

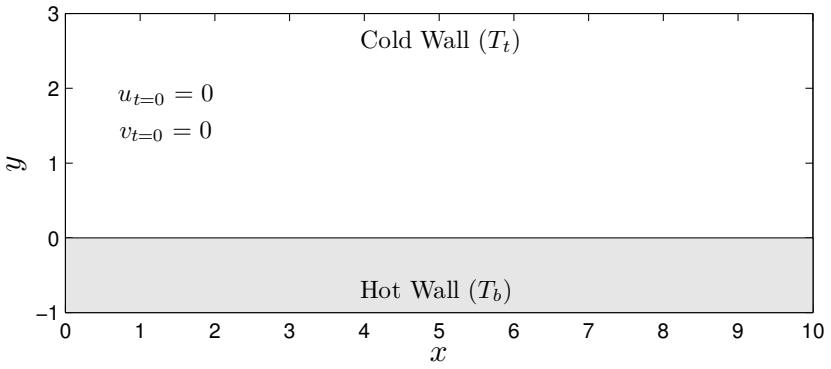

Figure 5.3: Schematic of the domain configuration for the simulations of natural convection. The shaded area indicates the part of the domain that is occupied by the porous medium.

prescribed for the fluid velocities. For the pressure, the boundary conditions that we apply are such that compatibility with the boundary conditions of the *provisional* velocities is secured via equations (3.2.13) and (3.2.20). As we explained in Section 3.4, the boundary condition for the normal component of the *provisional* velocity, $\tilde{\boldsymbol{u}} \cdot \hat{n}$, is the same as that of $\boldsymbol{u} \cdot \hat{n}$. On the top and bottom walls, both these velocities are set to zero. Then, from equation (3.2.13), the boundary condition for the pressure at the bottom wall is $\frac{\partial p'}{\partial y}\Big|_{y=0} = 0$, while that at the top wall is, $\frac{\partial p'}{\partial y}\Big|_{L_y} = Ri \, \frac{\partial \rho}{\partial y}\Big|_{L_y} L_y \, .$

Herein we are concerned with problems of unstable thermal stratification; therefore, the top and bottom walls are kept at temperatures T_t and T_b, respectively, with $T_b > T_t$. Furthermore, at the bottom boundary, which coincides with the bottom end of the porous structure, we assume that $T_s = T_f = T_b$.

Finally, as regards initial conditions, we assume that initially the fluid is at rest and in thermal equilibrium with the solid matrix. Then, the initial temperature distributions are given as the steady-state solutions of (2.3.11) and (2.3.13) with the prescribed boundary conditions at the top and bottom wall. This yields a linear profile for the solid matrix and a piecewise linear profile for the fluid that coincides with the temperature profile of the solid matrix inside the porous layer. A plot of the linear profiles of the two phases at the initial condition is provided in Figure 5.4. Further, following the approach of Chen & Chen (1992), the value of the temperature at the interface, T_i, is taken such that the overall conductive heat flux be continuous across the interface. In other words, T_i is

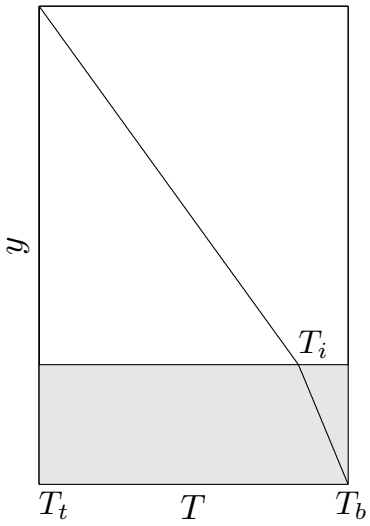

Figure 5.4: Natural convection between parallel walls. Profiles of the phasial temperatures at $t = 0$. At the beginning of the simulations, the two phases are assumed to be at thermal equilibrium.

evaluated by the following equation,

$$[k_{s22}(1-\phi)+k\phi]\,\frac{T_i - T_b}{l} \;=\; k\,\frac{T_t - T_i}{3l}\,. \tag{5.4.1}$$

5.4.1 Small wall-temperature ratio: $T_b/T_t = 1.05$

In this subsection, we present results from simulations with small wall-temperature ratio, $T_b/T_t = 1.05$. For this case, the Rayleigh number based on the reference values defined above, is $Ra_l = 5 \times 10^3$, while the Rayleigh number based on the height of the pure-fluid domain $3l$ is $Ra_{3l} = 1.35 \times 10^5$. For the problem of natural convection in a pure-fluid channel of width $3l$, these values are well above the critical Rayleigh number for convective instability, see Incropera *et al.* (2007).

According to our simulations, unstable stratification in superposed porous and pure fluid layers, and for the values of Rayleigh numbers mentioned above, results in the development of regular convective cells. In particular, we observe the formation of two pairs of counter-rotating cells of equal size; see Figure 5.5. Once the flow has evolved

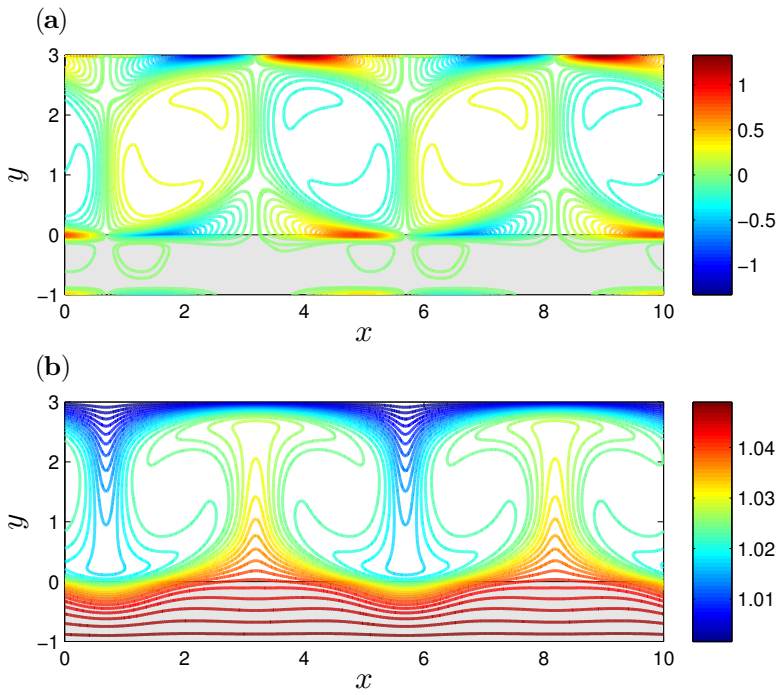

Figure 5.5: Natural convection with small wall-temperature ratio, $T_b/T_t = 1.05$: (a) Vorticity. Blue contours indicate negative vorticity and red contours indicate positive vorticity. All contours are at increments of 0.05 units. (b) Fluid temperature. Blue contours indicate temperatures below and red indicate temperatures above $\frac{T_b+T_t}{2}$. All contours are at increments of 0.0016 units.

sufficiently, both the size and shape of the convective cells get stabilized and remain constant with time. The arms of adjacent cells correspond to alternating hot and cold plumes whose shape is also constant with time.

It is worth noting that the extent of the convective cells is limited in the pure-fluid domain. This means that the porous layer has a stabilizing effect to natural convection. This is primarily due to the interphasial drag which reduces considerably the fluid momentum in the lateral directions. A secondary stabilizing effect due to the presence of the porous layer is that the interfacial heat transfer modulates the mechanism with which heat is eventually transferred from the hot bottom boundary to the fluid.

At the early stages of the simulation, the fluid temperature starts to vary in the pure-fluid domain upon initiation of the convective motions. Inside the porous medium, such a variation is also evidenced close to locations where the fluid velocity is non-negligible,

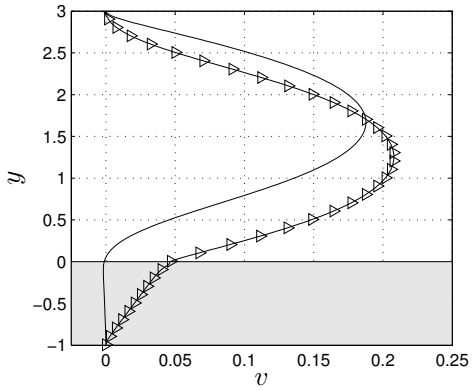

Figure 5.6: Natural convection with small wall-temperature ratio, $T_b/T_t = 1.05$. (—): profile of the normal velocity component, v, at the axis of the hot plume ($x = 3.2$). (▷): profile of $-v$ at the axis of the cold plume ($x = 5.7$). The normal velocity in a cold plume at the interface is non-negligible. By contrast, in the adjacent hot plume it is almost zero.

i.e. to locations with significant thermal convection. These are the locations where fluid moving downwards inside a cold plume penetrates the porous layer - pure fluid interface. Inside the porous layer and away from the cold plumes the temporal variations of the fluid temperature are small. On the other hand, the solid temperature changes very slowly with time, even after the formation of the convective cells.

At later times, the size and shape of the convective cells get stabilized. The vorticity and fluid-temperature fields at this stage are shown in Figure 5.5. We observe that the extent of the rolls in the wall-normal direction is limited in the pure-fluid domain. Furthermore, the vorticity induced by the cold plumes near the interface, is higher than the one induced by the hot plumes close to the top wall. This is due to the fact that the cold plume penetrates the interface and extents deep inside the porous layer.

Accordingly, the amplitude of the normal velocity component v in a cold plume and at the vicinity of the interface is substantial, as can be seen in Figure 5.6. By contrast, in the apex of the hot plumes, v approaches zero rapidly due to the presence of the top wall. The fluid velocity profiles in Figure 5.6 provide further information about the heat transfer mechanisms inside the porous layer. At the area below a cold plume, thermal convection is significant because of the increased fluid velocities. On the other hand, the velocities below a hot plume are negligible and, therefore, conduction becomes the dominant heat transfer mode. This is also corroborated by the fluid-temperature profiles

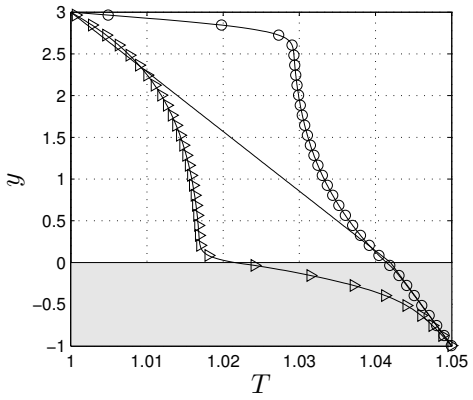

Figure 5.7: Natural convection with small wall-temperature ratio, $T_b/T_t = 1.05$. (—): Initial fluid temperature profile. (○): Profile of fluid temperature at the axis of the hot plume ($x = 3.2$). (▷): Profile of fluid temperature at the axis of the cold plume ($x = 5.7$).

along a hot and a cold plume that are shown in Figure 5.7. According to this figure, below a hot plume, the fluid temperature is very close to the initial distribution. By contrast, below a cold plume it has evolved substantially and it further exhibits strong gradients in the wall-normal direction.

Our simulations further predict that thermal non-equilibrium between the two phases is maximal at the intersection of the axis of cold plumes and the interface. The phasial temperatures along this axis are plotted in Figure 5.8(a). We further observe that, along this axis, the difference between the phasial temperatures increases with y until it reaches its peak on the interface. Away from the axis of the cold-plume, the difference between the phasial temperatures is significantly smaller. Globally, thermal non-equilibrium is non-negligible only in the vicinity of the interface, as can be inferred from the profiles of the x-averaged temperatures, $\langle T \rangle$ and $\langle T_s \rangle$ shown in Figure 5.8(b).

To better quantify this result, we have plotted the normalized difference between the phasial temperatures in Figure 5.9. According to this Figure, the maximum difference, which occurs at the intersection of the axis of the cold plume and the interface, is 0.12 but it drops to a value close to zero at $y \simeq -0.8$). On the other hand, the $x-$ averaged difference approach zero in much shorter distances from the interface, at $y \simeq -0.4$.

Additional insight of the evolution of the flow can be obtained by computing the conductive heat transfer rates of the two phases inside the porous material. To this

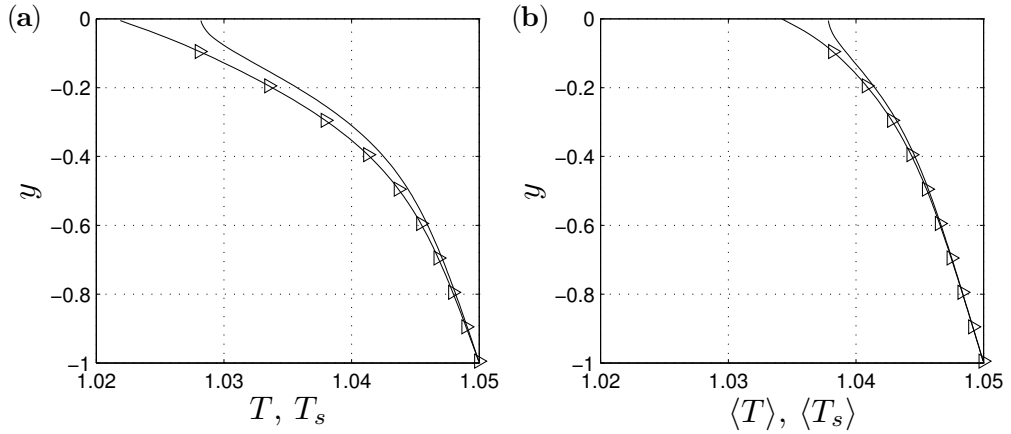

Figure 5.8: Natural convection with small wall-temperature ratio, $T_b/T_t = 1.05$. (a) Temperature profiles of the solid and fluid phase inside the porous layer at the axis of a cold plume ($x = 5.7$). (b) $x-$averaged temperature profiles profiles, $\langle T \rangle$ and $\langle T_s \rangle$. In both plots, ($\triangleright$) marks the fluid phase and (—) marks the solid phase.

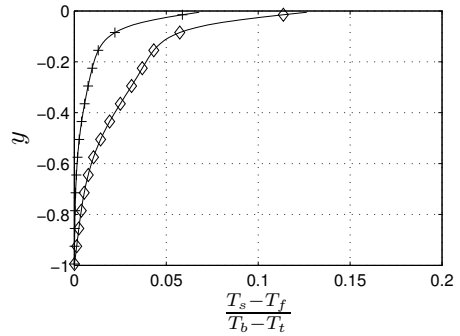

Figure 5.9: Natural convection with small wall-temperature ratio, $T_b/T_t = 1.05$. Normalized difference between the solid and fluid temperatures: ($\diamond$) at the axis of the cold plume ($x = 5.7$) and ($+$) averaged over the $x-$direction.

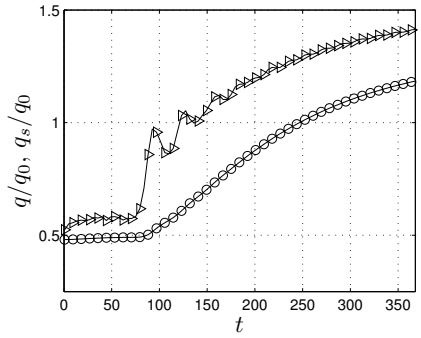

Figure 5.10: Natural convection with small wall-temperature ratio, $T_b/T_t = 1.05$. ($\triangleright$) : Normalized heat transfer rate of the fluid phase q. ($\circ$) : Normalized heat transfer rate of the solid matrix q_s. Both q and q_s are evaluated at the plane $y = -0.2$.

extent, let q and q_s denote the conductive heat transfer rates of the fluid the solid phase respectively, at a given plane parallel to the walls and to the interface *i.e.*,

$$q = \int_0^{L_x} \phi\, k\, \frac{\partial T}{\partial y}\, \mathrm{d}x \quad \textit{and} \quad q_s = \int_0^{L_x} (1-\phi)\, k_{\mathrm{s}22}\, \frac{\partial T}{\partial y}\, \mathrm{d}x, \tag{5.4.2}$$

Also, let q_0 denote the initial overall transfer rate, $q_0 = (q + q_s)_{t=0}$.

Figure 5.10 shows the evolution of the normalized rates q/q_0 and q_s/q_0 across the plane $y = -0.2$. It can be observed that both q and q_s remain almost constant at the early stages of evolution. At $t \simeq 75$, the hot and cold plumes begin to form and q increases at a high rate. This phase lasts for almost 20 time-units, which is the time that it takes for the plumes to reach their final shape. Subsequently, and until until $t = 180$, q keeps increasing albeit at a lower rate and in an oscillatory manner. At later times, the oscillations fade away and the increase rate of q becomes even lower. As regards q_s, it also starts increasing upon initialization of the convective motions. However, this increase is much smoother than that of q. Moreover, at later times, q_s also increases at a very low rate.

5.4.2 High wall-temperature ratio: $T_b/T_t = 2.0$

In this subsection, we study natural convection at a much higher wall-temperature ratio: $T_b/T_t = 2$. All other problem parameters are the same as before. The Rayleigh number based on the height of the porous medium is $Ra_l = 10^5$, while $Ra_{3l} = 2.7\times10^6$. According to the numerical simulation, initially the flow in the pure-fluid domain is organized in convection cells with the same main characteristics as the ones described above. However, we now observe the formation of four pairs of cells instead of two. The vorticity and temperature fields after the formation of the convection cells, at $t = 24$, are shown in Figure 5.11. Also, due to the increased Rayleigh number, the vorticity inside the convective cells is much stronger than in the previous case. Further, the cold and hot plumes soon start to oscillate, which leads to the breaking-up of the cells. Subsequently, the flow field becomes highly irregular, consisting of rollers of a wide range of sizes and vorticity magnitude, as is evidenced in Figure 5.12. The same figure also shows the fluid-temperature field at the same instance. As hot and cold patches of fluid pass through

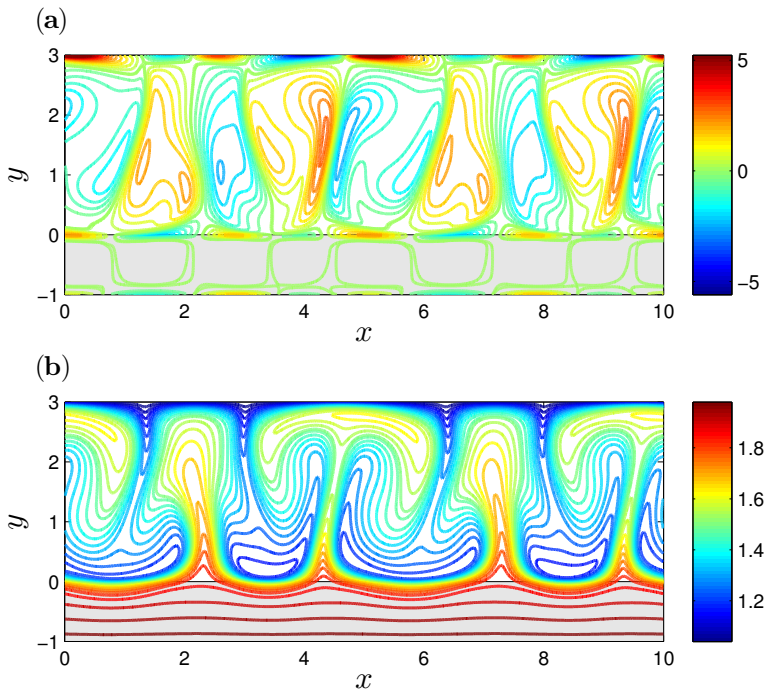

Figure 5.11: Natural convection with high wall-temperature ratio, $T_b/T_t = 2$. (a) Vorticity at $t = 24$, after the formation of the convection cells. Blue contours indicate negative vorticity and red contours indicate positive vorticity. All contours are at increments of 0.4 units. (b) Fluid temperature at the same time. Blue contours indicate temperatures below and red indicate temperatures above $\frac{T_b+T_t}{2}$. All contours are at increments of 0.04 units.

the porous material, the thermal non-equilibrium between the two phases becomes more evident and significantly more pronounced than in the previous case.

Figure 5.13 shows the profiles of the phasial temperatures inside the porous layer and at the location where a cold plume intersects the interface. As in the previous case, this is where thermal non-equilibrium is maximal. Also in this figure, we have plotted the $x-$averaged temperature profiles. From this plot it can be inferred that, globally, thermal non-equilibrium is no longer confined in the vicinity of the interface; instead, it is evidenced at larger distances below the interface. This is further confirmed by the plot of the normalized temperature difference between the two phases, shown in Figure 5.14. According to this figure, both the local and $x-$averaged normalized differences increase monotonically with y and attain their maximum values at the interface.

At later times, the flow evolves once again to two pairs of counter-rotating cells, similar

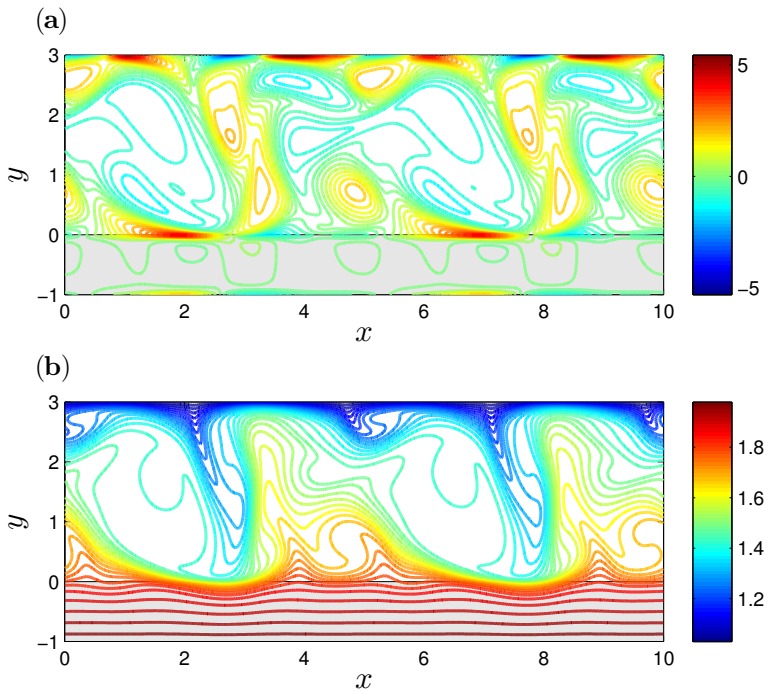

Figure 5.12: Natural convection with high wall-temperature ratio, $T_b/T_t = 2$. (a) Vorticity at $t = 39$. Blue contours indicate negative vorticity and red contours indicate positive vorticity. All contours are at increments of 0.3 units. (b) Fluid temperature at the same time. Blue contours indicate temperatures below and red indicate temperatures above $\frac{T_b+T_t}{2}$. All contours are at increments of 0.03 units.

to the ones observed in the case of small-temperature ratio. It should be stressed, however, that these results correspond to two-dimensional natural convection in superposed porous and pure-fluid domains. As such, three-dimensional effects have not been taken into account.

Finally, the evolution of the heat-transfer rates for this case is shown in Figure 5.15. As in the previous case, both q and q_s initially remain almost constant, until the plumes form. Subsequently, they both start to increase substantially. In particular, q increases in an oscillatory manner whereas q_s increases monotonically. After the formation of the stable two pairs of convective cells, both q and q_s increase smoothly but at a substantially lower rate.

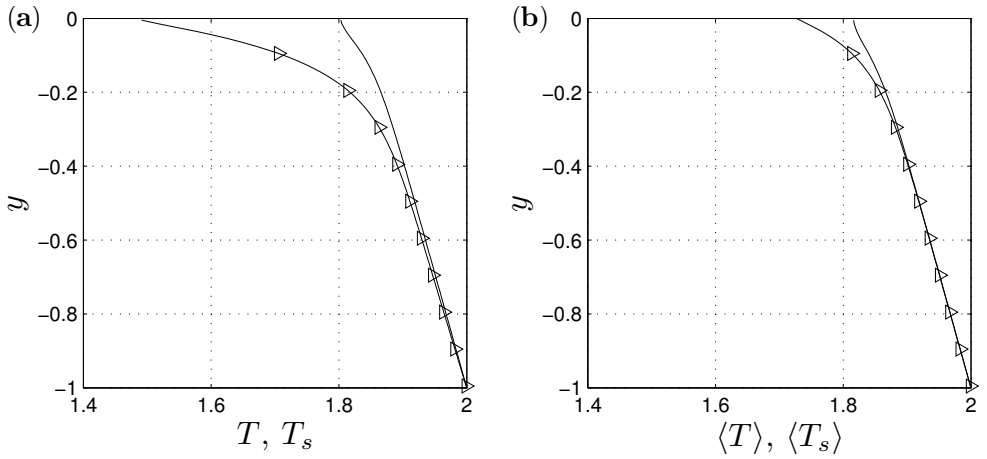

Figure 5.13: Natural convection with high wall-temperature ratio, $T_b/T_t = 2$: Temperature profiles of the solid and the fluid phase inside the porous material at $t = 39$, (a) at the location of the cold plume ($x = 7.6$), and (b) $x-$averaged profiles $\langle T\rangle$ and $\langle T_{\rm s}\rangle$. In both plots, ($\triangleright$) marks the fluid phase and (—) the solid phase.

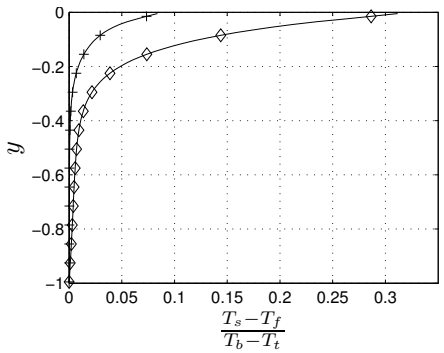

Figure 5.14: Natural convection with high wall-temperature ratio, $T_b/T_t = 2$. Normalized difference between the solid and fluid temperatures at $t = 39$: ($\diamond$) at the location of the cold plume ($x = 7.6$) and (+): averaged over the $x-$direction.

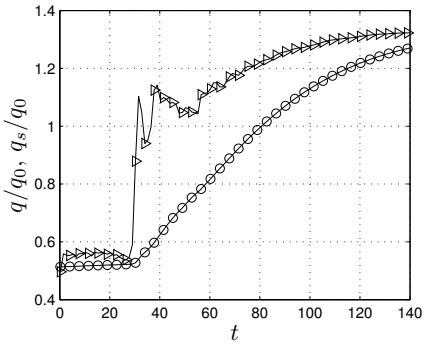

Figure 5.15: Natural convection with high wall-temperature ratio, $T_b/T_t = 2$. ($\triangleright$) : Normalized heat transfer rate of the fluid phase q. ($\circ$) : Normalized heat transfer rate of the solid matrix q_s. Both q and q_s are evaluated at the plane $y = -0.2$.

5.5 Unstably-stratified forced convection between parallel walls

In this section, we study the problem of unstably stratified forced flow in a channel with a porous strip attached to its lower wall. The domain configuration and numerical set-up are the same as the one used above for the study of natural convection. Namely, the domain dimensions, the location and physical properties of the porous layer as well as the boundary conditions are the same as above.

As regards the initial condition for the velocity, we prescribe the velocity distribution that is predicted numerically from the equivalent isothermal flow before the growth of the Kelvin-Helmholtz instabilities. This distribution consists of a very small value inside the porous layer, a transition profile across the interface and a parabolic profile in the pure-fluid domain. The plot of the streamwise velocity at the initial condition is shown in Figure 5.16. This distribution has been selected instead of zero initial velocity for purposes of computational savings. Further, as regards initial conditions for the temperatures of the two phases, we prescribe the same initial profiles as in the previous section, see Figure 5.4. These profiles correspond to steady-state conduction, assuming thermal equilibrium between the two phases.

The physical problem that we consider in the following, is active air-cooling over a heat sink of height equal to $0.13m$. The velocity of the air at half-width of the pure-fluid channel is $0.6m/s$, while the top cold wall is at room temperature (approximately $300K$).

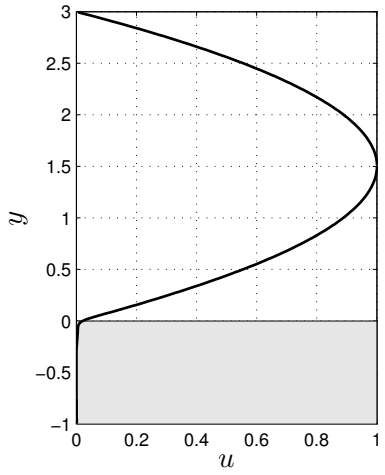

Figure 5.16: Unstably-stratified forced convection between parallel walls. Profile of the streamwise velocity component at $t = 0$.

The reference velocity for this problem is the initial streamwise velocity component along the centerline of the pure-fluid domain. As usual, the reference length is the height of the porous strip. As regards the material properties of the two phases, these are non-dimensionalized with the fluid-phase properties at the reference temperature, which is that of the cold wall. Based on these values, the Reynolds number is $Re = 5000$, the Richardson number is $Ri = 3.5493$ and the Prandtl number is $Pr = 0.71$.

5.5.1 Wall-temperature ratio $T_b/T_t = 1.5$

In the following, we present results when the wall-temperature ratio is set to $T_b/T_t = 1.5$. According to our simulation, the growth of the instabilities in the presence of unstable thermal stratification is more rapid than in the equivalent isothermal case. Accordingly, the rollers at the interface are formed at much earlier times. Figure 5.17 shows the vorticity field along-side the temperature field at four different instances during the evolution of the flow. From this figure we infer that the, in the present simulation the rollers have already been formed at $t = 11.5$. By comparison, in the isothermal case the roller formation occurs at $t \simeq 30$.

As the flow evolves, the vortices grow in size and change in shape; see Figure 5.17(c). As explained below subsequent paragraphs, this change in the shape of rollers is attributed

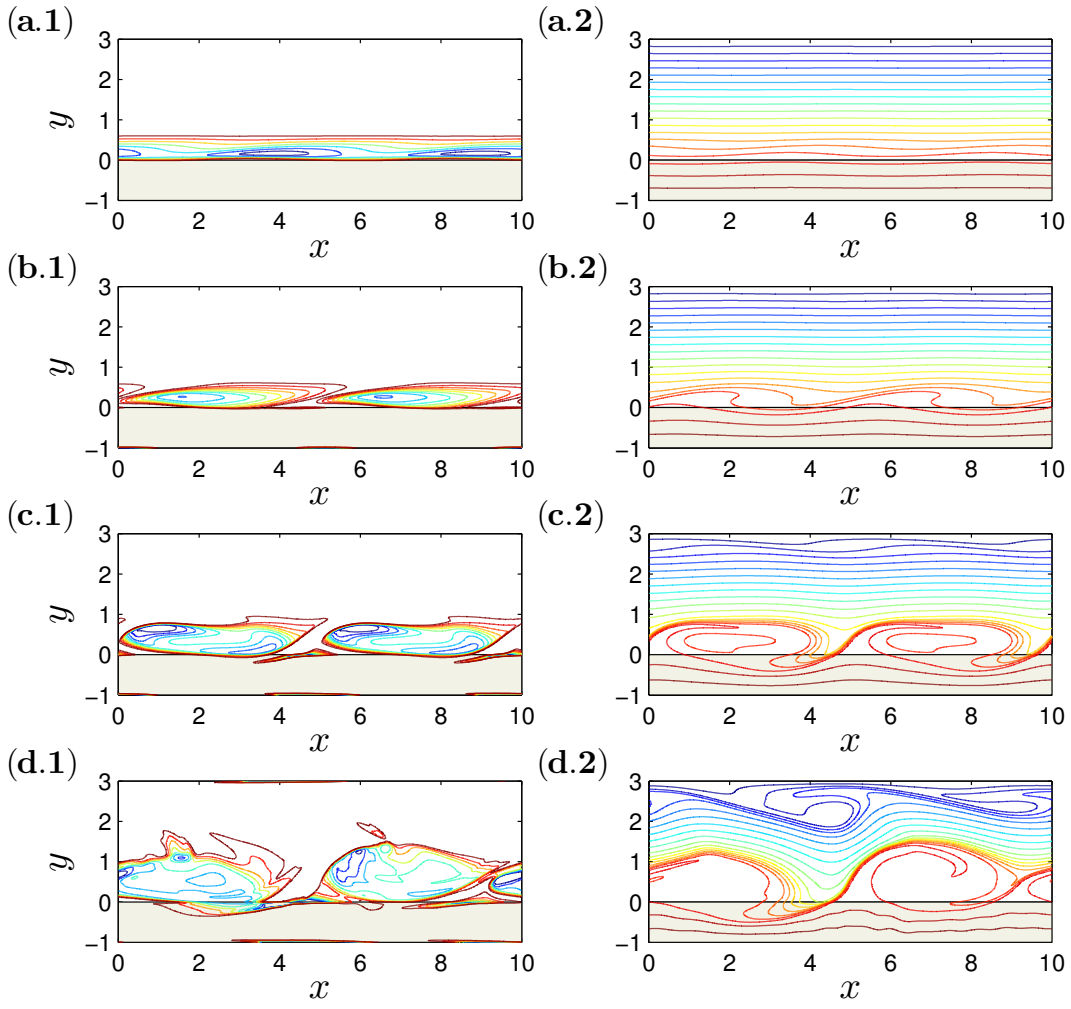

Figure 5.17: Forced flow in a channel with $T_b/T_t = 1.5$. Vorticity field (left) and the fluid temperature field (right) at four instances during the evolution of the flow. (a) $t = 6.15$; (b) $t = 11.5$; (c) $t = 20.13$; (d) $t = 44$.

to their interaction with streams of hot fluid emanating from the interior of the porous medium that move upwards. Eventually, the height of the rollers becomes equal to the pure-fluid domain's half-width. By that time, the vorticity distribution in the interior of the roller has become highly irregular (see Figure 5.17(d)). In the following paragraphs we describe the characteristics of the evolution of the flow as predicted by our simulation.

First we remark that the extent of the rollers in the porous strip is minimal. Further, the rollers do not resemble the round, symmetric srollers observed in isothermal flows (Chapter 4). In this case, the rollers are long and relatively thin, i.e. they have a "pancake"-like shape. Due to their limited height, the rollers appear to be squeezed and confined in between two unstably stratified layers of fluid, namely, the lower-density fluid inside the porous medium and the high-density fluid below the top wall. Moreover, as can be evidenced from Figure 5.17(b.1) and in contrast to the isothermal case, the vorticity maximum does not occur in the center of a roller, but very close to its (upstream) tail. Furthermore, vorticity peak inside the rollers is 26% higher than in the isothermal case.

Next we concentrate on the influence of the vortical structures (rollers) to thermal convection. Since the rollers induce fluid recirculation at the upper part of the porous layer, there is considerable thermal convection therein upon formation of the rollers. Further, our simulations predict that streams of hot fluid emanating from the interior of the porous medium move upward and cross the interface at the locations of the braid regions between two adjacent rollers. However, due to the strong circulation induced by the rollers, these hot streams are "pulled" by the rollers ahead of them and follow the rollers' motion. The interaction between the rising hot fluid and the rollers creates an area of positive vorticity which progressively grows and engulfs a significant part of the rollers. The rollers are then deformed and elongate even further, as can be seen in Figure 5.18. In turn, streams of low-temperature fluid are formed in the pure-fluid region and descend towards the interface at the braid regions. They pass behind the hot streams mentioned earlier and get pulled by their neighboring upstream roller.

A consequence of the entrainment of hot fluid by the rollers is that the area of the pure-fluid domain close to the top wall remains practically unaffected by the thermal convection phenomena that occur at the interface. This is so for times as advanced as $t \simeq 20$. In order to demonstrate this effect of fluid entrainment, we have plotted

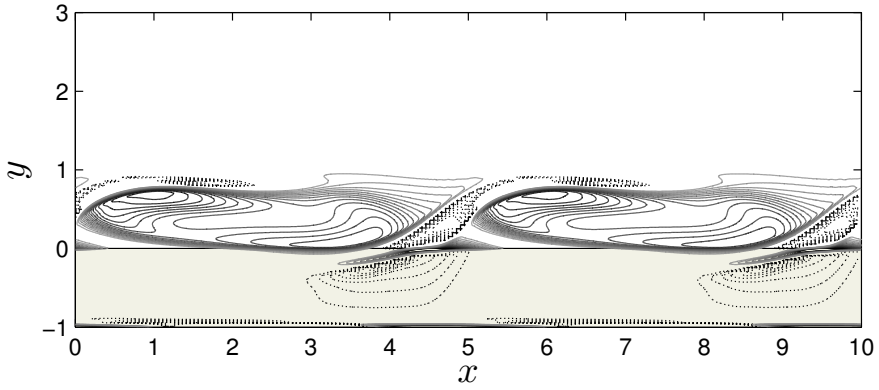

Figure 5.18: Forced channel flow, with $T_b/T_t = 1.5$. Vorticity field at $t = 20.13$. The solid contours indicate negative vorticity at increments of 0.08 units, while the dotted contours indicate positive vorticity at increments of 0.05 units.

the streamwise-averaged fluid temperature, in Figure 5.19. According to this plot, at $t = 20.13$ the difference of the mean fluid temperature from the profile at the initial condition for $y > 1$ is negligible. The isotherms for the same time are shown in Figure 5.17(c.2). This plot also shows that there are fluid-temperature variations along the x, close to the top wall, at $y \simeq 2.7$. However, these gradients develop due to the boundary layer at the top wall and not because of the interaction with the shear layer at the interface.

We now shift our attention to the characteristics of the flow field at later times. As mentioned earlier, the rollers grow in size and eventually their height becomes equal to the half-width of the pure-fluid domain, Figure 5.20. Due to their interaction with the emerging hot fluid from the braid regions, the vorticity amplitude in their interior does not increase monotonically toward the core of the roller. Instead, the vorticity distribution inside the rollers varies strongly and an irregular manner, thus exhibiting many local maxima. By contrast, the temperature variations inside the rollers are very small so that the fluid therein can be considered almost isothermal; see Figure 5.17(d.2).

From Figures 5.17(d.2) and 5.20 we also infer that a set of secondary vortices has developed close to the top in the form of sheets of weak positive vorticity.Eventually,

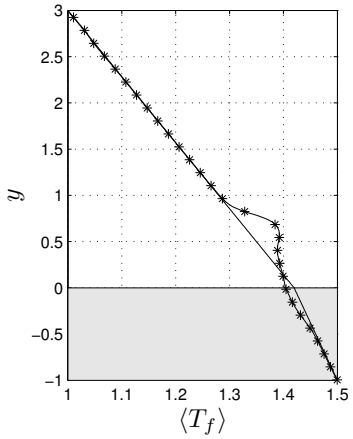

Figure 5.19: Forced channel flow with $T_b/T_t = 1.5$. Plots of the streamwise-averaged temperature $\langle T_f \rangle$ at: $(*)$ $t = 20.13$, and $(-)$ $t = 0$.

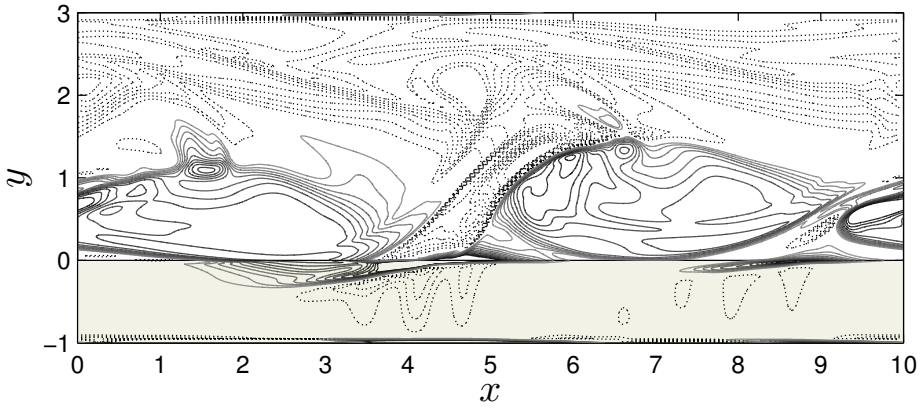

Figure 5.20: Forced channel flow with $T_b/T_t = 1.5$. Vorticity field at $t = 44$: the solid contours indicate negative vorticity, while the dotted contours indicate positive vorticity. All contours are at increments of 0.12 units.

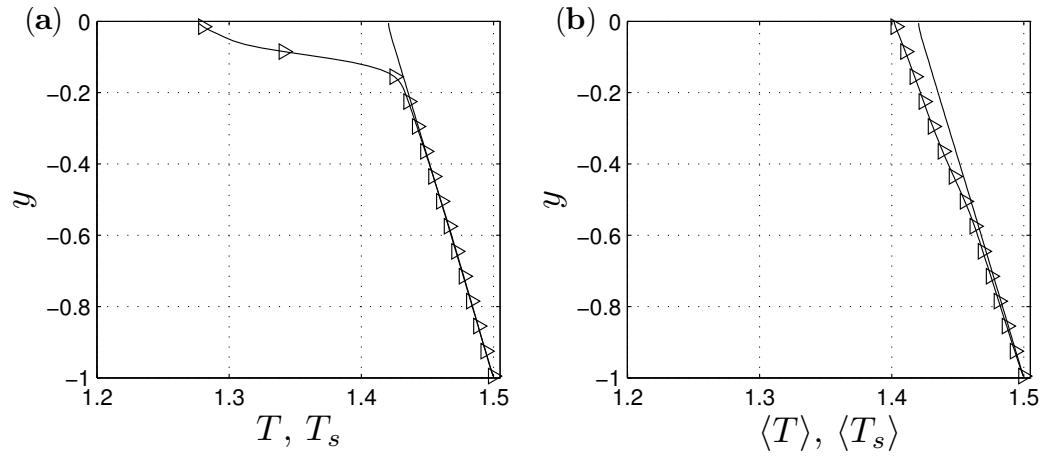

Figure 5.21: Forced channel flow with $T_b/T_t = 1.5$, at time $t = 44$. (a) Temperature profiles at a braid region. (b) Streamwise-averaged temperature profiles. ($\triangleright$): fluid temperature ; ($-$): solid temperature.

these structures grow in size and start to interact and blend with the rollers at the interface.

Next, we focus on the thermal non-equilibrium between the fluid and solid matrix in the porous medium. We first observe that, in analogy to natural convection, it is significant in the top part of the porous layer where there is significant fluid recirculation. Indeed, from Figure 5.21b, we see that the difference between $\langle T_f \rangle$ and $\langle T_s \rangle$ inside the porous layer, is considerable at distances up to $-0.5l$ from the interface. At larger depths, $y < -0.5l$, the two phasial temperatures are almost equal due to the limited fluid recirculation.

Furthermore, the locations where the temperature differences attain their maximal values are the braid region between rollers; see, for example, the phasial temperature profiles at $x = 4.23$ (which corresponds to a braid region according to Figure 5.20) and at time $t = 44$ that are shown in Figure 5.21a. At these locations, colder fluid from the pure-fluid domain approaches the interface from above, as can be infered from the streamlines in the region between the two rollers, plotted in Figure 5.22. By contrast, the fluid temperature inside the rollers at the interface is more or less uniform and close

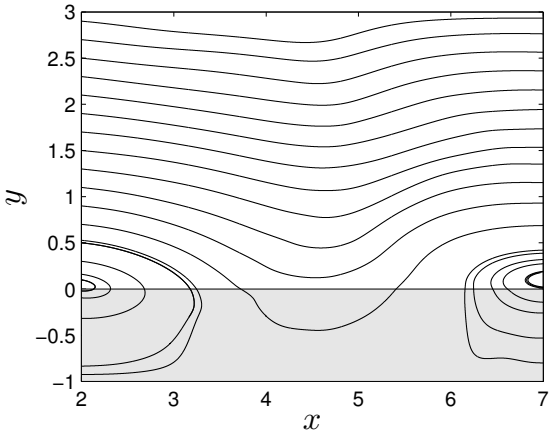

Figure 5.22: Forced channel flow with $T_b/T_t = 1.5$, at time $t = 44$. Streamlines in the region beween the two rollers that occupy the domain.

to the solid skeleton's temperature close to the interface, Figure 5.17(c.2). As such, the temperature of the fluid that is convected below the interface due to the rollers'motion, is not largely different from that of the surrounding solid matrix.

5.5.2 High wall-temperature ratio: $T_b/T_t = 2.0$

This subsection, focuses on the effect of higher wall-temperature ratios. In particular we discuss results from a simulation with $T_b/T_t = 2.0$. All the other problem parameters remain the same as before.

According to our numerical predictions, the flow evolves in the same manner as the one predicted for the previous case. However, the higher wall-temperature ratio results in a more rapid growth of the instabilities, as can be inferred from Figure 5.23. This figure shows plots of the normalized u_{rms} profiles at $t = 10.1$ for $T_b/T_t = 1.0$, 1.5 and 2.0. The normalization factor that we use is the friction velocity at the top wall, u_τ^{top}, for each case. Its definition is given in the presentation of our isothermal simulation, in Appendix A, but it is also provided here for completion purposes:

$$u_\tau^{top} = \sqrt{-\frac{\tau_{\text{t.w.}}}{\rho}}\ , \tag{5.5.1}$$

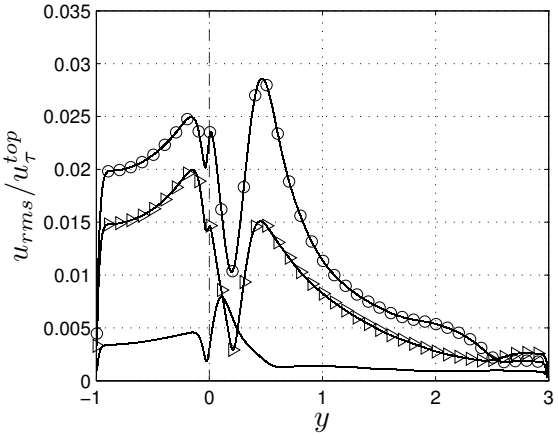

Figure 5.23: Forced channel flow. Plots of the normalized u_{rms} at time $t = 10.1$ for: $(-)$ $T_b/T_t = 1.0$, $(\triangleright)$ $T_b/T_t = 1.5$, and $(\circ)$ $T_b/T_t = 2.0$. The dashed vertical line indicates the position of the interface.

with $\tau_{\mathrm{t.w.}} = \mu \frac{\mathrm{d}U_{\mathrm{t.w.}}}{\mathrm{d}y}$ being the stress at the top wall. ($U_{\mathrm{t.w.}}$ is the plane-averaged streamwise velocity component at the top wall).

According to this figure, at $t = 10.1$, the shear layer in absence of stratification is at its early stages of development. This justifies the low amplitude of u_{rms} at all locations of the domain. On the other hand, in both cases of unstable stratification, the roller formation has already been completed by that time. This implies high peak values and steep gradients of u_{rms} at both sides of the interface. Further, we observe that the maximum of u_{rms} in the pure-fluid region for the case of $T_b/T_t = 2.0$ is almost double than in the case of $T_b/T_t = 1.5$, which highlights the effect of the higher wall-temperature ratio on the instability growth-rate.

Moreover, the higher stratification also affects the structure of the rollers. In particular, the buoyancy effects are strong enough to cause the rollers to stretch further in the streamwise direction, thus becoming even more elongated. In this manner, the downstream part (head) and the upstream part (tail) of a roller are pulled in different directions.

In particular, the head of the roller is pulled upwards and climbs over the tail of the roller ahead of it. This phenomenon can be evidenced in Figure 5.24 and it occurs at

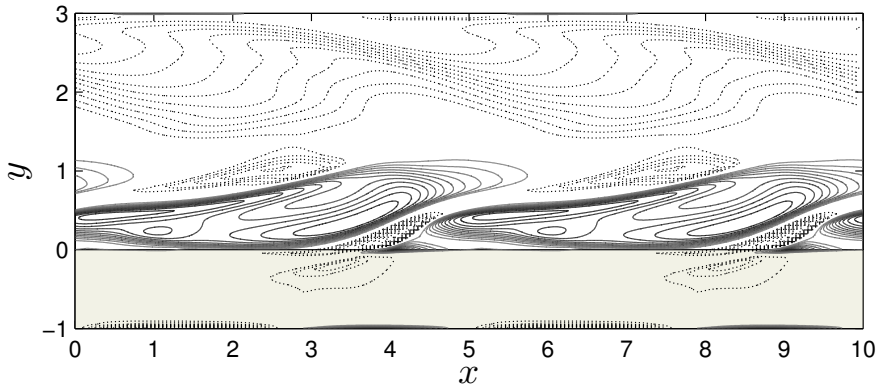

Figure 5.24: Forced channel flow with wall-temperature ratio $T_b/T_t = 2.0$. Vorticity field at $t = 17.34$: the solid contours indicate negative vorticity, while the dotted contours indicate positive vorticity. All contours are at increments of 0.12 units.

$x \simeq 5$ and at $x \simeq 9.5$. At the same time, the negative vorticity at the tail of the roller is sufficiently high to keep the fluid recirculating in the vicinity of the interface at $y = 0$. Overall, this stretching of the rollers and upward movement of their heads provide the circumstances for a pairing process to initiate.

More precisely, the head of an upstream roller and the tail of the downstream one merge by rotating around each other. This process is similar to the one that was predicted in our simulations of isothermal shear layers in Section 4.4. Once the pairing is completed, the newly formed roller is bigger in size and its height is equal to alsmost 2/3 of the height of the pure-fluid domain, as can be shown in figures 5.25a and 5.25b.

Of particular interest is the influence of the pairing process to the thermal non-equilibrium inside the porous medium. Following the rotating motion of the merging vortical structures, lower-temperature fluid from higher parts of the pure-fluid region, gets drawn through the braid regions and into the porous medium. This can be shown in Figure 5.25b and at locations $x \simeq 1$ and $x \simeq 5.6$. These are the locations where the temperature differences between the two phases become maximal. Plots of the phasial temperatures at $x = 5.6$ are provided in Figure 5.26a. The streamwise averaged profiles for the same time instance are given in Figure 5.26b. The differences in the curves of

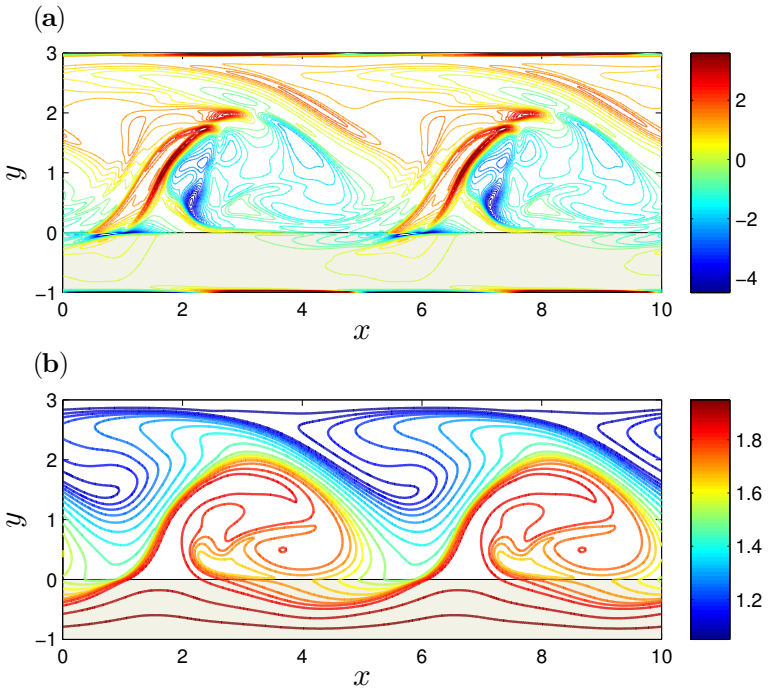

Figure 5.25: Forced channel flow, with $T_b/T_t = 2.0$. (a) Vorticity field at $t = 21$: the blue contours indicate negative vorticity, while the red contours indicate positive vorticity. All contours are at increments of 0.25 units. (b) Fluid temperature contours at the same time and at increments of 0.05 units.

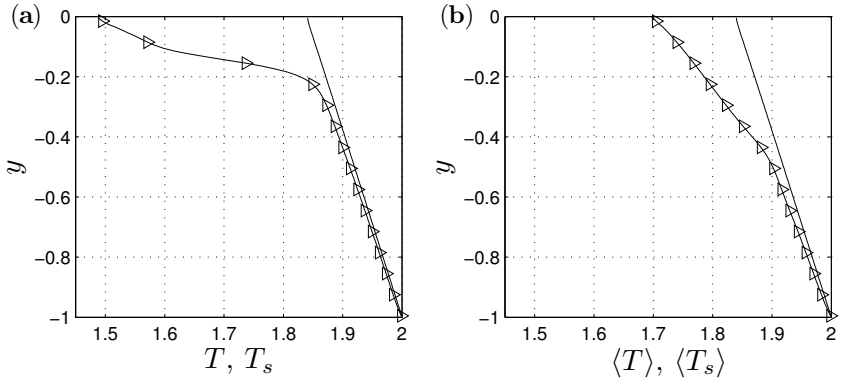

Figure 5.26: Forced channel flow, with $T_b/T_t = 2.0$, at time $t = 21$. (a) Temperature profiles at braid-region, $x = 5.63$. (b) Streamwise-averaged temperature profiles. ($\triangleright$): fluid temperature ; ($-$) solid temperature.

$\langle T_f \rangle$ and $\langle T_\mathrm{s} \rangle$ inside the porous layer are significantly increased in the upper half of the porous strip when compared to the case of lower wall-temperature ratio (Figure 5.21). This corroborates the fact that higher density stratification increases thermal convection and enhances thermal non-equilibrium inside the porous material.

5.6 Stratified shear layers

According to our previous numerical simulations of isothermal shear layers at the interface of a porous layer and a pure-fluid domain, the onset and growth of the Kelvin-Helmholtz instability leads to roller formation and pairings and significant growth of the shear layers. In this section, we analyze the effect of stratification on the characteristics of the shear layers of interest.

In the discussion that follows, we use U to denote the streamwise-averaged value of the streamwise component of the velocity, *i.e* $U = \langle u \rangle$. Further, the momentum thickness of the stratified shear layers is given by the following expression:

$$\delta_m \;=\; \frac{1}{(\langle \rho u \rangle_T - \langle \rho u \rangle_F)^2} \int_F^T \phi \left(\langle \rho u \rangle - \langle \rho u \rangle_F \right) \left(\langle \rho u \rangle_T - \langle \rho u \rangle \right) \mathrm{d}y \,, \tag{5.6.1}$$

where F denotes the lowest point of the free-stream region inside the porous medium and T denotes the coordinate of the top boundary of the domain.

For the purposes of our study, the dimensions of the pure-fluid and porous regions, as well as their positions in the flow domain are the same as the ones employed in our simulations of isothermal shear layers, Chapter 4, Section 4.4. As regards boundary conditions, the domain is assumed to be periodic along the streamwise direction. Along the cross-stream direction we prescribe a no-slip (wall) condition at the bottom boundary, and a free-slip condition at the top boundary. Further, both top and bottom boundaries are assumed to be adiabatic; as such, the normal gradients of the two phasial temperatures are assumed to be zero along these boundaries.

The initial conditions for the velocity and pressure fields are generated via a preliminary simulation of forced flow, identical to the one performed for the isothermal case. This yields the streamwise velocity profile shown in Figure 4.3, page 65, where the difference of the free-stream velocities between the porous and the pure-fluid regions is $\Delta U|_{t=0} = 2$.

As regards the initial fluid temperature distribution, it is homogeneous in the streamwise direction. In the cross-stream direction, we prescribe an arc-tangent profile,

$$T_{t=0} = tan^{-1}(\mathcal{C}\, y)\, \frac{T_t - T_b}{\pi} + \frac{T_t + T_b}{2}\,. \tag{5.6.2}$$

The value of $\mathcal{C}$ is set at $\mathcal{C} = 50$. With this particular profile, the fluid temperature converges rapidly to the value T_t for increasing y and to the value T_b for decreasing y. Also, its value at the interface, $y = 0$, is $(T_t + T_b)/2$. Further, we assume that the fluid and the solid matrix are initially at thermal equilibrium.

For this problem, the reference velocity is the initial free-stream velocity inside the porous layer, which is assumed to be $0.204m/s$. As in all cases considered in this thesis, the reference length is the height of the porous strip, herein set at $0.085m$. Finally, the reference temperature is that of the cold fluid, $300K$, whether it is at top free-slip boundary (unstable stratification) or at the bottom wall (stable stratification). Accordingly, relevant application examples in the case of unstable stratification, include the flow of cold air (temperature of $300K$), above heat exchangers or cooling devices which are at $450K$. On the other hand, for the problem of stable stratification, the porous structure is at reference temperature, while the air flowing through it, is at $450K$.

Based on the afore-mentioned reference values, the Reynolds number is $Re = 1110$. Also the Richardson number is set at $Ri = 20$, and the Prandtl number is $Pr = 0.71$.

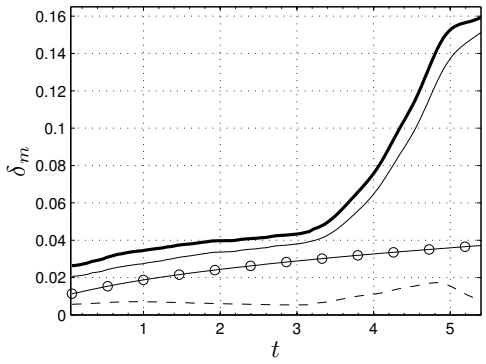

Figure 5.27: Growth history of the momentum thickness for an unstably stratified shear layer with with $T_b/T_t = 1.5$ and Richardson number $Ri = 20$. (—) : δ_m ; (—) : δ_m^+ ; (- - -) : δ_m^- . Also, ($\circ$) : δ_m of the isothermal shear layer.

Finally, for the case of unstable stratification we set $T_b/T_t = 1.5$, while for the case of stable stratification we set $T_t/T_b = 1.5$.

5.6.1 Simulation of shear layers with unstable stratification

Our numerical results predict that unstable stratification results in faster growth of the instabilities. This is evidenced clearly upon comparison of the plots of the histories of the momentum thickness δ_m for the unstably-stratified and the isothermal shear layers, shown in Figure 5.27. As can be inferred from this figure, at time $t = 5$, in the unstably stratified shear layer the rollers have already been formed and roller pairing has initiated. By contrast, the isothermal shear layer is still at the early stages of its evolution at that time.

As regards the unstably stratified shear layer in particular, the momentum thickness δ_m grows according to the $\sqrt{t}$- law up until $t \simeq 3$. After this time, the rollers start to form at the interface, see Figure 5.28(a)), and the growth-rate of δ_m increases substantially. Later on, vortex-pairings contribute to the further growth of δ_m. During this pairing process, lower-temperature fluid from the upper layers of the pure-fluid region enters the porous medium as is evidenced by the contour plots of the fluid temperature shown in Figure 5.28(c.2). At this point, thermal non-equilibrium becomes important even at

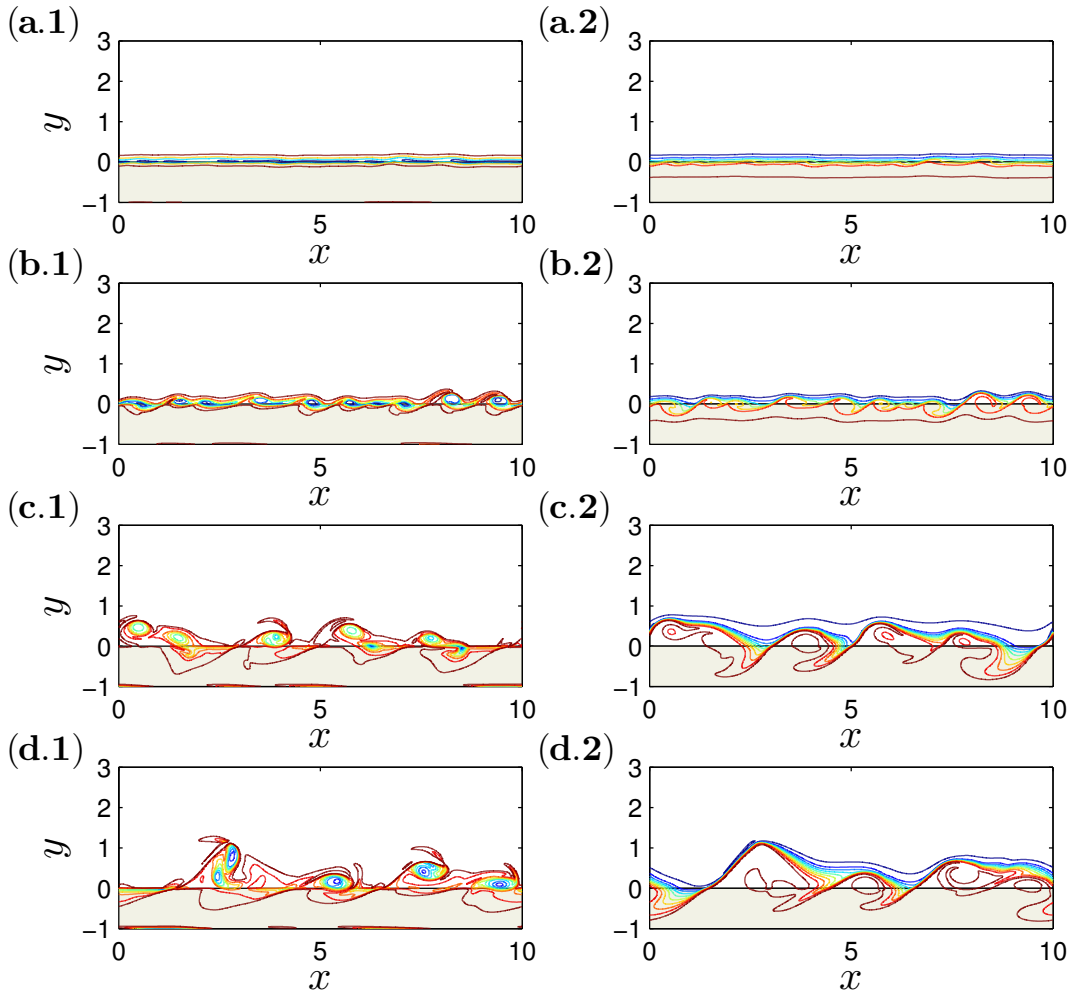

Figure 5.28: Unstably-stratified shear layer. Vorticity field (left) and fluid temperature field (right) at four instances during the evolution of the flow. (a) $t = 3.09$; (b) $t = 3.65$; (c) $t = 4.66$; (d) $t = 5.38$.

large distances from the interface. In the following paragraphs, we describe in detail some important aspects of the evolution of this shear layer.

At early times, the evolution of the shear layer is quite similar to the one of the isothermal case that was discussed in Section 4.4. In particular, up to time $t \simeq 3$, δ_m^+ grows as a function of $\sqrt{t}$, whereas δ_m^- remains almost constant, as can be evidenced in Figure 5.27. Thus, as mentioned earlier, the overall momentum thickness, $\delta_m = \delta_m^+ + \delta_m^-$ grows as a functions of $\sqrt{t}$.

During this period, the velocity inside the porous strip drops because of the interphasial drag and by $t = 1.62$ it reaches approximately 3% of the value at the initial condition. From this moment and up to $t \simeq 3$, the plots of $U/\Delta U$ collapse, which confirms that the layer grows in a self-similar manner. Up to this point, the instabilities do not grow enough to induce significant velocity fluctuations. This implies that the Reynolds stresses remain low during this period. It is interesting to mention that the duration of this first phase of evolution of the unstably stratified shear is $t \simeq 3$, whereas in the isothermal case it is much longer, $t \simeq 10.5$

At approximately $t \simeq 3$ the shear layer starts to roll-up. Because of this, the growth rate δ_m increases by a factor of 15, as can be inferred from Figure 5.27). Once the vortices are formed, a part of the fluid they entrain recirculates below the interface, thus inducing thermal non-equilibrium between the fluid and the solid matrix inside the porous medium. The temperature differences between the two phases are particularly large at the braid regions where streams of irrotational fluid at lower temperature enters the porous medium from the pure-fluid region. A similar phenomenon has been predicted in our simulations of forced flow that was described in the previous section.

Soon after, the vortices start to pair. In particular, rollers climb higher in the pure-fluid domain, as they rotate around their downstream neighbors. As we saw in Section 4.4 for the isothermal shear layer, this motion causes the momentum thickness above the interface to grow in an oscillatory manner. However in the unstably-stratified problem, the fluid entrained by the rollers is of lower density compared to the surrounding fluid higher in the domain. This reduces the contribution of the upward-moving roller to the growth of δ_m^+. As a result, the growth of δ_m^+ does no longer occur in an oscillatory fashion and pairing events can no longer be identified as local maxima in the history of δ_m^+.

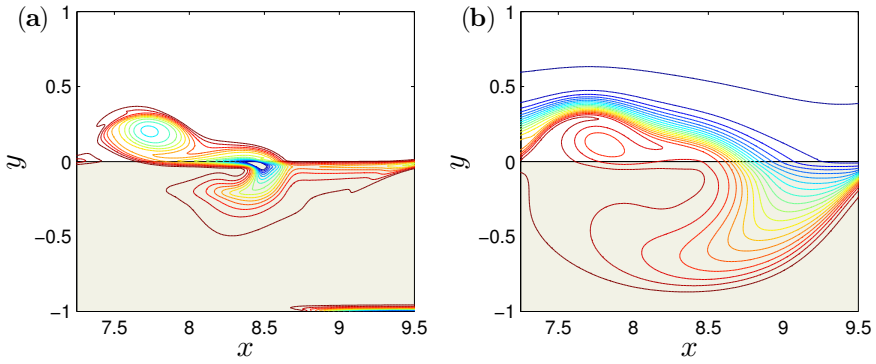

Figure 5.29: Unstably-stratified shear layer. (a) Contours of negative vorticity at time $t = 4.66$ and at increments of 2.5 units. (b) Contours of fluid temperature at the same time and at increments of 0.025 units.

Instead, δ_m^+ grows monotonically, albeit in a fast rate owing to the simultaneous pairings occurring throughout the domain (Figure 5.27).

Apart from this pairing mechanism that was also observed in the constant-density problem, our simulations predict an additional pairing mechanism in place. In particular, at certain braid regions, the streams of downward moving fluid of higher density dominates over weak vortices upstream of their location. When this occurs, a roller is forced inside the porous medium where it slows down due interphasial drag. Then, it is absorbed (consumed) by the neighboring upstream roller, thus allowing more space for higher-density fluid to reach deep inside the porous material. Figure 5.29 depicts a detail of the flow at time $t = 4.66$ where such a pairing occurs. In this figure, the deformed roller located at $x = 8.45$, is gradually being consumed by its upstream neighbor at $x = 7.75$ (Figure 5.29a). As expected, the temperature of the fluid that enters the porous medium through the weakened braid region increases due to heat conduction and interphasial heat exchange. Moreover, the normal velocity component of this stream is high enough to convect lower-temperature fluid close to the bottom wall.

Next, we elaborate on the differences between the phasial temperatures inside the porous medium. First we remark that the temperature of the solid matrix varies only slightly in the streamwise direction. Further, in the cross-stream direction, it decreases

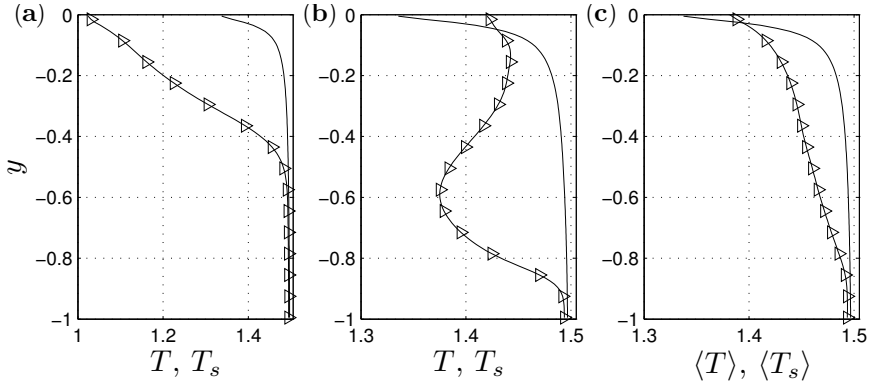

Figure 5.30: Unstably-stratified shear layer at time $t = 4.66$. (a) Temperature profiles at the braid region, $x = 9.31$. (b) Temperature profiles below the rollers during pairing. (c) Streamwise-averaged temperature profiles. ($\triangleright$): fluid phase ; ($-$): solid phase.

monotonically. Close to the bottom wall, this decrease is very small but it becomes much steeper as we approach the interface. The steep decrease of T_s starts at, approximately, $y \simeq -0.2$.

By contrast, the fluid temperature below the interface exhibits strong and non-monotone variations in both spatial directions. The bulk fluid motion below the interface that was described in the previous paragraph plays a significant role to the emergence of thermal non-equilibrium. Figure 5.30a shows the maximum temperature difference between the two phases at $t = 4.66$ (same time as in Figure 5.29. The maximum difference occurs at the weakened braid region, $x = 9.31$. Also, according to Figure 5.30b, thermal non-equilibrium between the two phases are significant below the rollers and peak at substantial depth, $y \simeq -0.6$. Finally, the impact of this pairing mechanism on thermal non-equilibrium, can also be evidenced in the mean temperature profiles shown in Figure 5.30c. According to this figure, the difference between the streamwise-averaged temperatures is significant even at small distances from the bottom wall.

As expected, the temperature gradients of the recirculating fluid inside the porous medium affect the momentum thickness as well. The influx of fluid of lower density from the braid regions, in combination with the rollers that reach below the interface during pairing, modulate the growth of the momentum thickness δ_m^- below the interface.

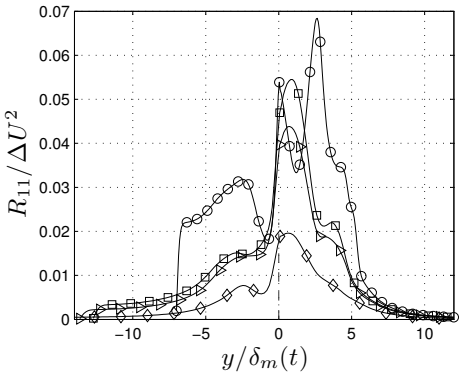

Figure 5.31: Unstably-stratified shear layer: Reynolds stresses during roller pairings. ($\diamond : t = 3.55$; $\triangleright : t = 3.95$; $\square : t = 4.4$; $\circ : t = 4.82$).

Interestingly, δ_m^- grows at a slow linear rate from the time of roller formation, $t \simeq 3.0$ until $t \simeq 4.8$, as evidenced in Figure 5.27). By contrast, in the isothermal case, δ_m^- fluctuates with time, as a consequence of the rollers's motion deep inside the porous medium during the pairing pairing.

Finally, we examine the growth of the velocity fluctuations after the roll-up. In Figure 5.31 we plot the Reynolds stresses at four times the rollers' formation and pairing processes. From this figure we can attest that(scaled) Reynolds stresses $R_{11}/\Delta U^2$ increase monotonically with time. Further, they are considerably higher than in the equivalent isothermal case. Evidently, this is expected since the unstable stratified shear layer grows much faster than the isothermal one. Finally, we remark that at $t = 4.82$, the Reynolds stresses below the interface remain considerably high until the drop fast to zero at a depth almost equal to the half-width of the porous layer. This indicates that by that time, the shear layer has grown enough to interact with the bottom wall.

5.6.2 Simulation of shear layers with stable stratification

In this subsection, we present results of simulations of a shear layer under stable stratification. The numerical set-up, boundary conditions and initial velocity distributions remain the same as in the previous case of unstable stratification. As regards the initial

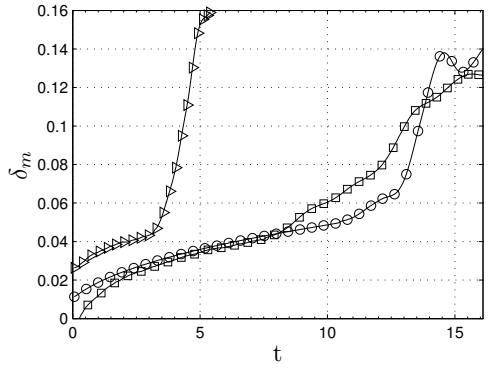

Figure 5.32: Growth history of the momentum thickness δ_m for the stably-stratified ($\square$), isothermal ($\circ$) and unstably-stratified ($\triangleright$) shear layers.

condition for the temperatures of the two phases, it is generated in the way that was described in the previous subsection, i.e. we consider an arc-tangent profile. In the case of stable stratification, however, we set that $T_t/T_b = 1.5$. Further, the reference length and the reference velocity are $0.068m$ and $0.257m/s$ respectively. Accordingly, the Reynolds and the Prandtl numbers have the same values as in the previous subsection, $Re = 1110$ and $Pr = 0.71$. However the Richardson number for this problem is set to $Ri = 10$.

We start again our presentation with the examination of the growth of the momentum thickness, δ_m. Its time history is plotted in Figure 5.32. In the same figure we have also included the plots of δ_m plots for the isothermal and the unstably-stratified cases. We can see that the roll-up of the shear layer under stable stratification occurs at $t \simeq 8$, which coincides with the time that the growth rate of δ_m increases abruptly. The same figure shows that the corresponding event in the isothermal cases occurs more than two time-units later. At later times, the slope of δ_m increases further, albeit at a slower rate, due to the process of. According to our results, the maximum slope of δ_m for the stably stratified shear layer is 0.0251. By comparison, for the isothermal case the maximum slope is 0.0509 and for the unstably-stratified it 0.0939. In other words, stable stratification results in milder growth of the shear layer. The same result is corroborated upon comparison of the Reynolds stresses of all three shear layers, plotted in Figure 5.33. In particular, under stable stratification the Reynolds stresses are smaller than in the isothermal case which,

in turn are smaller than in the case of unstable stratification.

Another point of interest is the structure of the rollers that are developed at the interface. Figure 5.34a shows the vorticity iso-contours of three rollers, at time $t = 9.67$. We observe that the maximum vorticity amplitude does not occur in the center of a roller. This is especially so for the two upstream rollers shown in this figure. Instead, the maximum is located at the roller's upper part, so that the vorticity contours around it form a hat-like shape on top of the rollers' core. In fact, upon inspection of the temperature field shown in Figure 5.34b, we see that the maximum of vorticity coincides with the local maximum of the gradient of the fluid temperature.

Finally, we discuss the temperature distributions inside the porous medium. As in the case of unstable stratification, T_s varies only slightly in the streamwise direction. Further, in the normal direction, it varies monotonically and it increases. Close to the bottom wall, this increase is very small but it becomes much steeper as we approach the interface. The steep increase of T_s starts again at, approximately, $y \simeq -0.2$. By contrast, the variations of the fluid temperature are significant in both directions. However, T also increase monotonically in the y direction inside the porous medium.

As regards the temperature differences between the two phases, we recall that, in the case of unstable stratification, they are maximized during roller pairings. This has been attributed mainly to irrotational fluid which moves from the higher regions of the pure-fluid domain down to the braid regions of the shear layer. Contrary to that case, in the stably-stratified shear layer the buoyancy effects tend to isolate the fluid in the pure region from that in the porous region. As such, there is no clear evidence of the development of a stream of higher-temperature fluid towards the braid regions when the vorticity in these region weakens during pairing. Consequently, the pairing events only mildly affect the temperature differences between the two phases inside the porous medium. In Figure 5.35 we provide the temperature profiles during pairing, at time $t = 13.38$. Figure 5.35a corresponds to the location of a braid region at $x = 3.4$, where $|T - T_{\mathrm{s}}|$ attains its maximum. Upon comparison with the equivalent figure for the case of unstable stratification, Figure 5.30a, we see that the difference is much smaller due to weaker convective motions inside the porous layer. Further, the temperature difference becomes negligible for distances higher than $0.2l$ from the interface. By contrast, below

the rollers, the temperature differences persists at longer distances from the interface. Figure 5.35b shows it is non-negligible even at $y \simeq -0.6$. A more global view of the difference between the phasial temperatures is provided in Figure 5.35c. According to this figure, the streamwise averaged profiles coincide for $y < -0.4$.

5.7 Conclusions

In this chapter, we have employed the thermo-mechanical model for flows in coupled porous medium - pure fluid domains, described in Chapter 2 , to perform numerical simulations of natural and forced convection, as well as simulations of stratified shear flows in these domains. All the problems considered in this chapter are summarized in Table 5.1, which is also included here for the convenience of the reader.

	T_b/T_t	Re	Ri	Pr	ϕ	Subsection
Comparison with Experiments	1.0341[a]	35.608	1	12671	0.38	5.2.1
Natural Convection	1.05	375	1	0.71	0.9	5.4.1
	2.0	375	1	0.71	0.9	5.4.2
Forced Convection	1.5	5000	3.5493	0.71	0.9	5.5.1
	2.0	5000	3.5493	0.71	0.9	5.5.2
Stratified Shear Layers	1.5	1110	20	0.71	0.9	5.6.1
	0.666	1110	10	0.71	0.9	5.6.2

[a]For the setup of the problem that is compared to experimental data, the side walls are kept in different temperatures, so that $T_L/T_R = 1.0341$.

First, we tested the numerical algorithm presented in Chapter 3, by comparing results from a numerical simulation of natural convection, with the corresponding experimental data reported for the same problem in Beckermann *et al.* (1988). Our predictions overestimate the convective heat transfer effects inside the porous medium and away from the top wall. However this is attributed to inaccuracies introduced by Beckermann *et al.* in their experimental procedure. The discrepancies between the numerical results and

the experimental data are reasonable, and the proposed method is found suitable for the treatment of the flows of interest.

Subsequently, we studied numerically natural convection in a horizontal channel. For small wall-temperature ratios, the flow evolves to the formation of regular and stable convective cells. Also, thermal non-equilibrium between the two phases is appreciable only in areas of pronounced fluid convection, close to the interface. On the other hand, at high wall-temperature ratios, the regularity of the initially formed convective cells breaks down while the hot and cold plumes of fluid start to oscillate. Subsequently, the plumes get distorted and mix. This process eventually leads to the formation of two stable pairs of convective cells. For this case, our simulations further predict large temperature gradients and significant thermal non-equilibrium between the two phases inside the porous domain. In all cases considered in our numerical study, the extent of the convective cells is limited in the pure-fluid domain, which implies that the porous layer has a stabilizing effect to natural convection.

Next, we studied numerically forced convection between two parallel plates unstable statification. According to our simulations, the rollers that are formed on the interface prevent the hot fluid from rising toward the upper part of the domain. This keeps the upper part of the domain unaffected by the thermal phenomena that occur at the interface in the early stages of development of the flow. However the rollers progressively grow and the entrained hot fluid is convected higher in the pure-fluid domain. The interaction between the hot fluid and the rollers results also in the stretching and elongation of the rollers. At high wall-temperature ratios, this stretching almost tears the rollers into two parts. These parts merge with their respective neighboring rollers merge, thus resulting to a set of new, larger rollers. The height of these new rollers is much larger so that the rollers eventually interact with the top wall. Further, the fluid recirculation below the interface that is induced by the rollers results in significant thermal non-equilibrium even at large distances below the interface. Interestingly, the maximum difference between the fluid and solid-matrix temperature occur below the braid regions in between the rollers, due to downward motion of cold fluid emanating from the pure-fluid domain.

Finally, we have investigated the effect of both stable and unstable stratification on temporally-developing shear layers at the interface between a porous and a pure-fluid

layer. The numerical predictions show that at early times the evolution of the stratified layers have the same characteristics as the isothermal ones. The momentum thickness grows as a function of $\sqrt{t}$ and the shear layers evolve in a self-similar manner. On the other hand, at later times and after the shear layers' roll-up, self-similarity is not re-established as it happens in the isothermal case.

In unstably stratified layers, the growth of the instabilities is faster than in the isothermal ones. The formation of the rollers occurs at earlier times and the subsequent growth-rate of the momentum thickness is steeper. During pairing, the weakened vorticity distribution at the the braid regions allows buoyancy to drive low-temperature fluid from the upper part of the domain into the porous region. Then, fluid convection below the interface is increased and thermal non-equilibrium becomes important even at short distances from the bottom wall.

As regards shear layers under stable stratification, the roll-up also occurs at an earlier time than in the isothermal problem. Even so, the slope of momentum thickness and the growth of the Reynolds stresses after the roll-up are smaller than in the isothermal case. In other words, the shear layer grows at a smaller rate. A noticeable difference from unstably stratified flows is that buoyancy effects in this case hinder the mixing of fluid from porous and pure-fluid regions of the domain. Therefore, fluid convection below the interface is weaker. This, in turn implies and thermal non-equilibrium is considerable at shorter distances from the interface.

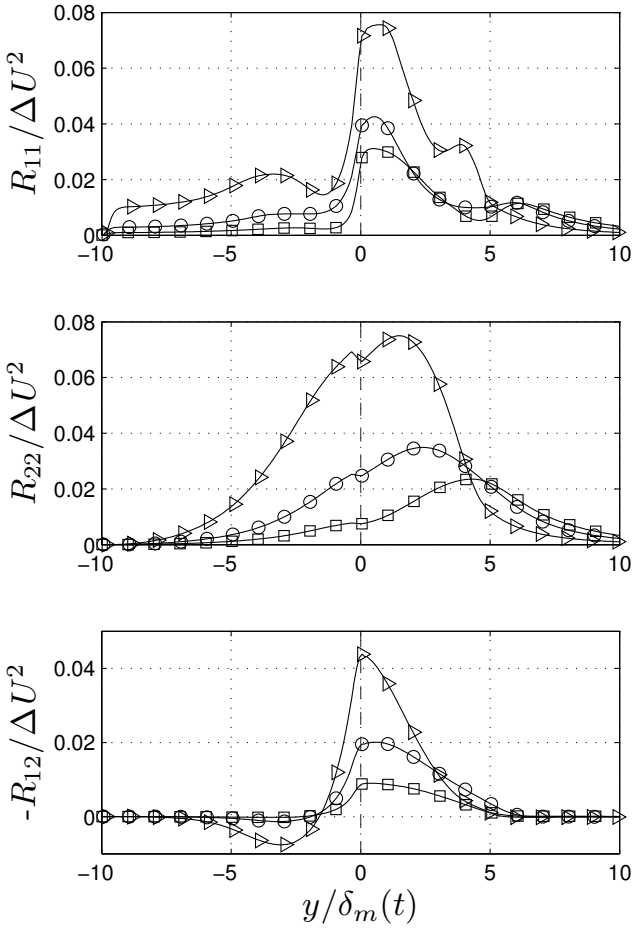

Figure 5.33: Reynolds stresses when $\delta_m = 0.1$. (□): stably-stratified shear layer at $t = 13.01$. (○): isothermal shear layer at $t = 13.61$. (▷): unstably-stratified shear layer at $t = 4.36$.

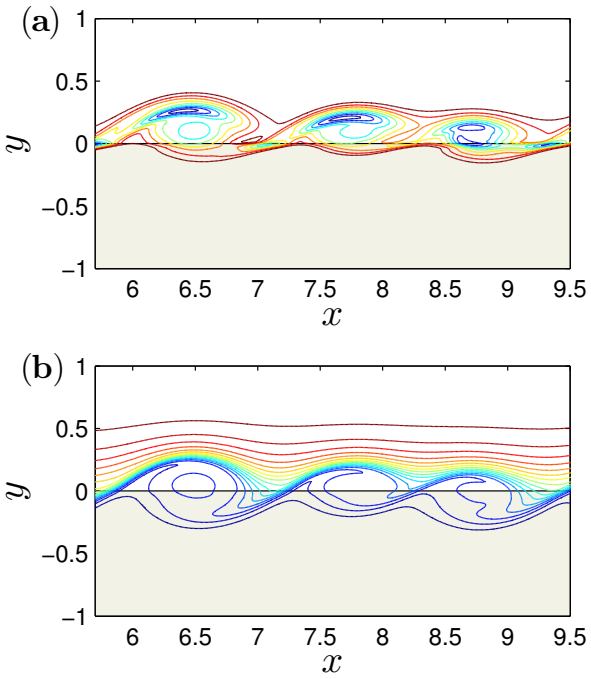

Figure 5.34: Stably-stratified shear layer with $T_t/T_b = 1.5$ and $Ri = 10$, at time $t = 9.67$ (a) Negative spanwise vorticity at increments of 1.5 units. (b) Fluid-temperature iso-contours at increments of 0.03 units.

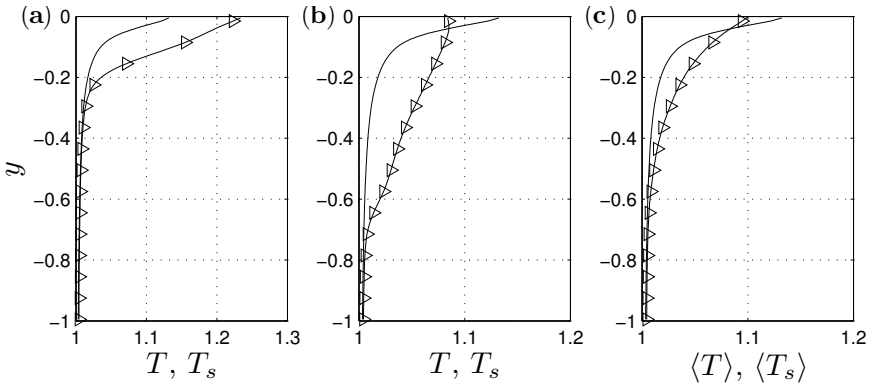

Figure 5.35: Stably-stratified shear layer with $T_t/T_b = 1.5$ and $Ri = 10$, at time $t = 13.38$. (a) Temperature profiles at the braid region, $x = 3.4$. (b) Temperature profiles below the upstream roller. (c) Streamwise-averaged temperature profiles. In all three figures ($\triangleright$) marks the fluid and ($-$) the solid phase.

Chapter 6

Simulation of burning of a porous fuel

6.1 Introduction

In this chapter, we are concerned with reacting flows through porous media. Such flows are of great interest to the scientific community because of their relevance to a wide range of industrial applications and natural processes. Examples pertinent to the industry include the fluid flow at the interior of porous combustors (Mujeebu *et al.* (2009)), over ablative thermal shields (Lachaud *et al.* (2010) , Panerai *et al.* (2014)), and others. Further, wildland and shrub fires are cases of environmental flows that can be modeled as reacting flows over and through porous structures, see for example, Séro-Guillaume & Margerit (2001).

The flows of interest entail several challenges because of the additional length and time scales introduced by the heterogeneous reaction. These include: i) stiff reaction rates, ii) large heat release in relatively short time, iii) large density and specific-heat ratios between the two phases, and others. Consequently, relevant computational works typically rely on certain modelling and/or numerical simplifications, mainly due to limited computational resources. For example, some studies focus on the heat transfer mechanisms and incorporate radiation, but on the other hand they are limited to one-dimensional steady state solutions; see, for example, Leonardi *et al.* (2003). Other works are concerned with more detailed chemical-kinetics mechanisms, but they are also limited to

one-dimensional simulations, as in the work of Zhou & Pereira (1997). Finally, other approaches are focused on multi-dimensional flows but they use simplified chemical kinetics schemes. A detailed review of the bibliography for the modeling of porous-media combustion is provided in Mujeebu *et al.* (2010).

In this work, we present two-dimensional simulations of a burning of a porous fuel. In order to simplify the complexity of the problem, we use a $1-$step chemical-kinetics mechanism and we ignore radiation. This model has certain well-known limitations, *i.e.* it cannot faithfully describe the adsorption of oxidizer in the active sites of the porous medium and the ensuing desorption of CO. However, it can provide useful insight for the flows of interest, and more importantly, it serves as a means to test the efficacy of our developed numerical algorithm and hydrodynamic model.

This chapter is organized as follows. In Section 2 we present our parametrization of the interphasial mass transfer between the fluid and the porous skeleton. In Section 3 we describe the setup of our simulation and we elaborate on the convective boundary condition that we use. Finally, in Sections 4 and 5 we present our numerical predictions for the evolution with time of reacting flow past a porous block inside a channel.

6.2 Parametrization of the transport coefficients

As in the previous chapters, we consider a *generic*, highly porous, orthotropic medium whose physical properties are those of birch wood. The expressions used for the transport parameters are inspired by those of an ensemble of vertical cylindrical elements which are identical to each other. The cylinders are assumed to be uniformly distributed and to sparsely populate the porous material. The diameter of a single element is $\hat{d}_p$ and its height is $\hat{l}$. As such, the interphasial drag parameters for the streamwise and cross-stream directions, β_{11} and β_{22}, are the ones provided by the expressions (4.3.1) and (4.3.2), derived in the Chapter 4. Also, the expression for the interphasial heat exchange parameter is given in the previous chapter, equation (5.3.3).

As regards the modelling of heterogeneous combustion, we assume that the fluid phase comprises a single chemical species. Further, the two phases react with each other at the

interface of the micro-structural elements via the following single-step mechanism:

$$Solid \rightarrow Gas + Q\,. \tag{6.2.1}$$

In this equation Q is the heat of reaction which is absorbed by the fluid phase. The starting point of our approximation for the interphasial mass exchange rate $\mathcal{M}$, is an Arrhenius-type expression provided in Sundaresan & Amundson (1980) for combustion at the surface of a spherical carbon particle.

After this expression is appropriately adapted so as to express the rate of mass exchange at the surface of N_s* cylindrical elements of the solid's microstructure, it is introduced into the continuity equation (2.3.9). Upon non-dimensionalization, we arrive at:

$$\mathcal{M} = K_{\mathrm{R}}\,\frac{4\,(1-\phi)}{d_p}\,e^{-\frac{E}{T}}\,. \tag{6.2.2}$$

In this expression, K_{R} is the pre-exponential factor non-dimensionalized with $\hat{\rho}_{ref}\hat{u}_{ref}$. E is the activation energy non-dimensionalized with $\hat{\mathcal{R}}\,\hat{T}_{ref}$, where $\hat{\mathcal{R}}$ is the universal gas constant. Finally, T is the fluid temperature non-dimensionalized with the reference temperature $\hat{T}_{ref}$.

At this point we should note that the heterogeneous reaction results in the consumption of the solid matrix. Therefore, the volume of a single burning micro-structural element is reduced due to combustion. In our approach, this effect is modeled as a reduction of the diameter d_p of a single element, while its height l and the number density N_{s} of the elements remain constant. Assuming that ϕ^0 and d_p^0 are the volume fraction and the cylinder diameter at $t = 0$, this results in the following expression,

$$d_p = d_p^0\,\sqrt{\frac{1-\phi}{1-\phi^0}}\,, \tag{6.2.3}$$

where d_p is given as a function of the fluid volume fraction ϕ. This expression is used for the calculation of d_p in the parametrization of all transport coefficients in this problem.

*N_s is the number density of cylinders, $N_s = 4(1-\phi)/(\pi\hat{d}_p^2\,\hat{l})$.

6.3 Ignition process

In numerical simulations of transient combustion phenomena, the modeling of the ignition process is always a delicate issue and demands particular attention. There are several techniques that aspire to initiate the reaction in such simulations. Here we cite two popular techniques. i) The "spark ignition". In this case, a heat source of sufficiently high temperature is applied locally and for a short time-window, until the reaction becomes self-sustainable. ii) The "spontaneous ignition". According to this technique, the temperature of the fuel is raised while the chemical-kinetics source terms are switched off. When the temperature is high enough, these terms are switched on, and the reaction starts; see, for example, Tomboulides *et al.* (1997). There is also the alternative option to consider that pre-heating and reaction zones are already developed, prior to the beginning of the simulation. The purpose of this option is to render the initialization of the combustion less computationally demanding. It is often implemented for simulations of the propagation of homogeneous-reaction fronts inside porous media, as is the case at the interior of porous combustors; see for example, Du & Xie (2011). This alternative however, is not viable for our purposes, because reaction profiles for porous fuels are not readily available in the literature.

In this work we examine two cases. At first, we consider a porous fuel that is initially cold and placed at the half-width of a channel. In the set-up of this problem, we opt for a different approach to initiate the chemical reaction, namely, the exposure of the porous medium to a stream of hot oxidizer. The temperature of the fuel increases progressively because of the hot oxidizer, and once it is sufficiently high, the reactants start to react. In the second case, the porous fuel is placed next to the lower wall of a channel. In this configuration, the stream of hot oxidizer is not an effective ignition mechanism. Buoyancy forces drive the stream above the porous fuel, thus failing to increase its temperature. As such, we choose to apply the "spark ignition" technique, that is, the temperature of the porous fuel is raised locally using a heat source.

6.4 Burning of a porous fuel placed at the centerline of a channel

We start the description of the problem set-up with the details of the computational domain. The porous fuel is assumed to be a square block and the dimension of its sides is l. At the beginning of the simulation the porosity of the material is $\phi^0 = 0.9$ and the characteristic length of its microstructure $d_p^0 = 0.032\,l$. Further, the dimensions of the domain in the streamwise and cross-stream directions is set to $L_x = 12\,l$ and $L_y = 4\,l$ respectively. The discretization of the domain is performed on a uniform grid with a resolution of 100 cells per unit-length. The porous block is placed at the half-distance between two parallel walls, *i.e.* it extends from $y = 1.5\,l$ to $y = 2.5\,l$. Along the streamwise direction, it extends from $x = 5\,l$ to $x = 6\,l$.

The initial condition for the velocities (u, v) is obtained via a preliminary run of isothermal pressure-driven flow, in a similar manner that we obtained the initial profiles for the isothermal shear layers, Chapter 4. Once the flow around the porous block is developed, this preliminary run is terminated. The computed velocity field is then applied as initial condition for our main simulation. We also impose the calculated velocity profile along the upstream boundary, as inflow boundary condition. For the downstream boundary of the domain, we require a more elaborate condition to ensure that the flow structures behind the porous block do not reflect back toward the interior of the domain. Accordingly, we prescribe a convective boundary condition. A more detailed description of the implementation of this boundary condition is provided in the subsection that follows. Along the vertical direction, both boundaries are assumed to be rigid walls.

As regards the phasial temperatures, the domain is initially isothermal and the two phases are assumed to be in thermal equilibrium. At the inflow boundary, we specify the fluid temperature T_{in} as a function of time according to the following expression,

$$T_{in}(t) = \begin{cases} 1 + \frac{1.5}{4}\,t\,, & t < 4, \\ 2.5\,, & t \geq 4, \end{cases} \tag{6.4.1}$$

where T_{in} is non-dimensionalized with the reference temperature $\hat{T}_{ref}$, and t is non-dimensionalized with $\hat{l}_{ref}/\hat{u}_{ref}$. At the outflow, we also use a convective boundary condition for the temperature, while the top and bottom walls are assumed to be adiabatic.

For the pressure, the initial condition is also obtained via the preliminary run of isothermal flow. The boundary conditions are such that compatibility with the boundary conditions of the *provisional* velocities is secured via equations (3.2.13) and (3.2.20). As explained in Section 3.4, the boundary condition for the *provisional* velocity $\tilde{\boldsymbol{u}} \cdot \hat{n}$ (the normal component) is the same as that of $\boldsymbol{u} \cdot \hat{n}$. On the top and bottom walls, both of these are set to zero. Then, from equation (3.2.13), the boundary condition for the pressure at the bottom wall is $\left.\frac{\partial p'}{\partial y}\right|_{y=0} = 0$, while that the top wall $\left.\frac{\partial p'}{\partial y}\right|_{t.w.} = Ri \left.\frac{\partial \rho}{\partial y}\right|_{t.w.} L_y$. However, because of the temperature boundary condition, we have that $\left.\frac{\partial \rho}{\partial y}\right|_{t.w.} = 0$ and, therefore, we also have that $\left.\frac{\partial p'}{\partial y}\right|_{t.w.} = 0$. At this point it is deemed useful to remind that p' is the piezometric pressure, $p' = p^1 + \rho Riy$, that was introduced in the momentum equation (3.2.9) as part of the numerical procedure.

For the problem that we consider herein, the dimension $\hat{l}$ of the square porous block is assumed to be equal to $7.27 \cdot 10^{-3} m$ and is used as the reference length. The reference velocity is the maximum inflow velocity which occurs at half-width of the channel, and is equal to $0.755 m/s$. As usual, all material properties are non-dimensionalized based on the properties of the fluid phase (air) at the reference temperature, which is set to $300K$. Also, the initial temperature throughout the domain is equal to the reference temperature. Based on these values, the Reynolds number is set to $Re = 350$, the Prandtl number is $Pr = 0.71$ and the Richardson number is $Ri = 0.125$.

As regards the parameters related to the chemical reaction, we set the pre-exponential factor equal to $\hat{K}_{\mathrm{R}} = 222.16\, kg/(m^2 s)$, the activation energy to $\hat{E} = 10729.8\, kcal/kmol$, and the heat of reaction to $\hat{Q} = 904.5\, kJ/kg$. Based on the reference quantities given above, the non-dimensional values of these parameters, that are used in expression (6.2.2), are $K_{\mathrm{R}} = 250$, $E = 18$, and $Q = +3$.

6.4.1 The convective boundary condition

According to the description of the simulation setup provided above, for the problems studied in this chapter, a convective boundary condition is applied at the downstream boundary of the domain. The purpose of such an open-boundary condition is to prevent flow structures that are convected downstream and away from the domain, to be reflected artificially back towards its interior. This type of boundary condition is considered among the most difficult to implement successfully, because it does not correspond to any particular natural condition.

The convective boundary condition employed herein, amounts to solving the following equation on the boundary:

$$\frac{\partial \vartheta}{\partial t} + U_c \frac{\partial \vartheta}{\partial x} = 0, \tag{6.4.2}$$

where ϑ is the quantity that is convected away from the domain and U_c is the convective velocity.

The first challenge in this task is the choice of U_c. Previous works have shown that a injudicious choice of U_c can lead to results of poor quality (Miyauchi *et al.* (1996), Ol'shanskii & Staroverov (2000)). In turbulent flows, a popular strategy is to use the velocity component normal to the boundary, averaged over the boundary (Sani & Gresho (1994), Miyauchi *et al.* (1996), Akselvoll & Moin (1996)). In other works where the mean velocity profiles at the location of the open boundary are well known, they are applied as distributions of U_c. This technique is applied for example in the simulations of turbulent jets and plumes of Craske & van Reeuwijk (2013). Herein we set U_c equal to the value of the boundary-normal component of the velocity, which applied uniformly along the boundary would ensure mass conservation in the domain. To calculate this value, we integrate the continuity equation (2.3.9) throughout the domain. This yields the following relation:

$$U_c = \frac{\int \mathcal{M}\,\mathrm{d}V - \int \frac{\partial(\phi\rho)}{\partial t}\mathrm{d}V + \int_{in}(\rho\phi u)\,\mathrm{d}S}{\int_{out}(\phi\rho)\,\mathrm{d}S}. \tag{6.4.3}$$

In this expression, $\int_{in}(\cdot)\,\mathrm{d}S$ and $\int_{out}(\cdot)\,\mathrm{d}S$ represent surface integrals over the upstream and downstream boundaries respectively, while $\int(\cdot)\,\mathrm{d}V$ is the volume integral over the entire domain.

Next we focus on the spatial and temporal discretization of equation (6.4.2). For notation purposes, we use the subscript (n) for the first cell at the interior of the domain and $(n+1)$ to denote the ghost cell next to the boundary. Also, we use the superscript (ti) to denote the time-level that is already computed via our algorithm and the superscript $(ti+1)$ for the time-level at which we are applying the boundary condition. Finally, let us assume that the quantity ϑ is already updated from the time-level (ti) to the time-level $(ti+1)$ at the interior of the domain and we proceed to evaluate its value at the ghost cell, ϑ_{n+1}^{ti+1}.

For the time-discretization of equation (6.4.2), the first term is treated via the backward Euler method, whereas the second term is evaluated at the time-level $(ti+1)$. As regards the spatial discretization, the first term is evaluated on the boundary as an average of the values at the cells (n) and $(n+1)$. For the second term we use first order centered differences. Finally, we arrive at,

$$\frac{1}{2}\frac{\vartheta_{n+1}^{ti+1}-\vartheta_{n+1}^{ti}}{\Delta t}+\frac{1}{2}\frac{\vartheta_{n}^{ti+1}-\vartheta_{n}^{ti}}{\Delta t}+U_c\frac{\vartheta_{n+1}^{ti+1}-\vartheta_{n}^{ti+1}}{\Delta x}=0 \tag{6.4.4}$$

from which we compute the value at the ghost cell, ϑ_{n+1}^{ti+1}.

6.4.2 Numerical results

At early times in the simulation, the hot fluid that enters the domain from the inflow is convected downstream towards the porous block. Figure 6.1 shows the vorticity and temperature fields at four different instances during the evolution of the flow. According to Figure 6.1(a), the first layers of hot fluid reach the porous block by $t = 10.1$. The same figure also shows that the isotherms are asymmetric around the centerline at $y = 2$. This is caused by the effect of buoyancy, which forces the hot fluid to shift towards the upper part of the channel. In fact, at this time, 49% of the mass flux at $x = 5$ passes above the porous block, 32% passes bellow and 19% passes through its upstream interface.

As the hot fluid enters the porous medium, it causes the temperature of the solid matrix to rise. However, the solid-temperature rises slowly. This results in significant thermal non-equilibrium inside the porous medium. Figure 6.2 shows the temperature profiles of both phases along the centerline $y = 2$, at the same four instances shown in Figure 6.1. At $t = 10.1$ (Figure 6.2(a)) the temperature differences are significant for

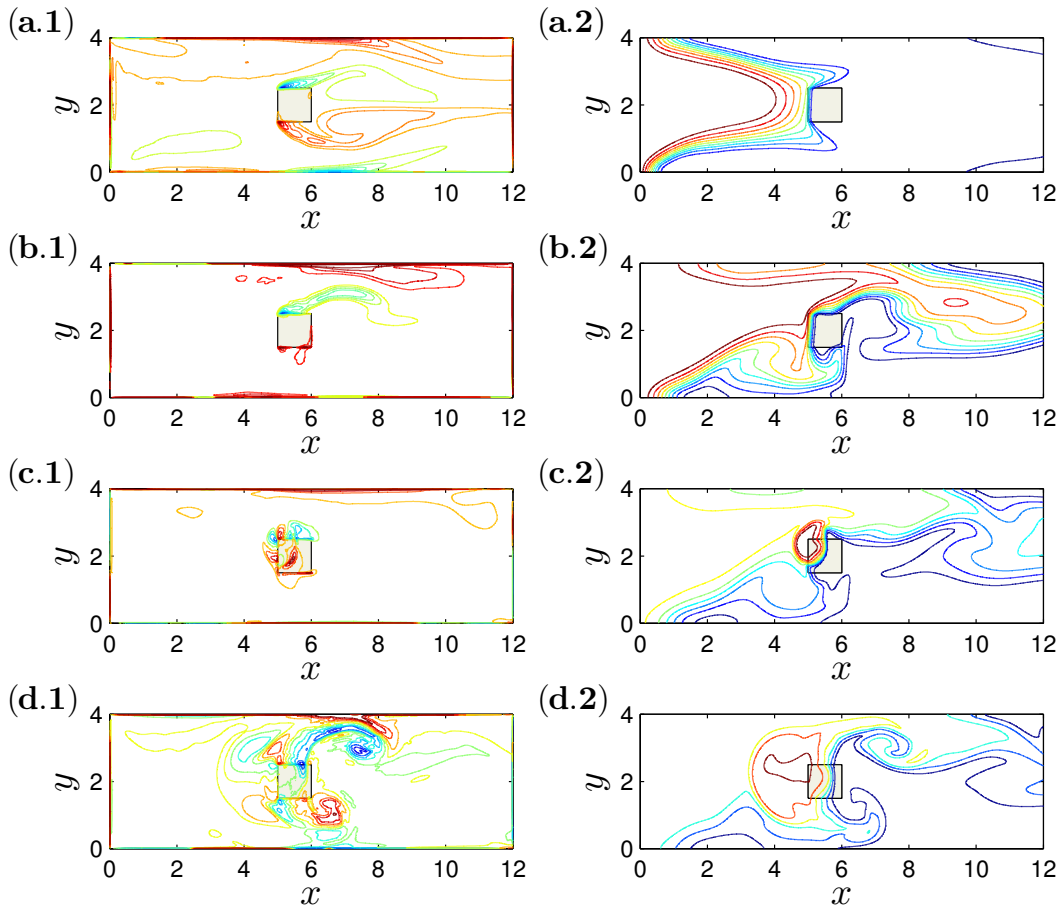

Figure 6.1: Simulation of a burning porous block placed at the centerline of a pure-fluid channel. Vorticity field (left) and fluid-temperature field (right) at four instances during the evolution of the flow. (a) $t = 10.1$; (b) $t = 27.10$; (c) $t = 32.67$; (d) $t = 34.07$.

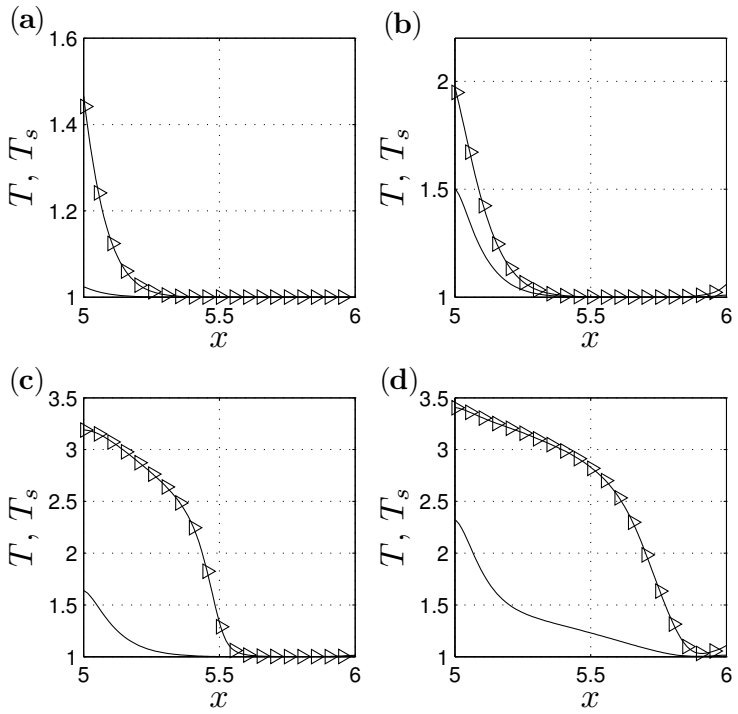

Figure 6.2: Simulation of a burning porous block placed at the centerline of a pure-fluid channel. Profiles of the phasial temperatures at the channel centerline. The times that correspond to the plots are the same as in Figure 6.1. (▷) marks the fluid temperature and (—) marks the solid temperature.

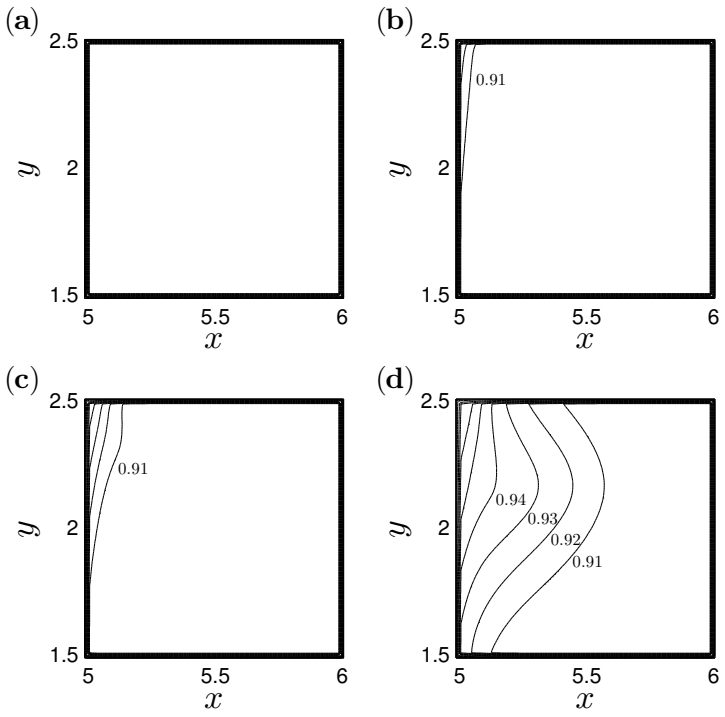

Figure 6.3: Simulation of a burning porous block placed at the centerline of a pure-fluid channel. Distribution of the fluid volume fraction at four instances during the evolution of the flow. The times that correspond to the plots are the same as in Figure 6.1.

$5 < x \leq 5.4$. For the rest of the porous region, $5.4 < x \leq 6$, they are both equal to the reference temperature. Until this time, the fluid temperature inside the porous material is not high enough to induce a significant reaction rate. As such, the distribution of the volume fraction remains the same as in the initial condition, see Figure 6.3(a).

However, the incoming fluid at the maximum prescribed temperature $T_{in} = 2.5$, progressively approaches the upstream front of the porous block. Eventually, at $t \simeq 18.74$, the fluid temperature becomes sufficiently high for the combustion to begin. From this instance, the evolution of the flow can be divided in following two phases.

i) The first phase lasts until $t = 31.9$. During this time, the rate of reaction is slow and the volume fraction changes only at the vicinity of the upstream interface between the porous block and the clear fluid.

ii) The second phase lasts until $t = 37.55$. The main characteristic of this phase is the

fast rate of the reaction. Moreover the reaction is not limited only to the upstream front of the block, but gradually spreads throughout the entire porous region.

The simulation is terminated at $t = 37.55$, when plumes of hot fluid that originate from the reaction zone interact with the upstream boundary. In the following paragraphs we focus on the characteristics of these two phases of burning of the porous fuel.

During the **first** phase, the fluid temperature exhibits steep negative gradients along the streamwise direction at the interior of the porous medium ($x > 5$). These can be evidenced from the density of the isotherms at the upstream interface of the porous block in Figure 6.1(b.2). In fact, the temperatures of both phases at the time that corresponds to this figure, $t = 27.10$, and at $y = 2.49$ are shown in Figure 6.2(b). According to this plot, T drops to a value of 1.5 within a distance 0.1 unit lengths from the upstream interface. Even so, the fluid-temperature field is high enough to induce a significant chemical reaction rate at the vicinity of the interface.

Further, the fluid-temperature field notes only small variations throughout the second phase. As such, the profiles of T are also persistent around $x = 5$. The cumulative effect of the reaction within this time, results in a noticeable consumption of the solid matrix locally, see Figure 6.3(b). At $t = 27.10$ and at the upper-upstream corner of the block, where the fluid temperature attains its maximum, ϕ is increased to 0.927. At the same time, heat is released from the reaction, which, is absorbed by the fluid phase, gradually raising its temperature. The temperature of the solid rises as well due to interphasial heat transfer, however it remains significantly lower than that of the fluid phase, as is shown in Figure 6.2(b).

Eventually the fluid temperature inside the porous medium reaches a critical value at which the rate of reaction increases abruptly. This marks the beginning of the **second** phase of the flow evolution, which is characterized by rapid burning of the porous fuel. At approximately $t = 31.9$, the fluid temperature at the upstream interface of the porous block raises up to $1.38\,T_{in}$. At this temperature, the reaction rate is fast and leads to the rapid expansion of the surrounding fluid due to heat release. The main body of the expanding hot fluid travels upstream. Nonetheless a significant part of it escapes towards the sides of the porous block and is drifted downstream as is evidenced in Figure 6.1(d). The same figure also shows a swirl of hot fluid on each side of the porous medium followed

by a short reverse flow downstream of it as is typical in flows around bluff bodies.

Another consequence of the fast reaction rate during the second phase is the rapid consumption of the solid matrix. Moreover, this is not limited only to the upstream front of the porous block as was predicted for the first phase. The solid volume fraction is reduced at a fast rate simultaneously in a wide area along the x, which advances downstream. By $t \simeq 35.9$ the reaction front has reached as far as the downstream end of the porous structure. At these advanced times in the simulation, the heat of the reaction increases the fluid temperature at the interior of the porous medium and at large distances from the upstream interface. The temperature of the solid notes a considerable increase as well. However, the difference between the phasial temperatures remains large for the most part of the area occupied by the porous medium, as is evidenced by Figure 6.2(d).

It is also interesting to notice that during the second phase of evolution, the reaction is more pronounced close to the center of the porous medium than it is close to the top and bottom sides of the block. This justifies the parabolic shape of the ϕ iso-contours in Figure 6.3(d). At this point we should recall that, according to our single-step chemical kinetics scheme the fluid phase comprises a single chemical species. As such, it does not capture phenomena relevant to the concentration of the oxydizer in the fluid. For example, a plausible scenario is the depletion of the oxydizer at the interior of the porous medium, due to high reaction rates in combination with reduced fluid convection. This would result in reduction of the chemical reaction rate or even suppression of the reaction. However, in the problem discussed herein, the initial volume fraction of the fluid phase is 0.9, namely the porous fuel is largely void. Accordingly, such phenomena are not expected to have a critical impact on the evolution of the flow.

By the end of the simulation, $t = 37.55$, the solid volume fraction is reduced to less than half of is original value, up to x=5.7 along the centerline of the channel. At the same time, at the upstream front of the porous block, it is reduced approximately 20 times.

6.5 Burning of a porous fuel placed next to the bottom wall of a channel

In this section, we discuss the simulation of a burning porous fuel that is placed next to the bottom wall of a channel and is ignited using a heat source. The size and shape of the porous medium is the same as before. Its initial upstream interface is placed at $x = 5$ unit lengths and its downstream interface at $x = 6$ unit lengths. Along the y direction, it extends from $y = 0$ to $y = 1$ unit length. The porosity of the material and the characteristic length of its microstructure at the beginning of the simulation, are the same as in the previous case, $\phi^0 = 0.9$ and $d_p^0 = 0.032\,l$ respectively. As the length of the porous structure remains the same in comparison with the problem examined above, the size of the domain in the streamwise and the cross-stream directions is also the same, namely $L_x = 12$ unit lengths and $l_y = 4$ unit lengths, respectively.

The initial condition as well as the boundary conditions for the pressure field and the two velocity components are configured as in the previous subsection. As regards the temperatures of the two phases, the domain is initially isothermal and the two phases are assumed to be in thermal equilibrium. At the inflow boundary the prescribed fluid temperature is equal to the initial temperature inside the domain, while a convective condition is applied at the downstream boundary.

The non-dimensionalization of the problem variables is performed as in the previous section, with the height of the porous medium l being the reference length. The non-dimensional parameters of the problem as well as the parameters related to the chemical reaction remain also the same.

For the ignition of the reactants, an external heat source is applied over a non-dimensional area 0.08×0.08 unit lengths at the upper upstream corner of the porous strip, until $t = 2.5$.

6.5.1 Numerical results

At the early stages of the evolution of the flow, the heat source increases the fluid temperature progressively without inducing significant reaction rates. Figure 6.4 shows the fluid-temperature and the porosity distribution at four times during the simulation. The

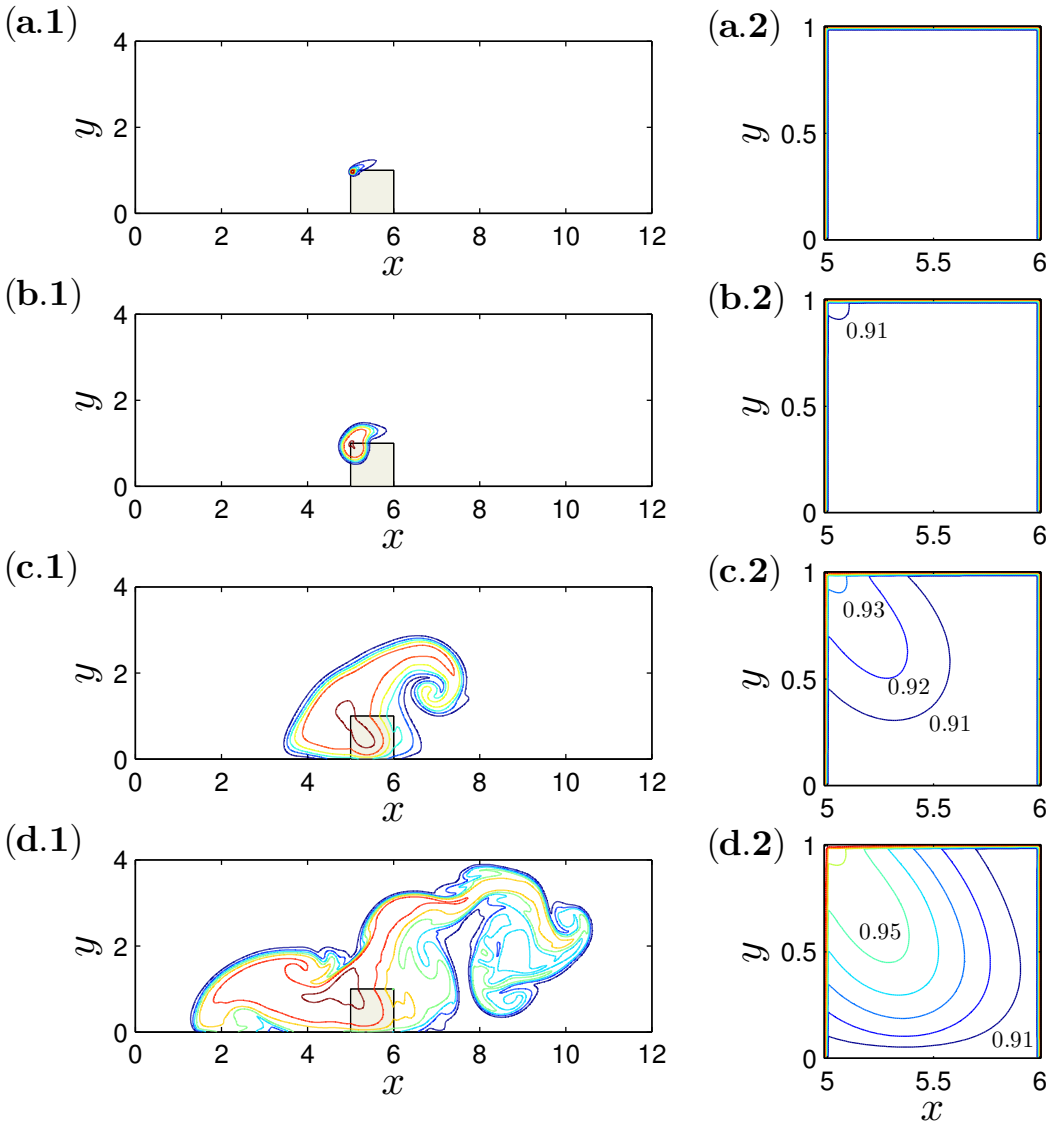

Figure 6.4: Simulation of a burning porous block placed next to the bottom wall of a pure-fluid channel. Fluid-temperature field (left) and fluid volume fraction (right) at four instances during the evolution of the flow. (a) $t = 1.45$; (b) $t = 2.0$; (c) $t = 2.85$; (d) $t = 3.86$.

isotherms in Figure 6.4a indicate the localized effect of the heat source. At $t = 1.5$, T raises up to 3.5 and the reaction starts. As the heat of reaction is diffused, a zone of hot fluid is formed around the top upstream corner of the porous medium, which expands. The high porosity of the material allows this expansion to progress symmetrically around the corner, so that the fluid temperature raises at the interior of the porous medium as well. This zone of hot fluid is shown in Figure 6.4b1. The same figure also shows that the top part of this zone curves toward the downstream direction because of the imposed inflow conditions. At this time, $t = 2$, the consumption of the solid matrix has also started as is evidenced from Figure 6.4b2. Moreover, the area of the porous medium where the solid matrix is consumed spreads radially, and at a fast rate from the corner toward the interior of the porous medium and along its sides.

By $t = 2.85$, the temperature of the fluid phase is higher than the initial temperature throughout the porous region. Also, some hot fluid escapes from the porous medium to the pure-fluid region through the downstream interface at $x = 6$, as can be seen in Figure 6.4c1. At this stage of evolution, the hot fluid around the reaction zone stops spreading radially around the location of the heat source. Its interaction with the oncoming cold fluid from the inflow, prevents it from traveling further upstream at the centerline of the channel. This results in the formation of two principal plumes of hot fluid that originate from the reaction zone.

The first plume is the one in which buoyancy effects dominate and cause it to raise to higher altitudes in the domain. However, instead of rising directly above the reaction zone, it interacts with the established cold-fluid inflow, and drifts downstream, forming a swirl at the height of the centerline of the channel. This swirl can be seen at $x \simeq 7$ in Figure 6.4c1. As the flow evolves, the size of the swirl grows by entraining more reaction products. At approximately $t = 3.7$ its size is sufficiently large, so that it interacts with the boundary layer of the top wall. In later times, the swirl gets distorted and breaks down in many smaller-scale structures, which dominate the channel downstream of the porous medium.

The second plume, travels upstream from the reaction zone, remaining close to the bottom wall, where the velocity of the inflow is lower. Its interaction with the wall eventually leads to the formation of a positive vorticity roller. This roller can be identified

by its trace in the isotherms of Figure 6.4d1, at $x = 2.6$. At $t = 4.1$, the plume reaches close to the upstream boundary of the domain and interferes with the inflow condition. At this point the simulation is terminated.

As can be evidenced from Figure 6.4d2, the reaction is not limited only at the vicinity of the top upstream corner of the porous block, but is also important further at its interior. According to this figure, the consumption of the solid solid matrix is more important in areas closer to the center of the porous structure, than it is close to the interfaces between the porous and the pure-fluid regions. This can be attributed to the fact that the amplitude of the fluid velocity is higher close to the interface areas, so that heat is convected away from these areas faster. On the contrary, further toward the inside of the porous medium the fluid velocities are low, convective heat transfer is reduced and higher temperatures are achieved. In turn, the higher temperatures lead to higher reaction rates. At the end of the simulation, the solid matrix is reduced by 67% ($\phi = 0.967$) at the vicinity of the heat source, by 50% ($\phi = 0.949$) at the center of the porous block and by 7% ($\phi = 0.908$) at the downstream interface of the porous medium.

6.6 Conclusions

In this chapter we presented results from two simulations of a burning porous block that is placed inside a pure-fluid channel.

In the configuration of the first simulation, the porous fuel is placed at the half-width of the channel. Further, the combustion is induced by high-temperature fluid which enters the domain from the upstream boundary. According to our predictions, after the hot fluid reaches the porous block, the rate of reaction is low and the reaction is limited to its upstream interface. At later times, the heat of the reaction causes the temperature to reach a critical value for which the reaction rate becomes fast. When this happens the fluid temperature at the interior of the porous medium increases rapidly and the volume fraction varies throughout the porous region. The solid temperature to rise as well due to interphasial heat transfer. However it remains significantly lower than that of the fluid in all areas inside the porous medium where the reaction rate is important. By the end of the simulation the porous skeleton is almost entirely consumed at the initial upstream

interface, while the solid volume fraction is reduced at the downstream end as well.

In our second simulation, the porous fuel is placed next to the lower wall of the channel. In this case, the reaction is initiated via the application of a localized heat source at one of the corners of the porous block. As soon as the temperature of the fluid becomes sufficiently high, the reaction starts. The consumption of the solid skeleton progresses radially from the location of the initially applied heat source, in a steady manner and at a high rate. The hot fluid that emanates from the reaction zone, forms two plumes. One of them rises in the higher layers of the domain and downstream of the porous block. Its interaction with the established cold-fluid flow leads to the formation of a swirl, which grows and eventually interacts with the boundary layer of the top wall of the channel. The second plume heads upstream and eventually interferes with the inflow boundary condition. At this time the simulation is terminated.

The results presented herein, exhibit several of the characteristics of reacting porous-media flows that render them challenging to resolve, such as large heat release in relatively short time, plumes with thin zones of large density gradients, thermal non-equilibrium, and others. The fact that the proposed numerical algorithm handles such challenges with success, demonstrates that it is suitable for numerical simulations of such flows.

Concluding remarks and perspectives

The objective of this dissertation has been to advance the state of the art of flows at the interface between porous and pure-fluid layers.

First, we have presented a single-domain approach, thermal non-equilibrium model, for flows with heat transfer and interphasial mass exchange. The resulting conservation equations are valid for both compressible and incompressible flows. It is interesting to mention that, by setting the volume fraction of the fluid phase equal to one at the smooth interface between the porous medium and the pure fluid, our equations yield an intrinsic condition for the temperature of the solid matrix at such interfaces. Further, we presented the the low-Mach number approximation of this model. The resulting equations are more simple than the full model, and therefore they are more convenient to use for incompressible flows.

Then, we have described a numerical algorithm for the treatment of the governing equations. This algorithm employs a projection step to decouple the pressure field from the velocity, which takes advantage of the kinematic constrain provided by the continuity equation of the fluid phase. Further, it uses a two-step advancement in time for improved accuracy in time and stability. The spatial discretization is performed on a collocated grid for reasons of simplicity and extensibility to more complex geometries. However, such systems are known to be sensitive to numerical instabilities, which manifest in the form of odd-even decoupling of the pressure field. To prevent this from happening, we use a flux interpolation scheme which handles successfully such instabilities.

Further, the proposed model and numerical method were employed in a study of isothermal flows in superposed porous and pure-fluid layers. First we provided the

constant-density limit of the governing equations, where our model reduces to a variation of the unsteady Darcy-Brinkman model. Subsequently, a linear stability analysis of inviscid shear layers was performed, to provide an insight to the basic characteristics of the flows of interest. According to this analysis, such layers are unstable. As such, the development of the flow leads to the formation of rollers, which in turn result in significant fluid recirculation inside the porous medium.

The evolution of the instabilities was further investigated via numerical simulations of temporally-evolving shear layers at the interfaces of interest. Both two-dimensional and three-dimensional flows have been considered. In the two-dimensional case, it was confirmed that the flow instabilities lead to the formation of spanwise vortices that grow and merge. In the three-dimensional problem, we also predicted the formation of streamwise, "rib" vortices. At advanced simulation times, the flow structures break down, and the vorticity field becomes irregular. Eventually, the shear layer experiences transition to turbulence. A detailed description of the evolution of the flow was provided and, where deemed appropriate, comparisons were made with plane mixing layers. According to our results, both the two-dimensional and the three-dimensional shear layers are self-similar in the early stages of their evolution, before the roller formation, and after the first roller pairings are completed.

At the end of this part, we also discussed the numerical results from a simulation of forced flow in a channel. The same type of Kelvin-Helmholtz instability is onset on the interface between the porous and the pure-fluid layers, which leads to the formation of rollers. These rollers grow with time and eventually interact with the boundary layer of the top wall of the channel. At later times, a new set of counter-rotating rollers is formed near the top wall. These occupy a significant part of the pure-fluid region and restrict the available space for upward displacement of the vortices at the interface. As a result, no vortex pairings occur during the evolution of this flow.

Next, we discussed the results from our numerical simulations of natural convection, forced convection and stratified shear layers. As regards the study of natural convection in a channel, the simulations predicted the formation of convective cells that are restricted in the pure-fluid region. In the case of low wall-temperature ratio, the convective cells are regular, while for large wall-temperature ratio they oscillate and they break down soon

after their formation. Even in the later case however, at large times, the flow leads to the formation of stable convective cells. Thermal non-equilibrium is important in areas of prounounced fluid convection inside the porous medium. As expected, for a high wall-temperature ratio, the differences between the phasial temperatures are higher and at larger distances from the interface as compared to the low wall-temperature case.

Then, we focused on the simulations of unstably stratified forced flow. In this problem, the rollers that are formed on the interface between the porous and the pure-fluid layer, initially isolate the upper part of the domain from the thermal phenomena that occur at the interface. As the flow evolves, the interaction between the hot fluid and the rollers results in the stretching and the elongation of the rollers. For high wall-temperature ratios, this stretching almost tears the rollers in two parts, and subsequently causes pairing between the rollers. In this problem, the differences between the temperatures of the two phases are more pronounced in the areas below the braid regions, due to the downward motion of cold fluid which emanates from the pure-fluid domain.

As regards semi-bounded shear flows, our simulations revealed that unstable stratification accelerates the growth of the instabilities. In this case, thermal non-equilibrium becomes pronounced during roller pairings, when buoyancy forces drive low-temperature fluid from the upper part of the domain into the porous medium. By contrast, stable stratification slows down the growth rate of the shear layer after roller formation. Further, buoyancy effects hinder the mixing of fluid from the porous and pure-fluid regions. This, in turn, results in lower temperature differences between the two phases, and at smaller distances from the interface as compared to the unstably-stratified case.

Finally, in the **sixth** chapter we studied flows through porous media with chemical reactions. In the setup of our simulation a porous fuel block is placed amidst a channel, in which hot oxydizer enters from the inflow. Eventually the hot fluid reaches the porous block and raises its temperature. Once the temperature inside the porous medium is sufficiently high, the combustion starts. The burning of the fuel can be divided in two distinct phases. In the first phase the rate of reaction rate is low, and the reaction zone is limited to the upstream front of the block, where the solid matrix is slowly consumed. The local temperature increases due to the heat released from the reaction, and at later times it reaches a critical temperature for which the reaction rate is much faster. This

introduces the second phase of burning. In this phase the reaction zone is wide so that the reduction of the solid volume fraction is important at long distances from the upstream interface as well. Further the reaction zone travels downstream in the porous medium as the flow evolves, and by the end of the simulation it reaches the downstream end of the porous block. Even though the chemical reaction is modeled using a simplified chemical kinetics mechanism, our results provide useful insight into the characteristics of reacting flows through media with high porosity.

Future work and perspectives

A first step toward extending the work presented in this PhD thesis, is the study of three-dimensional and turbulent heat transfer in the domains of interest. To this end, we propose the realization of a series of simulations for the three-dimensional counter-parts of the problems presented in Chapter 5. In particular, results from simulations of natural convection, forced convection and thermally-stratified shear layers, in comparison with the study presented in this work, are expected to provide valuable information on the way the third dimension affects the heat transfer effects in superposed porous and pure-fluid layers.

Next, an interesting development of the present work relevant to the study of reacting flows, is the implementation of more detailed models for the heterogeneous chemical reaction. A first step in this direction, is to assume the presence of two chemical species in the gaseous phase, the oxydiser and the products of the reation. In this case, the rate of reaction will be given as a function of the concentration of the oxydiser, so that the reaction is faster in areas where the convection of unburned gasses is more pronounced. Further improvements in this direction can include more chemical species in the fluid phase, as well as more chemical reactions taking place, depending on the targeted application.

Another extension of the study presented in this thesis is the adaptation of the proposed model and numerical algorithm for simulations of large scale flows.

As was mentioned at several points throughout this work, one of the main characteristics of the problems of interest is the large range of length-scales of the flow. This suggests that employing standard Large Eddy Simulation (LES) modeling techniques can have a

very high computational cost. Furthermore, the unsteady nature of the flows of interest renders the alternative of using Raynolds-averaged modeling, equally as challenging.

A viable strategy would be to employ a hybrid LES/Raynolds-averaged modeling methodology. One option in this direction, is to use Raynolds-averaged modeling to describe the flow inside the porous regions and use LES modeling to resolve critical parts of the flow in the pure-fluid domain. However, according to our results, in several occasions fluid recirculation inside the porous medium is important, and the separation of the length scales of the flow is not clearly identified. A more suitable approach, is to employ the *soft interface* technique. According to it, the interface between the regions where LES and Raynolds-averaged modeling is used, changes in time, depending on the computed solution. Even though such a strategy entails a significantly more involved implementation, it is expected to yield results of analogously-better quality.

Appendices

Appendix A

Constant-density forced flow in a channel

In this appendix, we present results from our simulation of forced flow in superposed porous and pure-fluid layers placed between two parallel plates. The discussion focuses on the characteristics of the flow evolution and, where deemed appropriate, comparisons are made with the simulations of shear layers in semi-bounded domains presented in Section 4.4. In Chapter 5, these results are compared with our simulations of forced convection under thermal stratification.

The configuration of the domain is the same as that of the other simulations of forced flows presented in Chapter 5. In particular, the physical properties of the porous layer are the ones described in Section 5.3, whereas the domain dimensions are provided in Section 5.5. As regards boundary conditions, the domain is periodic in the streamwise direction and both boundaries at the cross-stream direction are assumed to be rigid walls.

The initial velocity profile is constructed in the following manner. In the pure-fluid region we prescribe the parabolic profile that corresponds to fully-developed laminar flow in a channel of width $3l$. On the other hand, in the porous region the velocity vector is set to zero. This distribution has been selected instead of fluid at rest for purposes of computational savings.

The reference velocity $\hat{u}_{ref}$ for this problem is the maximum value of the initial streamwise velocity component at the centerline of the pure-fluid region. For reference length $\hat{l}_{ref}$ we use the height of the porous strip, as we did throughout this thesis. Accordingly,

the reference time is $\hat{t}_{ref} = \hat{l}_{ref}/\hat{u}_{ref}$. Based on these values, the Reynolds number of the problem is $Re = 5000$, whereas the Reynolds number based on the half-width of the pure-fluid layer $1.5l$, is equal to $Re_{p.f.} = 7500$. For this value of Re, according to the linear stability analysis of Tilton & Cortelezzi (2008), the flow is expected to be subject to the growth of the instabilities at the interface. Further, the forcing applied on the flow, is chosen so as to correspond to a parabolic (channel-flow) profile at $Re_{p.f.} = 7500$.

Finally, we provide the definition of the following quantities that are used in the presentation of our results. First, the friction velocity at the top wall is given by,

$$u_\tau^{\text{top}} = \sqrt{-\frac{\tau_{t.w.}}{\rho}} \, . \tag{A.0.1}$$

In this expression, $\tau_{t.w.}$ is the wall stress at the top of the domain, $\tau_{t.w.} = \mu \left.\frac{\mathrm{d}U}{\mathrm{d}y}\right|_{t.w.}$ and U is the plane-averaged streamwise velocity, as explained earlier in Section 4.3. Further, we make use of the r.m.s. velocities $(u_{rms}, v_{rms}) = (\sqrt{R_{11}}, \sqrt{R_{22}})$.

At the early stages of the simulation, the fluid velocity inside the porous medium increases due to the applied pressure forcing. A boundary layer is thus formed next to the bottom wall and a transition layer at the interface between the porous and pure-fluid layers. However, despite the high porosity of the material, the amplitude of the streamwise velocity remains very small inside the porous material. For example, at time $t = 5.15$ the maximum velocity for $y < 0$ does not exceed the 3% of the streamwise velocity at the half-width of the pure-fluid region. Subsequently, the onset of the instability at the interface causes the velocities to oscillate in both time and space. The amplitude of these oscillations increases progressively as the flow evolves. Figure A.1 shows the vorticity field at four different instances during the evolution of the flow. At $t \simeq 20$ the vorticity contours start to fold as we can see in Figure A.1(a), and within the next 10 time units (at $t \simeq 30$) the formation of the rollers at the interface is completed (Figure A.1(b)). At this time, the maximum streamwise velocity right bellow the interface is increased to 12% of the reference velocity. As the flow evolves, the vortices grow and eventually interact with the boundary layer of the top wall. At the end of the simulation, a new set of counter-rotating vortices is formed right bellow the top wall, as can be seen in Figure A.1(d). In the following paragraphs we describe in more detail the characteristics of the evolution of the flow.

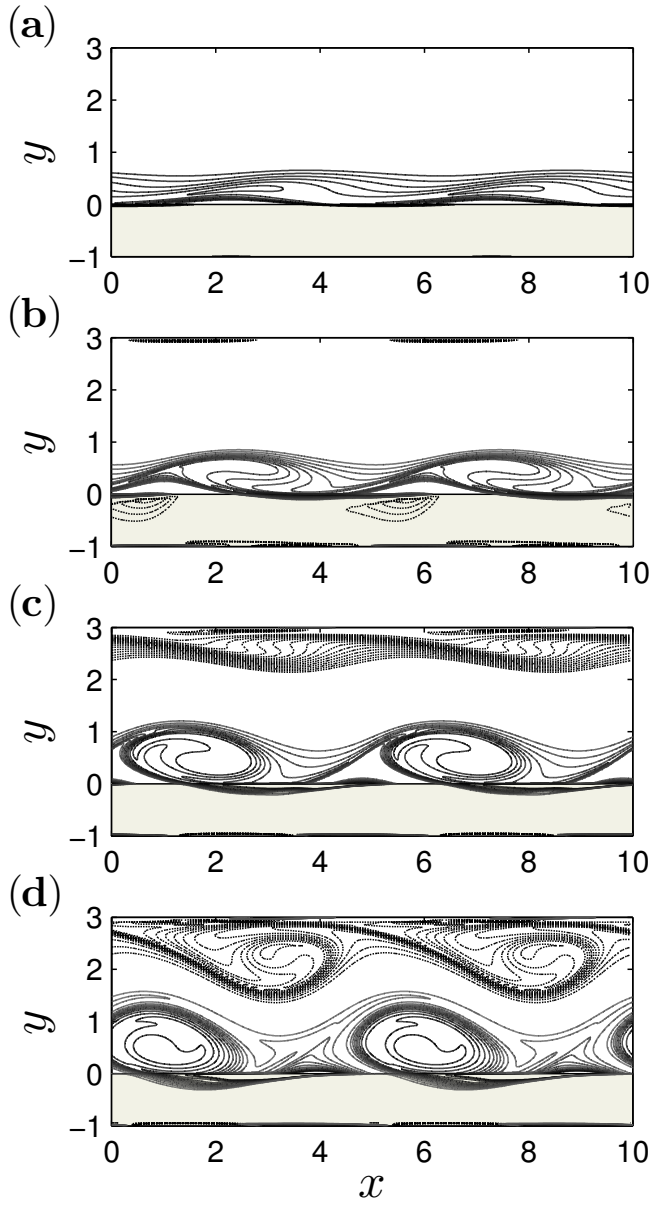

Figure A.1: Forced flow in a channel. Vorticity field at four instances during the evolution of the flow. (a) $t = 20.0$; (b) $t = 30.06$; (c) $t = 39.31$; (d) $t = 58.04$

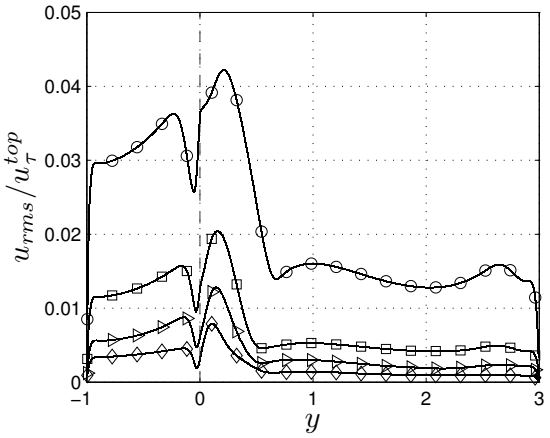

Figure A.2: Forced flow in a channel. Plots of the normalized u_{rms} at four instances from the beginning of the simulation and until the roller formation. ($\diamond : t = 10.1$; $\triangleright : t = 15.0$; $\square : t = 20.0$; $\circ : t = 30.06$). The dashed vertical line indicates the position of the interface.

We first examine the growth of the instability at the early stages of evolution. Figure A.2, shows the plots of u_{rms} at four instances from the beginning of the simulation and up to the completion of roller formation at $t \simeq 30$. As is evidenced from this figure, throughout this time interval, u_{rms} increases monotonically. The velocity fluctuations are more pronounced close to the interface and on both of its sides. Also, the fluctuations are somewhat higher in the pure-fluid domain. For example, when the rollers are fully developed at $t = 30.06$, the maximum of u_{rms} in the pure-fluid domain is 16% higher than its maximum below the interface.

Further, the velocity fluctuations attenuate as we move further away from the interface. In particular, in the pure-fluid domain and above $y =\simeq 0.7$ the velocity fluctuations remain low and the values of u_{rms} are less than half of those encountered at the vicinity of the interface; see Figure A.2. This difference reflects the distinction between the scales of the flow structures developed at the interface of the porous medium at $y = 0$ and those at the vicinity of the impermeable top wall at $y = 3$. In fact, the velocity fluctuations near the top are due to elongated small-scale structures; these structures can be seen in Figures A.1(b), and A.1(c). Similar predictions, relatively large-scale vortical

structures near the porous interface and elongated structures near the top, have also been reported in the work of Breugem & Boersma (2005) on simulations of turbulent flow over a permeable wall.

As the flow evolves, the elongated structures near the top wall develop into an additional series of rollers, as can be evidenced in Fig. A.1(d). The vorticity of these rollers is positive, whereas the one of the rollers at the interface is negative. In other words, the two sets of rollers rotate in opposite directions. Also, the vorticity amplitude inside the top rollers increases with time. By the end of the simulation, $t \simeq 60$, it is as high as 86% of the vorticity amplitude at the cores of the interface rollers.

The new set of rollers at the top of the domain also affects the evolution of the velocity fluctuations. Figure A.3 shows the u_{rms} profiles at 4 instances, from the beginning of their formation until they are fully developed. Upon comparison with Figure A.2, we see that the intensities of the velocity fluctuations close to the top wall grow fast in more advanced times, whereas before the formation of the new rollers they remained relatively low. In fact, from $t = 39.31$ to $t = 58.04$ the growth of u_{rms} is more rapid close to the top wall than it is close to the interface. For example, at $t = 58.04$ and according to Figure A.3, the maximum of u_{rms} near the top wall is higher than its peak close to the interface.

It is interesting to notice that, according to our numerical predictions, no vortex pairings occur during the evolution of this flow. Instead, the rollers grow by progressively entraining more of the surrounding fluid as their vorticity builds-up with time. Further, the fluid exchange of each roller with its neighbouring rollers occurs only in the braid regions. This comes in contrast to our simulations of shear layers at porous medium - pure fluid layers, which predict vortex pairing and a more complex evolution of the flow field. The absence of roller pairings can be attributed to the formation of the counter-rotating rollers near the top wall. These occupy a significant part of the pure-fluid region (see Figure A.1(d)) and therefore restrict the available space for upward displacement of the vortices on the interface. This prevents the rollers to climb on top of each other, as happens during roller pairings in the semi-bounded shear layers that were described in the Section 4.4.

Conclusions

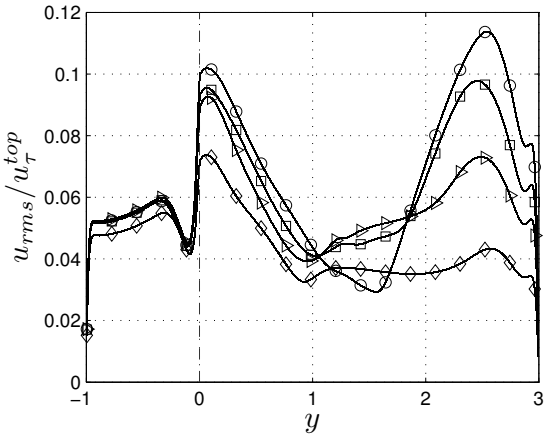

Figure A.3: Forced flow in a channel. Plots of the normalized u_{rms} at four instances, from the roller formation and until the end of the simulation. ($\diamond : t = 39.31$; $\triangleright : t = 45.69$; $\square : t = 52.05$; $\circ : t = 58.04$). The dashed vertical line indicates the position of the interface.

In this appendix, we discussed results from our simulation of forced flow in a channel, with a porous layer attached to its lower wall. The evolution of the flow in this problem, leads to the formation of rollers at the interface between the porous and the pure-fluid regions, as happens in the shear flows discussed above. However, in this case the rollers require longer times to develop, indicating the slower growth of the instabilities. Subsequent to their formation, the rollers grow, and eventually interact with the top wall of the channel. At the end of the simulation, this interaction leads to the formation of a new set of counter-rotating rollers next to the top wall. These occupy a significant part of the pure-fluid domain, thus restricting the available space for upward displacement of the vortices at the interface. As a result, neighbouring rollers at the interface do not pair with each other, as happens in the simulations of shear flows.

Appendix B

Non-dimensionalization of the drag parameter

In what follows, symbols with hat (ˆ) denote dimensional quantities. For example, $\hat{u}_r$ and $\hat{l}_r$ denote dimensional reference velocity and reference length, respectively. Moreover, symbols without hat denote dimensionless quantities.

Let us consider a spherical particle of diameter $\hat{d}_p$. The amplitude of the force acting on a sphere is given by the well known relation

$$\hat{F}_s \,=\, \frac{1}{2}\,\hat{\rho}\,C_D\,\hat{A}\,\hat{u}^2\,, \tag{B.0.1}$$

where

$$\hat{A} \,=\, \frac{1}{4}\pi\hat{d}_p{}^2 \tag{B.0.2}$$

is the sphere's reference area and C_D equals to the drag coefficient. Also in the above relation, $\hat{u}$ stands for the amplitude of the fluid' s velocity vector upstream the sphere. For Stokes flow around a sphere, the drag coefficient C_D is given by the following expression

$$C_D \,=\, \frac{24}{Re_s} \,=\, \frac{24}{\frac{\hat{u}\hat{d}_p}{\hat{\nu}}}\,, \tag{B.0.3}$$

Re_s being the particle's Reynolds number and $\hat{\nu}$ being the fluid's kinematic viscosity. By combining equations (1)-(3) we readily arrive in the following expression,

$$\hat{F}_s \,=\, 3\,\pi\,\hat{\rho}\,\hat{d}_p\,\hat{\nu}\,\hat{u}\,. \tag{B.0.4}$$

The force *per unit volume* on a conglomerate of spheres is equal to

$$\hat{F} \;=\; \hat{N}_s\,\hat{F}_s\,, \tag{B.0.5}$$

where $\hat{N}_s$ is the number density of spherical particles. $\hat{N}_s$ is given by

$$\hat{N}_s \;=\; \frac{6(1-\phi)}{\pi \hat{d}_p^{\,3}}\,, \tag{B.0.6}$$

ϕ being the fluid's volume fraction. By combining (4) - (6) we arrive at

$$\hat{F} \;=\; 18\,(1-\phi)\frac{\hat{\rho}\,\hat{u}\,\hat{\nu}}{\hat{d}_p^{\,2}}\,. \tag{B.0.7}$$

Evidently, the momentum equation (4.2.1b) is given in dimensionless form. The amplitude of the relaxation term in its right-hand-side is equal to the amplitude of the fluid deceleration due to the force acting on the fluid by the spherical particles; this force per unit volume is equal to $-\hat{F}$. Therefore, in view of relations (4.2.1b) and (4.2.2) we have, in dimensional form, that

$$(1-\phi)\hat{\beta}\hat{u} \;=\; \frac{\hat{F}}{\hat{\rho}}\,, \tag{B.0.8}$$

which by virtue of (7) results in

$$\hat{\beta} \;=\; 18\,\frac{\hat{\nu}}{\hat{d}_p^{\,2}}\,. \tag{B.0.9}$$

On the other hand, $\hat{\beta}$ is non-dimensionalized by the inverse of the reference time-scale, i.e. by $\frac{\hat{u}_r}{\hat{l}_r}$, where $\hat{u}_r$ is the reference velocity and $\hat{l}_r$ is the reference length. Thus, the non-dimensional value of $\hat{\beta}$, denoted by β, is given as

$$\hat{\beta} \;=\; \beta\,\frac{\hat{u}_r}{\hat{l}_r} \quad\Longrightarrow\quad \beta \;=\; 18\,\frac{\hat{\nu}}{\hat{d}_p^{\,2}}\,\frac{\hat{l}_r}{\hat{u}_r}\,. \tag{B.0.10}$$

But since $\hat{d}_p = d_p\,\hat{l}_r$, we get

$$\beta \;=\; \frac{18}{d_p^2}\,\frac{\hat{\nu}}{\hat{l}_r\,\hat{u}_r}\,. \tag{B.0.11}$$

Finally, by noting that $Re = \frac{\hat{u}_r\,\hat{l}_r}{\hat{\nu}}$, we arrive at the final result

$$\beta \;=\; \frac{18}{d_p^2}\,\frac{1}{Re}\,. \tag{B.0.12}$$

Bibliography

Akselvoll, K. & Moin, P. 1996 Large-eddy simulation of turbulent confined coannular jets. *J. Fluid Mech.* **315**, 387–411.

Alazmi, B. & Vafai, K. 2001 Analysis of fluid flow and heat transfer interfacial conditions between a porous medium and a fluid layer. *Int. J. Heat Mass Trans.* **44**, 1735–1749.

Banu, N. & Rees, D. A. S. 2002 Onset of Darcy-Bénard convection using a thermal non-equilibrium model. *Int. J. Heat Mass Tran.* **45**, 2221–2228.

Beavers, G.S. & Joseph, D.D. 1967 Boundary conditions at a naturally permeable wall. *J. Fluid Mech.* **30 (1)**, 197–207.

Beckermann, C., Diepers, H.-J., Steinbach, I., Karma, A. & Tong, X. 1999 Modeling melt convection in phase-field simulations of solidification. *J. Comput. Phys* **154**, 468–496.

Beckermann, C., Ramadhyani, S. & Viskanta, R. 1987 Natural convection flow and heat transfer between a fluid layer and a porous layer inside a rectangular enclosure. *J. Heat Trans.* **109**, 363–370.

Beckermann, C., Viskanta, R. & Ramadhyani, S. 1988 Natural convection in vertical enclosures containing simultaneously fluid and porous layers. *J. Fluid Mech.* **186**, 257–284.

Belcher, S.E., Harman, I.N. & Finnigan, J.J. 2012 The wind in the willows: flows in forest canopies in complex terrain. *Annu. Rev. Fluid Mech.* **44**, 479–504.

Bennon, W.D. & Incropera, F.P. 1987 A continuum model for momentum, heat and species transport in binary solid-liquid phase change systems. *Int. J. Heat Mass Tran.* **30**, 2161–2171.

de Boer, R. 2000 Contemporary progress in porous media theory. *Appl. Mech. Rev.* **53**, 323–370.

Breugem, W.P. & Boersma, B.J. 2005 Direct numerical simulations of turbulent flow over a permeable wall using a direct and a continuum approach. *Phys. Fluids* **17 (2)**, 025103.

Brown, D.L., Cortez, R. & Minion, M.L. 2001 Accurate projection methods for the incompressible navier-stokes equations. *J. Comput. Phys.* **168**, 464–499.

Chandesris, M., d'Hueppe, A., Mathieu, B., Jamet, D. & Goyeau, B. 2013 Direct numerical simulation of turbulent heat transfer in a fluid-porous domain. *Phys. Fluids* **25**, 125110.

Chandesris, M. & Jamet, D. 2007 Boundary conditions at a fluid-porous interface: An *a priori* estimation of the stress jump coefficients. *Int. J. Heat Mass Trans.* **50**, 3422–3436.

Chandesris, M. & Jamet, D. 2009 Jump conditions and surface-excess quantities at a fluid/porous interface: A multi-scale approach. *Transp. Porous Med.* **78**, 419–438.

Chang, M.-H. 2005 Thermal convection in superposed fluid and porous layers subjected to a horizontal plane Couette flow. *Phys. Fluids* **17 (6)**, 1–7.

Chang, M.-H., Chen, F. & Straughan, B. 2006 Instability of Poiseuille flow in a fluid overlying a porous layer. *J. Fluid Mech.* **564**, 287–303.

Chen, F. 1990 Throughflow effects on convective instability in superposed fluid and porous layers. *J. Fluid Mech.* **231**, 113–133.

Chen, F. & Chen, C.F. 1988 Onset of finger convection in a horizontal porous layer underlying a fluid layer. *J. Heat Trans.* **110**, 403–409.

Chen, F. & Chen, C.F. 1989 Experimental investigation of convective stability in a superposed fluid and porous layer when heater from below. *J. Fluid Mech.* **207**, 311–321.

Chen, F. & Chen, C.F. 1992 Convection in superposed fluid and porous layers. *J. Fluid Mech.* **234**, 97–119.

Chen, F., Yu, P., Winoto, S.H. & Low, H-T 2008 A numerical method for forced convection in porous and homogeneous fluid domains coupled at interface by stress jump. *Int. J. Num. Meth. Fluids* **56**, 1705–1729.

Chorin, A.J. 1967 A numerical method for solving incompressible viscous flow problems. *J. Comput. Phys.* **2**, 12–26.

Cowin, S. C. 2008 *Continuum Mechanics of Anisotropic Materials*. Springer.

Craske, J. & van Reeuwijk, M. 2013 Robust and accurate open boundary conditions for incompressible turbulent jets and plumes. *Comput. Fluids* **86**, 284–297.

Drazin, P.G. & Reid, W.H. 1982 *Hydrodynamic Stability*. Cambridge University Press.

Drumheller, D. S. 2000 On theories of reacting immiscible mixtures. *Int. J. Engng. Sci.* **38**, 347–382.

Du, L. & Xie, M. 2011 Numerical prediction of radiative heat transfer in reciprocating superadiabatic combustion in porous media. *J. Environ. Sci.* **23**, S26–S31.

Felten, F.N. & Lund, T.S. 2001 *Critical comparison of the collocated and staggered grid arrangements for incompressible turbulent flows, DNS/LES Progress and Challenges, editors: C. Liu, L. Sakell and T. Beutner*. Greyden Press.

Finnigan, J. 2000 Turbulence in plant canopies. *Annu. Rev. Fluid Mech.* **32**, 519–571.

Finnigan, J.J., Shaw, R.H. & Patton, E.G. 2009 Turbulence structure above a vegetation canopy. *J. Fluid Mech.* **637**, 387–424.

Ghisalberti, M. & Nepf, H. 2002 Mixing layers and coherent structures in vegetated aquatic flows. *J. Geophys. Res., No C2* **107**, 1–11.

Ghisalberti, M. & Nepf, H. 2009 Shallow flows over a permeable medium: The hydrodynamics of submerged aquatic canopies. *Transp. Porous Med.* **78**, 309–326.

Goodman, M. A. & Cowin, S. C. 1972 A continuum theory for granular materials. *Arch. Rat. Mech. Anal.* **44**, 249–266.

Goyeau, B., Lhuillier, D., Gobin, D. & Velarde, M.G. 2003 Momentum transport at a fluid-porous interface. *Int. J. Heat Mass Tran.* **46**, 4071–4081.

Gray, W.G. & Miller, C.T. 2010 Thermodynamically constrained averaging theory approach for modeling flow and transport phenomena in porous medium systems: 8. Interface and common curve dynamics. *Adv. Water Resour.* **33**, 1427–1443.

Gupta, V.P. & Joseph, D.D. 1973 Bounds for heat transport in a porous layer. *J. Fluid Mech.* **57(3)**, 491–514.

Harris, S.D., Fisher, Q.J., Karimi-Fard, M., Vaszi, A.Z. & Wu, K. 2005 *Modelling the effects of faults and fractures on fluid flow in pertroleum reservoirs,Transport Phenomena in Porous Media III, editors: D. B. Ingham and I. Pop*. Elsevier.

Hill, A.A. & Carr, M. 2010*a* Nonlinear stability of the one-domain approach to modelling convection in superposed fluid and porous layers. *Proc. R. Soc. A* **466**, 2695–2705.

Hill, A.A. & Carr, M. 2010*b* Sharp global nonlinear stability for a fluid overlying a highly porous material. *Proc. R. Soc. A* **466**, 127–140.

Hill, A.A. & Straughan, B. 2008 Poiseuille flow in a fluid overlying a porous medium. *J. Fluid Mech.* **603**, 137–149.

Hill, A.A. & Straughan, B. 2009 Global stability for thermal convection in a fluid overlying a highly porous material. *Proc. R. Soc. A* **465**, 207–217.

Hirata, S.C., Goyeau, B. & Gobin, D. 2009*a* Stability of thermosolutal natural convection in superposed fluid and porous layers. *Transp. Porous Med.* **78**, 525–536.

Hirata, S.C., Goyeau, B., Gobin, D., Carr, M. & Cotta, R.M. 2007 Linear stability of natural convection in superposed fluid and porous layers: influence of the interfacial modelling. *Int. J. Heat Mass Tran.* **50**, 1356–1367.

Hirata, S. C., Goyeau, B., Gobin, D., Chandesris, M. & Jamet, D. 2009*b* Stability of natural convection in superposed fluid and porous layers: equivalence of the one- and two-domain approaches. *Int. J. Heat Mass Tran.* **52**, 533–536.

Hong, W.-L. & Walker, D.T. 2000 Reynolds-averaged equations for free-surface flows with application to high-froude-number jet spreading. *J. Fluid Mech.* **417**, 183–209.

Horton, C.W. & Rogers, F.T. 1945 Convection currents in a porous medium. *J. Appl. Phys.* **16**, 367–370.

Hu, Z., Yu, B., Chen, Z., Li, T. & Liu, M. 2012 Numerical investigation on the urban heat island in an entire city with an urban porous media model. *Atmos. Environ.* **47**, 509–518.

Incropera, F.P., DeWitt, D.P., Bergman, T.L. & Lavine, A.S. 2007 *Fundamentals of Heat and Mass Transfer*, 6th edn. John Wiley.

Jackson, A.S., Rybak, I., Helmig, R., Gray, W.G. & Miller, C.T. 2012 Thermodynamically constrained averaging theory approach for modeling flow and transport phenomena in porous medium systems: 9. Transition region models. *Adv. Water Resour.* **42**, 71–90.

Jäger, W. & Mikelić, A. 2009 Modeling effective interface laws for transport phenomena between an unconfined fluid and a porous medium using homogenization. *Transp. Porous Med.* **78**, 489–508.

Katto, Y. & Masuoka, T. 1967 Criterion for the onset of convective flow in a fluid in a porous medium. *Int. J. Heat Mass Tran.* **10**, 297–309.

Kim, J. & Moin, P. 1985 Application of a fractional-step method to incompressible navier-stokes equations. *J. Comput. Phys.* **59**, 308–323.

Kooshkbaghi, M. & Lessani, B. 2013 A collocated grid, projection method for time-accurate calculation of low-mach number variable density flows in general curvilinear coordinates. *Int. J. Numer. Meth. Fl.* **72(3)**, 301–319.

Kumar, A.A.P., Goyal, H., Banerjee, T. & Bandyopadhyay, D. 2013 Instability modes of a two-layer Newtonian plane Couette flow past a porous medium. *Phys. Rev. E.* **87**, 063003.

Kuznetsov, A. V. & Nield, D. A. 2010 Forced convection in a channel partly occupied by a bidisperse porous medium: asymmetric case. *Int. J. Heat Mass Tran.* **53**, 5167–5175.

Lachaud, J., Cozmuta, I. & Mansour, N.N. 2010 Multiscale approach to ablation modeling of phenolic impregnated carbon ablators. *J. Spacecraft Rockets* **47(6)**, 910–921.

de Langre, E. 2008 Effects of wind on plants. *Annu. Rev. Fluid Mech.* **40**, 141–168.

Lapwood, E.R. 1948 Convection of a fluid in a porous medium. *Proc. Camb. Phil. Soc.* **44**, 508–521.

Le Bars, M. & Worster, M.G. 2006 Interfacial conditions between a pure fluid and a porous medium: implications for binary alloy solidification. *J. Fluid Mech.* **550**, 149–173.

Lebon, D. G., Jou, D. & Casas-Vázquez, J. 2008 *Understanding Non-equilibrium Thermodynamics: Foundations, Applications, Frontiers*. Springer.

Leonardi, S.A., Viskanta, R. & Gore, J.P. 2003 Analytical and experimental study of combustion and heat transfer in submerged flame metal fiber burners/heaters. *J. Heat Transf.* **125**, 118–125.

Lessani, B. & Papalexandris, M.V. 2006 Time-accurate calculation of variable-density flows with strong temperature gradients and combustion. *J. Comput. Phys.* **212**, 218–246.

Liu, R. & Liu, Q.S. 2010 Instabilities and transient behaviors of a liquid film flowing down a porous inclined plane. *Phys. Fluids* **22 (7)**, 074101.

Liu, R., Liu, Q.S. & Zhao, S.C. 2008 Instability of plane Poiseuille flow in a fluid-porous system. *Phys. Fluids* **20 (10)**, 104105.

Malashetty, M.S., Shivakumara, I.S. & Kulkarni, S. 2005 The onset of Lapwood-Brinkman convection using a thermal non-equilibrium model. *Int. J. Heat Mass Tran.* **48**, 1155–1163.

Marle, C. M. 1982 On macroscopic equations governing multiphase flow with diffusion and chemical reactions in porous media. *Int. J. Eng. Sci.* **20(5)**, 643–662.

Miller, C.T. & Gray, W.G. 2005 Thermodynamically constrained averaging theory approach for modeling flow and transport phenomena in porous medium systems: 2. Foundation. *Adv. Water Resour.* **28**, 181–202.

Min, J. Y. & Kim, S. J. 2005 A novel methodology for thermal analysis of a compositye system consisting of a porous medium and an adjacent fluid layer. *J. Heat Trans.* **127**, 648–656.

Miyauchi, T., Tanahashi, M. & Suzuki, M. 1996 Inflow and outflow boundary conditions for direct numerical simulations. *JSME Int. J., Ser. B* **39**, 305–314.

Moser, R.D. & Rogers, M.M. 1991 Mixing transition and the cascade to small scales in a plane mixing layer. *Phys. Fluids A* **3 (5)**, 1128–1134.

Moser, R.D. & Rogers, M.M. 1993 The three-dimensional evolution of a plane mixing layer: pairing and transition to turbulence. *J. Fluid Mech.* **247**, 275–320.

Mosthaf, K., Baber, K., Helmig, R., Leijnse, A., Rybak, I. & Wohlmuth, B. 2011 A coupling concept for two-phase compositional porous-medium and single-phase compositional free flow. *Adv. Water Resour.* **47**, W10522.

Mujeebu, M.A., Abdullah, M.Z., Bakar, M.Z.A., Mohamad, A.A., Muhad, R.M.N. & Abdullah, M.K. 2009 Combustion in porous media and its applications - A comprehensive survey. *J. Environ. Manage.* **90**, 2287–2312.

Mujeebu, M.A., Abdullah, M.Z., Mohamad, A.A. & Bakar, M.Z.A. 2010 Trends in modeling of porous media combustion. *Prog. Energ. Combust.* **36**, 627–650.

Nield, D.A. 1968 Onset of thermohaline convection in a porous medium. *Water Resour. Res.* **4(3)**, 553–560.

Nield, D.A. & Bejan, A. 2013 *Convection in Porous Media, 4th Edition*. Springer.

Nield, D. A. 2012 A note on local thermal non-equilibrium in porous media near boundaries and interfaces. *Transp. Porous Med.* **95**, 581–584.

Nield, D. A. & Kuznetsov, A. V. 2011 Forced convection in a channel partly occupied by a bidisperse porous medium: symmetric case. *J. Heat Trans.* **133**, 072601.

Ochoa-Tapia, J.A. & Whitaker, S. 1995 Momentum transfer at the boundary between a porous medium and a homogeneous fluid - I. Theoretical development. *Int. J. Heat Mass Tran.* **38**, 2635–2646.

Ochoa-Tapia, J.A. & Whitaker, S. 1997 Heat transfer at the boundary between a porous medium and a homogeneous fluid. *Int. J. Heat Mass Tran.* **40**, 2691–2707.

Ol'shanskii, M.A. & Staroverov, V.M. 2000 On simulation of outflow boundary conditions in finite difference calculations for incompressible fluid. *Int. J. Numer. Meth. Fl.* **33(4)**, 499–534.

Panerai, F., Mansour, N.N., Lachaud, J. & Martin, A. 2014 Experimental and numerical study of carbon fiber oxidation. *Proc. 52nd AIAA Aero. Sci. Meet.* pp. 2014–1208.

Papalexandris, M.V. 2004 A two-phase model for compressible granular flows based on the theory of irreversible processes. *J. Fluid Mech.* **517**, 113–112.

Pascal, J.P. 1999 Linear stability of fluid flow down a porous inclined plane. *J. Phys. D* **32**, 417.

Pascal, J.P. 2006 Instability of power-law fluid flow down a porous incline. *J. Non-Newton. Fluid Mech.* **133**, 109–120.

Pope, S.B. 2000 *Turbulent Flows*. Cambridge University Press.

Poulikakos, D. & Bejan, A. 1983 Natural convection in vertically and horizontally layered porous media heated from the side. *Int. J. Heat Mass Tran.* **26**, 1805–1814.

Promislow, K., Stockie, J. & Wetton, B. 2006 A sharp interface reduction for multiphase transport in a porous fuel cell electrode. *Proc. R. Soc. A* **462**, 789–816.

Quintard, M. & Whitaker, S. 2005 *Coupled, nonlinear mass transfer and heterogeneous reaction in porous media. Handbook of Porous Media, editor K. Vafai*. Taylor & Francis.

Raupach, M.R., Finnigan, J.J. & Brunet, Y. 1996 Coherent eddies and turbulence in vegetation canopies: the mixing-layer analogy. *Bound.-Lay. Meteorol.* **78**, 351–382.

Raupach, M.R. & Thom, A.S. 1981 Turbulence in and above plant canopies. *Annu. Rev. Fluid Mech.* **13**, 97–129.

Rees, D. A. & Pop, I. 2005 *Local thermal non-equilibrium in porous medium convection, Transport Phenomena in Porous Media III, editors: D. B. Ingham and I. Pop*. Elsevier.

Rhie, C.M. & Chow, W.L. 1983 Numerical study of the turbulent flow past an airfoil with trailing edge separation. *AIAA J.* **21 (11)**, 1525–1532.

del Rio, J. A. & de Haro, M. Lopez 1992 Extended irreversible thermodynamics as a framework for transport phenomena in porous media. *Trans. Porous Media* **9**, 207–221.

Rogers, M.M. & Moser, R.D. 1994 Direct simulation of a self-similar turbulent mixing layer. *Phys. Fluids* **6 (2)**, 903–923.

Sadiq, I.M.R. & Usha, R. 2008 Thin Newtonian film flow down a porous inclined plane: Stability analysis. *Phys. Fluids* **20 (2)**, 022105.

Sadiq, I.M.R., Usha, R. & Joo, S.W. 2010 Instabilities in a liquid film flow over an inclined heated porous substrate. *Chem. Eng. Sci.* **65 (15)**, 4443–4459.

Saffman, P.G. 1971 On the boundary condition at the surface of a porous medium. *Stud. Appl. Math.* **1**, 93–101.

Sahraoui, M. & Kaviany, M. 1992 Slip and no-slip velocity boundary conditions at interface of porous, plain media. *Int. J. Heat Mass Tran.* **35 (4)**, 927–943.

Sani, R.L. & Gresho, P.M. 1994 Résumé and remarks on the open boundary condition minisymposium. *Int. J. Numer. Meth. Fl.* **18(10)**, 983–1008.

Sen, S., Mittal, S. & Biswas, G. 2009 Steady separated flow past a circular cylinder at low reynolds numbers. *J. Fluid Mech.* **620**, 89–119.

Séro-Guillaume, O. & Margerit, J. 2001 Modelling forest fires. Part I: a complete set of equations derived by extended irreversible thermodynamics. *Int. J. Heat Mass Tran.* **45**, 1705–1722.

Straughan, B. 2005 *Stability and Wave Motion in Porous Media*. Springer.

Straughan, B. 2006 Global stability in porous convection with a thermal non-equilibrium model. *Proc. R. Soc. A* **462**, 409–418.

Sundaresan, S. & Amundson, N.R. 1980 Diffusion and reaction in a stagnant boundary layer about a carbon particle. 5. pseudo-steady-state structure and parameter sensitivity. *Ind. Eng. Chem. Fundam.* **19** (4), 344–351.

Temam, R. 1968 Une méthode d'approximation de la solution des quations de navier-stokes. *Bull. Soc. Math. France* **96**, 115–152.

Thiele, U., Goyeau, B. & Velarde, M.G. 2009 Stability analysis of thin film flow along a heated porous wall. *Phys. Fluids* **21 (1)**, 014103.

Tilton, N. & Cortelezzi, L. 2006 The destabilizing effects of wall permeability in channel flows: A linear stability analysis. *Phys. Fluids* **18**, 051702.

Tilton, N. & Cortelezzi, L. 2008 Linear stability analysis of pressure-driven flows in channels with porous walls. *J. Fluid Mech.* **604**, 411–445.

Tomboulides, A.G., Lee, J.C.Y. & Orszag, S.A. 1997 Numerical simulation of low mach number reactive flows. *J. Sci. Comput.* **12(2)**, 139–167.

Valdés-Parada, F.J., Goyeau, B. & Ochoa-Tapia, J.A. 2007 Jump momentum boundary condition at a fluid-porous dividing surface: Derivation of the closure problem. *Chem. Eng. Sci.* **62**, 4025–4039.

Varsakelis, C. & Papalexandris, M.V. 2011 Low-mach-number asymptotics for two-phase flows of granular materials. *J. Fluid Mech.* **669**, 472–497.

Varsakelis, C. & Papalexandris, M.V. 2014 A numerical method for two-phase flows of dense granular mixtures. *J. Comput. Phys.* **257**, 737–756.

Varsakelis, C. & Papalexandris, M. V. 2010 The equilibrium limit of a constitutive model for two-phase granular mixtures and its numerical approximation. *J. Comput. Phys.* **229**, 4183–4207.

van der Vorst, H.A. 1992 Bi-cgstab: A fast and smoothly converging variant of bi-cg for the solution of nonsymmetric linear systems. *SIAM J. Sci. and Stat. Comput.* **13**, 631–644.

Whitaker, S. 1999 *The Method of Volume Averaging*. Springer Science.

Yang, K. & Vafai, K. 2010 Analysis of temperature gradient bifurcation in porous media: an exact solution. *Int. J. Heat Mass Trans.* **53**, 4316–4325.

Yu, Z.T., Xu, X., Fan, L.W., Hu, Y.C. & Cen, K.F. 2011 Experimental measurements of thermal conductivity of wood spevies in china Effects of density, temperature, and moisture content. *Forest Prod. J.* **61(2)**, 130–135.

Zhou, X.Y. & Pereira, J.C.F. 1997 Numerical study of combustion and pollutants formation in inert nonhomogeneous porous media. *Combust. Sci. Technol.* **130**, 335–364.